The Crystal Chemistry of Novel Thorium and Uranium Compounds with Oxo-Anions from Group VI of Periodic Table (S, Se, Te, Cr, Mo and W)

Von der Fakultät für Georessourcen und Materialtechnik der
Rheinisch -Westfälischen Technischen Hochschule Aachen

Zur Erlangung des akademischen Grades eines
Doktors der Naturwissenschaften

genehmigte Dissertation

Vorgelegt von
Magister für Technik und Technologie

Bin Xiao

aus Sichuan, China

Berichter: Prof. Dr. rer.nat. Evgeny V. Alekseev
Univ.-Prof. Dr. rer. nat. Georg Roth
Univ.-Prof. Dr. rer. nat. Dirk Bosbach

Tag der mündlichen Prüfung: 26. Januar 2016

Abstract

This dissertation focus on the synthesis, phase studies and physicochemical properties of novel thorium and uranium compounds with the Group VI (S, Se, Te, Cr, Mo, W) of the Periodic Table. All the studied compounds are listed in **Table** 2.2 from the **page** 15. I subdivided all the newly synthesized compounds into several chapters according to their structural and topological differences.

First, for thorium molybdates and tungstates, almost all of these compounds are based on corner-sharing of ThO_x (x = 6, 8 and 9) and MoO_4 or WO_x (x = 4, 5, 6) polyhedra. Interestingly, all these compounds can be seen as derived from a pure thorium molybdate compound ($ThMo_2O_8$) which was isolated from high-temperature solid-state synthesis method. Therefore, the polymorphs of this most basic $ThMo_2O_8$ compound is firstly introduced (see **Chapter** 3.1 from **page** 18). The thermodynamic, electronic and vibrational properties of all investigated $ThMo_2O_8$ polymorphs were studied using *ab initio* calculations.

Then, two subfamilies of thorium molybdates, that is, rubidium thorium molybdate and cesium thorium molybdate and their thermal and vibrational behaviors were discussed in details in **Chapter** 4.1 from **page** 37 and **Chapter** 4.2 from **page** 50, respectively.

Moreover, some new insights about the complexity of thorium tungstates were also discussed (**Chapter** 4.3 from **page** 59). Some novel thorium molybdate and chromate compounds synthesized from aqueous condition are discussed in **Chapter** 5 from **page** 71.

In the **Chapter** 8.2.4, the stereochemistry for thorium and uranium compounds are introduced, especially thorium selinites and uranyl tellurites (see **Chapter** 6.1 from **page** 82), thorium tellurites (**Chapter** 6.2 from **page** 93), and uranyl tellurites (**Chapter** 6.3 from **page** 99 for sodium uranyl tellurium and **Chapter** 6.4 from **page** 110 for potassium uranyl tellurium, respectively). In the actinide tellurium systems, additional MoO_3/WO_3 were also used as the flux for the high-temperature synthesis method to decrease the crystal growth temperature. This also gives an opportunity to allow Te^{4+} anion to interact with anion of Mo^{6+} or W^{6+}, leading to a more complex mixed oxo-anion system, which is reported in **Chapter** 7 from **page** 122.

Last, some attractive features of structural chemistry of actinides, such as cation-cation interaction

of uranyl groups(**Chapter** 8.1 from **page** 136), and the first thorium compounds containing alkaline-earth or rare earth metals (**Chapter** 8.2 from **page** 145) are discussed in **Chapter** 8.

Contents

Chapter 1

Introduction

The crystal chemistry of actinide compounds, especially uranium materials containing oxo-anions from the group VI (S, Se, Te, Cr, Mo, W) of the Periodic Table, has been actively investigated for decades owing to their environmental importance and fundamental interest.[1] Firstly, these compounds are widely observed within uranium deposits, being the common constituents of the oxidized zones of uranium minerals.[2] For example, moctezumite ($Pb(UO_2)(TeO_3)_2$) and schmitterite (UO_2TeO_3) are the secondary minerals commonly observed in telluride-bearing ores;[3] deloryite ($Cu_4(UO_2)(MoO_4)_2(OH)_6$) can form in oxidized portion of a uranium deposit in sandstones;[4] iriginite ($[(UO_2)Mo_2O_7] \cdot 3(H_2O)$) is the most abundant secondary mineral in the oxidized zones of hydrothermal U-Mo deposits.[5] It is reported to commonly occur on the walls of mine shafts. The fundamental information, such as structures or thermal stabilities, is prerequisite for understanding the alteration and mobility of radionuclides around geological repositories of nuclear waste.

Secondly, the actinide compounds containing elements of VI group play an important role in affecting the long-term disposal of spent nuclear fuel (SNF).[6] Mo and Se are high yield fission products formed as a result of the spent nuclear fuel in reactors.[7] Te is also an important fission product with moderate yield, therefore it may involve in a large array of chemical interactions among fission products with nuclear fuel, leading to formation of complex actinide compounds and in turn affecting the integrity and behavior of fuel. Therefore, knowledge of chemical properties of these actinide compounds becomes essential for evaluating and manipulating their behavior regarding nuclear safety management.

---

[1] Sergey V. Krivovichev and Peter C. Burns. "Chapter 4 - Actinide compounds containing hexavalent cations of the VI group elements (S, Se, Mo, Cr, W)" in: *Structural Chemistry of Inorganic Actinide Compounds* ed. by Sergey V. KrivovichevPeter C. BurnsIvan G. Tananaev. Amsterdam: Elsevier, 2007. 95–182

[2] Robert Finch and Takashi Murakami. *Reviews in Mineralogy and Geochemistry*, **38**: 91–179, 1999.

[3] G.H. Swihart et al. *Am. Mineral.*, **78**: 835–839, 1993.

[4] D.Yu. Pushcharovsky, R.K. Rastsvetaeva, and H. Sarp. *J. Alloys Compd.*, **239**: 23–26, 1996.

[5] A.A. chernikov. *Behaviour of Uranium in the Hypergene Zone.* Nedra, Moscow, Russia (in Russ.), 1981.

[6] Peter C Burns. *Can. Mineral.*, **43**: 1839–1894, 2005.

[7] S. V. Krivovichev, C. L. Cahill, and P. C. Burns. *Inorg. Chem.*, **41**: 34–39, 2001.

Thirdly, from a more fundamental point of view, actinides and hexavalent elements (S^{6+}, Se^{6+}, Te^{6+}, Cr^{6+}, Mo^{6+} and W^{6+}) exhibit rich coordination geometries. On the one hand, actinides in high oxidation states (5+, 6+, 7+) typically form an approximately linear actinyl cation ($AnO_2{}^{2+}$) with the ability to connect with four to six donor atoms in their equatorial planes, forming tetrahedral, pentagonal and hexagonal bipyramidal configuration. By contrast, actinides in lower oxidation states (2+, 3+, 4+) are usually found to result in a more homogeneous geometry, which can achieve considerably high coordination numbers.[6] Thorium(IV), for instance, can coordinate with up to fifteen ligands to result in fascinating topological geometries.[8] On the other hand, the M^{6+} (M = S, Se, Te, Cr, Mo and W) cations are often observed in six-fold coordinated MO_6 octahedral polyhedra. The combination of thorium with group(VI) cations are known to form structures with unusual topological features such as hexanuclear clusters in thorium selenate[9], microporous frameworks in thorium sulfate[10]. In particular, the coordination modes for these Group VI elements can become more complex if they are interlinked together. This can be especially exemplified from chromium, tellurium, molybdenum and tungsten, which are favorable for forming polyoxo-chains, polyoxo-layers and polyoxo-frameworks (*e.g.* the structural architects for tellurium polyoxoanions from 1D to 3D are shown in **Figure 1.2 of Chapter 1.2 on page 6**).

In this dissertation, I subdivided all the newly synthesized compounds (listed in **Table** 2.2 on **page 15**) into six chapters according to their structural and topological differences.

1.1 Basic chemistry of uranium and thorium

Uranium and thorium are the only actinides which occur in nature in appreciable quantities. Both elements are very important for the nuclear energy. From a fundamental point of view, the actinides have extremely diverse structural chemistry due to their unique coordination geometries and different oxidation states. Actinides in high oxidation states (5+, 6+, 7+) typically form an approximately linear actinyl cation ($AnO_2{}^{2+}$).[6] In contrast, actinides in lower oxidation states (2+, 3+, 4+) are usually found to result in a more complex geometry with the ability to achieve high coordination numbers.

Table 1.1: Oxidation states of uranium and thorium (bold font means stable state)

	Oxidation States	Basic oxide compounds
U	2+ 3+ **4+** 5+ **6+**	U_2O_5 U_3O_8 $\mathbf{UO_2}$ $\mathbf{UO_3}$
Th	2+ 3+ **4+**	$\mathbf{ThO_2}$

---

[8] Jonathan A. Webb and Indrajit Charit. *Nucl. Eng. Des.*, **241**: 2968–2973, 2011.

[9] Bin Xiao et al. *Inorg. Chem.*, **54**: 3022–3030, 2015.

[10] Richard E. Wilson et al. *Inorg. Chem.*, **47**: 9321–9326, 2008.

The variable coordination numbers and numerous oxidation states of actinide elements allow these compounds to expand practically without limitation. Table **1.1** lists the most common oxidation states of uranium and thorium and the corresponding compounds. Uranium is an important element from the actinides series. It owns valences from II to VI in the solid state where IV and VI are most usual and stable.[11] Under oxidizing condition, uranium is normally found in hexavalent state in both solution and solid-state. The U(VI) is dominated by the configuration of so-called uranyl cation ($\mathrm{UO_2}^{2+}$) formed *via* connecting two oxo oxygen atoms with one uranium center. It is a linear geometry that can further coordinate with four to six ligands perpendicular to its linear direction to result in tetragonal, pentagonal and hexagonal bipyramidal polyhedra.[6]

For the past two decades, due to the efforts of many research groups, lots of new U(VI) compounds have being isolated. Most of these uranium compounds are based on two-dimensional layers (*e.g.* see **Figure 1.1**). In this case, the uranyl cations are oriented almost perpendicularly to the equatorial plane, with relatively weak interactions between the uranyl oxygen anions and other lower-valence ions located in the interlayer space. This phenomenon can be attributed to the terminal feature of the *trans* dioxo oxygen from the $\mathrm{UO_2}^{2+}$ units that are normally arranged in a parallel fashion. However, recent studies among the explosive growth of uranium compounds provide some unprecedented results that are competing and expanding the understanding of such typical uranium (VI) geometry.[12,13] In particular, the cation-cation interactions (referred to herein as CCIs) has gained attention. CCIs provide a means of U polyhedral linkage with anomalous connectivity and enable the development of novel structural features. CCIs can serve as effective routes to diversify the linkages of uranyl groups and increase the dimensional complexity of uranium compounds. Compared to the overwhelming majority of 2D sheet structures of uranyl moieties, the uranyl compounds containing CCIs prefer to adopt 3D frameworks.

As the case of U(IV), its coordination environment shares the similarity to that of Th(IV), which presents variable number of coordination states. This ranges from six-coordinate to twelve-coordinate, of which the eight and nine are most common. The pentavalent U(V) is not stable. It contains only single 5f electron, and has the simplest electron configuration. Therefore U(V) provides a practical model for not only simplifying theoretical calculations but also fundamental understanding of f electronic behavior of actinides.[14]

Compare to the versatile uranium, the thorium is much simpler. Thorium is the most abundant radioactive element in nature. Owing to the absence of 5f electrons, thorium occurs predominantly in the tetravalent oxidation state, achieving high coordination numbers that exhibits fascinate properties with diverse topological configuration and rich coordination chemistry.[15] Due to the lack of electrons in the 6d and 5f orbitals of thorium(IV), the typical thorium compounds are colorless. Additionally,

---

[11] Grégory Nocton et al. *J. Am. Chem. Soc.*, **132**: 495–508, 2010.
[12] Liam P. Spencer et al. *Angew. Chem. Int. Ed.*, **48**: 3795–3798, 2009.
[13] Chih-Shan Chen, Shang-Fan Lee, and Kwang-Hwa Lii. *J. Am. Chem. Soc.*, **127**: 12208–12209, 2005.
[14] Shuao Wang et al. *Inorg. Chem.*, **51**: 7016–7018, 2012.
[15] Monica Vasiliu et al. *J. Phys. Chem. A*, **116**: 6917–6926, 2012.

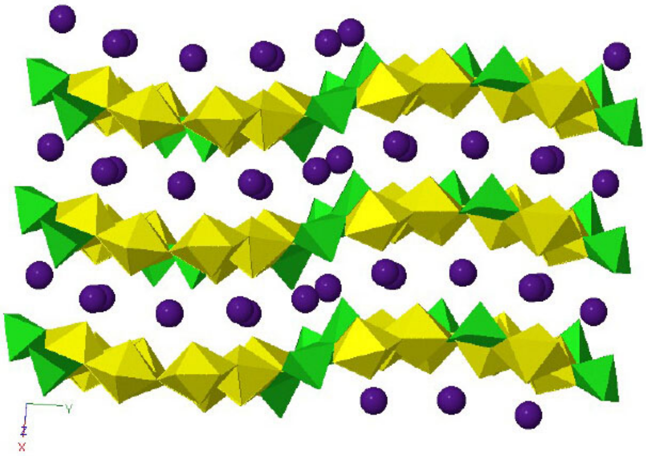

Figure 1.1: View of a typical uranyl compound with layered structure. This example is from the newly synthesized $Cs_4[(UO_2)_4(WO_5)(W_2O_8)O_2]$, and more structural information about this example can be seen in Section 8.1 on page 137

due to the stability of Th in the tetravalent state, Th(IV) is frequently used as an structural surrogate for studying other actinides (IV), especially those with high handling issues such as Np(IV) and Pu(IV).[16]

In aqueous solution, Th(IV) tends to hydrolyze and to construct a wide diversity of $\mathrm{Th(OH)_n}^{4-n}$ hydroxide complexes, the olation or oxolation of which can further result in the formation of polynuclear compounds.[17] Numerous polynuclear hydroxide Th species have already been isolated, including dimers such as $\mathrm{Th_2(OH)_2}^{6+}$, $\mathrm{Th_2(OH)_3}^{5+}$ and $\mathrm{Th_2(OH)_4}^{4+}$, respectively, tetramers such as $\mathrm{Th_4(OH)_8}^{8+}$ and $\mathrm{Th_4(OH)_{12}}^{4+}$, pentamers $\mathrm{Th_5(OH)_{12}}^{8+}$ and hexamers such as $\mathrm{Th_6(OH)_{14}}^{10+}$, and $\mathrm{Th_6(OH)_{15}}^{9+}$.[18] The largest Th oligomer up to now, to the best of knowledge, is the decanuclear $\mathrm{[Th_{10}F_{16}O_8(NH_3)_{32}]}^{8+}$ formed in $\mathrm{[Th_{10}F_{16}O_8(NH_3)_{32}](NO_3)_8]\cdot 19.6NH_3}$.[19] These polynuclear compounds, in conjunction with the aggregates and colloids of actinides, have already gathered extensive attention due to the role of transporting and migrating of radionuclides to the environment.[20]

1.2 Basic structural chemistry of S, Se, Te, Cr, Mo and W

The actinide compounds containing Group VI elements M (M = S, Se, Te, Cr, Mo and W) have diverse structural features. Generally, all these M^{6+} cations are coordinated with four O atoms, creating a $M(VI)O_4$ tetrahedral configuration. These $M(VI)O_4$ tetrahedra can further connect together through corner-, edge-, or face-sharing manners with actinide polyhedra to create clusters, one-dimensional (1D) chains, two-dimensional (2D) sheets and three-dimensional (3D) framework structures.

---

[16] Clément Falaise et al. *Inorg. Chem.*, –, 2015.

[17] Karah E. Knope et al. *Inorg. Chem.*, **51**: 4239–4249, 2012.

[18] Karah E. Knope et al. *Inorg. Chem.*, **50**: 9696–9704, 2011.

[19] Patrick Woidy and Florian Kraus. *Z. Anorg. Allg. Chem.*, **640**: 1547–1550, 2014.

[20] Alexander P. Novikov et al. *Science*, **314**: 638–641, 2006.

Sulfur

Sulfur can form in sulfite $S^{IV}O_3{}^{2-}$ and sulfate $S^{VI}O_4{}^{2-}$. The $S^{VI}O_4{}^{2-}$ are dominant in sulfur chemistry. Actinide sulfates have very long research history. For example, the first thorium sulfate was reported in 1829 by *Berzelius*, who noted that the hydration degree changes with the temperature of crystallization. [21]

Selenium

The predominant forms of Se are either selenite $Se(IV)O_3{}^{2-}$ or selenate $Se(VI)O_4{}^{2-}$ in oxosalt compounds. Owing to the existence of the stereochemically active lone-pair electrons in Se^{4+}, the $SeO_3{}^{2-}$ ions can act as the so-called structure-directing agents to yield relatively large number of structure types with consequently promising physical properties such as second-harmonic generation (SHG), piezoelectricity, ferroelectricity, and magnetic properties.[22,23] In recent years, one could witness the robust growth related to the synthesis and characterization of uranium(VI) selenium compounds, which exhibit diverse structural units from common sheet to the unique $[(UO_2)_3(SeO_4)_5]^{4-}$ nanotubes.[24]

Tellurium

Similarly, the tellurium, normally occurring as either tetravalent or hexavalent oxidation state, also bears fascinating structural chemistry. Te(VI) ubiquitously occurs in a distorted $Te^{VI}O_6$ octahedral geometry by coordinating with six O atoms, whereas the coordination environment of Te(IV) is more complicated due to its nonbonded electron pairs. Te(IV) can achieve three kinds of different structural building blocks: $Te^{IV}O_3$ trigonal pyramid, $Te^{IV}O_4$ disphenoid and $Te^{IV}O_5$ square pyramid.[25,26] These structural units can be further interconnected *via* corner-sharing, leading to complex tellurium polymers. **Figure 1.2** lists some of the common structural units of Te(IV) anions. $NH_4ATe^{IV}{}_4O_9 \cdot 2\,H_2O$ (A = Rb^+ or Cs^+) is a rare example in which three types of tellurium polyhedral coordination (TeO_3, TeO_4 and TeO_5) are found in a single phase.[27]

Chromium

Chromium is often found in 6+ (chromate). The simplest chromate is the CrO_3, which is based on one-dimensional infinite chains of corner-sharing tetrahedra.[28] In the aqueous condition, the Lewis acid CrO_3 can easily react with H_2O to form H_2CrO_4 with red color. It is known that $CrO_4{}^{2-}$ ions have the ability to polymerize, leading to the formation of a variety of units, including $Cr_2O_7{}^{2-}$ dimers, $Cr_3O_{10}{}^{2-}$ trimers and even $Cr_4O_{13}{}^{2-}$ tetramers.

Molybdenum

Mo(VI) centers can coordinate with four to six oxygen atoms, giving rise to tetrahedral, square

---

[21] J. J. Berzelius. *Poggendorf'sAnn.*, **16**: 385–415, 1829.

[22] Hyun Sun Ahn, Dong Woo Lee, and Kang Min Ok. *Inorg. Chem.*, **52**: 12726–12730, 2013.

[23] Sang-Hwan Kim, Jeongho Yeon, and P. Shiv Halasyamani. *Chem. Mater.*, **21**: 5335–5342, 2009.

[24] Sergey V. Krivovichev et al. *Angew. Chem. Int. Ed.*, **117**: 1158–1160, 2005.

[25] Fang Kong, Xiang Xu, and Jiang-Gao Mao. *Inorg. Chem.*, **49**: 11573–11580, 2010.

[26] Jian Lin et al. *Inorg. Chem.*, **51**: 10083–10085, 2012.

[27] Jun-Ho Kim and P. Shiv Halasyamani. *J. Solid State Chem.*, **181**: 2108–2112, 2008.

[28] Oleg I. Siidra et al. *Inorg. Chem.*, **52**: 4729–4735, 2013.

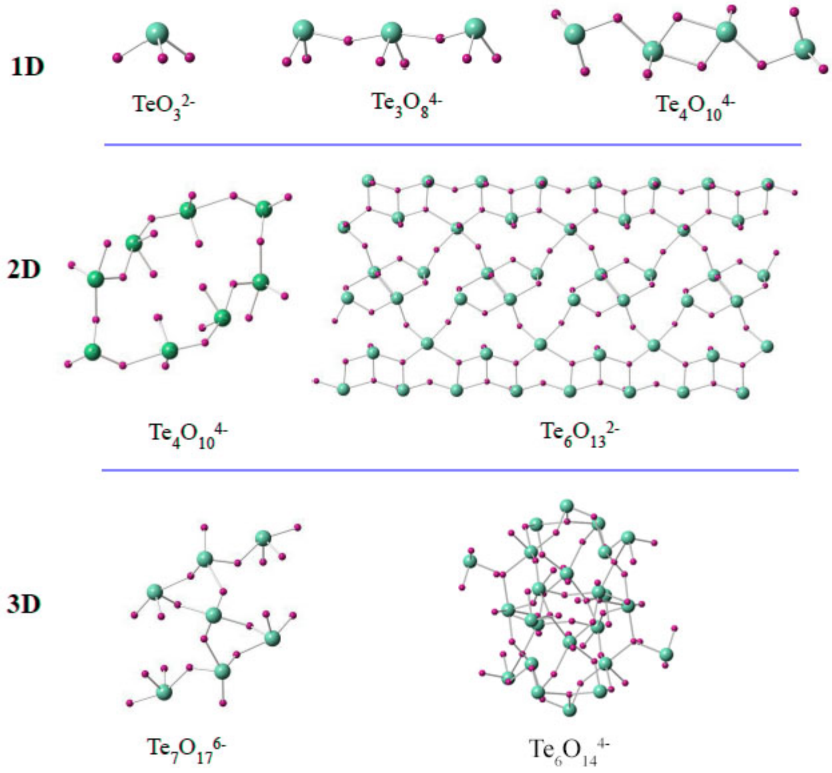

Figure 1.2: The connection of oxo-anion units of $Te^{IV}O_3$ trigonal pyramids, $Te^{IV}O_4$ disphenoids and $Te^{IV}O_5$ square pyramids formed in one-dimensional (1D) chains, two-dimensional (2D) sheets and three-dimensional (3D) framework structures.

pyramidal, trigonal bipyramidal and octahedral geometries. Among them, the tetrahedra (MoO_4^{2-}) are the most commonly observed coordination geometry. Moreover, these molybdenum polyhedra can be aggregated as a result of metal complexation to form various polymeric networks.[7] As a consequence, the actinide molybdate family demonstrates an inexhaustible potentiality of structural flexibility to form various structural motifs.

Tungsten

Tungstates also exhibit a very diverse structural chemistry with rich coordination geometries. Such diversity in oxo-tungstates is based on a flexible structural chemistry of WOx (x = 4, 5, 6) polyhedral units that are commonly found in the form of WO_4 tetrahedra, WO_6 octahedra and WO_5 square pyramids or WO_5 trigonal bipyramids.[29,30]

---

[29] Evgeny V. Alekseev et al. *Inorg. Chem.*, **46**: 8442–8444, 2007.

[30] Chuan-De Wu et al. *J. Am. Chem. Soc.*, **124**: 3836–3837, 2002.

1.3 Overview of the previously reported uranium and thorium compounds

Actinide sulfates are often observed in nature as important minerals that form when the sulfide minerals are oxidized in the presence of uranium.[2] Many uranyl sulfates belong to the zippeite family ($K_4(UO_2)_6(SO_4)_3(OH)_{10}\cdot 4\,(H_2O)$), with two-dimensional layers constructed by vertex-sharing sulfate tetrahedra.[31] Another common known uranyl mineral is uranopilite ($[(UO_2)_6(SO_4)O_2(OH)_6(H_2O)_6]$ $\cdot 8\,(H_2O)$),[32] containing chains formed by clusters of six uranyl pentagonal bipyramids and SO_4 tetrahedra. In both minerals, the sulfate tetrahedra connect between four uranyl units. In the case of synthetic actinide sulfate, *Knope, et al.* reported that in aqueous condition, the sulfate ligands trend to coordinating with early actinide such as Th in a monodentate manner, while bidentate sulfate complexation is more favorable for the later actinides.[33]

There are lots of uranium chromates reported in the literature. In contrast, with respect to thorium chromate, there are only two compounds in the database. The first is $Th(OH)_2(CrO_4)(H_2O)$ which was synthesized by *Lundgren, et al.* in 1949.[34] This 3D compound is based on eight-coordinated Th and four-coordianted Cr connected by sharing corners with each other. After this initial study, no new thorium chromate compounds were then reported for nearly 50 years. Until $Th(CrO_4)_2(H_2O)$ has been obtained by *Sullens, et al.* through mild hydrothermal condition in 2006.[35] $Th(CrO_4)_2(H_2O)$ is a far more complex structure encompassing Th cations in both ThO_8 dodecahedral and ThO_9 tricapped trigonal prismatic coordination geometries.

The thorium selenium system, as well as many other low-valent actinide such as Np(IV) and Pu(IV), have already been known for more than half of the century.[36] The first synthesized thorium selenium compounds are the octahydrate $Th(SeO_3)_2\cdot 8\,H_2O$ and monohydrate $Th(SeO_3)_2\cdot H_2O$ produced by the precipitation method, but there is a lack of crystallographic studies that support or confirm these proposed compounds. The first reported crystal structure of the thorium selenium system is $Th(SeO_3)(SeO_4)$ by *Sullens, et al.* in 2006.[35] It is an interesting mixed anion compound consisting of both $SeO_3{}^{2-}$ trigonal pyramidal and $SeO_4{}^{2-}$ tetrahedral oxoanions. Following on this, recently, by investigating the condensation of Th(IV) in aqueous condition, *Knope, et al.* have obtained and reported four novel selenate compounds containing an octanuclear $[Th_8O_4(OH)_8]^{16+}$ core.[17]

The first crystal structures of U-Te family were reported from three uranyl tellurite minerals, cliffordite ($UO_2(Te_3O_7)$)[37], moctezumite ($Pb(UO_2)(TeO_3)_2$)[3] and schmitterite (UO_2TeO_3)[38], from the deposi-

---

[31] P.C. Burns, K.M. Deely, and L.A. Hayden. *Can. Mineral.*, **41**: 687–706, 2003.

[32] P.C. Burns. *Can. Mineral.*, **39**: 1139–1146, 2001.

[33] Karah E. Knope et al. *Inorg. Chem.*, **50**: 8621–8629, 2011.

[34] Georg Lundgren and LarsGunnar Sillén. *Naturwissenschaften*, **36**: 345–346, 1949.

[35] Tyler A. Sullens et al. *J. Solid State Chem.*, **179**: 1192–1201, 2006.

[36] R. W. M. D'Eye, P. G. Sellman, and J. R. Murray. *J. Chem. Soc.*, 2555–2562, 1952.

[37] RV Gaines. *Am. Mineral.*, **54**: 697–701, 1969.

[38] G. Meunier and J. Galy. *Acta Crystallogr., Sect. B: Struct. Sci*, **29**: 1251–1255, 1973.

tion site in west Sonora, Mexico, near the town Moctezuma. Among them, $UO_2(Te_3O_7)$ is the first three-dimensional (3D) uranyl tellurite framework containing Te_6O_{18} hexagonal rings constructed from six corner-sharing TeO_5 square pyramids. Recently, it has been shown that low-temperature (180 $-$220 °C) mild hydrothermal synthesis is an effective route for formation of new tellurites,[39] which is generating more interest in exploring and studying the U-Te family. Following this trend, eleven new uranyl tellurite compounds with considerable structural diversities have been isolated. The structure of α- $Tl_2[(UO_2)(TeO_3)_2]$, simple on the outside formula, yet complex on the inside structure, is the most outstanding representative among these newly synthetic uranyl tellurite compounds. It contains a rarely observed $[Te_2O_6]^{4-}$ group constructed from overcoming significant repulsive coulombic forces between two edge-sharing TeO_3 polyhedra.[40] Shortly after this report, *Woodward, et al.* indicated that the molten salts can be used as an excellent reaction medium in the high-temperature (around 800 °C) flux synthetic method.[41] This method again results in another two alkali metal uranyl tellurites, $A_2[(UO_2)_3(TeO_3)_2O_2]$ (A = K, Rb, Cs) and $K_4[(UO_2)_5(TeO_3)_2O_5]$, with two-dimensional layers composed of novel uranyl chains, which are dramatically different from those synthesized at low-temperature hydrothermal conditions. Similar to uranyl tellurites, the crystal structure of the first uranyl tellurate compound, $Pb[(UO_2)(TeO_6)]$ (Markcooperite), was also discovered from minerals. It consists of sheets of corner-sharing UO_6 tetragonal bipyramids and TeO_6 octahedra, with Pb^{4+} acting as compensating ions in between. In continuation of this, very recently, also using hydrothermal method, *Ling, et al.* increased the total quantity of uranium tellurium compounds to sixteen by isolation of the first two synthetic uranyl tellurates, $Ag[(UO_2)(HTeO_5)]$ and $Pb_2[(UO_2)(TeO_6)]$.[42]

In the past few decades, the actinide molybdate compounds with high-valence, especially U(VI), have been experienced extensive research.[43] The structures for these compounds range from infinite cluster in $K_8Th(MoO_4)_6$ to the unprecedented framework of $(NH_4)_4[(UO_2)_5(MoO_4)_7](H_2O)_5$ that is built upon open $[(UO_2)_5(MoO_4)_7]^{4-}$ channels in the size of 4.8×4.8 Å^2. In 1970s, *Tabuteau, et al.* studied the $A_2MoO_4-M(MoO_4)_2$ ($A = K^+, Rb^+, Cs^+$; $M = Np^{4+}, Pu^{4+}$) system by means of X-ray powder diffraction and micro-thermal analysis method, where compound $A_2Pu(MoO_4)_3$ was found to adopt scheelite ($CaWO_4$-type) structure with A and Pu sites situated on the 8-coordinated Ca sites.[44,45] Compared to these actinide families, however, very less information is available on structural chemistry of thorium molybdate compounds. Most researches on the thorium molybdates were carried out more than two decades ago.[46] Until recently, after thorium being considered in the new generation of nuclear fuel cycles, have the thorium molybdates achieved renewed attention. The thermodynamic properties of $A_2Th(MoO_4)_3$ and $A_4Th(MoO_4)_4$ (A = Na, Tl) have been investigated by *Dahale, et al.*[47]

---

[39] Kang Min Ok and P. Shiv Halasyamani. *Chem. Mater.*, **14**: 2360–2364, 2002.

[40] Philip M. Almond, Michael L. McKee, and Thomas E. Albrecht-Schmitt. *Angew. Chem. Int. Ed.*, **41**: 3426–3429, 2002.

[41] J. D. Woodward, P. M. Almond, and T. E. Albrecht-Schmitt. *J. Solid State Chem.*, **177**: 3971–3976, 2004.

[42] Jie Ling, Matthew Ward, and Peter C. Burns. *J. Solid State Chem.*, **184**: 401–404, 2011.

[43] Sergey V. Krivovichev and Peter C. Burns. *Inorg. Chem.*, **41**: 4108–4110, 2002.

[44] Alain Tabuteau and Monique Pages. *Journal of Inorganic and Nuclear Chemistry*, **42**: 401–403, 1980.

[45] A. Tabuteau, M. Pags, and W. Freundlich. *Mater. Res. Bull.*, **7**: 691–697, 1972.

[46] J. THORET. *Comptes Rendus De L Academie Des Sciences Serie Ii*, **302**: 707–709, 1986.

[47] N.D. Dahale, Meera Keskar, and K.D. Singh Mudher. *J. Alloys Compd.*, **415**: 244–250, 2006.

$Cs_2Th(MoO_4)_3$ and $Cs_4Th(MoO_4)_4$ were characterized by high temperature X-ray diffraction and TGA techniques but the structure details are still not known. Following on this, very recently, *Orlandi, et al.* have discovered the first two natural thorium molybdate hydrates, $Th(MoO_4)_2 \cdot 3\,H_2O$ (ichnusaite) and $Th(MoO_4)_2 \cdot H_2O$ (nuragheite), respectively.[48,49]

The combination of tungsten with versatile actinides has already yielded some unprecedented results. For example, $Na_2Li_8[(UO_2)_{11}O_{12}(WO_5)_2]$ is a rare example among all actinide compounds to simultaneously consist three different actinyl coordinations.[50] The α/β-$Cs_2[(UO_2)_2(W_2O_9)]$ is the first case in the chemistry of uranium compounds involving in corner-sharing fivefold W_2O_8 polyhedra.[51] Typically, the WO_x polydedra can be aggregated through corner- and edge-sharing connectivity to construct condensed oxo-tungstates but rarely crystallize in face-sharing structures, since the electrostatic repulsion between these highly charged metal centers keep them from moving close to each other. Some exceptions to this generalization have been experimentally verified and characterized with low oxidation states of W ions from +3 to +5. They include a few metal halide compounds containing confacial bioctahedral $M(III)_2Cl_6$ (M = Mo, W) units.[52] Their existence is due to the low oxidation state of the central W atoms. Because of the low tungsten valence state, the d^3-d^3 electronic configuration of W atoms are favorable for stabilizing metal-metal bonding interactions.[52]

1.4 Motivation

During My Ph.D research, I am mainly focusing on study the crystal chemistry of actinide compounds containing hexavalent cations (S^{6+}, Se^{6+}, Te^{6+}, Mo^{6+} and W^{6+}). Based on this, the objective of this dissertation is to increase the fundamental knowledge of crystal and chemical properties of actinides using Th and U as examples. This goal has been achieved by isolation of nearly 100 new actinide compounds by carefully tuning the experiment conditions from a variety of conventional and novel synthesis methods, including room-temperature slow evaporation method, mild-hydrothermal method high-temperature solid-state method and high-temperature/high-pressure method (see description of synthesis method in **Section 2.1** from **page 11**). The actinide compounds with novel structures are chosen to be described in this dissertation, and they are systematically classified into several groups (See **Table 2.2** on **page 15**). As mentioned above, the actinide compounds with hexavalent cations have been the subject of extensive research due to their importance in the mineralogical, environmental and fundamental point of view. Most of the previous studies on structural chemistry of these phases have focused on the high-valent based uranium compounds. Very less information is available for low-valent actinides (Th(IV), Np(IV) and Pu(IV)). Therefore, a large amount of compounds discussed in this dissertation are related to the thorium families. Besides, before this dissertation, there

---

[48] Paolo Orlandi et al. *Am. Mineral.*, **100**: 267–273, 2015.

[49] Paolo Orlandi et al. *Am. Mineral.*, **99**: 2089–2094, 2014.

[50] Evgeny V. Alekseev et al. *Angew. Chem. Int. Ed.*, **45**: 7233–7235, 2006.

[51] Andrey N. Seliverstov et al. *Dalton Trans.*, **41**: 8512–8514, 2012.

[52] F. Albert Cotton and Sanjay K. Mandal. *Inorg. Chem.*, **31**: 1267–1274, 1992.

were no literatures reported on high-pressure study of actinide compounds containing hexavalent oxo-anions. Moreover, some topological and structural trends are also summarized in this dissertation based on examining the structural and chemical differences between the previous reported and newly synthesized actinide compounds.

Chapter 2

Experimental Methods

2.1 Crystal synthesis and pure phase preparation

There are several successful methods for preparing the single crystals of actinide compounds. In our lab, I could use four different kinds of methods: room-temperature slow evaporation method, mild-hydrothermal method, high-temperature (HT) solid-state method and high-temperature and high-pressure (HT/HP) method. The differences among these methods are listed in **Table 2.1**.

Table 2.1: Comparison of the different crystal synthesis methods in the group of "Solid State Chemistry of Actinides".

	pressure	temperature	need H_2O	sealed condition
slow evaporation	atmosphere	room-temperature	✓	×
hydrothermal	up to 2 Mpa	100-230 °C	✓	✓
HT solid-state synthesis	atmosphere	400-1200 °C	×	×
HT and HP synthesis	up to 25 Gpa	600-2400 °C	×	✓

The most common ones are the high-temperature solid-state method and hydrothermal method. The high-temperature solid-state method requires relative high temperature condition (normally $> 800\,^{\circ}\mathrm{C}$), and thus water is completely excluded from incorporation into the structures. In comparison, water in most case is an important structural unit for compounds synthesized from hydrothermal method. In fact, most reported actinide sulfates, selenates and tellurates are prepared under hydrothermal condition.

Room-Temperature Slow Evaporation Method

The key point for this method is to find a suitable solvent which can dissolve the reagents. The crystals

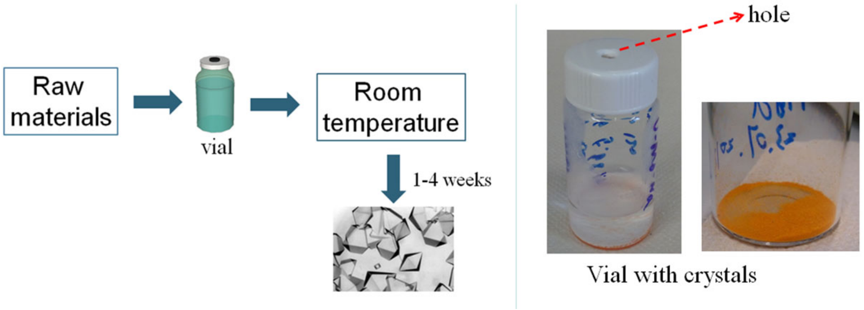

Figure 2.1: The basic procedure of slow evaporation method.

could be grown either under atmosphere or under inert condition. As the case of my research system (thorium and uranium compounds), I used distilled water as the solvent to dissolve the raw materials. The detailed procedure is shown in **Figure 2.1**. First, weight the raw materials and transfer them into a glass vial (In most cases I used 20 ml). Depending on the solubility of the compounds, the crystals can be found after being kept from 1 to 4 weeks. With this method, I obtained several tetravalent uranium molybdates using the reducing agent of $Na_2S_2O_3$.

Mild-Hydrothermal Method

Some substances are insoluble under normal condition but can be dissolved at elevated temperature and pressure. In this case, these compounds can be prepared by hydrothermal method. This method is performed in a reaction vessel called autoclave that is composed by sealed Teflon as the interior tank and a steel cylinder. The detailed experiment procedure is shown in **Figure 2.2**. Firstly, put raw materials into the autoclaves. After being sealed tightly, the autoclaves are transferred into slightly high-temperature condition (In most cases, I used around 220 °C). The crystals can be found after slowly cooling to the room temperature.

The hydrothermal method can be modified by replacing water with boric acid in the autoclaves. Compare to the traditional hydrothermal synthesis, this modified method which uses the boric acid as a reactive flux allows borate to easily access to the inner-sphere coordination sites of actinide elements.[53] Water may also be used in a tiny amount as a chemical reactant. Using this modified method, a large family of uranyl borates, multi mixed-valence neptunium borates as well as a plutonium(VI) borate have already been prepared over the past several years.[54–56] These actinide borates adopt a wide variety of unusual topological structural types and display a vast array of fascinating properties. One outstanding example, $[ThB_5O_6(OH)_6][BO(OH)_2]\cdot 2.5H_2O$ is composed of supertetrahedral cationic framework structure and performs a remarkable anion exchange capacities.[57] My motivation to use this modified method was to obtain a novel series of mixed-metal thorium molybde-

---

[53] Shuao Wang et al. *Inorg. Chem.*, **49**: 6690–6696, 2010.
[54] Shuao Wang et al. *Angew. Chem. Int. Ed.*, **49**: 1263–1266, 2010.
[55] Shuao Wang et al. *Inorg. Chem.*, **49**: 9755–9757, 2010.
[56] Shuao Wang et al. *Inorg. Chem.*, **49**: 2948–2953, 2010.
[57] Shuao Wang et al. *Angew. Chem. Int. Ed.*, **49**: 1057–1060, 2010.

num borate compounds, and also try to find out how the melt boric acid would affect the associated reactions compared to the normal hydrothermal synthesis.

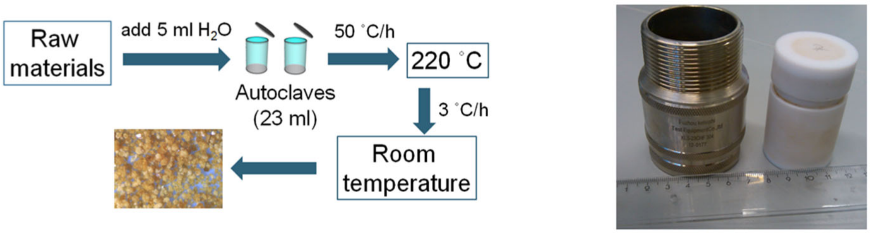

autoclave

Figure 2.2: The basic procedure of hydrothermal method.

High-Temperature Solid-State Synthesis Method

Most of the actinide compounds (nearly 70 %, see **Table** 2.2 on **page** 15) described in this dissertation were isolated from this method. In particularly, all the new thorium tungstates and uranium tungstates during my PhD work are found by this method. As shown in **Figure** 2.3, the first step is to weight the raw materials. After being finely ground in a mortar, the mixture is transferred to a Pt crucible. Then fast increase the temperature above the melting point of mixture (normally I used 1050 °C). The crystals can be isolated during slow cooling processes.

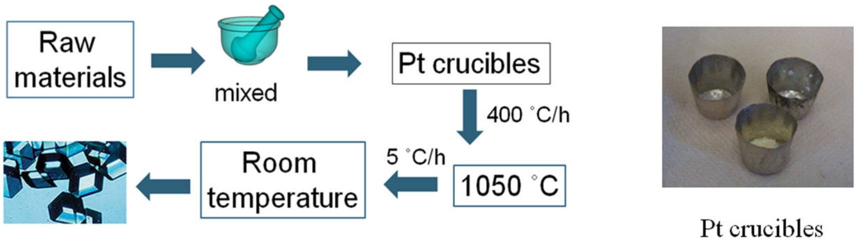

Pt crucibles

Figure 2.3: The basic procedure of high-temperature solid-state synthesis method.

High-Temperature/High-Pressure Method

In addition to the methods described above, our group is also use unconventional synthesized method to enhance the structural diversity and complexity that actinide compounds can adopt. The device is shown in **Figure** 2.4. Recently, our group reported the influence of high-temperature/high-pressure conditions on the formation of atypical structural features present in several uranium compounds. Under high-temperature (up to 1200 °C) and high-pressure (near 2.5 GPa) condition, a totally novel family of uranyl borates where UO_6, UO_7, and UO_8 tetragonal, pentagonal, and hexagonal bipyramids are all within one compound were prepared.[58] Moreover, this method is also helpful for yielding structural features that have not been observed with traditional synthesis conditions, as exemplified

---

[58] Shijun Wu et al. *Inorg. Chem.*, **52**: 5110–5118, 2013.

by the isolation of the first thorium compound with mixed-valent oxoarsenic(III)/arsenic(V),[59] as well as the first actinide aluminoborate.[60] Based on this method, I have successfully isolated a large number of uranyl compounds with novel coordination environments using high-temperature/high-pressure synthesis method (*e.g.* see **Chapter 6.2** from **page 93** for thorium tellurium family).

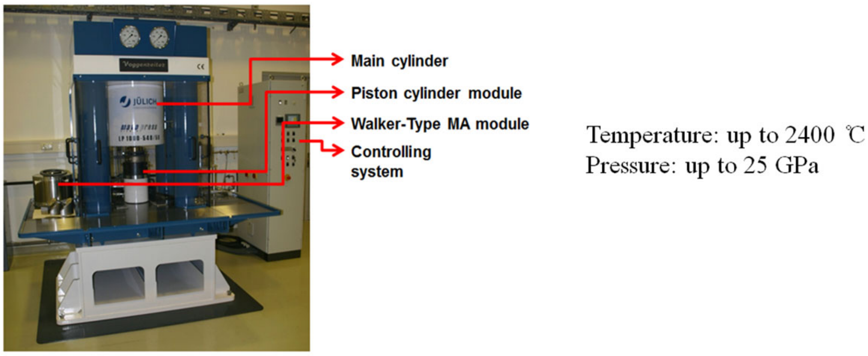

Figure 2.4: The basic procedure of high-temperature and high-pressure method.

par **Pure Crystalline Powder Synthesis**
All the pure powder samples of studies phases were prepared by conventional solid-state reaction. The raw chemicals were used according to each stoichiometric ratio. The procedure was performed as follows: After being thoroughly ground, the reaction mixtures were initially heated in air up to 450 °C and kept at this temperature for 30 h. After that, the room-temperature X-ray powder diffraction was required to analyze the phase content and purity. The same grinding and heating steps were repeated several times with temperature increasing of 50 °C/step until the pure phases were obtained.

2.2 Characterization techniques

Crystal Structure Studies
The single crystals were mounted on glass fibers and optically aligned on an Agilent diffractometer (SuperNova, Dual Source) for single crystal X-ray diffraction experiment. The data collection was done by a monochromatic Mo-Kα tube which has the incident wavelength of 0.71073 Å and runs at 50 kV and 0.8 mA providing a beam size of approximately 30 μm. The unit-cell dimensions for these crystals were refined using least-square techniques against the positions of all measured reflections. More than a hemisphere of data were collected for each crystal and the three-dimensional data were reduced and filtered for statistical outliers using the standard CrysAlisPro program. Data were corrected for Lorentz, polarization, absorption and background effects. The crystal structure determination and refinement were carried out using the SHELXL-97 program.

---

[59] Na Yu et al. *Inorg. Chem.*, **53**: 8194–8196, 2014.
[60] Shijun Wu et al. *Inorg. Chem.*, **52**: 7881–7888, 2013.

Scanning Electron Microscopy/Energy-Dispersive Spectroscopy

Scanning electron microscopy images and energy-dispersive spectroscopy (SEM/EDS) data were collected on FEI Quanta 200F Environment Scanning Electron Microscope.

DSC and TG Analysis

The thermal behavior of the dried pure polycrystalline powders was studied from room-temperature up to 1200 °C by differential scanning calorimetry analysis (DSC) and thermogravimetry (TG) in air. Using a Netzsch STA 449C Jupiter apparatus, 20 mg of sample was each loaded in a platinum crucible which was closed with a platinum cover. During the measurements a constant air flow of 20 30 ml/min at a heating rate of 10 °C/min was applied.

Raman Spectroscopy

Utilizing a peltier cooled multi-channel CCD detector, the unpolarized Raman spectra were recorded with a Horiba LabRAM HR spectrometer. All the samples were in the form of single crystals. An objective with a 50 x magnification was linked to the spectrometer, allowing the analysis of samples as small as 2 μm in diameter. The incident radiation was produced by a He-Ne laser at a power of 17 mW (λ = 632.81 nm). The focal length of the spectrometer was 800 mm and a 1800 gr/mm grating was used. The spectral resolution was around 1 cm^{-1} with a slit of 100 μm. The Raman spectroscopic investigation for all samples was executed at room temperature in the range of 100−1050 cm^{-1}.

All the actinide compounds which are systematically described in this dissertation are listed in Table 2.2.

Table 2.2: Actinide compounds which are described in this dissertation.

Formula	**Space group**	***a***	***b***	***c***	***α***	***β***	***γ***	**Description**
Molybdates and tungstates								
α- $Th(MoO_4)_2$	$P2_1/n$	6.10	9.83	12.35	90.00	97.52	90.00	see **page 20**
HTHP−$Th(MoO_4)_2$	$Pna2_1$	10.92	13.05	4.06	90.00	90.00	90.00	see **page 22**
$Rb_8Th(MoO_4)_6$	$C2/c$	18.16	12.51	5.39	90.00	105.06	90.00	see **page 38**
$Rb_2Th(MoO_4)_3$	$C2/c$	26.89	6.39	11.36	90.00	114.00	90.00	see **page 39**
$Rb_4Th(MoO_4)_4$	$C2/c$	10.72	18.06	14.99	90.00	103.42	90.00	see **page 39**
$Rb_4Th_5(MoO_4)_{12}$	$C2/c$	29.39	16.80	10.20	90.00	101.54	90.00	see **page 41**
$Cs_2Th(MoO_4)_3$	$Pnnm$	5.26	9.73	26.85	90.00	90.00	90.00	see **page 51**
$Cs_4Th(MoO_4)_4$	$P2/c$	12.69	6.62	11.46	90.00	90.15	90.0	see **page 55**
$Cs_2Th_3(MoO_4)_7$	$P1$	12.45	14.93	15.96	78.21	78.70	78.00	see **page 52**
$K_6Th_6(WO_4)_{14}O$	$R3$	11.65	11.65	68.14	90.00	90.00	120.00	see **page 60**
$Rb_6Th_6(WO_4)_{14}O$	$P\bar{6}2c$	11.72	11.72	46.23	90.00	90.00	120.00	see **page 60**
$Th_2(MoO_4)_3(NO_3)_2(H_2O)_3$	$C2/a$	10.39	9.34	17.44	90.00	91.77	90.00	see **page 72**
$Th(MoO_4)_2(H_2O)$	$Pbcm$	7.34	10.58	9.66	90.00	90.00	90.00	see **page 73**
$(NH_4)_2Th_4(MoO_4)_9$	$I\bar{4}3d$	14.33	14.33	14.33	90.00	90.00	90.00	see **page 75**
$Cs_4[(UO_2)_4(WO_5)(W_2O_8)O_2]$	$P2_1/c$	8.19	32.81	10.74	90.00	117.60	90.00	see **page 137**
$Cs_4[(UO_2)_7(WO_5)_3O_3]$	$P2_1/c$	8.68	41.89	10.82	90.00	116.46	90.00	see **page 138**
$K_2MgTh_3(MoO_4)_8$	$C2/c$	18.67	18.08	9.46	90.00	90.22	90.00	see **page 146**
$Rb_2MgTh_3(MoO_4)_8$	$C2/c$	18.56	18.02	9.41	90.00	90.35	90.00	see **page 146**
$K_2SrTh_2(MoO_4)_6$	$P\bar{1}$	8.01	8.44	16.03	101.55	102.89	97.38	see **page 148**

$Nd_2Th_3(MoO_4)_9$	$P6_3/m$	17.56 17.56 6.27 90.00 90.00 120.00	see **page 150**
Selenium and tellurium compounds			
α- $ThSe_2O_6$	$P2_1/n$	7.18 10.78 7.42 90.00 107.57 90.00	see **page 84**
β- $ThSe_2O_6$	$Pna2_1$	7.22 11.08 6.64 90.00 90.00 90.00	see **page 85**
$Th(Se_2O_5)_2$	$Pbca$	12.40 11.84 12.98 90.00 90.00 90.00	see **page 87**
$Th_3Se_3O_{14}(OH)_2$	$I4/m$	11.12 11.12 10.81 90.00 90.00 90.00	see **page 88**
$Th_2Te_3O_{11}$	$P21/c$	12.43 5.28 17.36 90.00 130.67 90.00	see **page 93**
$Na_4Th_2Te_3O_{15}$	$R\bar{3}c$	9.91 9.91 45.13 90.00 90.00 120.00	see **page 96**
$K_2ThTe_3O_{12}$	$Pnma$	11.45 7.33 12.49 90.00 90.00 90.00	see **page 97**
$ThWTe_2O_9$	$I41/a$	19.48 19.48 7.74 90.00 90.00 90.00	see **page 124**
$Th(WO_4)(TeO_3)$	$P2_1/c$	4.12 8.51 15.36 90.00 92.59 90.00	see **page 126**
$ThMoTe_2O_9$	$C2/c$	10.92 7.04 20.39 90.000 99.82 90.00	see **page 127**
$Th_2(MoO_4)(TeO_3)_3$	$P2_1/c$	11.37 7.12 14.06 90.00 90.00 90.00	see **page 128**
$Na[UO_2Te_2O_5(OH)]$	$Pmn2$	8.00 5.77 7.70 90.00 90.00 90.00	see **page 100**
$Na[(UO_2)Te_6O_{13}(OH)]$	$Pa\bar{3}$	11.32 11.32 11.32 90.00 90.00 90.00	see **page 102**
$Na_2(UO_2)Te_2O_8$	Cm	12.78 3.76 8.50 90.00 93.89 90.00	see **page 104**
$Na_2(UO_2)(TeO_5)$	$C2$	7.53 10.36 7.52 90.00 90.00 90.00	see **page 105**
$K_2(UO_2)_3Te_4O_{12}$	$P\bar{1}$	6.84 7.03 9.40 73.51 81.03 81.70	see **page 111**
$K_2(UO_2)Te_6O_{14}$	$Pa\bar{3}$	11.39 11.39 11.39 90.00 90.00 90.00	see **page 114**
$\alpha - K_2(UO_2)(TeO_5)$	$P2_1/n$	7.90 10.13 8.56 90.00 95.59 90.00	see **page 115**
$\beta - K_2(UO_2)(TeO_5$	$C2/c$	14.20 13.86 7.11 90.00 113.76 90.00	see **page 117**
Chromates			
$Th_2(CrO_4)_3(OH)_2$	$C2/c$	14.80 11.16 7.31 90.00 115.25 90.00	see **page 77**
$Th_3(CrO_4)_6(H_2O)_{10}(H_2O)_4$	$P2_1/c$	8.066 19.134 13.170 90.00 127.01 90.00	see **page 77**
$Li_2Th_4(CrO_4)_9$	$I\bar{4}3d$	14.31 14.31 14.31 90.000 90.000 90.000	see **page 79**

Chapter 3

Giant Volume Change and Topological Gaps in Temperature and Pressure Induced Phase Transitions of $ThMo_2O_8$ Polymorphs

The modern industrialized world's thirst for energy has stimulated progressive researches into diverse energy substitutes. Future electricity generation will need a range of options, although they must be low carbon if greenhouse gas emissions are to be reduced. Among numerous substitutes, nuclear energy provides reliable supplies of electricity with very low carbon emissions and relatively small amounts of waste that can be safely stored and eventually disposed of in a final repository. Currently, the most common nuclear fuel supplied for nuclear reactors is based on uranium. Nevertheless, a number of concerns have been raised about using uranium as energy source, which eventuates in increasing interest in thorium as a possible alternative to uranium in next nuclear fuel generation. The thorium fuel cycle has some attractive features, though it is not yet in commercial use. Thorium is reported to be three times as abundant in the earth crust as uranium. With regard to proliferation significance, thorium-based power reactor fuels would be very poor source for fissile material usable in the illicit manufacture of nuclear weapons.[61] The application of thorium in the nuclear reactor involves a large array of chemical interactions among fission products with nuclear fuel, leading to formation of complex thorium compounds and in turn to affect the integrity and behavior of fuel. Therefore, knowledge of chemical properties of these thorium compounds becomes the necessary prerequisite for utilizing this promising energy.

By applying high temperature (1270 K) and high pressure (3.5 GPa), significant changes occur in the structural volume and crystal topology of $ThMo_2O_8$, allowing the formation of an unexpected new $ThMo_2O_8$ polymorph (HT/HP orthorhombic-$ThMo_2O_8$). Compared to the other three $ThMo_2O_8$

---

[61] Mujid Kazimi. *AmSci*, **91**: 408–15, 2003.

polymorphs prepared at the ambient pressure (monoclinic-, orthorhombic- and hexagonal-phases), the molar volume for the HT/HP orthorhombic-$ThMo_2O_8$ is decreased by almost 20 %. As a result of such dramatic structural transformation, a permanent high-pressure state is possible to sustain when the pressure is released. The crystal structures of the three ambient $ThMo_2O_8$ phases are based on three-dimensional (3D) frameworks constructed from corner-sharing of ThOx (x = 6, 8 and 9) polyhedra and MoO_4 tetrahedra. The HT/HP orthorhombic-$ThMo_2O_8$, however, crystallizes in a novel structural topology, exhibiting very dense arrangements of ThO_{11} and MoO_{4+1} polyhedral connection along the crystallographic ***c***-axis. The phase-transition among all these four $ThMo_2O_8$ polymorphs is unveiled and fully characterized regarding to the structural transformation, thermal stability, and vibrational properties. The complementary first principles calculations of Gibbs free energies reveal underlying energetics of the phase transition, which supports the experimental findings.

3.1 Crystal structures of AMo_2O_8 family (A = Zr, Hf, Th; M = Mo, W)

$ThMo_2O_8$, as the simplest compound among all thorium molybdates, belongs to AM_2O_8 family (A = Zr, Hf, Th; M = Mo, W). Many compounds in this family display fascinating physical properties such as negative thermal expansion (NTE),[62] photocatalytic activity[63] and catalysis[64]. Compounds of this family exhibit diverse structural alternations depending on pressure, temperature and hydration state. For instance, at ambient-pressure, the thermodynamically stable polymorph for $ZrMo_2O_8$ is the trigonal α-$ZrMo_2O_8$ at high temperature while monoclinic β-$ZrMo_2O_8$ at low temperature[65], and the $\beta \to \alpha$ phase transition was observed at roughly 0 K. Under high-pressure, the transformation from trigonal α-$ZrMo_2O_8$ to the monoclinic δ-$ZrMo_2O_8$ happens at nearly 1.11 GPa and further to a triclinic ε-$ZrMo_2O_8$ above 2.0 GPa. Unlike the versatile $ZrMo_2O_8$, the tungsten based ZrW_2O_8 can keep its cubic phase (refer to as α-ZrW_2O_8) over the entire temperature range at ambient pressure.[66] However, a first-order transition to the orthorhombic γ phase, accompanied by 5 % volume reduction, was observed while increasing the pressure above 0.21 GPa.[67] Similar to ZrW_2O_8 under ambient condition, α-HfW_2O_8 adopts an equilibrium structure which is isostructural to α-ZrW_2O_8, however, it can be converted to the orthorhombic γ phase at 0.6 GPa. At room-temperature, $HfMo_2O_8$ follows a trigonal structure with space group $P\bar{3}m$; whereas, it undergoes a second-order phase transition at 463 K to a higher-symmetry structure (space group $P\bar{3}m1$).[68]

We have recently studied a series of thorium compounds containing hexavalent cations (S^{6+}, Se^{6+},

---

[62] Christy De Meyer et al. *J. Mater. Chem.*, **14**: 2988–2994, 2004.

[63] Prangya Parimita Sahoo et al. *J. Phys. Chem. C*, **113**: 10661–10666, 2009.

[64] F. Monroy-Guzmn, L.V. Daz-Archundia, and A. Contreras Ramrez. *Applied Radiation and Isotopes*, **59**: 27 –34, 2003.

[65] R.F. Klevtsova et al. , **35**: 286–290–, 1994.

[66] T. A. Mary et al. *Science*, **272**: 90–92, 1996.

[67] J. D. Jorgensen et al. *Phys. Rev. B*, **36**: 3608–3616, 1987.

[68] Simon Allen et al. *Acta Crystallogr., Sect. B: Struct. Sci*, **60**: 32–40, 2004.

Te^{6+}, Cr^{6+}, Mo^{6+} and W^{6+}).[69–71] Our purpose is to develop a systematical trend which may aid in new understanding about the chemical behavior of actinides in the area of nuclear energy. Along with in-depth study of thorium molybdate system, it is found that $ThMo_2O_8$ not only inherits the prominent characteristic of polymorphic diversity from its AM_2O_8 family (A = Zr, Hf; M = Mo, W), it is also unusual and structurally more flexible with respect to the rest of this family. Unlike all the other compounds in the AM_2O_8 family which involves A atoms (A = Zr, Hf) exclusively in a six-fold octahedral coordination, the corresponding Th sites observed in $ThMo_2O_8$ occur in multi-geometries, that is, ThO_6 octahedra, ThO_8 square antiprisms, ThO_9 tricapped trigonal prisms and even exceptional ThO_{11} all-face capped trigonal prisms. This uniqueness is attributed to the considerably variable coordination numbers of Th which has the ability of achieving extremely fascinating topological geometries. During study, a novel low-temperature $ThMo_2O_8$ polymorph (monoclinic-$ThMo_2O_8$) was isolated for the first time from the ambient pressure synthesized material. Besides, the use of high-temperature/high-pressure technique for the phase stability study of $ThMo_2O_8$ resulted in an unexpected new $ThMo_2O_8$ polymorph (HT/HP-orthorhombic $ThMo_2O_8$), which presents a complete new Th-Mo structural topology and giant volume change comparably to ambient phases. In this work, the detailed structures, high-temperature and high-pressure behavior, topology of the structures and vibrational spectra of all $ThMo_2O_8$ polymorphs are discussed.

Synthesis of HT/HP orthorhombic-$ThMo_2O_8$

The experiment was performed using the piston cylinder module of a Voggenreiter LP 1000- 540/50 (Forschungszentrum Juelich, IEK-6). Pressure calibration of the piston cylinder apparatus was accomplished using the reactions $MgO + H_2O = Mg(OH)_2$ (1120 K, 1.05 GPa) and $NaAlSi_2O_6 + SiO_2 = NaAlSi_3O_8$ (870 K, 1.6 GPa). A pressure correction of 15 % is required based on the calibrations. The temperature of the batch was measured and controlled using a C-Type thermocouple. The uncertainties in temperature and pressure determination are assumed to be ± 5 K and ± 0.05 GPa, respectively.

Thorium nitrate $Th(NO_3)_4 \cdot 5\,H_2O$ (0.100 g, 0.175 mmol) and MoO_3 (0.076 g, 0.526 mmol) in a molar ratio of 1:3 were mixed together and finely grounded. After this, the mixture was filled into a Platinum capsule (outer diameter: 4 mm, wall thickness: 0.2 mm, length: 7 mm). The capsule was sealed on both sides with an impulse micro welding device (Lampert PUK U4) and placed into the center of a 1/2-inch piston cylinder talc-pyrex assembly. Then, the capsule was inserted into a 6 mm diameter MgO spacer and positioned in the center of a tapered graphite furnace. The final run pressure of 3.5 GPa was applied within 20 minutes, then the temperature program was started. With a heating rate of 100 K/min the temperature was increased to the maximum temperature of 1270 K. After 1 hour of annealing the temperature was decreased to 570 K over a time period of 106 h (cooling rate 0.11 K/min). At 570 K the experiment was automatically quenched to room-temperature. After decompression for 20 min, the capsule was extracted out of the high-pressure assembly and broken.

---

[69] Bin Xiao et al. *Chem. Eur. J.*, **21**: 7746–7754, 2015.
[70] Bin Xiao et al. *Inorg. Chem.*, **53**: 3088–3098, 2014.
[71] Bin Xiao et al. *Cryst. Growth Des.*, **14**: 2677–2684, 2014.

The products containing colorless crystals were picked up for further analysis. The yield was again impossible to be determined due to the similarity of broken glass pieces and obtained crystals.

Structures of new $ThMo_2O_8$ polymorphs

The Greek letters α, β, γ *etc.* are commonly used to identify different polymorphs among structural phase-transition diagrams. For example, as mentioned before, the newly synthesized monoclinic-$ThMo_2O_8$ is a third polymorph for $ThMo_2O_8$. The other two polymorphs were named as α-$ThMo_2O_8$ and β-$ThMo_2O_8$ for hexagonal and orthorhombic, respectively. Such notation is simple and often contains specific thermodynamic and/or crystallographic information (for instance, the α-$ThMo_2O_8$ crystallizes in lower symmetry than β-$ThMo_2O_8$). However, in some cases, this is inconvenient and easy to get confused because the discovery of a new phase will usually require the introduction of more complicated letters such as α' and β' to keep this sequence. For this reason, here, one can choose the crystal lattice system as the nomenclature to distinguish all known and newly obtained $ThMo_2O_8$ polymorphs. We name α-$ThMo_2O_8$ as hexagonal-$ThMo_2O_8$, β-$ThMo_2O_8$ as orthorhombic-$ThMo_2O_8$. The two new $ThMo_2O_8$ polymorphs synthesized at ambient and high-temperature/high-pressure condition are named as monoclinic-$ThMo_2O_8$ and HT/HP-orthorhombic $ThMo_2O_8$, respectively.

3.2 Phase formation of three ambient $ThMo_2O_8$ polymorphs

As shown in **Figure 3.2** three different polymorphs of $ThMo_2O_8$ can be formed, under ambient pressure, in the range from room-temperature to the melting point of the compound. The hexagonal- and monoclinic-$ThMo_2O_8$ polymorphs can be found within the low-temperature range, while the orthorhombic-$ThMo_2O_8$ is more favorable at higher temperatures. The hexagonal-$ThMo_2O_8$ is formed roughly from 720 - 820 K, whereas the monoclinic-$ThMo_2O_8$ can only be obtained at a very narrow temperature range around 800 K. When the temperature is increased, orthorhombic-$ThMo_2O_8$ becomes more stable and can be prepared as a pure phase. **Figure 3.2** also indicates a direct phase transition from low-temperature monoclinic and hexagonal polymorphs to the high-temperature orthorhombic-$ThMo_2O_8$ at approximately 820 K. In fact, the ab initio calculations show that orthorhombic-$ThMo_2O_8$ is the most stable phase at the temperature range above 920 K (see **page 30**).

Monoclinic-$ThMo_2O_8$

The structure determination reveals that this newly observed phase crystallizes in space group $P2_1/c$ and contains one symmetrically independent Th and two Mo atoms. The bond-valence sums for Th and Mo atoms in the monoclinic-$ThMo_2O_8$ were calculated utilizing the data according to *Brese* and *OKeefee*.[72] The results of 4.17 v.u. for Th(1), 6.29 v.u. for Mo(1) and 5.92 v.u. for Mo(2) are well coincident with the expected bond-valence values. The structure of monoclinic-$ThMo_2O_8$ based on distorted ThO_8 square antiprisms and MoO_4 tetrahedra, leading to a three-dimensional framework structure, as shown on **Figure 3.3**. The ThO_8 polyhedra are isolated from each other by nearby

---

[72] NE Brese and M O'keeffe. *Acta Crystallographica Section B: Structural Science*, **47**: 192–197, 1991.

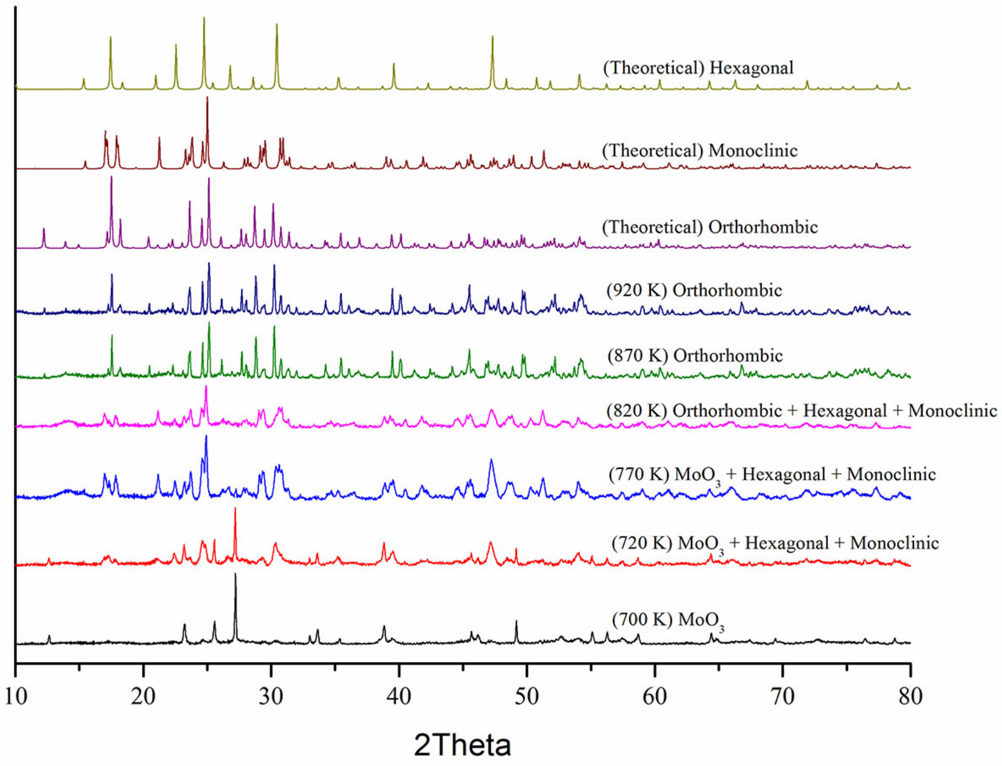

Figure 3.1: The powder diffraction patterns for $ThMo_2O_8$ at different temperature. The theoretical diffraction patterns for hexagonal-, monoclinic- and orthorhombic-$ThMo_2O_8$ obtained from the single crystal structure solutions are also supplied. This result indicates the phase evolution for all the $ThMo_2O_8$ polymorphs. At first, below 700 K, the peaks shown are predominantly attributed from the contribution of MoO_3. When the temperature attends to 720 K, the reaction product is the result of mixed MoO_3, monoclinic- and hexagonal-$ThMo_2O_8$. The content of MoO_3 becomes less as the temperature increases. The diffraction data obtained from 820 K demonstrate coexisting of monoclinic- and hexagonal- and orthorhombic-$ThMo_2O_8$ phases. When the temperature exceeds 870 K, all the phases are transformed to the pure orthorhombic-$ThMo_2O_8$.

MoO_4 tetrahedra, which is common for most of the thorium molybdates.[73,74] The 8-fold coordinated Th polyhedron exhibits the most frequently observed Th geometry in thorium molybdate systems with only four exceptions. The first exception is hexagonal-$ThMo_2O_8$ which shows Th in 6- and 9-fold coordination. The second one is $Cs_2Th_3(MoO_4)_7$ which simultaneously contains three different Th polyhedra (ThO_7 pentagonal bipyramids, ThO_8 square antiprisms and ThO_9 tricapped trigonal prisms).[71] The remaining two are the newly found thorium molybdate minerals ($Th(MoO_4)_2{\cdot}H_2O$ and $Th(MoO_4)_2{\cdot}3\,H_2O$).[48,49] The ThO_8 square antiprisms in monoclinic-$ThMo_2O_8$ are distorted with one short (ThO(1)) and one rather long ThO bond (ThO(3)) with distances of 2.326(4) Å and

---

[73] T. L. Cremers, P. G. Eller, and R. A. Penneman. *Acta Crystallogr., Sect. C: Cryst. Struct. Commun.*, **39**: 1165–1167, 1983.

[74] Geng Bang Jin and L. Soderholm. *J. Solid State Chem.*, **184**: 337–342, 2011.

[48] Paolo Orlandi et al. *Am. Mineral.*, **100**: 267–273, 2015.

[49] Paolo Orlandi et al. *Am. Mineral.*, **99**: 2089–2094, 2014.

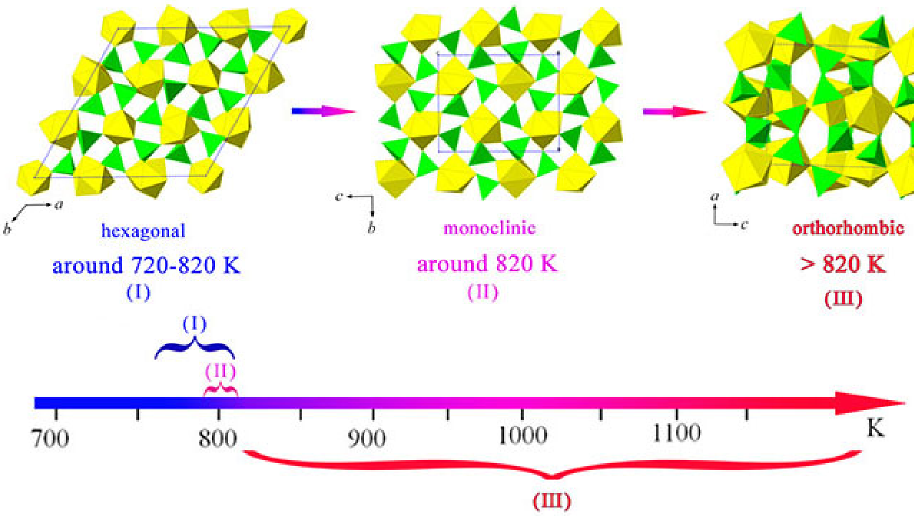

Figure 3.2: Formation temperature of $ThMo_2O_8$ polymorphs at ambient pressure. This figure was made according the powder diffractions results shown in Figure 3.1. As can be seen from this figure, the monoclinic-$ThMo_2O_8$ can only be obtained at very narrow temperature range around 820 K. A phase transition behavior (from mixed hexagonal- and monoclinic-$ThMo_2O_8$ to orthorhombic-$ThMo_2O_8$) can also be detected at the temperature of approximately 820 K.

2.513(5) Å, respectively. The ThO bond lengths in monoclinic-$ThMo_2O_8$ are less uniform compared to those in orthorhombic-$ThMo_2O_8$ (ranging from around 2.36 Å to 2.46 Å) and comparable to those in hexagonal-$ThMo_2O_8$ polymorph. The two symmetrically unique Mo atoms are forming a MoO_4 configuration slightly distorted from an idealized geometry. The average MoO distances for Mo(1) and Mo(2) are 1.761(5) Å and 1.747(6) Å, respectively, which are similar to those in orthorhombic-$ThMo_2O_8$ (about 1.75 Å) and hexagonal-$ThMo_2O_8$ (around 1.76 Å) in data. The O-Mo-O angles ranging from 107.5(3)° to 110.8(3)° and exhibiting the slight deviation of molybdenum atoms from tetrahedral T_d symmetry.

HT/HP-orthorhombic $ThMo_2O_8$

The HT/HP-orthorhombic $ThMo_2O_8$ can be described as a framework composed by thorium and molybdenum polyhedral (**Figure 3.4**). There are one crystallographic Th site and two Mo sites in the asymmetric unit. The Th(1) centers are 11-coordinated, forming a rather unusual coordination polyhedron in a shape of all-face capped trigonal prism. It is noteworthy that such ThO_{11} coordination polyhedron is observed for the first time among all inorganic thorium compounds. The Th-O bond lengths are in the range of 2.318(4) to 3.083(4) Å. These ThO_{11} polyhedra share common faces to form chains running along ***c***-axis. Both Mo sites are found to appear as MoO_5 trigonal bipyramids which are linked into $[MoO_4]^{2-}$ chains by corner sharing of common oxygen atoms. Within each MoO_5 trigonal bipyramids, an elongated Mo-O bond, arising from the movement of Mo out of the central trigonal plane of trigonal bipyramid, is observed. This leads to alternately short and long Mo-O bond configuration in the $[MoO_4]^{2-}$chains extending along ***c***-axis. More specifically, for Mo(1), the

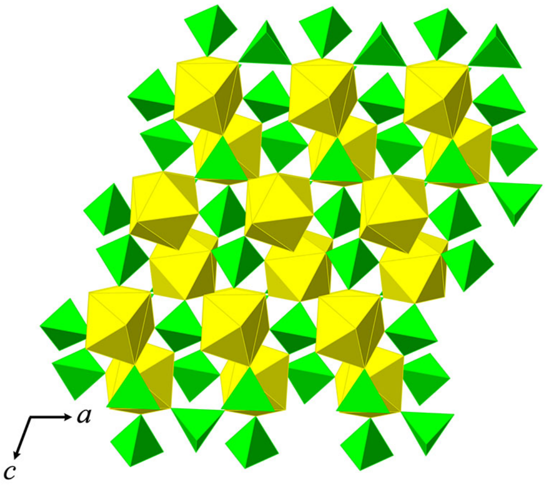

Figure 3.3: Depiction of crystal structure of monoclinic-$ThMo_2O_8$ polymorph. The 3D framework constructed from eight-coordinated ThO_8 antiprisms and four-coordinated MoO_4 tetrahedra is projected perpendicular to the b-axis.

center Mo atom is sited out of the O(4)-O(5)-O(6) plane so that the Mo(1)-O(8) bond (2.342(5) Å) is relevantly longer than the other Mo-O bonds (range from 1.744(5) to 1.860(3) Å). A similar situation happens for Mo(2) and the distortion can especially be viewed along the Mo-O(7) direction as being the longest Mo-O distance of 2.335(5) Å. Thereby, the MoO_5 polyhedra are severely distorted with four short and one longer Mo-O bond, the latter interacting more weakly with the respective O atom. From this perspective, the relatively long Mo-O distances can be regarded as secondary coordination bonds. In this way, the Mo sites in HT/HP-orthorhombic $ThMo_2O_8$ can be considered as extended (4+1) configuration with MoO_{4+1} geometry.

3.2.1 Structural relationships in all $ThMo_2O_8$ polymorphs including both ambient and high-pressure phases

The heteropolyhedral frameworks of all three ambient $ThMo_2O_8$ polymorphs can be fully understood as being constructed from basic Th-Mo chains formed from corner-sharing ThOx (x = 6, 8, and 9) and MoO_4 polyhedra (**Figure 3.5**). Using *black-and-white node presentation*,[24] the topological linkage of each Th-Mo chain is also indicated in **Figure 3.5**. One dissimilarity should be emphatically noted: In contrast to the chains in orthorhombic-$ThMo_2O_8$, in which ThO_8 antiprisms are connected to each other by three MoO_4 tetrahedra, the adjacent Th polyhedra are bridged by two MoO_4 tetrahedra in both chains of monoclinic- and hexagonal-$ThMo_2O_8$. From this respect, one can note that splitting of the frameworks by means of basic chains is not enough to compare the structural difference between monoclinic- and hexagonal-$ThMo_2O_8$. Thus, these two polymorphs are divided into 2D pseudo-sheets to further inspect their chain arrangements (highlighted in **Figure 3.6** (a, b)). As one can see from **Figure 3.6** (a, b), both polymorphs have similar topology of pseudo-sheets, that is, the structures can be seen as being constructed by fusing the basic building chains along [001] and [100] directions

---

[24] Sergey V. Krivovichev et al. *Angew. Chem. Int. Ed.*, **117**: 1158–1160, 2005.

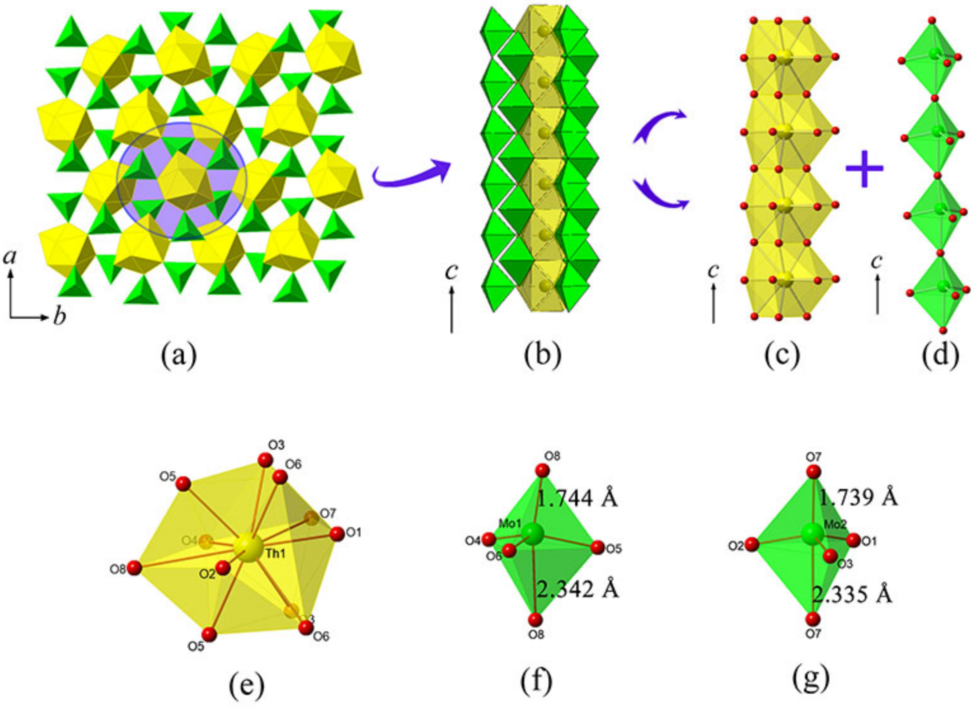

Figure 3.4: View on the HT/HP orthorhombic-$ThMo_2O_8$ structure.

for monoclinic- and hexagonal-$ThMo_2O_8$, respectively. Once taken as a whole, it is easy to find that monoclinic-$ThMo_2O_8$ and hexagonal-$ThMo_2O_8$ are very similar to each other, and the structural transformation from one to the other only involves rearrangement of the basic building Th-Mo chains. This result is also well consistent with those of the DFT calculations which show that monoclinic-$ThMo_2O_8$ and hexagonal-$ThMo_2O_8$ have similar Gibbs energies (the difference is only 0.5 KJ/mole) at ambient temperature and pressure (See **Figure 3.12**).

A striking feature of HT/HP-orthorhombic $ThMo_2O_8$ is the significant increase in its density. At ambient pressure, the density of $ThMo_2O_8$ is around 5 g/cm^3 (5.03(6), 4.93(4) and 5.04(4) g/cm^3 for monoclinic-, hexagonal- and orthorhombic-$ThMo_2O_8$, respectively), while it climbs to nearly 5.9 g/cm^3 when the pressure is reached to 3.5 GPa. The nearly 20 % density increase from ambient to high-temperature high-pressure polymorphs is obviously associated with the change of the polyhedral configuration. The nature of high-pressure induced phase transition is illustrated in **Figure 3.7**. The neighboring Th polyhedra are separated from each other among all three ambient polymorphs. They are, however, connected together *via* face-sharing at high-pressure condition. As a result, the interatomic distance between Th atoms in HT/HP orthorhombic-$ThMo_2O_8$ is around 4 Å, being significantly shorter than the Th-Th distance equal 6 Å in the ambient pressure polymorphs. Similar for Mo polyhedra, instead of being isolated from each other in the structures of ambient pressure polymorphs, they form a corner-sharing chain with much shorter Mo-Mo distance in HP polymorph. Because of such a giant volume change followed by a significant structural transformation, the high

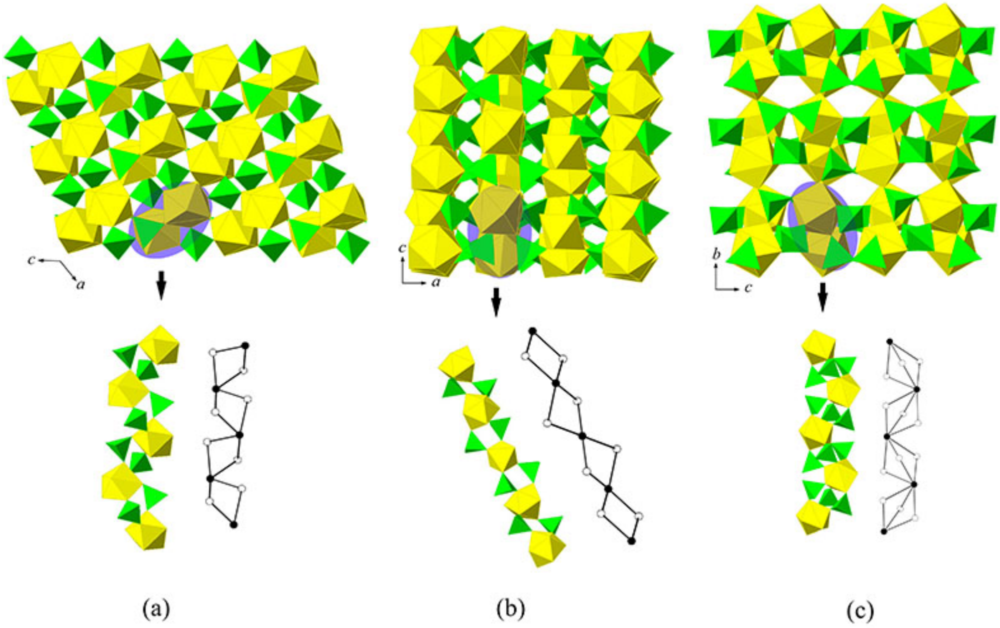

Figure 3.5: Different $ThMo_2O_8$ polymorph frameworks based upon fundamental chains of corner-sharing polyhedra. (a) The basic chain in monoclinic-$ThMo_2O_8$ polymorph where the adjacent ThO_8 antiprisms are bridged by two MoO_4 tetrahedra. (b) The framework of hexagonal-$ThMo_2O_8$ also consists of basic chains with the same topology as the monoclinic-$ThMo_2O_8$. (c) The neighboring ThO_8 antiprisms are connected by three MoO_4 tetrahedra in orthorhombic-$ThMo_2O_8$. (Legend: Th polyhedra = yellow, Mo polyhedra = green; black and white nodes in topological connections symbolize Th and Mo polyhedra, respectively)

pressure polymorph is stable after the pressure release. The energetics of polymorphic modifications is discussed in DFT part (see **Page 30**) of this section.

Topological and Crystal Chemical Analysis

As mentioned above, both monoclinic- and orthorhombic-$ThMo_2O_8$ possesses the eightfold coordinated Th atoms and tetrahedral oxo-molybdate anions. Additional analysis of structural diversity was performed with calculation of so-called coordination sequences,[75] which show the number of metal atoms in the nth coordination shell (**CS**). This coordination shell analysis shows no difference between CSs of the Th atoms in monoclinic- and orthorhombic-$ThMo_2O_8$. In monoclinic-$ThMo_2O_8$, CSs of both Mo(1) and Mo(2) atoms are quite similar and show slight difference in the 4 th and the 7 th coordination shells. In orthorhombic-$ThMo_2O_8$, the CS of Mo(1) is quite similar to those of Mo(1) and Mo(2) in monoclinic-$ThMo_2O_8$, while Mo(2) shows the difference starting from the 2 nd coordination shell (23 atoms against 20 for Mo(1) and Mo(2), respectively). Taking into account that both Mo nodes are four-coordinated, significantly less amount of surrounding atoms in the 2 nd coordination shell of Mo(2) site can lead to formation of smaller cycles by this atom. This is clearly evidenced by a comparison of the point symbols (**PS**) of Mo1 and Mo2 sites, $4^3 \cdot 6^3$ and $4^5 \cdot 6^1$, respectively, which

---

[75] D.V. Pushkin et al. *Russ. J. Inorg. Chem.*, **57**: 175–180, 2012.

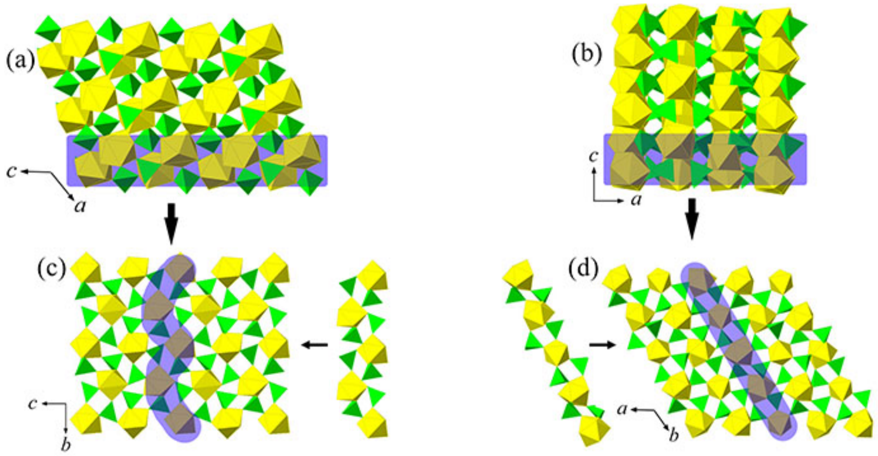

Figure 3.6: (a) The frameworks of monoclinic-$ThMo_2O_8$ and (b) the framework of hexagonal-$ThMo_2O_8$. Projection of the frameworks along [100] and [001] in monoclinic- and hexagonal-$ThMo_2O_8$ ((c) and (d), respectively) shows the arrangement of $ThMo_2O_8$ chains in one pseudo-layer in each structure.

represents type (line number) and amount (superscript number) of the shortest cycles.

The crystal structure of hexagonal-$ThMo_2O_8$ is more complicated due to the presence of 6 independent crystallographic metal sites comparing to only 3 sites in the other two polymorphs. Changes of the coordination numbers of Th atoms in the structure of hexagonal-$ThMo_2O_8$ compared to monoclinic- and orthorhombic-$ThMo_2O_8$ leads to significant changes in Th site CSs. The CSs of the Mo sites in hexagonal-$ThMo_2O_8$ start to differ from those of the Mo sites in monoclinic-$ThMo_2O_8$ only from the 4th coordination shells, nevertheless, the difference grows together with the number of CSs. Thus, all the nodes corresponding to the Mo sites have the same $\{4^5; 6^1\}$ PS due to the same first four coordination shells responsible for short cycles formation.

In both crystal structures of monoclinic- and orthorhombic-$ThMo_2O_8$ Th atoms in the Th sublattices have similar Voronoi-Dirichlet polyhedra (**VDP**) in the shape of Fedorov cuboctahedron with $4^6 6^8$ combinatorial-topological type (**CTT**). In a CTT designation, line numbers show amount of vertices in a face and superscript numbers show amount of such a faces in a polyhedron, *e.g.* $4^6 6^8$ describes a polyhedron with 6 square and 8 hexagonal faces, shown in **Figure 3.8**. The same CTT of Th atom VDP in Th sublattice means, in fact, the similar spatial distribution of the Th atoms in both structures. Due to this, the only difference between the monoclinic- and orthorhombic-modifications is in distribution and connectivity of MoO_4 tetrahedra with respect to the Th sites. For the crystal structure of hexagonal-$ThMo_2O_8$, a calculation of VDP in Th sublattice shows $4^6 6^8$ CTT for both Th(1) and Th(2) sites, while Th(3) has VDP with $4^4 5^4 6^6$ CTT. According to the stereoatomic model of crystal structures, which treats atoms like a soft (easily deformable) spheres with a fixed volume, the most likely heavy atom sites distribution is body-centered cubic (**bcc**), where each atom has VDP in the shape of truncated octahedron with $4^6 6^8$ CTT. This model agrees well with the energies of the crystal structures of the thorium molybdates, as monoclinic- and orthorhombic-$ThMo_2O_8$ with Th atoms distributed in bcc

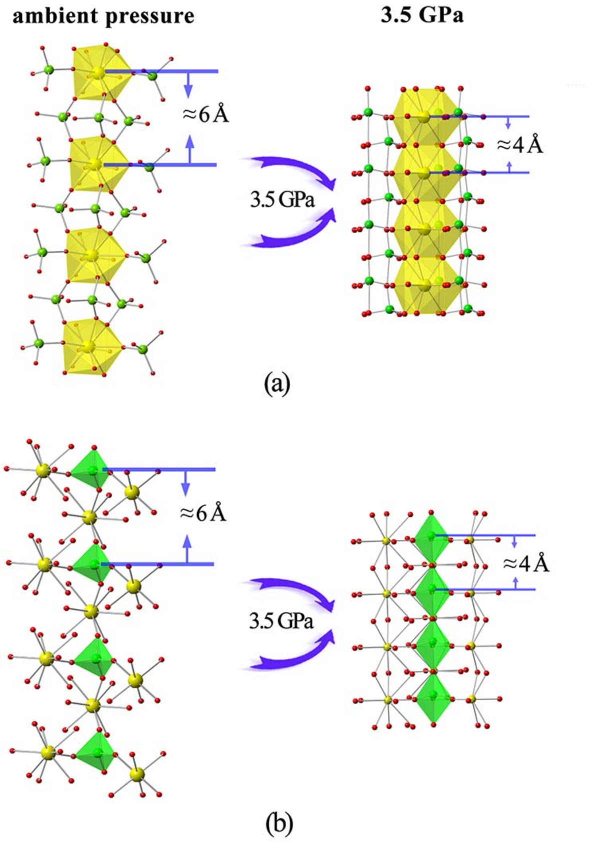

Figure 3.7: The effect of high-temperature/high-pressure induced phase transition. (a, b) Th and Mo polyhedral geometries change among the ambient and high-pressure (3.5 GPa) condition.

lattice mode have lower energy than hexagonal-modification, in which one of three Th atoms has VDP with $4^4 5^4 6^6$ CTT. Nevertheless, Th(1) and Th(2) atoms in hexagonal-$ThMo_2O_8$ still have VDP with $4^6 6^8$ CTT and this corresponds to a small energy gap between these three ambient pressure modifications that allows them to be obtained under similar synthetic conditions.

Coordination numbers of the Mo atoms in the structure of HT/HP orthorhombic $ThMo_2O_8$ calculated by means of the method of intersecting spheres clearly indicates the fivefold coordination. In the MoO_{4+1} coordination polyhedra, Mo atoms and four oxygen atoms form $_4$ intersections, while the fifth oxygen atom forms $_2$ one. Changes of the Mo atom coordination polyhedra raise structural features of the HT/HP orthorhombic phase and complicate its topological comparison with the structures of the other $ThMo_2O_8$ phases. In the structure of the HT/HP orthorhombic phase, the Th atoms in the Th sublattice have VDP with 12 faces and $4^8 6^4$ CTT. Along with other possible reasons, this fact might explain the high energy of this phase.

Phase transition analysis with in situ HT-PXRD at ambient pressure

In order to analysis the phase transition behavior for all the ambient $ThMo_2O_8$ phases, we sent our

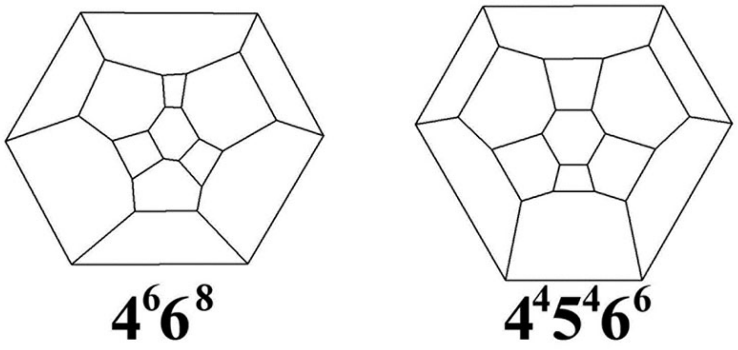

Figure 3.8: Schlegel projections of the polyhedra with $4^6 6^8$ and $4^4 5^4 6^6$ combinatorial-topological types (CTTs).

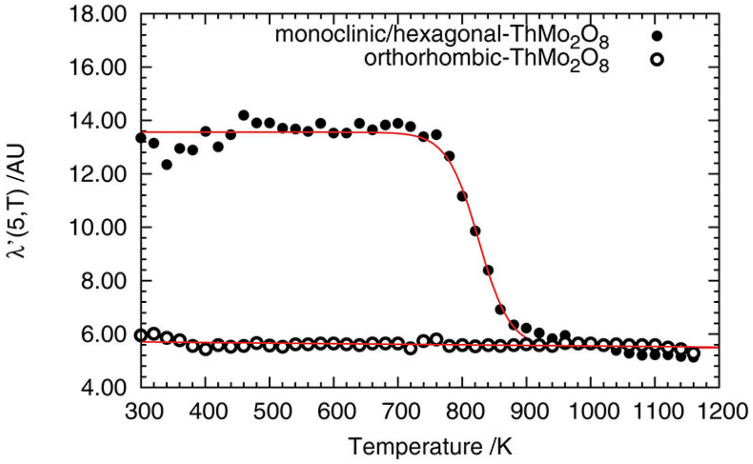

Figure 3.9: Temperature-dependent $\lambda'(5)$ parameter development of two different samples on X-ray investigations.

samples to the Prof. Thorsten M. Gesing in the University of Bremen for making the temperature-dependent phase powder X-ray diffraction experiment. As shown in **Figure 3.9**, the temperature-dependent *CorrNorm*(1) values obtained by the autocorrelation analysis of the temperature-dependent PXRD data of orthorhombic-$ThMo_2O_8$ can be fitted with a linear function (slope: 2.2(6) 10^{-5}, intercept: 5.77(5)) and show only a slight decrease with increasing temperature. As it is the first heating measurement, the monoclinic- and hexagonal-$ThMo_2O_8$ containing sample on the other hand shows a more complex behavior, which can be described by a logistic function :

$$\lambda'(T) = \lambda'_{min}(T) + \frac{\lambda'_{max}(T) - \lambda'_{min}(T)}{1 + exp(-k \times (T - T_0))} \tag{3.1}$$

Where the indices *min* and *max* denote the minimum and maximum plateau values of $\lambda'(T)$, the variable k and determines the steepness and the points of inflection of the logistic function. With this function the change in the temperature-dependent behavior of this sample could be described by the steepness $k = -0.041(4)$ and the point of inflection (825(3) K), which corresponds to a fifty percent change is; the onset of the treansformation is visible in the data collected at 780 K. The observed $\lambda'(5, T)$ parameter observed after inflection decreases linearily for the measurements at temperatures higher than 880 K. The final value corresponds well to the respective parameter of the β-phase heating experiment, where only a slight decrease of the $\lambda'(T)$ parameter could be observed in the whole temperature range, indicating no further phase-transition of this phase once it is formed. The slight decrease of $\lambda'(T)$ could be interpreted with an decrease of the reflex broadness due to an virtual increase of the average crystallite size caused by the increase of the lattice-parameters as an effect of their thermal expansion.

From the temperature-dependent powder pattern of mixed monoclinic- and hexagonal-$ThMo_2O_8$ with the ratio of 7:3, as given in **Figure 3.10**, one can clearly determine the phase-transition to the orthorhombic-$ThMo_2O_8$. This transition corresponds to the midpoint temperature of 825(3) K found in the autocorrelation analysis. A second transition could not be seen, which makes it most likely to interpret the second broadening of the autocorrelation as an ongoing crystallization behavior. The temperature-dependent powder pattern of the orthorhombic-$ThMo_2O_8$ does not show any phase-transition as expected from the autocorrelation analysis.

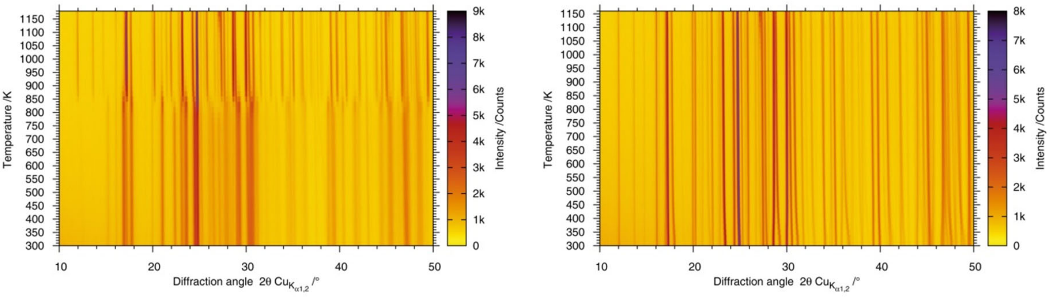

Figure 3.10: Temperature-dependent X-ray powder pattern given as 2D-plot. Left: monoclinic- and hexagonal-$ThMo_2O_8$ in the ratio of 7: 3; right orthorhombic-$ThMo_2O_8$.

Rietveld analysis of the temperature-dependent diffraction data confirms the transformation from both, the monoclinic- and hexagonal-$ThMo_2O_8$ to orthorhombic-$ThMo_2O_8$. From the refinement results of the corresponding phase fractions, given in **Figure 3.11**, one can clearly see that the phase-transformation starts with a decrease of hexagonal-$ThMo_2O_8$ and a corresponding increase of monoclinic-$ThMo_2O_8$ accompanied also with a slight increase of orthorhombic-$ThMo_2O_8$. Thereafter the phase fraction of both monoclinic- and hexagonal-$ThMo_2O_8$ decreases and orthorhombic-$ThMo_2O_8$ is formed.

To get intrinsic energy information of the phases the thermal expansion of solids can be adequately modeled using both Debye quasi-harmonic and Einstein harmonic models. In the Einstein harmonic model the atoms in a solid are independent oscillators and free from other sources of dynamical entropy. The Debye quasi-harmonic model also assumes independent oscillators, however, with altered frequencies. If none of the thermal expansion coefficient (**TEC**) of the metric parameters saturate at a temperature-independent region for the observed range, which is assumed to be associated with intrinsic anharmonicity leading to anisotropic and anomalous thermal expansion. We carried the first refinements of both phases out using one Debye and the Anharmonicity term ($d = 1$, $e = 0$, k_A) in the general equation:

$$M(T) = M_0 + \sum_{i=1}^{d} K_{Di}UDi(T) + \sum_{i=1}^{e} K_{Ei}U_{Ei}(T) + K_AU_A(T) \tag{3.2}$$

as given together with further details elsewhere. In this equation $M(T)$ refers to any of the temperature-dependent metric parameters ($V(T)$, $a(T)$, $b(T)$ and $c(T)$), k_{Di}, k_{Ei} and k_A are adjustable fitting parameters representing thermoelastic information, contributing to Debye (U_{Di}), Einstein (U_{Ei}) and anharmonic (U_A) internal energies, respectively.

For monoclinic-$ThMo_2O_8$ the thermal expansion could finally be fitted with only one Debye contribution ($d = 1$, $e = 0$, $k_A = 0$). The deviation of the observed data indicates the change of the structure driven by the following/ongoing phase-transition to orthorhombic-$ThMo_2O_8$. The same could be observed for hexagonal-$ThMo_2O_8$. To fit these data phonon contributions of $d = 1$, $e = 0$, k_A for the unit-cell volume and $d = 1$, $e = 1$, $k_A = 0$ for the ***a***, ***b***, and ***c*** lattice parameters were used. Beside the positive thermal expansion behavior of most of the lattice parameters a negative thermal-expansion for the ***c*** lattice parameter with increasing temperature is observed. The deviation of the observed data points from the calculated one again shows the following/ongoing phase-transition to orthorhombic-$ThMo_2O_8$. For orthorhombic-$ThMo_2O_8$ the thermal behavior is the most complex and could not finally be understood without taking the low-temperature structure behavior into account which could not be measured until now. Therefore only one Debye parameter could (and must only be) used for the internal energy calculations. For the volume curve calculations 2 Einstein terms were used whereas for the ***a*** and ***b*** lattice parameter 2 Einstein and the anharmonicity term and for the ***c*** lattice parameter 1 Einstein and the anharmonicity term were needed. For this polymorph a negative thermal expansion was observed for the ***a*** lattice parameter which could be correlated with a negative Debye contribution as well as a negative contribution from one Einstein term. Interesting for this phase is also the deviation from the calculated curve at temperature between 300 K and 400 K for the ***c*** lattice parameter. No explanation could be given in the moment. Further investigations are needed to bring more light into this behavior.

3.2.2 DFT investigation of thermodynamic behavior of $ThMo_2O_8$ and derived phase diagram

The thermodynamical stability of different $ThMo_2O_8$ polymorphs under certain temperature and pressure condition can be determined from the Gibbs free energy (G) which is computed as

$$G = U + ZPE - T \times S + PV, \tag{3.3}$$

where U is the internal energy, ZPE is the zero point energy rising from the 0 K vibrations of the crystalline lattices T is the temperature, S is the vibrational entropy that can be obtained from the

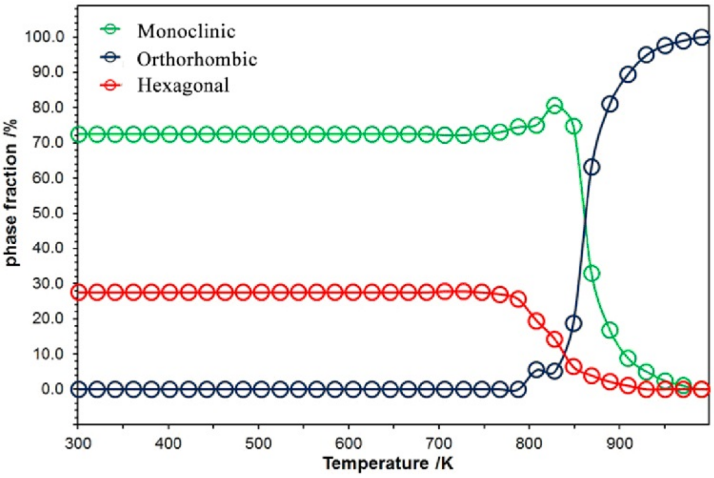

Figure 3.11: Temperature-dependent phase fraction changes of $ThMo_2O_8$.

vibrational frequencies, P is the pressure and V is the volume. The Gibbs free energy computed at different temperature for all the considered $ThMo_2O_8$ polymorphs is illustrated in **Figure 3.12**. At ambient condition, the orthorhombic phase has higher energy than those of the hexagonal and monoclinic polymorphs. The latter two polymorphs are close in energy (the difference is only 0.5 kJ/mol), which is consistent with the experimental results indicating the coexistence of these two phases at low temperatures. However, as the temperature increases, the free energy for the monoclinic and hexagonal polymorphs reveals a general trend of increase and exceeds that of the orthorhombic polymorph when the temperature is higher than ∽900 K.

The free energy of the HT/HP orthorhombic polymorph at ambient conditions is much larger (48.3 kJ/mol) than that of the orthorhombic polymorph. However, due to the giant volume reducing (by 20 %), one should expect much less contribution from PV term to the Gibbs free energy at pressure, which should make this phase the most stable at some high pressure. Because of the heavily reduced volume, the Gibbs free energy of the HT/HP orthorhombic polymorph is substantially reduced (taking the Gibbs free energy of the monoclinic phase as reference) and much smaller than those of the ambient pressure polymorphs. The dramatic change in the free energy of the HT/HP orthorhombic polymorph with pressure is clearly visible in **Figure 3.12**. It should be noted that because of the temperature variations of the vibrational entropies, the energy difference of the ambient polymorphs becomes more pronounced with increasing the temperature. This indicates that the threshold pressure at which the HT/HP orthorhombic polymorph forms should vary with temperature. This threshold pressure can be estimated from the difference of the Gibbs free energies of the two phases.

The resulting transition pressure among monoclinic, orthorhombic, and HT/HP orthorhombic polymorphs can be estimated from equality of Gibbs free energies (Eq. 3.3) as

$$P(T) = \triangle G(T, P = 0 \text{ GPa})/\triangle V, \tag{3.4}$$

where $\triangle G(P = 0 \text{ GPa})$ and $\triangle V$ are the difference in ambient pressure free energies and volumes of the HP/HP orthorhombic and the initial phase. The computed phase diagram of $ThMo_2O_8$ is given in

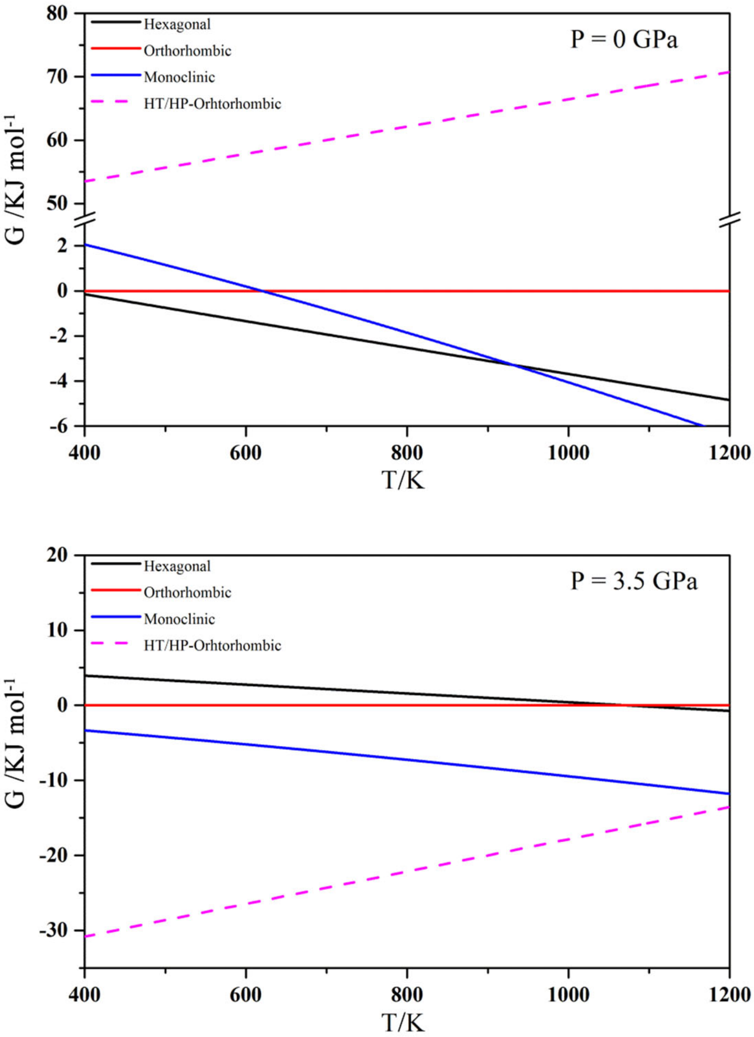

Figure 3.12: Gibbs free energy as the function of T at (a) P = 0 GPa and (b) P = 3.5 GPa, respectively.

Figure 3.13. From this **Figure 3.13**, one can note that the transition pressure for HT/HP orthorhombic polymorph increases with increasing temperature and ranges from 2.1 GPa at room-temperature to 3.6 GPa for 1350 K.

Structural Summary of AM_2O_8 Family (A = Zr, Hf, Th; M = Mo, W)

The compounds of the AM_2O_8 (A = Zr, Hf, Th; M = Mo, W) family exhibit unprecedentedly structural flexibility associated with the ability to adopt various polymorphic forms under different pressure, temperature and hydration state. Among them, due to the isotropic NTE behavior observed over a broad temperature range, the cubic phases of the AM_2O_8 family (A = Zr, Hf, Th; M = Mo, W) have recently received intensive studies. Their structural frameworks are composed of six-fold AO_6 octahedra and four-fold MO_4 tetrahedra. The AO_6 octahedra share all the corners with six MO_4

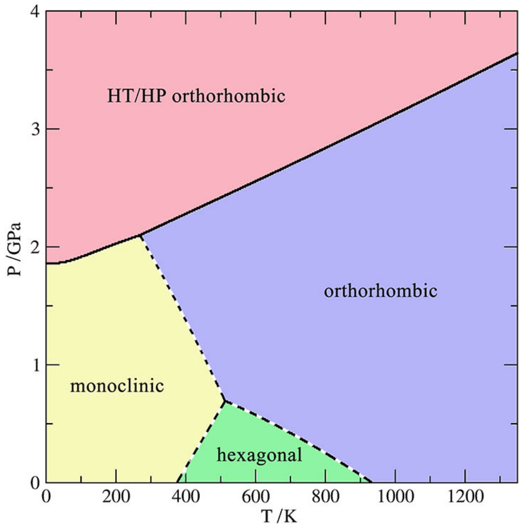

Figure 3.13: The derived P-T phase diagram of $ThMo_2O_8$ from DFT calculations. Because the Gibbs free energies among monoclinic- orthorhombic- and hexagonal-$ThMo_2O_8$ are quite close, the phase formation borders among these three might be not very precise, as indicated by dash lines.

tetrahedra, while the MO_4 tetrahedra are tridentate, thus leaving the fourth corner non-shared. The terminal oxygen corners which are oriented along the body diagonal direction ([111]) play a key role during the phase transition procedure. As the temperature increases, these terminal oxygen atoms can change the orientation and react with the nearest adjacent tetrahedra, leading to oxygen migration.

In total, four polymorphs are found for $ThMo_2O_8$ and the NTE is detected in hexagonal- and orthorhombic-$ThMo_2O_8$. Unlike its radioactive counterparts in AM_2O_8 family, where M sites are fixed in four-fold tetrahedral geometry with one unshared corner, the corresponding four-fold or five-fold coordinated M sites (MoO_4 or MoO_{4+1}) in $ThMo_2O_8$ are fully connected with neighboring Th polyhedra. Compared to the transition metals Zr or Hf, the actinide element Th bears more coordination numbers from 6 to 15. This causes the polymorphs of $ThMo_2O_8$ to be more versatile and complex, which is demonstrated by presenting four different coordination geometries (ThO_6 octahedra, ThO_8 square antiprisms, ThO_9 tricapped trigonal prism and ThO_{11} all-face capped trigonal prism). In contrast, only one octahedral geometric configuration is found in Zr- and Hf- based polymorphs. The extraordinary coordination of both Mo and Th sites in HT/HP-orthorhombic-$ThMo_2O_8$ also account for the remarkable volume shrink behavior observed when pressure changes from ambient to extreme condition.

3.2.3 Raman spectroscopic analysis

For the three thorium molybdates prepared at the ambient pressure, the recorded spectra are dominated by three parts, which is typical for compounds containing Mo atoms only in tetrahedral $MoO_4{}^{2-}$ units. The ideal $MoO_4{}^{2-}$, with the T_d symmetry, has four normal motions which can be assigned to $A_1(\nu_1)$, $E(\nu_2)$, F_1(rot) and $F_2(trans, \nu_3, \nu_4)$. The A_1, E and F_2 are Raman active and F_2 is also IR permitted.[76] For these three ambient compounds, the bending modes ν_2 and ν_4 are located in the

---

[76] V.P. Mahadevan Pillai et al. *Spectrochim. Acta, Part A*, **53**: 867–876, 1997.

region of around 250 cm^{-1} to 410 cm^{-1}. The spectra from around 720 cm^{-1} to 815 cm^{-1}, shown in **Figure 3.14**, can be attributed to the stretching modes ν_3, while the vibrations from around 890 cm^{-1} to 1000 cm^{-1} are due to the symmetric stretching modes of ν_1. For HT/HP-orthorhombic $ThMo_2O_8$ obtained in high-temperature high-pressure condition, the vibrations also demonstrate a certain similarities in the $MoO_4{}^{2-}$ environment. However, its signal is slightly broadened in the stretching bands region compared with those of ambient polymorphs. This can be ascribed to the deformed tetrahedral geometry (MoO_{4+1}) in the high-temperature high-pressure polymorph, which induces the break of T_d symmetry and thus results in strongly couple effect of stretching vibrations (ν_1 and ν_3).

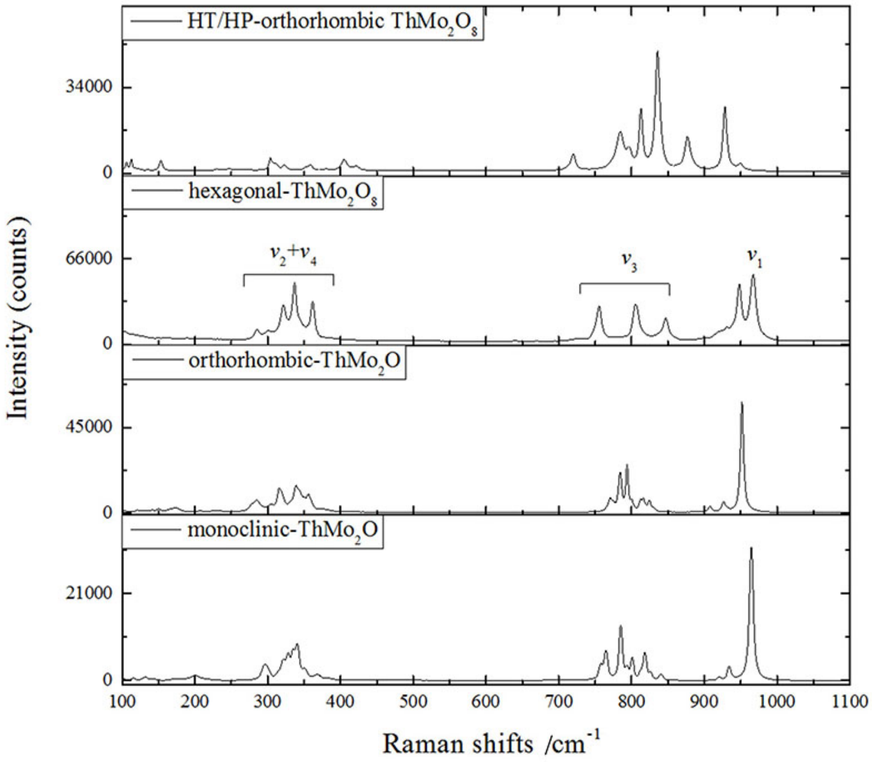

Figure 3.14: Raman shifts for all the $ThMo_2O_8$ polymorphs from 100 cm^{-1} to 1100 cm^{-1}.

3.3 Conclusions

Two new $ThMo_2O_8$ polymorphs, monoclinic- and HT/HP-orthorhombic-$ThMo_2O_8$, have been successfully synthesized under ambient and high-temperature/high-pressure conditions, respectively. These two polymorphs, together with the previous reported orthorhombic- and hexagonal-$ThMo_2O_8$, indicate the ability of $ThMo_2O_8$ to adopt various polymorphic forms with demonstration of its polymorphic flexibility. Among all these four $ThMo_2O_8$ polymorphs, three of them, monoclinic-, hexagonal- and orthorhombic-$ThMo_2O_8$, can be synthesized at ambient pressure. The crystal structures and topological relations of these three ambient polymorphs are highly related with each other, and all can be seen as being constructed from the basic Th-Mo building chains arranged in different directions. Among them, the most stable polymorphs are the monoclinic and hexagonal forms, and both phases can be irreversibly transformed to orthorhombic-$ThMo_2O_8$ at onset temperature of 797 K. In addition, a negative thermal-expansion behavior with increasing temperature is observed for orthorhombic- and hexagonal-$ThMo_2O_8$ in the ***a*** and ***c*** directions, respectively.

The study of $ThMo_2O_8$ under high-temperature/high-pressure condition at 3.5 GPa reveals a giant, 20 % volume change, accompanied by the significant structural contraction along the ***c***-axis. Due to such enormous density increase, the HT/HP polymorph is kinetically stable at ambient conditions. In HT/HP orthorhombic-$ThMo_2O_8$ polymorph, the Th or Mo polyhedra are linked through face-sharing or corner-sharing manners, respectively, leading to very dense Th or Mo chains, whereas these polyhedra centers are completely isolated from each another in the ambient pressure polymorphs. Using first principle calculations, the Gibbs free energies were calculated for different investigated polymorphs and constructed the stability phase diagram for $ThMo_2O_8$. The obtained phase diagram indicates that the transition to high-temperature high-pressure polymorph happens even at room-temperature for a pressure higher than 2.1 GPa and this transition pressure increases with temperature. This confirms thermodynamical stability of the new HT/HP polymorph at the synthesis conditions.

Chapter 4

Crystal Chemistry of Thorium Molybdates and Tungstates Synthesized Using Traditional High-Temperature Solid-State Method

This chapter will introduce some of the thorium molybdates and tungstates compounds which were isolated by high-temperature solid-state technique. The crystal chemistry of thorium molybdate and tungstate families is the main task of my PhD research. Actinide molybdates and tungstates have been extensively studied for a few decades due to the fascinating activity of actinides and d-block metals toward the discovery of new compounds related to nuclear applications. The actinide elements enjoy considerably rich structural chemistry. Pentavalent and hexavalent U, for example, are normally observed in the configuration of a linear $\mathrm{UO_2}^{2+}$ dioxo cation, adopting coordination numbers from four to six, yielding tetragonal, pentagonal and hexagonal bipyramids. Tetravalent Th, by comparison, adopts higher coordination numbers and demonstrates very rich structural chemistry. Molybdenum is one of the significant fission products created with high yield in the nuclear reactor.[43,77] In addition, actinide molybdates may be considered as important materials for long-term evolution of a geological repository for spent nuclear fuel.[78] The Mo(VI) centers can coordinate with four to six oxygen atoms giving rise to tetrahedral, square pyramidal, trigonal bipyramidal and octahedral geometries. Tungstates also exhibit a very diverse structural chemistry with rich coordination geometries, having high potential for demonstrating remarkable physiochemical applications in a variety of fields. Moreover, these molybdenum and tungsten polyhedra can be aggregated as a result of metal complexation to form various polymeric networks. As a consequence, the thorium molybdates and tungstates demonstrate an inexhaustible structural flexibility to form various structural motifs.

---

[43] Sergey V. Krivovichev and Peter C. Burns. *Inorg. Chem.*, **41**: 4108–4110, 2002.

[77] Christopher C. Underwood et al. *Inorg. Chem.*, **50**: 11825–11831, 2011.

[78] Evgeny V. Suleimanov et al. *J. Chem. Thermodyn.*, **42**: 873–878, 2010.

4.1 Study of phase transition in rubidium thorium molybdate family

Four new rubidium thorium molybdates have been synthesized from high-temperature solid-state reactions. The structures of $Rb_8Th(MoO_4)_6$, $Rb_2Th(MoO_4)_3$, $Rb_4Th(MoO_4)_4$ and $Rb_4Th_5(MoO_4)_{12}$ were determined using single crystal X-ray diffraction. All these compounds construct from MoO_4 tetrahedra and ThO_8 square anti-prisms. The studied compounds adopt the whole range of possible structure dimensionalities from 0D to 3D: finite clusters, chains, sheets and frameworks. $Rb_8Th(MoO_4)_6$ crystallizes in zero-dimension containing clusters of $[Th(MoO_4)_6]^{8-}$. $Rb_2Th(MoO_4)_3$ is formed based upon one-dimensional chains with configuration units $[Th(MoO_4)_3]^{2-}$. Two-dimensional sheets occur in compound $Rb_4Th(MoO_4)_4$ and three-dimensional framework with channels formed by thorium and molybdate polyhedra are observed in $Rb_4Th_5(MoO_4)_{12}$. The Raman and IR spectroscopic properties of these compounds are reported. Temperature-depended phase transition effects were observed in $Rb_2Th(MoO_4)_3$ and $Rb_4Th(MoO_4)_4$ using DSC and high-temperature powder diffraction methods.

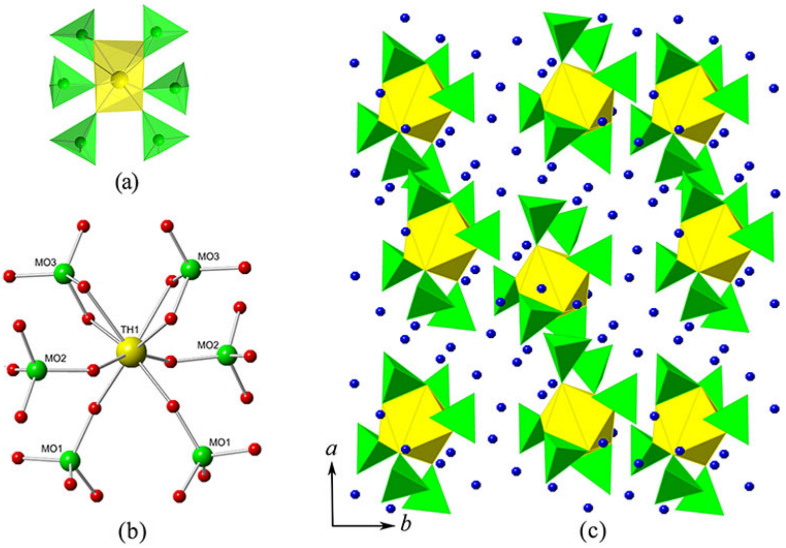

Figure 4.1: Depiction of finite clusters of $Rb_8Th(MoO_4)_6$.

Compounds of Rb-Th-Mo in this chapter were obtained by high-temperature solid-state reactions. Analytical reagent grade chemicals were used without further purification. $Th(NO_3)_4 \cdot 5H_2O$ (Merck), $RbNO_3$ (Alfa-Aesar) and MoO_3(Alfa-Aesar) with the molar ratio of 1:2:2, 1:3:4, 1:2:4 and 1:1:1 were thoroughly ground together and loaded into a platinum crucible. About 5 % excessive amounts of MoO_3 were added into each mixture in order to compensate its evaporation at high temperature. The reaction mixtures were then placed into a program-controlled furnace (CARBOLITE CWF 1300) and heated to 900 °C in 4 h, staying at this temperature for 10 h in order to let the mixture react homogeneously. After that, slowly cooling to 400 °C at a rate of 5 °C/h was followed by a rate of 50 °C/h to room-temperature. The reaction product of $Rb_8Th(MoO_4)_6$ consisted of colorless prism-like crystals. $Rb_8Th(MoO_4)_6$ could also be found as minor product in 3:1:8 and 3:2:5 reactions. $Rb_2Th(MoO_4)_3$

was present in trace amounts and could be manually separated based on different crystal morphology. The major product was orthorhombic $ThMo_2O_8$. Crystals in the blocks with colorless amorphous phases as by-products were found for the reaction of $Rb_4Th(MoO_4)_4$. $Rb_4Th_5(MoO_4)_{12}$ could also be found as a well-formed colorless prism-like crystals in the experiment with Th : Rb : Mo molar ratios of 1:1:3, 2:3:2, 2:3:4, and 3:2:5.

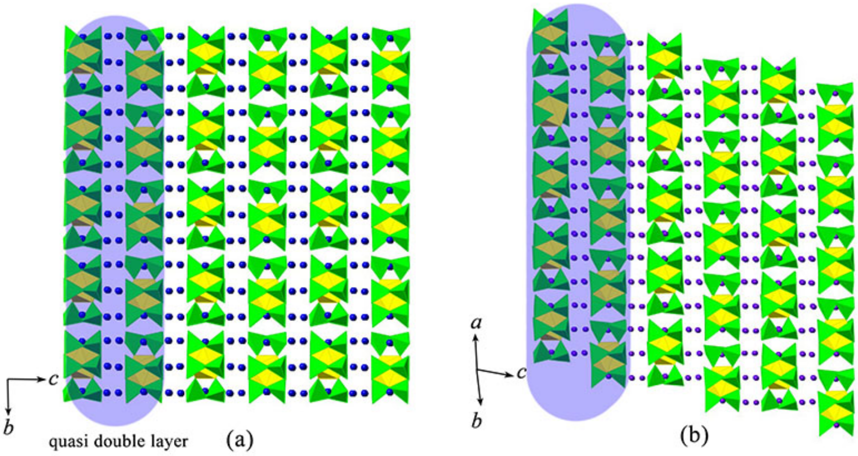

Figure 4.2: A view of packing modes in the structures of (a) $Rb_8Th(MoO_4)_6$ and (b) $K_8Th(MoO_4)_6$. The quasi double layers are highlighted in both structures.

4.1.1 Structural aspects of rubidium thorium molybdate family

$Rb_8Th(MoO_4)_6$. The crystal structure of $Rb_8Th(MoO_4)_6$ is based upon finite $[Th(MoO_4)_6]^{8-}$ clusters as shown in **Figure 4.1 (a,b)**. The Th centers of these clusters are linked by four monodentate MoO_4 as well as two bidentate MoO_4 tetrahedra. The O-Mo-O bond angles of the monodentate MoO_4 tetrahedra are found in a range from 107.0(3)° to 112.5(3)° representing a normal deviation from the ideal tetrahedra angle of 109.4°. In the bidentate MoO_4 tetrahedra one rather small O-Mo-O angle of 95.5(2)° could be found whereas the other angles are slightly bigger up to 116.1(3)°. The rather small tetrahedra angle is found between those two oxygen atoms (O1 and O2) which are additionally bonded to the central thorium atom showing also longer Mo-O bond distances of 1.795(5) Å (O1) and 1.804(5) Å (O2) compared to O5 (1.742(5) Å) and O3 (1.741(5) Å). The thorium molybdate clusters are separated from each other by intercalated rubidium cations which results in zero-dimensional thorium molybdate building units (**Figure 4.1 (c)**). $Rb_8Th(MoO_4)_6$ is the second known thorium molybdate with cluster structure. The first example is a structure of chemically similar $K_8Th(MoO_4)_6$.[79] The structure of $K_8Th(MoO_4)_6$ also comprises the finite $Rb_8Th(MoO_4)_6$ clusters which are topologically identical to those in $Rb_8Th(MoO_4)_6$. However, due to the presence of different alkali cations with different ionic radii, the packing mode of the clusters within the structures is different in K and Rb analogues and resulting structures are not isostructural. As could be seen in

---

[79] M. Huyghe et al. *Acta Crystallogr., Sect. C: Cryst. Struct. Commun.*, **49**: 950–954, 1993.

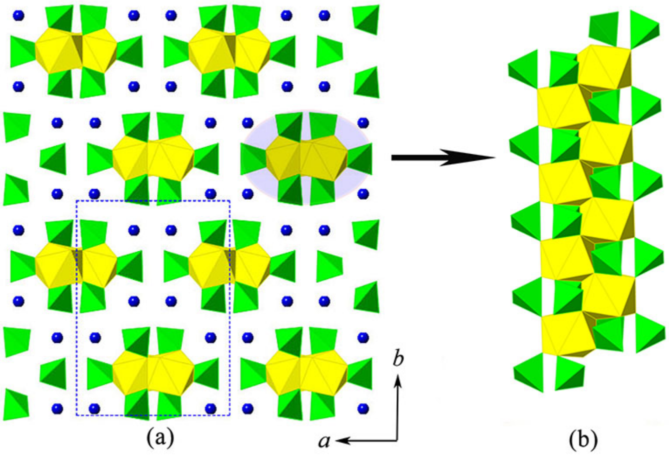

Figure 4.3: . Depection of one-dimensional chain of $Rb_2Th(MoO_4)_3$. (a and b) View along two different directions shows the chains with configuration of $[Th(MoO_4)_3]^{2-}$.

Figure 4.2, the packing modes resulting in a quasi-double layer perpendicular to the crystallographic **c**-axis in $Rb_8Th(MoO_4)_6$ is shifted by half a cluster unit in the structure of $K_8Th(MoO_4)_6$. In addition, the two layers which comprise each quasi double layer in the structure of $Rb_8Th(MoO_4)_6$ are severely twisted in the structure of $K_8Th(MoO_4)_6$. The structural difference is also reflected by the different symmetries of the two structures: triclinic for $K_8Th(MoO_4)_6$ (SG $P\bar{1}$) and monoclinic for $Rb_8Th(MoO_4)_6$ (SG $C2/c$).

$Rb_2Th(MoO_4)_3$. The crystal structure of $Rb_2Th(MoO_4)_3$ adopts a one-dimensional chain structure as given in **Figure 4.3**. This compound crystallizes in space group $C2/c$ and is isotypic to $K_2Th(MoO_4)_3$ that can be seen as deriving from $Am_2(MoO_4)_3$ which follows the scheelite structure.[80] In $Rb_2Th(MoO_4)_3$, the slightly distorted thorium square anti-prisms share a common edge with two neighboring thorium atoms each and are surrounded by vertex-sharing MoO_4 tetrahedra to form infinite $[Th(MoO_4)_3]^{2-}$ chains (**Figure 4.3 (b)**) oriented parallel to [001]. Each single Th site is connected to eight MoO_4 tetrahedra with Th-O distances ranging from 2.346(4) Å to 2.544(4) Å. It is interesting to note that thorium based $Rb_2Th(MoO_4)_3$ has similar structure with lanthanide family $KBaGd(MO_4)_3$ (M = Mo, W) compounds which are synthesized under similar condition.[81] Both structures can be evolved from the scheelite-related $CaMoO_4$ by superseding 1/3 of Ca atoms with Th^{4+} or Gd^{3+} ions and 2/3 with alkali or alkaline-earth metals. Rb^+ ions are fully reside in $8f$ sites within $Rb_2Th(MoO_4)_3$ structure and surrounded by eight oxygen atoms with bond lengths ranging from 2.837(4) Å to 2.967(4) Å. For lanthanide $KBaGd(MO_4)_3$, however, the monovalent K^+ and divalent Ba^{2+} ions require a partial occupancy of the same sites in order to accomplish the valence as well as atoms balance during replacement. The average bond distances for the ThO_8 and GdO_8 polyhedra are 2.433 Å and 2.420 Å in $Rb_2Th(MoO_4)_3$ and $KBaGd(MO_4)_3$, respectively.

$Rb_4Th(MoO_4)_4$. Single crystal X-ray diffraction studies reveal that $Rb_4Th(MoO_4)_4$ crystallizes in the monoclinic space group $C2/c$. $Rb_4Th(MoO_4)_4$ has been previously studied by powder X-ray diffraction however, no structural information has been given except for the cell parameters. A [010] projection

---

[80] M. Huyghe et al. *Acta Crystallogr., Sect. C: Cryst. Struct. Commun.*, **47**: 244–246, 1991.

[81] Yi Yu et al. *PLoS ONE*, **8**: e54450, 2013.

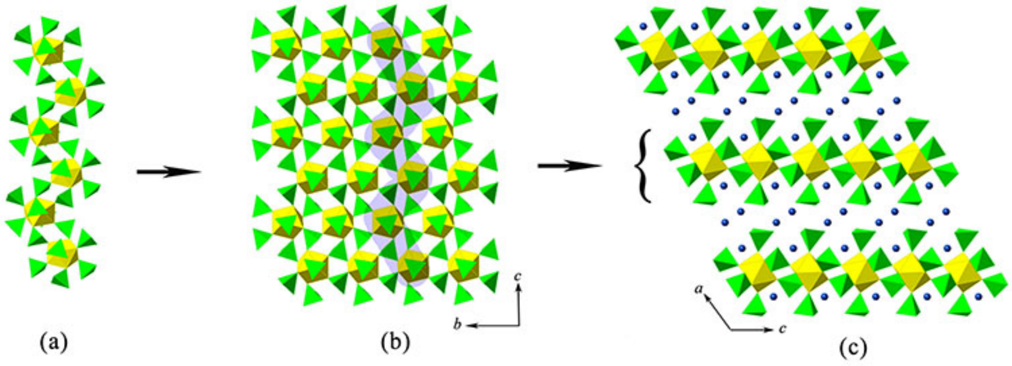

Figure 4.4: Depection of two-dimensional sheets of $Rb_4Th(MoO_4)_4$

shows that $Rb_4Th(MoO_4)_4$ is based on two-dimensional thorium molybdate sheets (**Figure 4.4 (c)**). Each ThO_8 square anti-prism is surrounded by eight vertex-sharing MoO_4 tetrahedra. For comparison to the first two structures one can separate thorium molybdate single-chains within the 2D layer. These chains are based on ThO_8 square anti-prisms bridged by two MoO_4 tetrahedra to form a $[Th(MoO_4)_4]^{4-}$ composition (**Figure 4.4 (a)**). The $[Th(MoO_4)_4]^{4-}$ chains are fused side-by-side in the same orientation along [010] direction to result in mentioned two-dimensional sheet (**Figure 4.4 (b)**). The Rb(2) cations are resided within the sheets whereas the Rb(1) cations provide a crosslink of neighboring layers stacking parallel to **c**-axis (**Figure 4.4 (c)**). The building chains, $[Th(MoO_4)_4]^{4-}$, in the structure of $Rb_4Th(MoO_4)_4$ are similar to those found in $A_4Th(MoO_4)_4$ (A = Na, K) series.[47] The $Th[(MoO_4)_4]^{4-}$ chains in these structures have similar topology with those in $Rb_4Th(MoO_4)_4$ but are different from the geometrical point of view. One crystallographic independent Th site and two Mo sites occur in the chain observed in $Rb_4Th(MoO_4)_4$, whereas, only one Th site and one Mo site each are found in the $K_4Th(MoO_4)_4$ chains. The average Th-O bond length in $Rb_4Th(MoO_4)_4$ is 2.407(3) Å, which is similar to that in $K_4Th(MoO_4)_4$ (2.416(3) Å). A comparison of $[Th(MoO_4)_4]^{4-}$ chain structures in $Rb_4Th(MoO_4)_4$ and in the $A_4Th(MoO_4)_4$ series is presented in **Figure 4.5**. The topology of $Rb_4Th(MoO_4)_4$ sheets and $A_4Th(MoO_4)_4$ framework can be illustrated using white-and-black representation where black nodes and white nodes correspond to ThO_8 square anti-prism and MoO_4 tetrahedron, respectively, as shown in **Figure 4.5 (d)** and **Figure 4.5 (c)**. In both topologies, all black vertexes (Th sites) are 8-connected. Every Mo site is 2-connected in $A_4Th(MoO_4)_4$, whereas in $Rb_4Th(MoO_4)_4$ half of the Mo sites are 3-connected and the remaining Mo sites are only 1-connected. As a consequence, $Th[(MoO_4)_4]^{4-}$ chains lead to a three-dimensional framework in $A_4Th(MoO_4)_4$ while a layered-structure results in $Rb_4Th(MoO_4)_4$. The topological transformation from the three-dimensional framework conformation to two-dimensional sheets can be made by using the cutting and gluing procedure, which involves reconstruction of the local coordination of the Mo sites. First of all, the Mo-O connections within the edge side of each $Th[(MoO_4)_4]^{4-}$ fragment in the framework structure of $A_4Th(MoO_4)_4$ have to be broken to obtain a single $Th[(MoO_4)_4]^{4-}$ chain. The equivalent

---

[47] N.D. Dahale, Meera Keskar, and K.D. Singh Mudher. *J. Alloys Compd.*, **415**: 244–250, 2006.

Mo points (white nodes) on the side of each Th$[(MoO_4)_4]^{4-}$ chain have been labeled with letters a, b, c, d. The topological transformation from the three-dimensional framework to the two-dimensional sheet structure can be completed by jointing of the corresponding white nodes $a-a$, $b-b$, $c-c$, $d-d$, as it is shown in **Figure 4.5**. This transformation only involves changing the coordination number of Mo atoms, without reconstructing the topology of the Th$[(MoO_4)_4]^{4-}$ chains. Different structural arrangement with similar basic units is reflecting the nature of Th-O-Mo linkages. It is also interesting that similar $[X(MoO_4)_4]^{n-}$ chains are observed in another molybdate compounds, such as $Na_5La(MoO_4)_4$ or $Na_5Tb(MoO_4)_4$.[82]

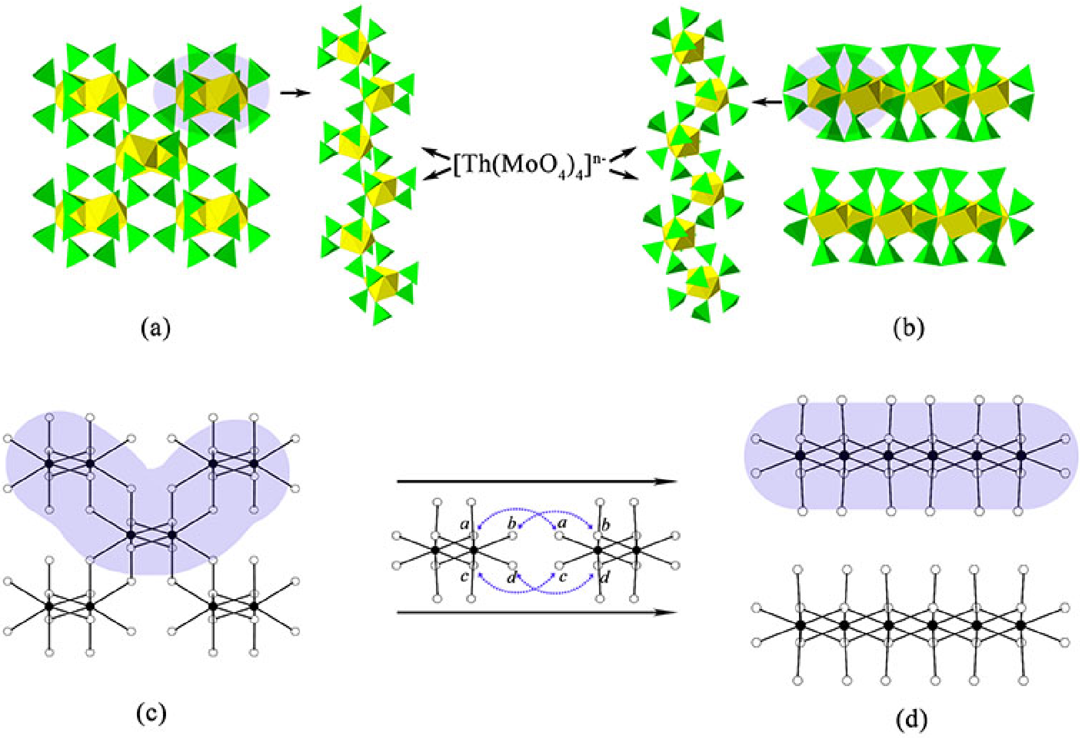

Figure 4.5: Chains of square anti-prism tetrahedral in different thorium molybdate compounds: (a) framework of $Na_4Th(MoO_4)_4$ and its fundamental chains. (b) two-dimensional structure of $Rb_4Th(MoO_4)_4$ and its fundamental chains. (c and d) Black-and-white graphs describing transformation from three-dimensional framework to two-dimensional chains by connecting equivalent white points labeled by same letters.

$Rb_4Th_5(MoO_4)_{12}$. This compound adopts a porous 3D structure and is the most complex thorium molybdate to date (**Figure 4.6 (a)**). It contains three symmetrically independent Th sites with geometry of its environment shown in **Figure 4.6 (b)**. Each of the Th atoms is surrounded by eight oxygen atoms resulting in square anti-prism geometry and linked to eight monodentate MoO_4 tetrahedra. All oxygen atoms in Mo(5)O4 and are fully bonded with Th atoms while Mo(1)O_4, Mo(2)O_4, Mo(3)O_4, Mo(4)O_4 and Mo(6)O_4 tetrahedra have one terminal oxygen atoms. The Mo-O distance ranging

---

[82] C. de Mello Donega et al. *Journal of Luminescence*, **6061**: 74 –77, 1994.

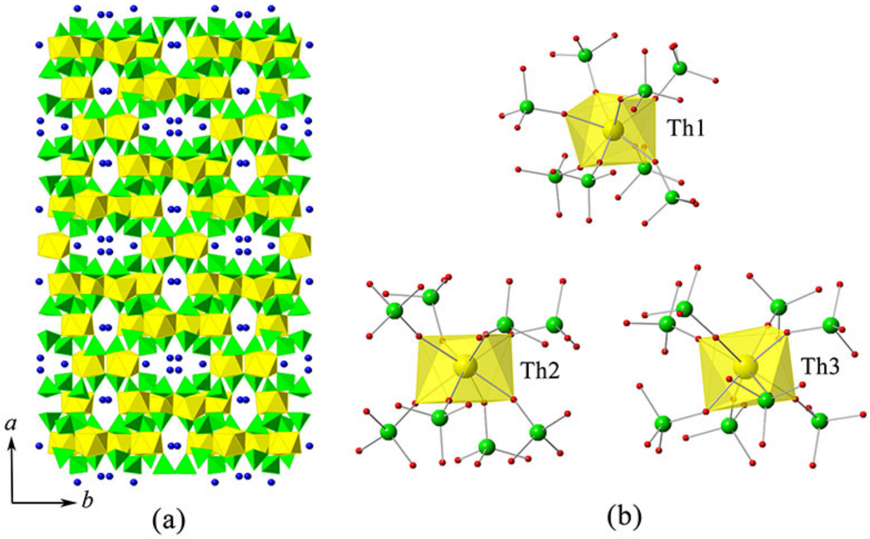

Figure 4.6: Depection of three-dimensional framework of $Rb_4Th_5(MoO_4)_{12}$

from 1.674(8) Å to 1.784(5) Å is consistent with other thorium molybdate structures involving monodentate molybdate linkages.[83] The structure of $Rb_4Th_5(MoO_4)_{12}$ can be described as based upon corrugated butterfly-shaped ribbons which are highlighted in **Figure 4.7**. These anionic ribbons act as the fundamental building block (**FBB**) of the $Rb_4Th_5(MoO_4)_{12}$ structure and consist of MoO_4 tetrahedra and ThO_8 square anti-prism. Two ribbons related by inversion transformation connect together, resulting in a porous bow-knot shaped fragment that occurs identically in the corner- and body- center of the unit cell. Within this, the pores have the internal size of 3.0 × 6.4 Å and are occupied by Rb(3) atoms. The bow-knot shaped fragments further pack into a three-dimensional framework, which leads to large, approximately elliptical channels with inner dimensions of 8.7 × 3.1 Å, running parallel to the **c**-axis. The Rb(1) and Rb(2) atoms are partially and fully reside in the center and side of the channels, respectively. It is noted that the large channels in framework $Rb_4Th_5(MoO_4)_{12}$ may indicate its ability to host diverse cations of various radii as well as valence without considerable geometric parameters change. This means the Rb cations can be substituted by other ions while keeping the same structural skeleton. In this case $Rb_4Th_5(MoO_4)_{12}$ may be considered as an ion-exchange candidate.

Structural dimensionality

The structural variability of the four rubidium thorium molybdates reported here is observed from a finite cluster compound to a three-dimensional framework structure realized by corner- and edge-sharing ThO_8 square anti-prisms and MoO_4 tetrahedra, respectively. The dimensionality changing in these phases can be explained using the concept of "dimensional reduction" which was first discussed by *Long, et al.*.[84] It has been shown that the structural dimensionality of metal chalcogenides decreases while increasing the ratio of electropositive cations or ionic salts. Later, this method has been dis-

---

[83] S Launay et al. *J. Solid State Chem.*, **136**: 199–205, 1998.

[84] Jeffrey R. Long, Logan S. McCarty, and R. H. Holm. *J. Am. Chem. Soc.*, **118**: 4603–4616, 1996.

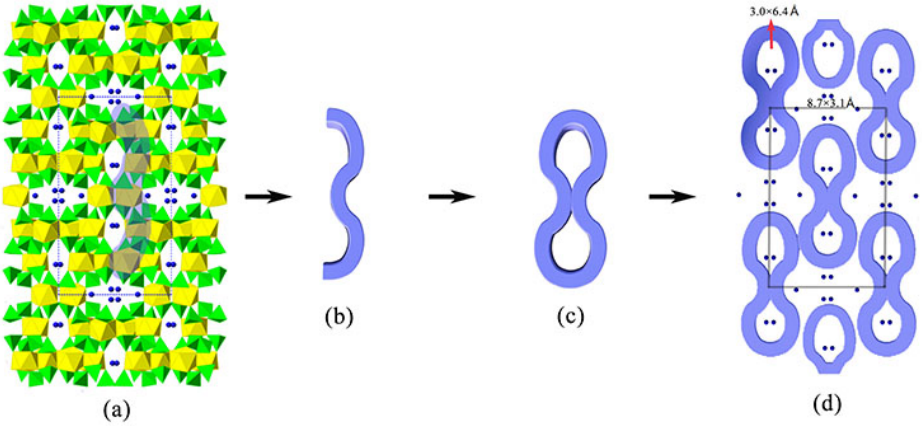

Figure 4.7: The process of butterfly-shaped fundamental building block forming the channels in structure $Rb_4Th_5(MoO_4)_{12}$.

cussed in detail as a mean to rationalize composition-structure association in the alkali metal uranyl molybdates.[85] Following this principle, one can consider each of the rubidium thorium molybdate compounds as a member of the homologous formula $[Rb_2MoO_4]_x[Th(MoO_4)_2]_y$, as shown in **Figure 4.8**. The dense three-dimensional framework orthorhombic $Th(MoO_4)_2$ is a member of the series in this expression with x/y ratio of 0. With increasing x/y ratio, the dimensionality of the framework is reduced. Thus, the $Rb_4Th_5(MoO_4)_{12}$ framework at a x/y ratio of 0.4 is relatively open with tunnels resided by Rb cations. A further increase of the x/y ratio up to 2 stabilizes the two-dimensional $Rb_4Th(MoO_4)_4$ and the largest x/y ratio of 4 gives the cluster $Rb_8Th(MoO_4)_6$. The only exception here is $Rb_2Th(MoO_4)_3$ owing a chain structure. This deviation is due to the different connection behavior of Th in $Rb_2Th(MoO_4)_3$. There are edge-sharing Th anti-prisms (Th-Th) in $Rb_2Th(MoO_4)_3$, but all the Th cations in the other three rubidium thorium molybdates are bonded to eight oxygen atoms with no Th-Th polyhedra connectivity. Essentially, as the x/y ratio increases, the dense packed lattice of the parent compound ($Th(MoO_4)_2$) is diluted by incorporated Rb atoms which breaks the Th-O-Mo linkage and lowers the dimensionality of the rubidium thorium molybdates.

4.1.2 Raman and IR spectra

All four rubidium thorium molybdate compounds crystallize in space group $C2/c = C^6_{2h}$. In order to determine their vibrational modes, the nuclear-site group analysis is performed.[86] Generally, the Mo^{6+}, Th^{4+} and Rb^+ cation in all 4 structures have only two nonequivalent Wyckoff positions $4e$ and $8f$, occupying C_2 and C_1, respectively. Since all the four compounds have the equivalent space group, specific steps of nuclear-site group analysis for each compound are also similar. Moreover, excepting for $Rb_2Th(MoO_4)_3$ which has two different crystallographic sites for Mo^{6+} ions, that is, $8f$

---

[85] Evgeny V. Alekseev et al. *Z. Anorg. Allg. Chem.*, **633**: 1979–1984, 2007.

[86] D. L. Rousseau, R. P. Bauman, and S. P. S. Porto. *J. Raman Spectrosc.*, **10**: 253–290, 1981.

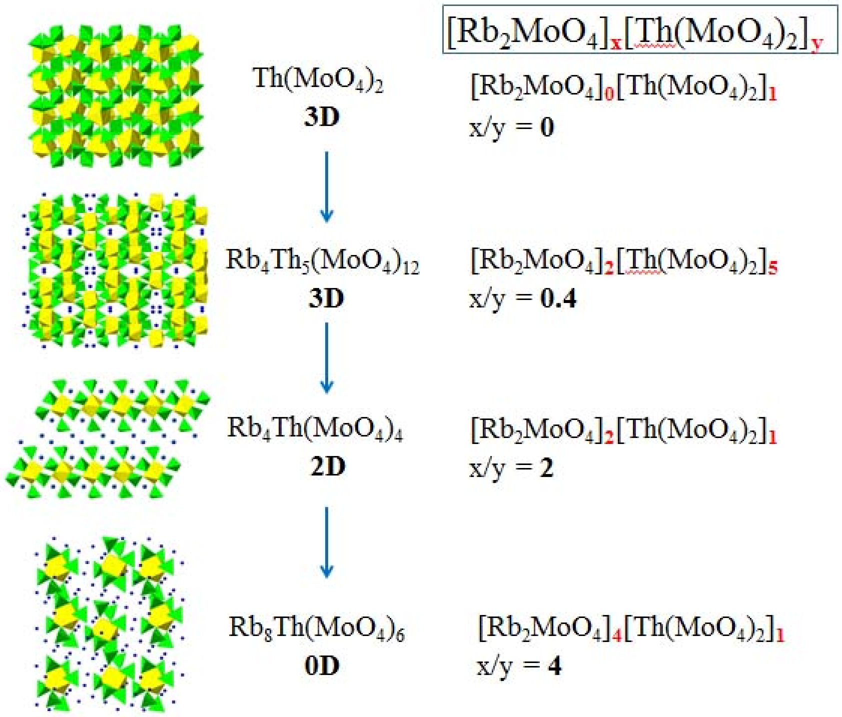

Figure 4.8: As the x/y ratio increases, the compounds are diluted by incorporated Rb atoms which breaks the Th-Mo linkage and lowers the dimensionality of the Rb-Th-Mo.

and $4e$, Mo^{6+} ions in the other three molybdates only occupy one $8f$ crystallographic site. From these points and also for the simplicity, the $Rb_2Th(MoO_4)_3$ is chosen as the most suitable representative to exhibit the procedure of the nuclear-site group analysis. The structure of $Rb_2Th(MoO_4)_3$ involves two formula units (N = 2 × 18 atoms) per primitive cell (Th atoms at $4e$ site; Rb atoms at $8f$ site; Mo(1), Mo(2) atoms at $4e$, $8f$ sites, respectively; and O atoms at $8f$ site) giving rise to total of 3 × N = 108 modes of vibration at the Brillouin zone center, which results in following irreducible representations:

$$\Gamma = 26A_g + 26A_u + 28B_g + 28B_u \tag{4.1}$$

Of these modes, subtracting 3 acoustic modes (A_u + $2B_u$), one can obtain 105 optical modes ($26A_g$ + $25A_u$ + $28B_g$ + $26B_u$). Traditionally, the vibrational modes of molybdate compound are classified into two categories.[87] One is external modes resulting from treating the motion of MoO_4^{2-} unit as a rigid group and also from motion of Rb^+ and Th^{4+} cations, the other is called internal modes where the center mass of MoO_4^{2-} unit is stationary. In order to trace the origin of these vibrations, a complete correlation of the vibrational modes for $Rb_2Th(MoO_4)_3$ is calculated (see **Figure 4.9**). Due to the effect of crystal field in the unit cell, the triply degenerate F_1 and F_2 vibrations in the free MoO_4^{2-} tetrahedra are split into non-degenerate A, B vibrations associated with T_d site breaking into C_2 and C_1 sites. Besides, the coupling among different cations in the crystal lattice further splits the vibrational modes. For the total 108 vibrational modes, 54 are internal modes generating from MoO_4^{2-} tetrahedra, that is, symmetric stretching $6\nu_1$ ($2A_g$ + $2A_u$ + B_g + B_u) and anti-symmetric stretching $18\nu_3$ ($4A_g$ + $4A_u$ + $5B_g$ + $5B_u$) as well as symmetric bending $12\nu_2$ ($4A_g$ + $4A_u$ + $2B_g$

---

[87] Jr. Barker A. S. *Phys. Rev.*, **135**: A742–A747, 1964.

+ $2B_u$) and anti-symmetric bending $18\nu_4$ ($4A_g$+ $4A_u$ + $5B_g$ + $5B_u$). The remaining 54 modes correspond to translational motions of Th^{4+} ions (A_g + A_u+ $2B_g$ + $2B_u$), Rb^+ ions ($3A_g$ + $3A_u$ + $3B_g$ + $3B_u$) and MoO_4^{2-} tetrahedra ($4A_g$ + $4A_u$ + $5B_g$ + $5B_u$) and librations of MoO_4^{2-} tetrahedra ($4A_g$ + $4A_u$ + $5B_g$ + $5B_u$). Because of an existing inverse center in space group $C2/c$, Raman and infrared modes are completely separated. All even (g) vibrations stand for Raman active while all the odd (u) ones are infrared active. As a consequence, there are 54 Raman active $26A_g$ + $28B_g$ modes and 51 infrared active $25A_u$ + $26B_u$ modes.

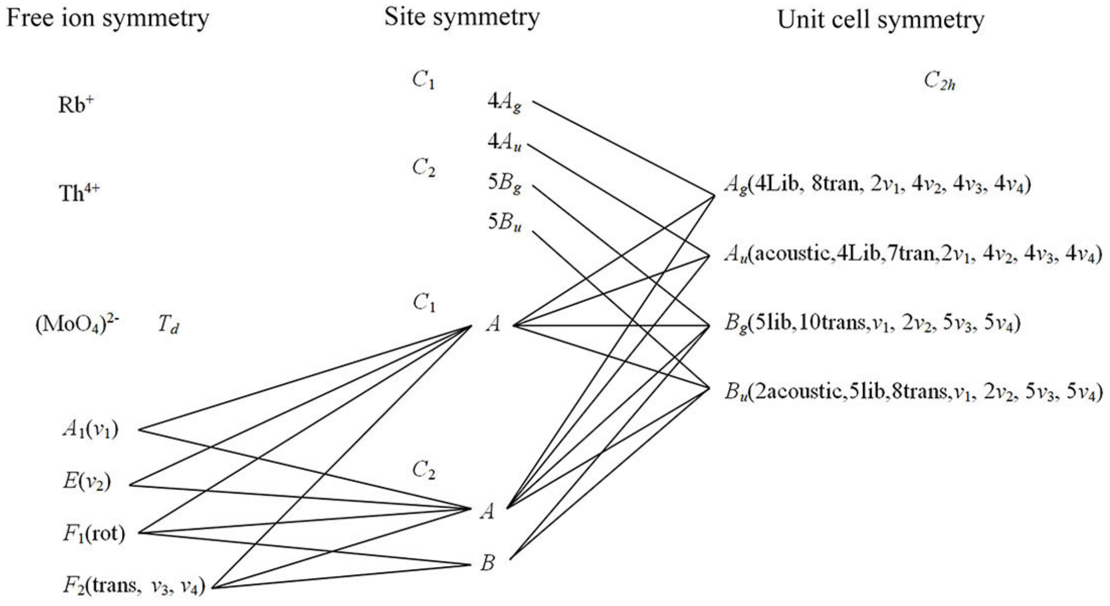

Figure 4.9: Correlation of the vibrational modes of $Rb_2Th(MoO_4)_3$.

$Rb_8Th(MoO_4)_6$ has also two formula units (N = 2×39 = 78 atoms) in a primitive cell resulting in 234 vibrational modes: $57A_g$ + $57A_u$ + $60B_g$ + $60B_u$. Each MoO_4^{2-} on $8f$ site contributes 36 internal modes, that is, symmetric stretching $4\nu_1$ (A_g + A_u + B_g + B_u) and anti-symmetric stretching $12\nu_3$ ($3A_g$ + $3A_u$ + $3B_g$ + $3B_u$) as well as symmetric bending $8\nu_2$ ($2A_g$ + $2A_u$ + $2B_g$ + $2B_u$) and anti-symmetric bending $12\nu_4$ ($3A_g$ + $3A_u$ + $3B_g$ + $3B_u$). Each primitive unit cell of $Rb_8Th(MoO_4)_6$ contains 3 MoO_4^{2-} tetrahedra hosted in $8f$ sites, leading to 108 internal modes. For $Rb_4Th(MoO_4)_4$, 150 vibrations are distributed among A_u + $2B_u$ acoustic, $8A_g$ + $8A_u$ + $8B_g$ + $8B_u$ stretching, $10A_g$ + $10A_u$ + $10B_g$ + $10B_u$ bending, $13A_g$ + $12A_u$ + $14B_g$ + $12B_u$ translational and $18A_g$ + $18A_u$ + $18B_g$ + $18B_u$ librational modes. The primary difference for $Rb_4Th_5(MoO_4)_{12}$, as stated before, is that one of the Rb(1) ions partially occupied the $8f$ site, with occupancy of 0.5. But here, for the convenience of nuclear-group analysis, one can consider such ion makes full contribution to vibrational modes. The total 420 vibrational modes of $Rb_4Th_5(MoO_4)_{12}$ can be divided into 204 external and 216 internal modes. **Figure 4.10** shows the Raman spectra of $Rb_8Th(MoO_4)_6$, $Rb_2Th(MoO_4)_3$, $Rb_4Th(MoO_4)_4$ and $Rb_4Th_5(MoO_4)_{12}$. All the vibrational wavenumbers measured are located below 1050 cm^{-1}, which is typical for inorganic molybdate compounds.[88] It is obvious to coarsely divide all the spectra into two frequency parts; a low frequency part between 100 cm^{-1} and 250 cm^{-1} where the modes are contributed from the vibrations of the "lattice skeleton", and a high-frequency part from 300 cm^{-1} to 1000 cm^{-1}, which are assigned to the internal motions of MoO_4^{2-}.

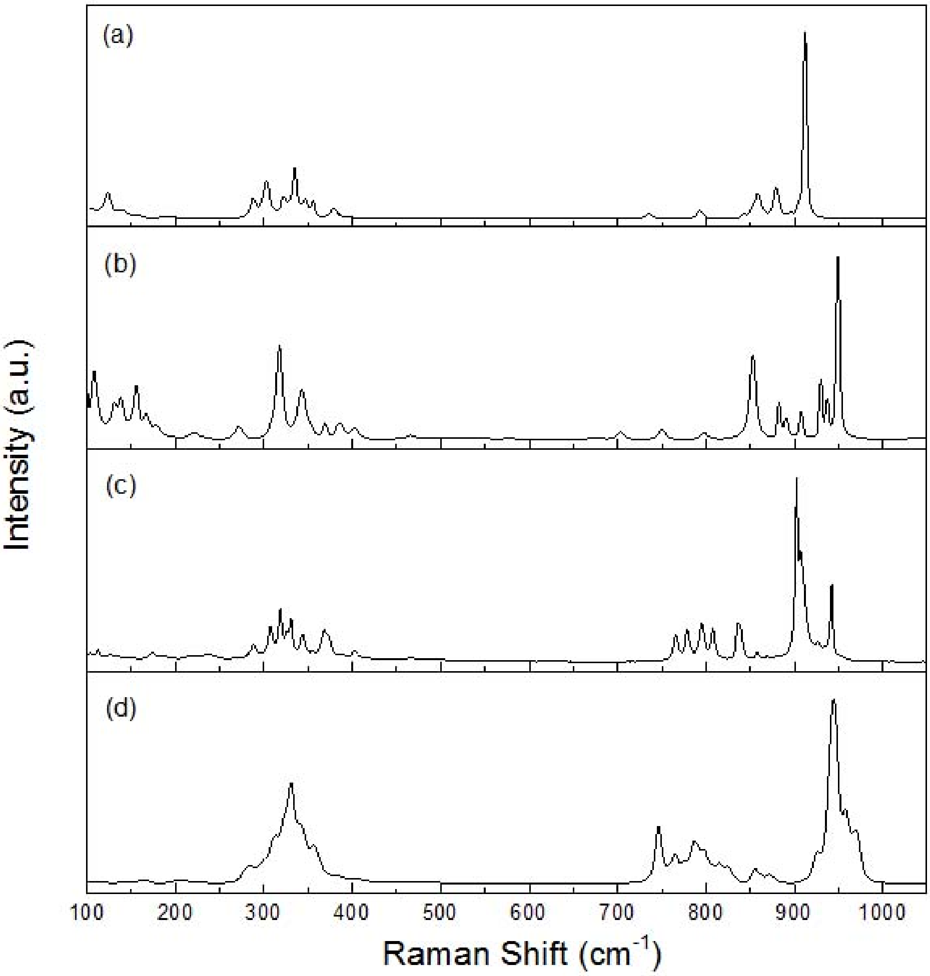

Figure 4.10: Raman spectra of (a): $Rb_8Th(MoO_4)_6$, (b): $Rb_2Th(MoO_4)_3$, (c): $Rb_4Th(MoO_4)_4$, (d): $Rb_4Th_5(MoO_4)_{12}$ measured from 100 to 1050 cm^{-1}.

The peaks of the four compounds, in this range, are predominantly attributed to motions of MoO_4^{2-}, displaying three band parts which are centered around 940 cm^{-1}, 820 cm^{-1} and 420 cm^{-1} and corresponding to ν_1, ν_3 and $\nu_2 + \nu_4$ modes of MoO_4^{2-}. Because $Rb_4Th_5(MoO_4)_{12}$ has the most vibrational modes, its infrared spectrum is less well resolved which lead the spectrum to be broad. As noted above, each structure is based upon the similar ThO_8 square anti-prism and MoO_4 tetrahedral units, and because of the flexibility of Th-O-Mo connection, ThO_8 and MoO_4 fundamentals can combine in differ-

---

[88] S. A. Klimin et al. *Phys. Rev. B*, **68**: 174408–, 2003.

ent ways to exhibit various structural forms. However, obviously, the coordination details of MoO_4 and ThO_8 are distinct in these structural forms. For example, in $Rb_8Th(MoO_4)_6$, the shortest Mo-O distance of 1.739(6) Å is longer than that of any of the other 3 rubidium thorium molybdates, such as 1.716(3) Å in $Rb_4Th(MoO_4)_4$, 1.705(4) Å in $Rb_2Th(MoO_4)_3$, and 1.674(8) Å in $Rb_4Th_5(MoO_4)_{12}$. This means that the MoO_4 tetrahedra are distorted lightest in $Rb_8Th(MoO_4)_6$ and highest in $Rb_4Th_5(MoO_4)_{12}$. This trend is consistent with the equation reported by *Hardcastle* and *Wachs*[89]

$$R_{Mo-O} = 0.48239ln(32895/\nu_1), \tag{4.2}$$

where the Mo-O bond length (R) could be calculated as a function of the ν_1. From the Raman spectra, the symmetric stretching modes ν_1 of $Rb_8Th(MoO_4)_6$ appear at lower wavenumbers, namely, 880912 cm^{-1} compared to that in $Rb_2Th(MoO_4)_3$ (883949 cm^{-1}), in $Rb_4Th(MoO_4)_4$ (881951 cm^{-1}), and in $Rb_4Th_5(MoO_4)_{12}$ (888984 cm^{-1}). Using the ν_1 values 4 (912(2) cm^{-1}, 949(2) cm^{-1}, 951(2) cm^{-1}, and 984(2) cm^{-1} for $Rb_8Th(MoO_4)_6$, $Rb_2Th(MoO_4)_3$, $Rb_4Th(MoO_4)_4$, and $Rb_4Th_5(MoO_4)_{12}$, respectively), the MoO bond length can be calculated to be 1.730(1) Å, 1.710(1) Å, 1.709(1) Å and 1.693(1) Å, respectively, which is in agreement with the structure resolution results. As a consequence, one may conclude that the lower wavenumber for stretching modes ν_1, the longer is the distance for the shortest Mo-O bond, and the more regular is the MoO_4 tetrahedron.

4.1.3 Thermal properties and phase transitions

The thermal behavior of as-prepared pure phases obtained by TG-DSC on heat flow with temperatures between 30 °C and 1250 °C is shown in **Figure 4.11**. The peak located at 725.1(3) °C symbolizes the melting point of $Rb_8Th(MoO_4)_6$. A small endothermic peak detected at 484.6(7) °C can be attributed to impurities in $Rb_8Th(MoO_4)_6$ as these samples always show very small amount ($\approx 5\,\%$ of total weight) of $Rb_4Th(MoO_4)_4$ during the powder synthesis. This endothermic peak becomes obvious in the DSC of $Rb_4Th(MoO_4)_4$. Three endothermic peaks of $Rb_2Th(MoO_4)_3$ were obtained during heating, with the onset points start at 555.1(3) °C, 719.7(4) °C and 773.7(7) °C, respectively. The highest peak corresponds to the solid-liquid transformation and the following one, which shifts about 60 °C with regard to the corresponding endothermic peak, means the ending of the melting, with all the material becoming liquid. The most interesting behavior for $Rb_2Th(MoO_4)_3$ is the first endothermic event, because there is no obvious variation of weight loss and it is reasonable to assume that the first peak results from the solid-solid phase transition of the $Rb_2Th(MoO_4)_3$ phase. $Rb_4Th(MoO_4)_4$ shows a incongruent melting starting at around 666.0 °C with maximum heat flow at 705.5(8) °C. In addition, a potential solid phase transition feature is noticed at 485.6(7) °C. The board endothermic behavior from 715(7) °C to 1210(6) °C may be attributed to the sample decomposition. For $Rb_4Th_5(MoO_4)_{12}$, a single sharp endothermic peak is located at 835.9(8) °C, which relates to the melting point of this phase. Similar to $Rb_2Th(MoO_4)_3$ it is also evident to find the solid-liquid finishing point for

---

[89] Franklin D. Hardcastle and Israel E. Wachs. *J. Raman Spectrosc.*, **21**: 683–691, 1990.

$Rb_4Th_5(MoO_4)_{12}$, although the ending point of $Rb_4Th_5(MoO_4)_{12}$ is a little higher (960.9(8) °C). The TG curve indicates the melting product of $Rb_4Th_5(MoO_4)_{12}$ begins to evaporate at 1195.9(6) °C.

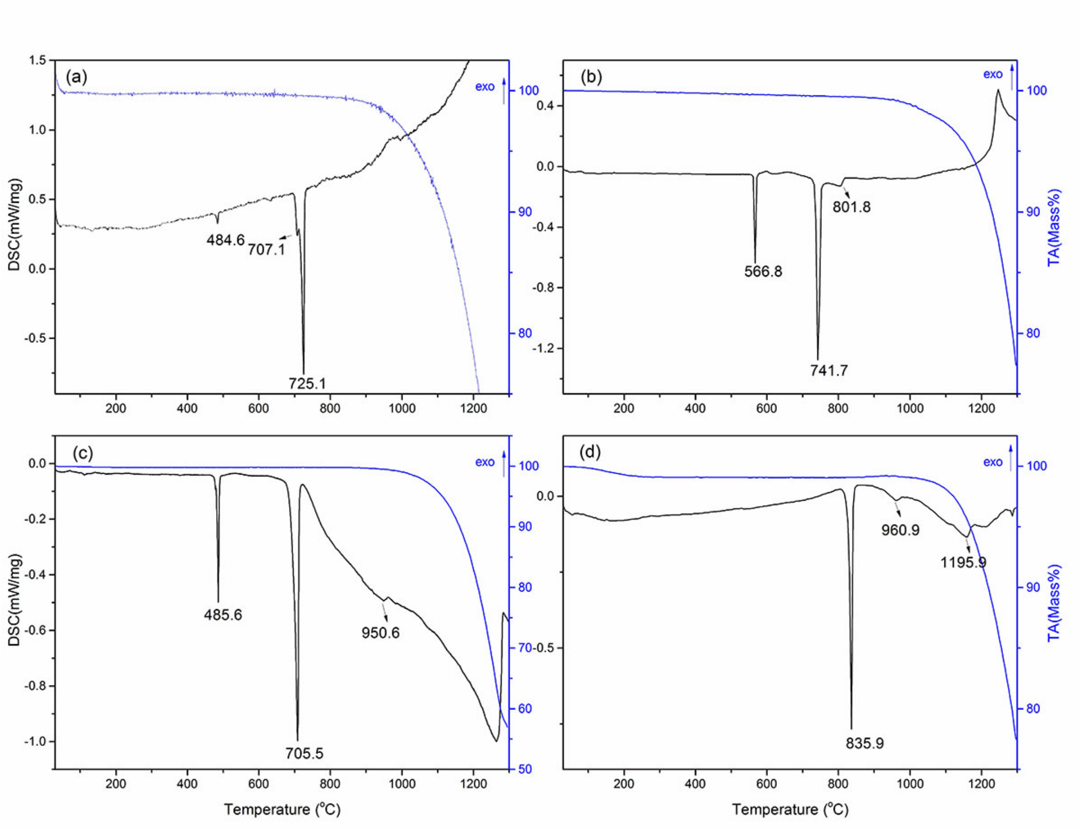

Figure 4.11: DSC (black) and TG (blue) curves of (a): $Rb_8Th(MoO_4)_6$, (b): $Rb_2Th(MoO_4)_3$, (c): $Rb_4Th(MoO_4)_4$, (d): $Rb_4Th_5(MoO_4)_{12}$ measured from 100 to 1050 cm^{-1}.

High-temperature powder diffraction

In addition to the temperature-dependent behavior of the samples investigated using TG-DSC analyses, high-temperature X-ray powder diffraction was used to further confirm the assumption of phase transition behavior of $Rb_2Th(MoO_4)_3$ and $Rb_4Th(MoO_4)_4$. The thermal volume expansion behavior was calculated (**Figure 4.12**) using the extended metric expression taking the quasi-harmonic Debye UDi, the harmonic Einstein U_{Ei} and the anharmonic internal energy U_A contribution into account. During the refinement the U_{D2}, U_{E2} and U_A contribution was found to be zero. For $Rb_2Th(MoO_4)_3$, V_0 = 1170.0(1) Å^3, k_{D1} = 1069(19) 10^{-14} Å^{3}K^{-1}, θ_{D1} = 419(7) K, K_{E1} = 1872(33) 10^{-14} Å^{3}K^{-1} and θ_{E1} = 706(13) K were found. For $Rb_4Th(MoO_4)_4$ the same calculations were carried out to V_0 = 1931(10) Å^3, k_{D1} = 1699(187) 10^{-14} Å^{3}K^{-1}, θ_{D1} = 600(66) K, K_{E1} = 4544(499) 10^{-14} Å^{3}K^{-1} and θ_{E1} = 1066(117) K. As could be seen from the standard deviations as well as in **Figure 4.12** the model describes only slightly the temperature-dependent behavior of this compound up to about 277 °C (550 K). Therefore the calculated energy contributions should not be further used to calculate the internal energy. Nevertheless, the deviations from this equation as well as from the anisotropy of the thermal expansion coefficient (**TEC**) which was calculated using the internal energy equation clearly show the dynamic of both phases. In $Rb_2Th(MoO_4)_3$ the TEC anisotropy factor (**Figure 4.12**) stays constant around $50(2)\times10^{-6}K^{-1}$ followed by an unsteady step beginning around 767 K, showing the maximum slope at 840 K (which corresponds well with the signal maximum of 567 °C in the DSC) and to come back to $52(2)\times10^{-6}K^{-1}$. This is a clear indication for a structural change of $Rb_2Th(MoO_4)_3$ in this temperature range. Comparing the room-temperature pattern before and after the heating cycle up to 650 °C in $Rb_2Th(MoO_4)_3$ only a few very weak reflections disappear which might be explainable by minor impurities. At the highest measured temperature slight changes in the intensities of the reflections are visible compared to the room-temperature pattern which might serve as a hint for a displacive phase transition. Nevertheless, the changes are small and within a few standard deviations no significant deviations could be calculated from the recorded powder data.

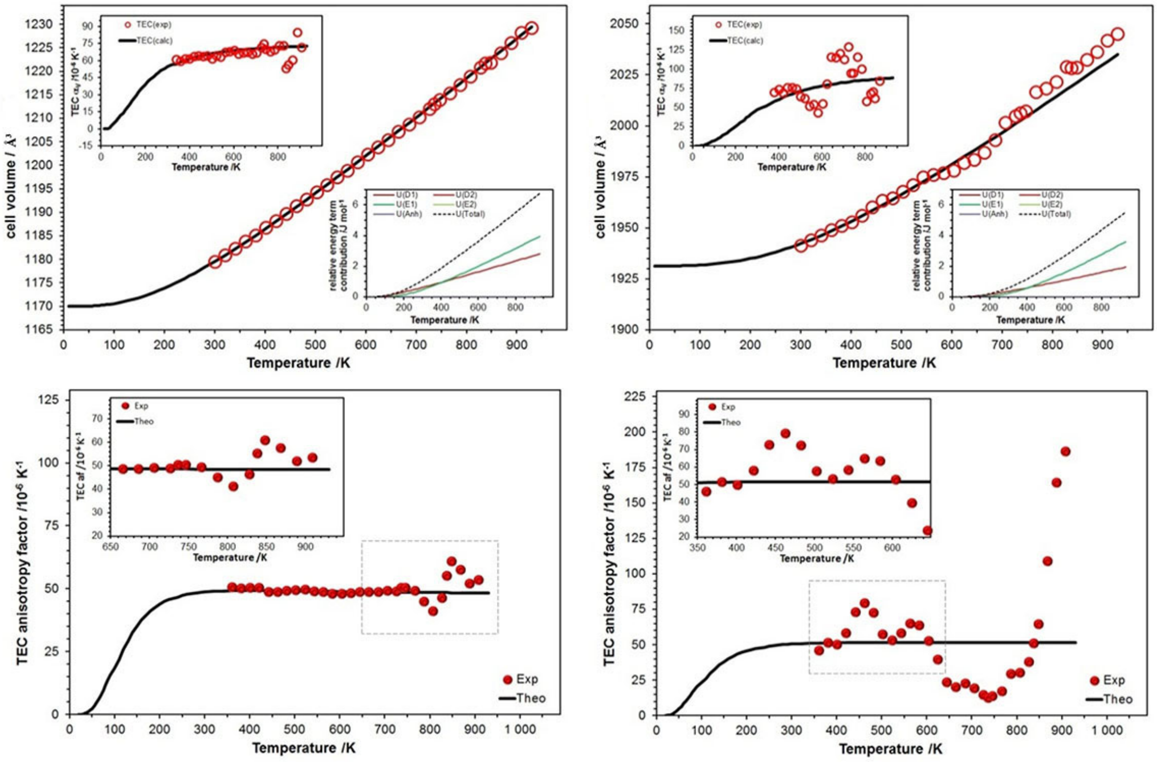

Figure 4.12: Temperature-dependent evolution of the unit cell-volume (upper row) of $Rb_2Th(MoO_4)_3$ (left) and $Rb_4Th(MoO_4)_4$(right). The top left inserts show the respective change of the thermal expansion coefficient (TEC), the bottom right one the expansion energy of the respective phonon contributions. In the lower part the anisotropy of the thermal expansion coefficients is given. The black lines correspond to the calculated values using a DE model.

In $Rb_4Th(MoO_4)_4$ the TEC anisotropy behavior is much more pronounced (**Figure 4.12**). For this compound small deviations are seen between 400 K and 600 K. For these deviations have no counterpart in the DSC measurements it is not clear if these effects are real and if there is only one or two motions as might be deduced from the inset in the respective figure. On the other hand there is, after a decrease of the TEC anisotropy factor from about $22(2)\times10^{-6}K^{-1}$ to $12(2)$ $10^{-6}K^{-1}$, a rapid increase of these values starting at 760(10) K which is at the same temperature as the endothermic DSC signal maximum at 485.6(3) °C. The increase of the TEC anisotropy factor reaches $186(2)\times10^{-6}$K^{-1} at 910 K which was the highest temperature measured to not destroy the material. Also for $Rb_4Th(MoO_4)_4$ the pattern at room-temperature look (neglecting also here some minor impurities) same before and after the measurement and again the pattern at the highest measured temperature show only small deviations in intensities and no significant deviations could be calculated from the recorded powder data.

4.1.4 Conclusions

Thorium rubidium molybdates adopt different structure types from simple 0D to complex 3D structures with remarkable dimensionality reduction along $[Rb_2MoO_4]_x[Th(MoO_4)_2]_y$ series. Despite this fact Th has only one type of oxygen coordination ThO_8 anti-prism. Detailed spectroscopic analysis demonstrates that structural evolution effects in Raman and IR spectra of titled compounds. DSC shows that two phases $Rb_8Th(MoO_4)_6$ and $Rb_4Th_5(MoO_4)_{12}$ keep the same structure until melting point, respectively. The temperature-dependent X-ray powder diffraction data analysis confirms phase-transitions of $Rb_2Th(MoO_4)_3$ and $Rb_4Th(MoO_4)_4$ corresponding to the endothermic DSC. Nevertheless, the deviations are really small and the high-temperature structures could not be finally evaluated from powder data (which is not surprising due to the large unit-cell volume of each phase).

4.2 Structural complexity observed in cesium thorium molybdate family

Three cesium thorium molybdates $Cs_2Th(MoO_4)_3$, $Cs_2Th_3(MoO_4)_7$ and $Cs_4Th(MoO_4)_4$ were synthesized *via* the high-temperature solid-state method. Structure $Cs_2Th(MoO_4)_3$ is in orthorhombic, Pnnm, containing $[Th(MoO_4)_3]^{2-}$ one-dimensional chains extending along [100] direction. $Cs_2Th_3(MoO_4)_7$ is based on an open framework with large channels resided by Cs^+ ions in [100] direction. It is the first case where thorium atoms coordinate simultaneously in 3 distinct environments, namely, 7-coordinated pentagonal bipyramid, 8-coordinated square anti-prism and 9-coordinated tricapped trigonal prism. The $Cs_4Th(MoO_4)_4$ is monoclinic, built from $[Th(MoO_4)_4]^{4-}$ sheets formed by vertex-sharing of MoO_4 tetrahedra and ThO_8 anti-prisms. The Raman and IR spectra were carried out and the vibrations related to internal and external Mo-O bonds in $MoO_4{}^{2-}$ coordination geometry are discussed.

The crystals of Cs-Th-Mo family in this chapter were prepared by solid-state reaction method using the A. R. grade chemicals of $Th(NO_3)_4\cdot5\,H_2O$ (Merck), $CsNO_3$ (Alfa-Aesar) and MoO_3 (Alfa-Aesar) without further purification. Th used in this study belongs to α emitting radioisotope and thus standard precautions for handling radioactive materials should be strictly obeyed at all times. 10 different Th:

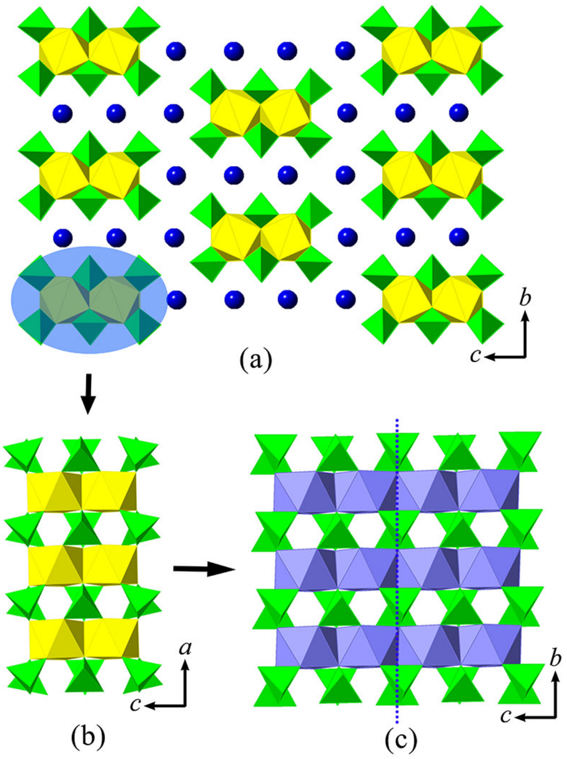

Figure 4.13: (a) Projection of the structure of $Cs_2Th(MoO_4)_3$ perpendicular to [100] direction. (b) one-dimensional chain of $[Th(MoO_4)_3]^{2-}$ extends along [100] direction. (c) The two-dimensional sheets in the $CsLn(MoO_4)_2$ (Ln = Dy, Pr). The chains in $Cs_2Th(MoO_4)_3$ can be seen as the fundamental building unit to form this two-dimensional sheet. (The yellow and light blue polyhedra stand for Th, green polyhedral means Mo and blue circles symbolize Cs atoms.)

Cs: Mo ratios were carefully ground and loaded into platinum crucibles. The mixtures were heated initially at 1050 °C in air for 5 hour in order to get melt homogeneously, then cooled down to 400 °C at the rate of 5 °C/h followed by quenching. Crystals in the form of blocks were found in each reaction after turning off the furnace. The products of $Cs_2Th(MoO_4)_3$ occurs in the ratio of 1:1:2, 1:2:2, 1:2:4 and 1:2:5. $Cs_2Th_3(MoO_4)_7$ and $Cs_4Th(MoO_4)_4$ can be found and easily isolated in 1:1:5 and 1:4:5, respectively.

4.2.1 Crystal chemistry of cesium thorium molybdate family

$Cs_2Th(MoO_4)_3$ The crystal structure of $Cs_2Th(MoO_4)_3$ was solved and refined in the $Pnnm$ space group (No. 58). It is based on $[Th(MoO_4)_3]^{2-}$ one-dimensional chains propagating parallel to [100] direction which are held together by interleaving Cs^+ ions, as depicted in **Figure 4.13 (a, b)**. In chains, the Th(1) atoms experience anti-prism geometry configuration deriving from coordinating to eight O atoms. Linkages of two Th anti-prisms *via* sharing edges lead to Th-Th dimers which are then interconnected through two symmetrically distinct $Mo(1)O_4$ and $Mo(2)O_4$ tetrahedra, with tridentate- and bidentate-bridging behavior, respectively. In both cases, the Mo-O bond lengths with the bridging oxygen atoms (1.79(1) Å–1.84(1) Å) are significantly longer than those with the terminal oxygen atoms (1.70(2) Å–1.73(1) Å). The O-Mo-O angles are all nearly to the expected tetrahedral values, with the minimum 102.8(7)° existing in O(2)-Mo(1)-O(2) and maximum 115.7(5)° in O(3)-Mo(2)-O(5). The Th-O average length, 2.42 Å, is consistent with the mean distance described for

8-coordinated thorium in oxygen surroundings.[90]

The one-dimensional chains in the structure of $Cs_2Th(MoO_4)_3$ can be seen as a fundamental structure building unit happened in many lanthanum-containing molybdate compounds. For instance, it is strongly related to the sheets observed in $CsLn(MoO_4)_2$ (Ln = Dy, Pr).[91] From **Figure 4.13 (b, c)**, one can see that the sheets of lanthanum molybdates in the latter structure can be obtained by simply fusing the respective chains along [001] direction. It is noteworthy to see that the formation of $[Th(MoO_4)_3]^{2-}$ chains in $Cs_2Th(MoO_4)_3$ is reminiscent of those found in $K_2Th(MoO_4)_3$, a superstructure deriving from scheelite structure $CaWO_4$ by replacing divalent Ca^{2+} sites simultaneously by monovalent K^+ and tetravalent Th^{4+} cations. The topological similarities of polyhedral linkages within $Cs_2Th(MoO_4)_3$ and scheelite-related $K_2Th(MoO_4)_3$ can be better depicted if using the black and white node representation. Within this approach, as seen in the **Figure 4.14**, black and white nodes stand for ThO_8 anti-prisms and MoO_4 tetrahedra, respectively. Nodes in the graph are linked by a line segment if the corresponding polyhedra share at least one common vertex. The double bonds indicate an edge-sharing behavior between two coordination polyhedra. From the construction point of view, both structures themselves are built upon analogous assemblage of $[Th_2Mo_{12}]$ dimers (The idealized version is shown in **Figure 4.14 (a)**). Nevertheless, the linking topology of adjacent dimers is different. Unlike the structure of $Cs_2Th(MoO_4)_3$ in which the neighboring dimers are connected solely by MoO_4 tetrahedra (**Figure 4.14 (b)**), the same dimers are united also through edge-sharing of Th within $K_2Th(MoO_4)_3$ (highlighted in **Figure 4.14 (c)**). The characteristic of linkage by common edges in $K_2Th(MoO_4)_3$ results in corrugated Th chains with denser configuration, which may be detected in the slightly higher density in $K_2Th(MoO_4)_3$ (4.74(1) g/cm^{-1}) compared to 4.73(1) g/cm^{-1} in $Cs_2Th(MoO_4)_3$ in spite of containing lighter alkaline cations in the former structure.

$Cs_2Th_3(MoO_4)_7$ The compound of $Cs_2Th_3(MoO_4)_7$ crystalizes in a novel 3D structure type in the triclinic space group $P1$. It is has an exceptionally complex composition with asymmetric units containing 12 symmetrically different Th sites as well as 28 unique Mo sites. To the best of knowledge, this is the first occurrence of thorium inorganic compound where Th atoms have three distinct coordination geometry patterns. The presence of ThO_7 for Th(1), Th(2), Th(3), Th(4) in this compound gives rise to the case of a quite unusual ThO_7 polyhedral geometry, because thorium atoms normally form eight-fold (65 %) or higher coordination number (9-12: 32 %). The coordination environment of all Th atoms is shown in **Figure 4.15**. The ThO_7 can be described as a highly distorted pentagonal bipyramid with bond lengths ranging from 2.270(7) Å to 2.426(5) Å. In contrast, Th(5), Th(6), Th(7), Th(8) exist as more frequently observed ThO_8 square anti-prisms. Up to now, except for trigonal-$Th(MoO_4)_2$ which contains thorium in ThO_6 and ThO_9 coordination environment, ThO_8 square anti-prism is the only thorium configuration for all other thorium molybdates in literature. The third thorium coordination is distorted ThO_9 tricapped trigonal prisms. Again, ThO_9 is also a common thorium polyhedral formation happened in a large number of thorium chalcogenides, such as tel-

---

[90] Miguel A. Salvad et al. *Inorg. Chem.*, **44**: 3512–3517, 2005.

[91] Olga D. Chimitova et al. *Proc. SPIE*, **8771**: 87711A–87711A–9, 2013.

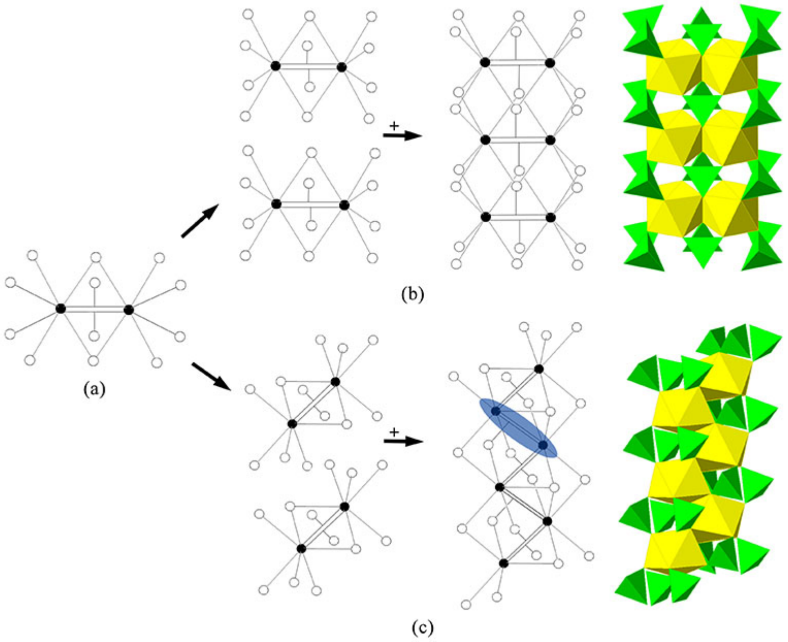

Figure 4.14: The chains in structure of $Cs_2Th_3(MoO_4)_7$ and $K_2Th(MoO_4)_3$ are derived from the same assemblage of $[Th_2Mo_{12}]$ dimers. (a) The $[Th_2Mo_{12}]$ dimers. (b) The topological connection procedure of $[Th_2Mo_{12}]$ dimers to chain structure of $Cs_2Th_3(MoO_4)_7$. (c) The topological connection procedure of $[Th_2Mo_{12}]$ dimers to chains in $K_2Th(MoO_4)_3$. Note that the dimers are also linked by edge sharing of Th polyhedra, as highlighted in the figure.

lurium ($Th(VO_2)_2(TeO_6)$[92]), chromium ($Th(CrO_4)(IO_3)_2$)[35], and selenium ($Th(SeO_3)(SeO_4)$[35]). The Th-O bond distances in ThO_9 anti-prism range from 2.300(6) Å to 2.631(6) Å which is less uniform compared to those in ThO_7 but analogous well with those in ThO_8 (between 2.343(6) Å and 2.614(6) Å). In all cases, each thorium polyhedron shares all its vertexes with adjacent MoO_4 tetrahedra groups to form the framework structure.

The thorium molybdate framework with corner-sharing coordination in $Cs_2Th_3(MoO_4)_7$ is shown in **Figure 4.16 (a)**. This structure can be described as being based upon the fundamental building block of infinite channels which have elliptic-shaped cross-sections, measuring as 9.26(5) Å × 2.89(5) Å, and are situated parallel to crystallographic $\boldsymbol{a}$-axis and are encapsulated by Cs^+ ions. For better interpreting the composition of these channels, here they are cut into 2D sheets. As can be seen from **Figure 4.16 (b)**, the sheets are constructed from successive connection of three types of Th polyhedral building chains (ThO_7, ThO_8, ThO_9) in the sequence of ThO_7 - ThO_9 - ThO_8 - ThO_7 - ThO_8 - ThO_9. Note that the connection sequence occurs without periodicity, that is, the connection environment around each chain type is totally different. This is also the reason that the structure of $Cs_2Th_3(MoO_4)_7$ cannot be solved in centrosymmetric space group. The Th polyhedra in chains of

---

[92] T. A. Sullens and T. E. Albrecht-Schmitt. *Inorg. Chem.*, **44**: 2282–2286, 2005.

[35] Tyler A. Sullens et al. *J. Solid State Chem.*, **179**: 1192–1201, 2006.

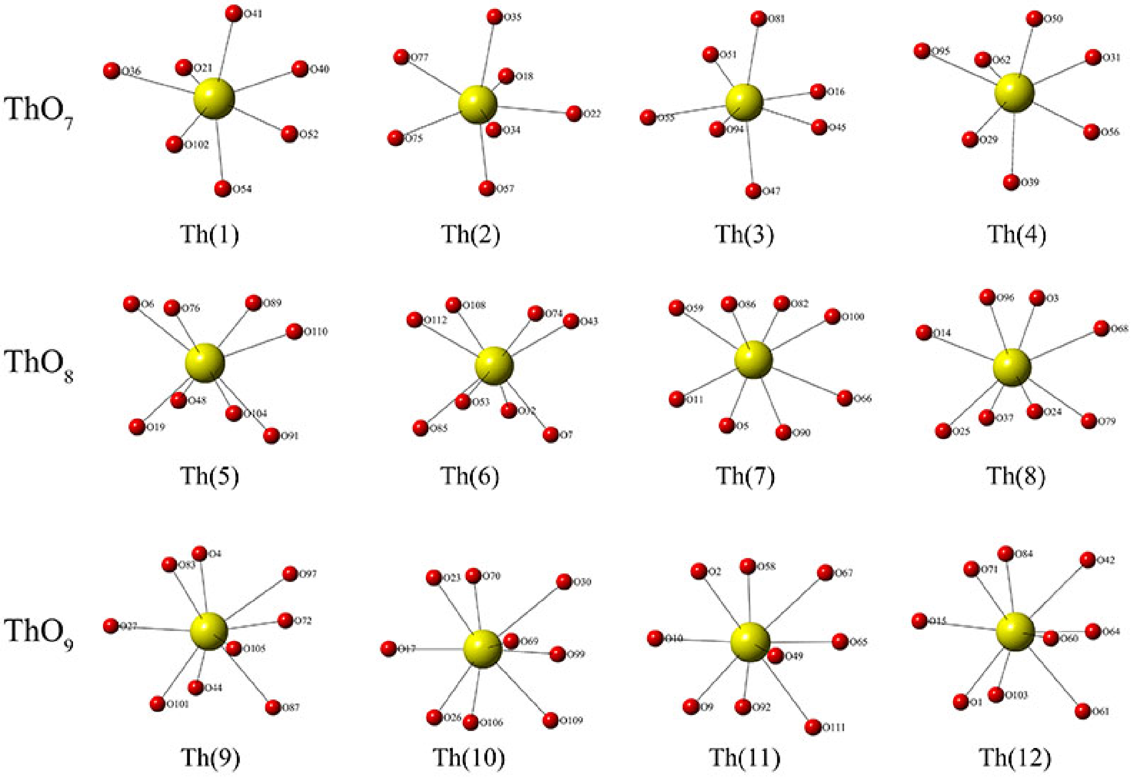

Figure 4.15: Coordination environments of ThO_7 pentagonal anti-prisms, ThO_8 square anti-prisms and ThO_9 tricapped trigonal prisms in the structure of $Cs_2Th_3(MoO_4)_7$

ThO_7 and ThO_8 are linked by bidentated MoO_4 tetrahedra, whereas, in the chains of ThO_9, adjacent ThO_9 tricapped trigonal prisms share three MoO_4 tetrahedra. As a consequence, the Th polyhedra in the ThO_9 chains are linked more tightly than those in other two chains, which can be manifested by the shorter Th-Th distance in ThO_9 chains (average 6.226 Å) compared to 6.301 Å in ThO_7 and 6.227 Å in ThO_8. These ThOx (x = 7, 8, 9) chains are further fused together by corner-sharing additional MoO_4 tetrahedra, and receive rather bent linkage conformation, as one can imagine, that finally leads to closed cylinders.

Cutting the channels into sheet can give detailed demonstration of variant Th polyhedral geometries inside the channels, it however, not enough to recognize the Th-Mo polyhedral junctions around the one-dimensional cylinders. Herein, in order to understand the interior structure of framework channels, the method of tubular units is adopted here to describe the topology of channel network. This method has been widely used to demonstrate the tubular units formed in inorganic compounds, such as uranyl selenate tubules $[(UO_2)_3(SeO_4)_5]^{4-}$. The topological net of channels is shown in **Figure 4.16 (c)**. It is assembled solely from 6-menbered rings. All black (Th) and white (Mo) nodes are 3-connected. It can be transformed using idealized unfolding tape of regular honeycomb-shaped hexagons (**Figure 4.16 (d)**) *via* the *folding and gluing* procedure. Firstly, label the equivalent points on sides of the tap by letters a, b, c, d, e, f, g and h. Then fold the tape by jointing the corresponding

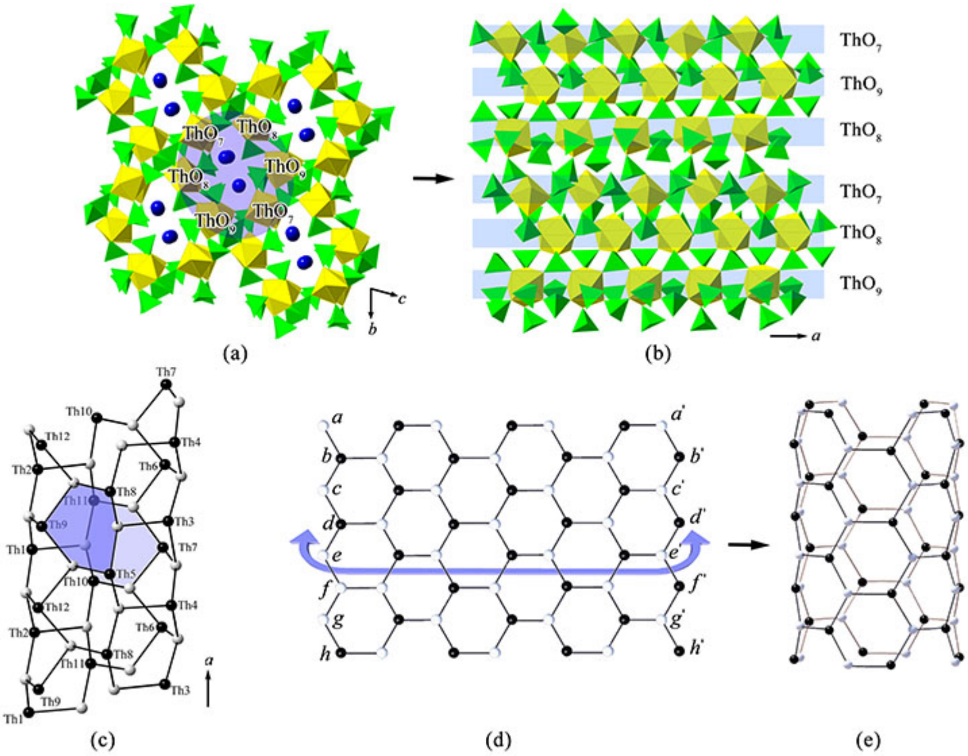

Figure 4.16: (a) Framework structure of $Cs_2Th_3(MoO_4)_7$ with channels propagating along [100] direction. (b) The channels are expanded into 2D sheets. They are built from thorium molybdate polyhedral with Th in the sequence of ThO_7 - ThO_9 - ThO_8 - ThO_7 - ThO_8 - ThO_9. (c) The black and white representation of channels. (d, e) The channels can be transformed from simple 6-membered rings by folding the corresponding latters in the opposite ends.

opposite sides ($a-a'$, $b-b'$, $c-c'$, $d-d'$, $e-e'$, $f-f'$, $g-g'$ and $h-h'$) to make a cylinder. The idealized topological structure for the tubular unit in $Cs_2Th_3(MoO_4)_7$ is shown in **Figure 4.16 (e)**.

$Cs_4Th(MoO_4)_4$ $Cs_4Th(MoO_4)_4$ was first investigated by *Bushuev, et al.* in 1975. By analyzing powder X-ray diffraction patterns, they obtained only 3 crystallographic axes (***a*** = ***b***= 6.627 Å, ***c*** = 12.682 Å) but gave no other lattice information. Recently, based on this inadequate crystallographic data, *Keskar, et al.*, has concluded that the lattice system of $Cs_4Th(MoO_4)_4$ is hexagonal. However, By means of single crystal X-ray diffraction and symmetry analysis, I found that $Cs_4Th(MoO_4)_4$ crystallized in monoclinic system with $P2/c$ space group and β = 90.146(6) Å. This structure built from sheets of composition $[Th(MoO_4)_4]^{4-}$ composed of ThO_8 anti-prisms and MoO_4 tetrahedra (see **Figure 4.17**). It is isostructural with $Rb_4Th(MoO_4)_4$. However, because of the larger ionic radius of the Cs^+ cations between the $[Th(MoO_4)_4]^{4-}$ sheets in comparison to that of Rb^+ cations, 1.74 Å for Cs and 1.61 Å for Rb, respectively,[93] the interlayer distance is larger for $Cs_4Th(MoO_4)_4$ (12.69(5) Å) than that for $Rb_4Th(MoO_4)_4$ (12.29(5) Å). Both compounds can be seen as deriving from fundamental building chains $[Th(MoO_4)_4]^{4-}$. The three-dimensional framework compounds $A_4Th(MoO_4)_4$ (A =

---

[93] R. D. Shannon. *Acta Cryst. A*, **32**: 751–767, 1976.

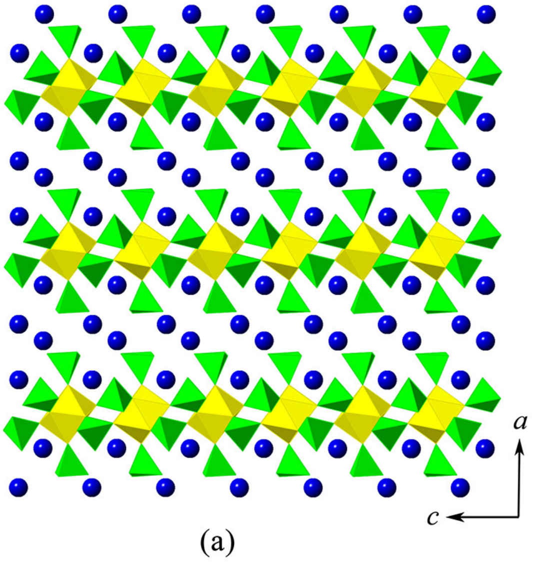

Figure 4.17: The structure of 2D layers in $Cs_4Th(MoO_4)_4$. Legends: The yellow polyhedra stand for Th, green polyhedral means Mo and blue circles symbolize Cs atoms.

Na, K) with similar stoichiometric composition but containing smaller cations can also be described as constructing from similar building chains $[Th(MoO_4)_4]^{4-}$. Different structural dimensionality with similar fundamental building units suggests the flexibility of Th-O-Mo linkages.

4.2.2 Raman spectroscopic analysis

The vibrational data on molybdate units are well-established in a number of literatures.[94,95] Nevertheless, very few vibrational spectra of thorium contained molybdates have been published. As discussed above, the Mo in all 3 thorium molybdates in this work are based on the MoO_4^{2-} group. The ideal MoO_4^{2-} has the T_d symmetry with the 4 normal motions being assigned as $A_1(\nu_1)$; $E(\nu_2)$; F_1(rot), $F_2(trans, \nu_3, \nu_4)$ where A_1, E and F_2 are Raman permitted while F_2 is IR active. The ν_1, ν_2, ν_3 and ν_4 modes are denoted as non-degenerated symmetric stretching, doubly degenerated symmetric bending, triply degenerated asymmetric stretching and asymmetric bending vibrations, respectively. The stretching vibrations of ν_1 and ν_3 in free MoO_4^{2-} are placed in the region of 700 cm^{-1}−1000 cm^{-1}, while the bending vibrations (ν_2 and ν_4) are situated in the scope of 300 cm^{-1}−500 cm^{-1}. When it comes to specific structure, however, due to symmetry alteration the MoO_4^{2-} groups are distorted, thus more than 4 modes will be observed in the spectra. As can be seen in **Figure 4.18**, the spectra for all 3 thorium molybdates, both in Raman and IR, can be grossly separated into two frequency ranges. The first is low frequency region from 100 cm^{-1} to 250 cm^{-1}, where the modes result from the skeletal lattice vibrations. Since the strongly coupling between MoO_4 translations and Cs transitional modes, the modes located in this zone can be assigned as a conjunction of T(MoO_4) + T(Cs). The other is higher frequency region originating from the internal vibrational motions of MoO_4^{2-}

---

[94] G.D. Saraiva et al. *Vib. Spectrosc.*, **58**: 87–94, 2012.

[95] S. P. S. Porto and J. F. Scott. *Phys. Rev.*, **157**: 716–719, 1967.

between 250 cm^{-1} and 915 cm^{-1}.Based on group theoretical principles[96], the standard analysis of the crystal selection rules for vibrational modes and the completed correlational relationships between the mode symmetries for all 3 cesium thorium molybdates are analyzed. Here, one of the example ($Cs_2Th(MoO_4)_3$) is given in **Figure 4.19**.

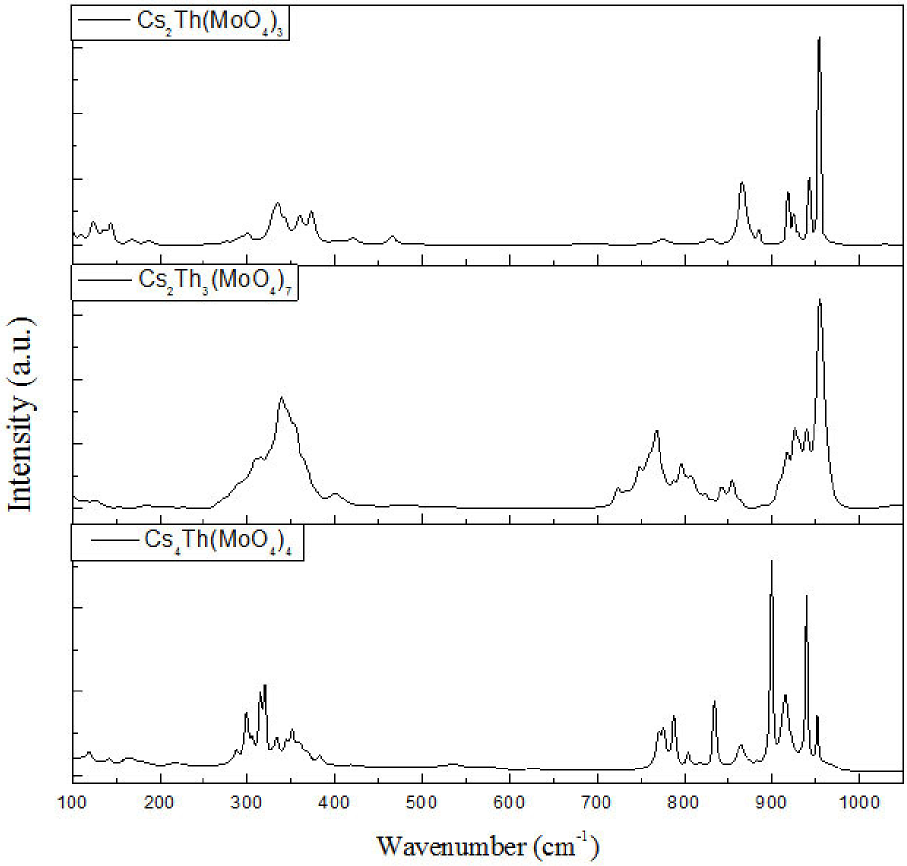

Figure 4.18: The Raman spectra of $Cs_2Th(MoO_4)_3$, $Cs_2Th_3(MoO_4)_7$ and $Cs_4Th(MoO_4)_4$

For the $Cs_2Th(MoO_4)_3$, the unit cell (Z = 4) comprises 8 MoO_4^{2-} groups situating in two systematically non-equivalent sites (C_s, C_i). 2 Th atoms occupy the C_2 sites, and the 4 C_s atoms are located at sites of C_2 symmetry. With the total 72 atoms in the unit cell, the group theory results in 216 zone-center degrees of freedom which are distributed among the irreducible representations as

$$\Gamma(D_{2h}^{12}) = 27A_g + 24A_u + 27B_{1g} + 24B_{1u} + 27B_{1g} + 30B_{2u} + 27B_{3g} + 30B_{3u}, \tag{4.3}$$

This modes can be divided into B_{1u} + B_{2u} + B_{3u} acoustic modes, $7A_g$ + $5A_u$ + $7B_{1g}$ + $5B_{1u}$ + $5B_{1g}$ + $7B_{2u}$ + $5B_{3g}$ + $7B_{3u}$ stretching modes, $8A_g$ + $7A_u$ + $8B_{1g}$ + $7B_{1u}$ + $7B_{1g}$ + $8B_{2u}$ + $7B_{3g}$ + $8B_{3u}$ bending modes, $8A_g$ + $7A_u$ + $8B_{1g}$ + $7B_{1u}$ + $10B_{1g}$ + $11B_{2u}$ + $10B_{3g}$ + $11B_{3u}$ translational modes and $4A_g$ + $5A_u$ + $4B_{1g}$ + $5B_{1u}$ + $6B_{1g}$ + $4B_{2u}$ + $5B_{3g}$ + $4B_{3u}$ librational modes. The A_g,

---

[96] BN Ganguly et al. *Phys. Rev. B*, **13**: 1344, 1976.

B_{1g}, B_{1g} and B_{3g} modes are Raman active while the B_{1u}, B_{2u} and B_{3u} are IR active. The A_u modes are silent. The sharp and intense Raman bands appearing at slightly high frequency, that is to say, 840 cm^{-1}−980 cm^{-1}, strongly indicates that the coordination geometry of Mo atoms in $Cs_2Th(MoO_4)_3$ are in the form of MoO_4^{2-}. The most narrow and intensive peak, at 954 cm^{-1}, should be associated with ν_1 stretching mode MoO_4^{2-}, while the peaks at 829 cm^{-1} and 775 cm^{-1} are considered to be due to the asymmetric stretching vibrations (ν_3) of MoO_4^{2-}. The structure of $Cs_2Th_3(MoO_4)_7$ has a triclinic system with P_1 space group. In this structure, all atoms occupy C_1 sites. Owing to the huge number of atoms in the unit cell and to the comparatively low crystal symmetry, both Raman and IR spectra of $Cs_2Th_3(MoO_4)_7$ are rich in modes. It is noted that the lines in Raman of $Cs_2Th_3(MoO_4)_7$ are not split well. They are broader and cannot be well recognized in comparison with those of other 2 thorium molybdates. This behavior may be result from the existence of strong coupling among MoO_4^{2-} groups in the lattice. The monoclinic $Cs_4Th(MoO_4)_4$ compound crystallizes in a space group $P2/c$ (No. 13), where Th atoms occupy $2f$ sites of C_2 symmetry and Mo are in $4g$ sites of C_1 symmetry. All the O atoms are situated at general positions ($4g$). It has $37A_g$ + $36A_u$ + $38B_g$ + $36B_u$ optical modes and A_u + $2B_u$ acoustic modes. Lattice transitional of the Cs, Th and Mo atoms give rise to $13A_g$ + $13A_u$ + $14B_g$ + $14B_u$ modes. The Raman-active modes of the $Cs_4Th(MoO_4)_4$ occur at the species $37A_g$ + $38B_g$. Because of presence of distorted tetrahedra in the structure of $Cs_4Th(MoO_4)_4$, (Mo-O bond distances are in the range of 1.730(3) Å to 1.838(3) Å), great splitting of ν_1 and ν_3 modes are observed, as shown by the considerable intensity of lines in the spectra. Due to the different chemical bonding configuration of MoO_4^{2-} owing to presence of different cations, the stretching modes for $Cs_4Th(MoO_4)_4$ move toward the high energy side comparing to the Raman spectrum of $Rb_4Th(MoO_4)_4$, but are in agreement with the vibrational data of MoO_4^{2-} in literature.

4.2.3 Conclusions

The thorium-molybdate $[Th(MoO_4)_3]^{2-}$ chains in $Cs_2Th(MoO_4)_3$ are topologically related to those in $K_2Th(MoO_4)_3$, an example of scheelite related CaWO4 structure which is a well-known structure type accommodated by a wide range of inorganic compounds. Compound $Cs_2Th_3(MoO_4)_7$, with 3 different Th polyhedral environment: ThO_7, ThO_8, ThO_9, is by far the most complicated thorium molybdate phase. The channels existing in $Cs_2Th_3(MoO_4)_7$ compound depicted in terms of tubular building units can be topologically transformed by regular honeycomb-shaped hexagons. This section reports the correct structural information of $Cs_4Th(MoO_4)_4$. The analysis of stretching and bending shifts in Raman and IR spectra show that all molybdenum atoms in these three compounds are adopted solely in MoO_4^{2-} tegrahedra geometry.

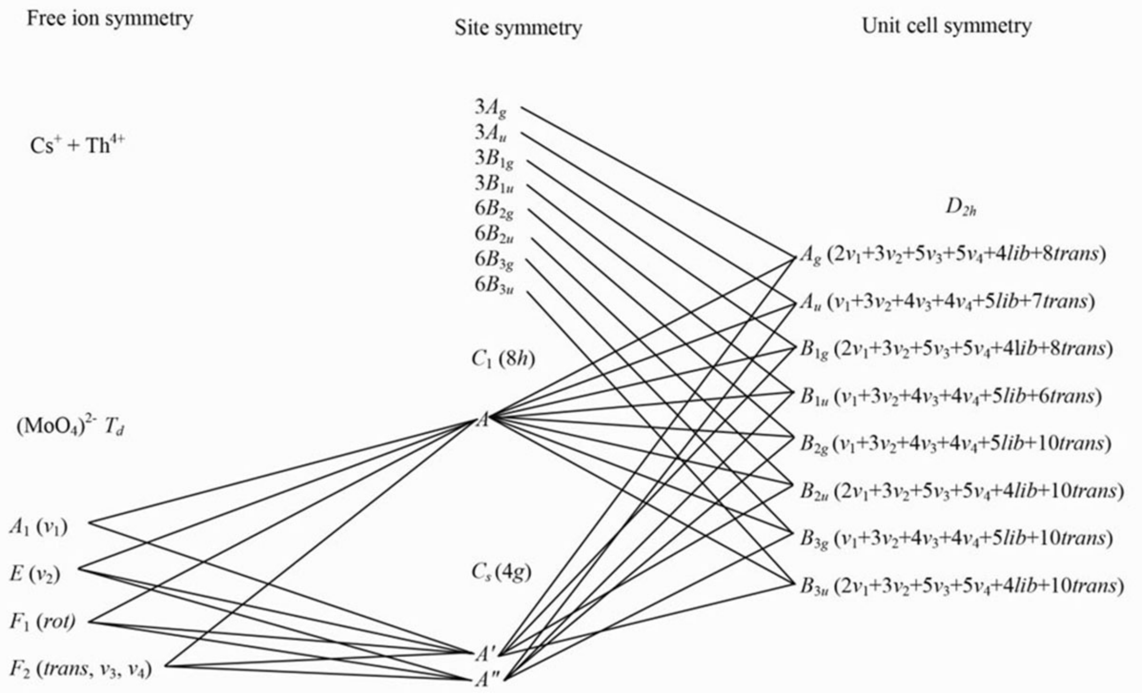

Figure 4.19: The correction relation among different symmetries in internal MoO_4^{2-} units for $Cs_2Th(MoO_4)_3$

4.3 Dinuclear face-sharing bioctahedral tungsten(VI) core in complex Th tungstates

Two new thorium tungstates $A_6Th_6(WO_4)_{14}O$ (A = K and Rb) were synthesized via high-temperature solid-state reactions. $Th(NO_3)_4(H_2O)_5$ (0.1 g), $RbCO_3$ (0.041 g) and WO_3 (0.244 g) were loaded into a platinum crucible after being fully ground in an agate mortar. The crucible was then heated in a furnace (CARBOLITE CWF 1300) for 6 h at 1323 K, and slowly cooled to 1023 K at a rate of 5 K/h followed by quenching. The resulting products consisted of $Rb_6Th_6(WO_4)_{14}O$ crystals and glassy mass were isolated after experiment. The yield cannot be obtained because of the similar morphologies between crystals and glass pieces.The structures of both phases are based on a rare dinuclear confacial bioctahedral $[W_2O_9]^{6+}$ core, encapsulated in a $[Th_6W_7O_{45}(W_2O_9)]^{32-}$ cage showing a cross-section geometry similar to a six-leafed lily. The adjacent cages are connected in two dimensional layers by WO_4 tetrahedral linkers. Due to the dissimilarities in mutual orientations of adjacent layers in these two structures, $K_6Th_6(WO_4)_{14}O$ crystallizes in space group of $R32$ while $Rb_6Th_6(WO_4)_{14}O$ stabilizes in $P\bar{6}2c$. The high-temperature phase transition was observed in $Rb_6Th_6(WO_4)_{14}O$ and investigated using high-temperature PXRD technique. The results demonstrate a very unusual thermal behavior of this compound. The Raman and IR spectra of both phases were analyzed in respect to their complex structures.

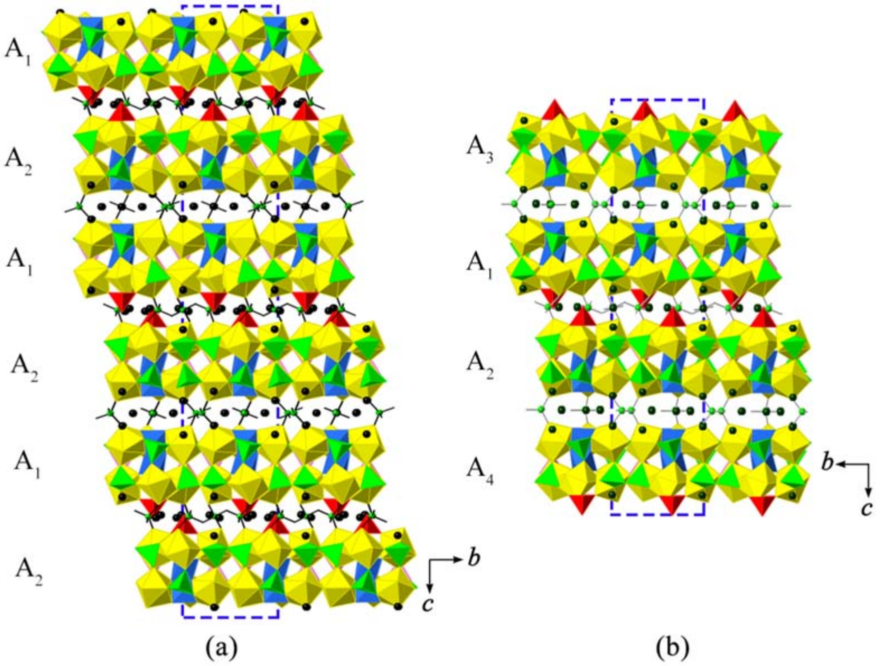

Figure 4.20: View of the layer arrangements between (a) $K_6Th_6(WO_4)_{14}O$ and (b) $Rb_6Th_6(WO_4)_{14}O$. K and Rb cations are in black nodes.

4.3.1 The W_2O_9 core

The structure of $Rb_6Th_6(WO_4)_{14}O$ is highly related to that of $K_6Th_6(WO_4)_{14}O$. Both thorium tungstates are built from Th-W oxo-layers which stack along the crystallographic ***c***-axis, as shown in **Figure 4.20**. The difference between these two structures could be found only in the arrangement of the adjacent layers, which is discussed in detail in **Page 62**. Six ThO_8 square antiprisms and six WO_4 tetrahedra connect in a vertex-sharing manner to compose a barrel-shaped shell of a $[Th_6W_6O_{45}(W_2O_9)]^{36-}$ polyanion (see **Figure 4.21 (a)**). Two WO_6 octahedra, namely W(3) and W(5) sharing a common face to form a dimeric W_2O_9, build a core. This W_2O_9 core is encapsulated into the shell, with its bottom located approximately in the plane composed *via* three Th(1), by attaching three O(13) atoms from three different $Th(2)O_8$ polyhedra of the cage in vertex-sharing manner. Additional three pairs of O(4) and O(5) atoms from the remaining three $Th(1)O_8$ polyhedra in edge-sharing configuration (**Figure 4.21 (b)**) complete the coordination. The Th-O bond distances in described shell range from 2.29(1) to 2.51(1) Å with average value of 2.41(1) Å. This shell is further capped with an apex of a$W(7)O_4$ tetrahedron, result in a $[Th_6W_7O_{46}(W_2O_9)]^{32-}$ polyanion which can be viewed as a fundamental building block (**FBB**), shown in **Figure 4.21 (c)**. In both tungstate structures, the FBB has a lateral size of around 11.8×11.8 Å^2 and a height of about 10.8 Å^2. The FBBs, with a cross-section geometry similar to a six-leafed lily (**Figure 4.21 (d)**), are connected together in two dimensions with a help of $W(1)O_4$ and $W(6)O_4$ linkers (shown in on **Figure 4.21 (e)** in purple). Each linker, in tetrahedral coordination, crosslinks three FBBs in a tridentate way by sharing of three corner oxygen atoms. The resulting 2D layers stack parallel to (001) and are connected by isolated W(8) and W(9) tetrahedral, completing the 3D complexity (see **Figure 4.21 (f)**).

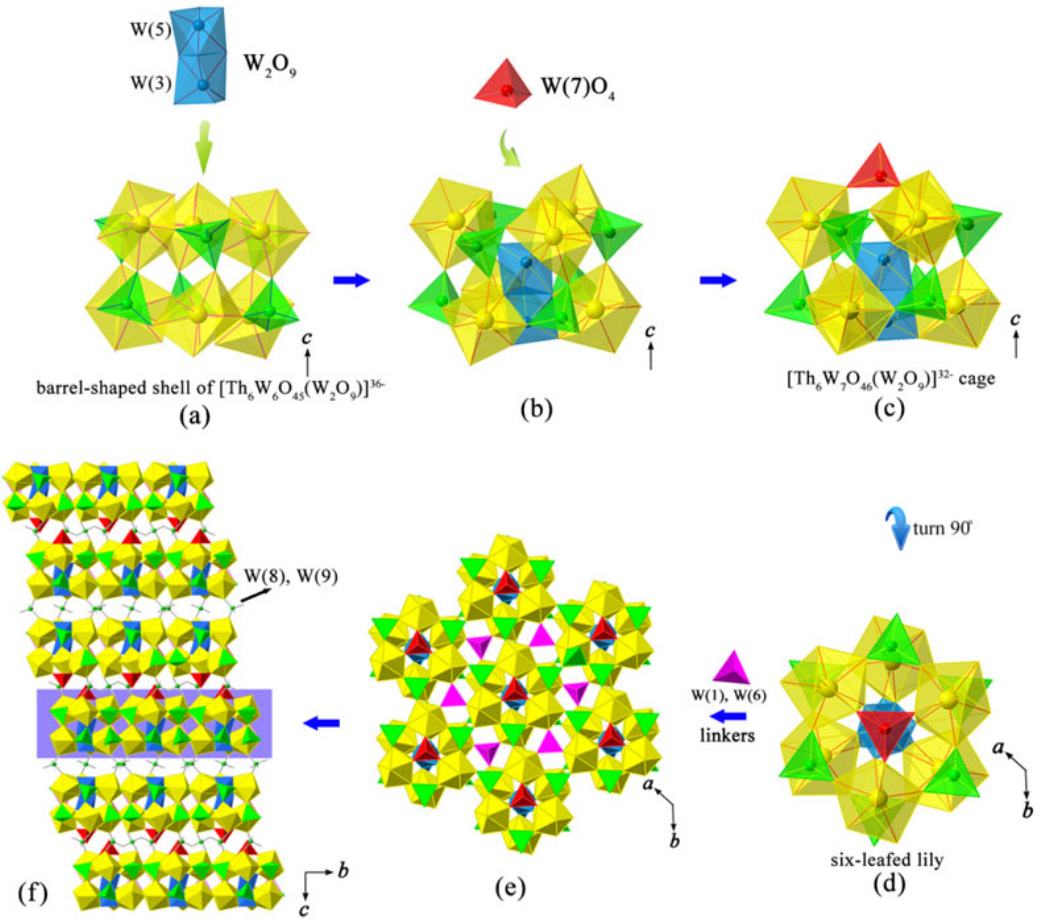

Figure 4.21: A schematic representation of fragments hierarchy in $K_6Th_6(WO_4)_{14}O$. ThO_8 antiprisms are represented in yellow, WO_4 tetrahedra in the barrel-shaped shell are in green, $W(7)O_4$ apexes are coloured in red and WO_4 linkers are in purple. The $[W_2O_9]^{6-}$ confacial cores are in light blue.

One of the emphatic structural features of $A_6Th_6(WO_4)_{14}O$ (A = K, Rb) is the facing-shared octahedral tungsten core W_2O_9 (see **Figure 4.22**). The distance between confacial sharing tungsten atoms is 3.054(2) Å for $K_6Th_6(WO_4)_{14}O$ and 3.031(3) Å for $Rb_6Th_6(WO_4)_{14}O$, respectively, much shorter than that in corner-shared and edge-shared octahedra (around 3.7 Å and 3.4 Å, respectively).[6] The coordination geometries of the $[W_2O_9]^{6-}$ confacial cores are approximately identical for both compounds, except for minor variations in bond lengths and angles. Thus, for the simplicity, only the coordination geometries of $K_6Th_6(WO_4)_{14}O$ are discussed here. Owing to existing a three-fold rotation axis extending through the cage center and therefore through the octahedrally coordinated tungsten atoms, each WO_6 octahedron undergoes a distortion from the regular octahedron as W^{6+} cations move out

---

[6] Peter C Burns. *Can. Mineral.*, **43**: 1839–1894, 2005.

from the octahedral center towards the face formed by three terminal oxygen ligands, thus leading to a C_3 distortion for each octahedra in the $[W_2O_9]^{6-}$ bioctahedral core. Such distortion can be clearly manifested by the geometry of three short W-Oterminal (1.80(2) Å) and three long W-Obridging (2.08(1) Å) bonds distances for WO_6 octahedron (**Figure 4.22 (c)**). Taking additionally the *trans* O-W-O angles into account one can calculate the out-of-center distortion index for each octahedron. They were found to be $0.87(1)\times10^{-10}$ m ($0.85(1)\times10^{-10}$ m for $Rb_6Th_6(WO_4)_{14}O$) for the vertex octahedra where each octahedra oxygen atom is connected to six different ThO_8 polyhedra and $0.98(1)\times10^{-10}$ m ($1.12(1)\times10^{-10}$ m for $Rb_6Th_6(WO_4)_{14}O$) for the octahedra which is connected to three different ThO_8 polyhedra only. This lower number of binding polyhedra increases the distortion in the WO_6 octahedra, which is more pronounced for the rubidium compound. Nevertheless, both out-of-center distortion indices are quite high, comparable to those found in $A_2TeW_3O_{12}$ (A = Na, K) varying between 0.72×10^{-10} m and 1.21×10^{-10} m for C_3 distortions. Also because of the threefold axis, the apical W(7) atom on the top of the cage has one short bond W(7)-O(15) = 1.65(5) Å and three long bonds W(7)-O(16) = 1.77(3) Å for the tetrahedral coordination. For the same reason, a similar bond distribution configuration observed in the tridentate W(1), W(6) linkers, each with one short W-O and three long W-O bond distances (1.70(3) Å and 1.61(9) Å and 1.79(4) Å and 1.71(3) Å for W(1) and W(6), respectively). The W-O bond distances for other tetrahedrally coordinated W cations (W(2), W(4), W(8) and W(9)) are found close to the ideal tetrahedral geometry, varying from 1.73(3) Å to 1.81(2) Å. The Th-O bond lengths, between 2.29(1) Å and 2.51(2) Å, fall in the expected ranges for ThO_8 square antiprismatic geometry.

4.3.2 Structural relationship analysis

As mentioned above, $K_6Th_6(WO_4)_{14}O$ and $Rb_6Th_6(WO_4)_{14}O$ are composed from the same six-leafed lily shaped $[Th_6W_7O_{46}(W_2O_9)]^{32-}$ cage and the coordination geometries for both compounds are also very similar. However, $K_6Th_6(WO_4)_{14}O$ crystallizes in space group $R32$ while $Rb_6Th_6(WO_4)_{14}O$ stabilizes in $P\bar{6}2c$. The difference in symmetry arises from the mutual orientations of adjacent layers in the two structures, as shown in **Figure 4.20**. It is obvious to note that all the layers in both structures are structurally related to each other and can be converted from one into another by simple crystallographic symmetry operations. For the convenience of elucidation, I only extract the unique fragment which can stand for the whole layer features, that is, one $[Th_6W_7O_{46}(W_2O_9)]^{32-}$ cage plus six WO_4 linkers as shown in **Figure 4.23**. The packing sequence of $K_6Th_6(WO_4)_{14}O$ is constructed from only the two different layer types A_1 and A_2 (**Figure 4.20 (a)**). These two layers are quite similar and are related by a two-fold axis in the direction of [010] (**Figure 4.23 (a)**). The two nearest A_1 (or A_2) layers can be converted from one to each other *via* translating along the ***ab*** plane with distances of 1/3***a*** and 2/3***b***. As a consequence, $K_6Th_6(WO_4)_{14}O$ crystallizes in space group $R32$ that contains only rotational symmetry elements. The structural composition for $Rb_6Th_6(WO_4)_{14}O$ is more complex, there are four different layers (A_1, A_2, A_3, A_4). As shown in **Figure 4.23**, the fragments of A_1 and A_2 in $Rb_6Th_6(WO_4)_{14}O$ are equal to those found in $K_6Th_6(WO_4)_{14}O$. A_3 and A_1 layers are enantiomorphic

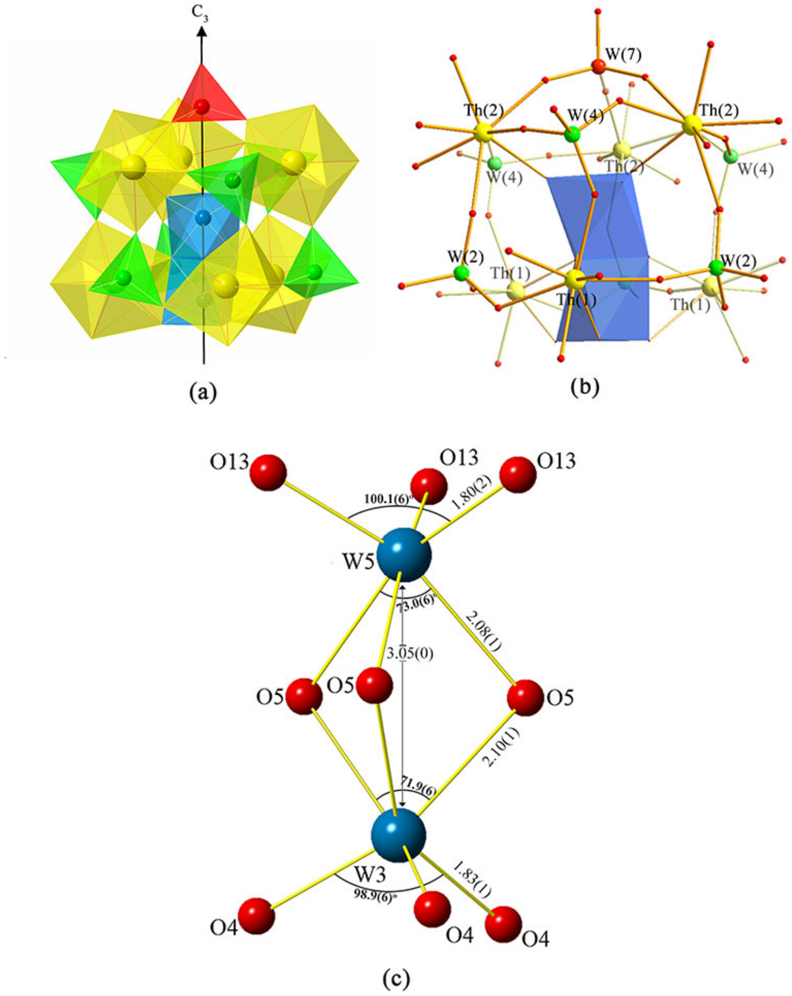

Figure 4.22: Coordination geometry of $[W_2O_9]^{6-}$ core in the crystal of $K_6Th_6(WO_4)_{14}O$.

and can be transformed by a mirror plane perpendicular to the [001] direction. The A_3 and A_2 are also enantiomorphic to each other; however, in this case, the enantiomorphism is related by the mirror parallel to ***b***-axis. The transformation relationship between A_3 and A_4 is the same as the relationship between A_1 and A_2. Rotating the A_3 or A_1 through 180° about an axis pointing to [100] or [010] can bring each layer into agreement with A_4 or A_2, respectively.

4.3.3 Thermal behavior analysis

The thermal behaviors for both thorium tungstates are characterized by DSC/TGA techniques and shown in **Figure 4.24**. The melting for $K_6Th_6(WO_4)_{14}O$ has an onset temperature around 1206 K with the maximum heat flow at 1215(3) K. The DSC curve indicates a clear product melting accompanied with decomposition, that is, incongruent melting, by the presence of a small peak at around 1254

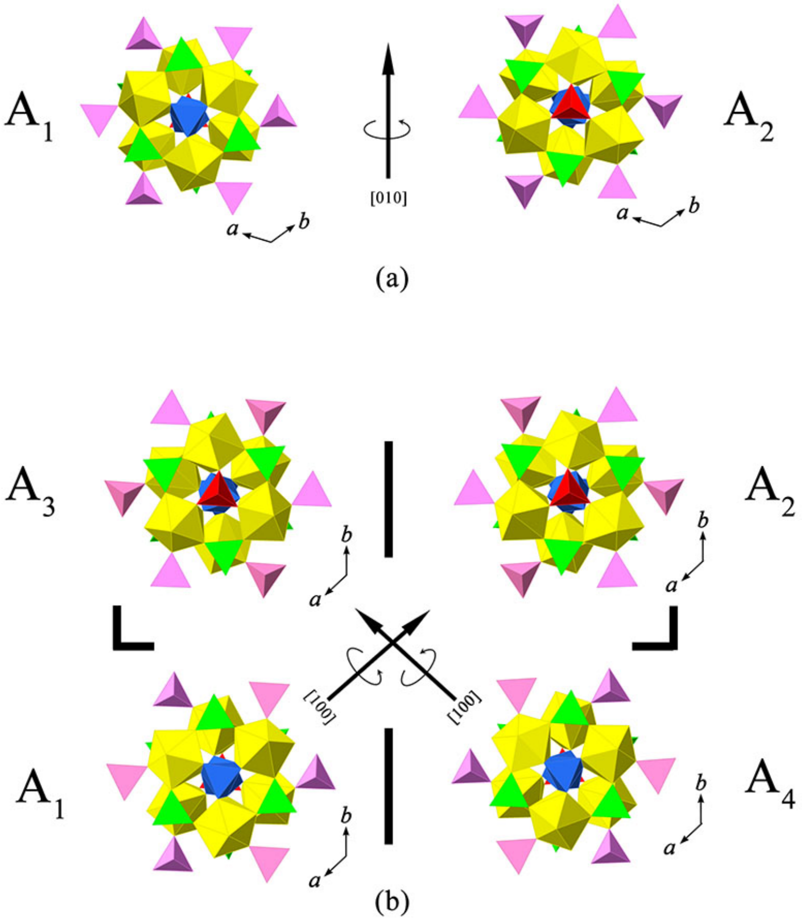

Figure 4.23: Views of the crystallographic along a-axis and the transformations in different layers in (a) $K_6Th_6(WO_4)_{14}O$ and (b) $Rb_6Th_6(WO_4)_{14}O$. (Owing to the hexagonal crystal system for both tungstate structures, the [100] and [010] directions are symmetrically the same).

K. There is no endothermic peak observed before the melting point, which means no other thermal behavior happened in this range. For $Rb_6Th_6(WO_4)_{14}O$ two endothermic peaks are observed upon heating its polycrystalline powder to 1523 K. The peak at the higher temperatures, with the onset at about 1209 K which is close to that of $K_6Th_6(WO_4)_{14}O$, again shows the incongruent melting and has the maximum heat flow at 1221(3) K. The solid-liquid finishing point for $Rb_6Th_6(WO_4)_{14}O$, 1272(5) K, is a little higher than that of $K_6Th_6(WO_4)_{14}O$. The first peak, with the onset point starting at approximate 1080 K, deserves particular attention since it might be assumed as a solid-state phase transition in the structure of $Rb_6Th_6(WO_4)_{14}O$ because there is no obvious mass loss detected around this peak.

Thermal expansion and phase transition of $Rb_6Th_6(WO_4)_{14}O$

Temperature-dependent X-ray diffraction was used to get a deeper insight in the thermal behavior of $Rb_6Th_6(WO_4)_{14}O$. Data were collected across the assumed phase-transition and the decomposi-

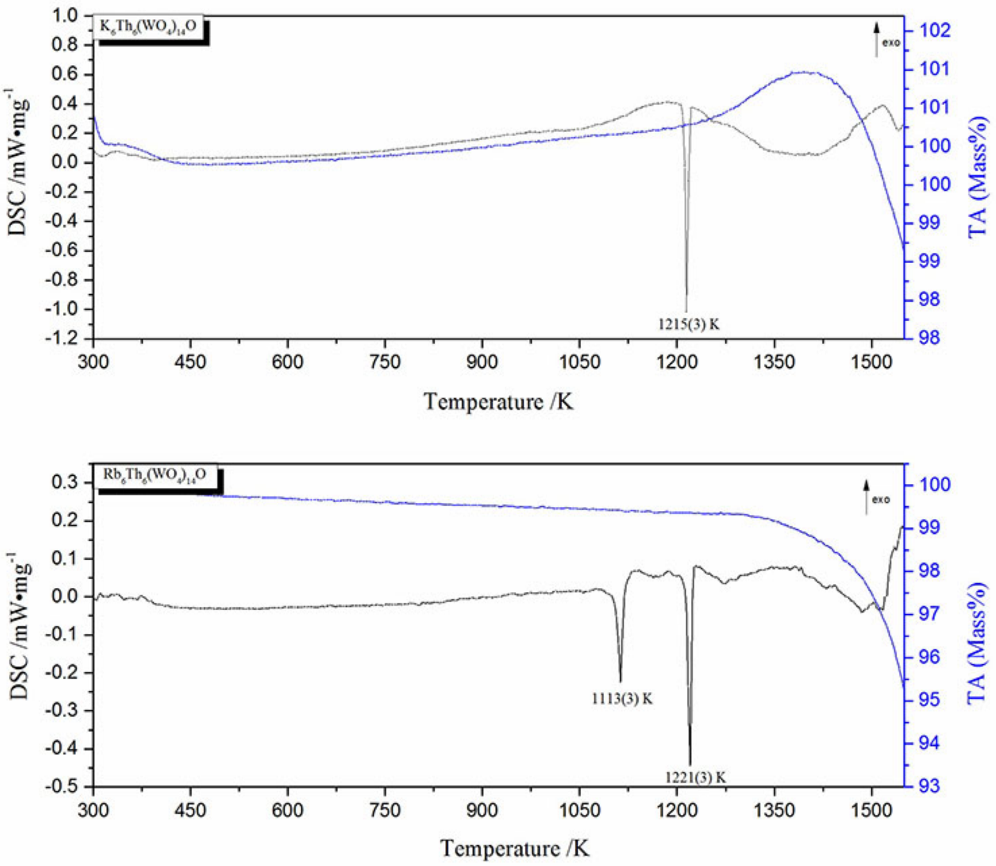

Figure 4.24: The DSC and TA curves for $K_6Th_6(WO_4)_{14}O$ and $Rb_6Th_6(WO_4)_{14}O$, respectively.

tion/melting with onset temperatures of 1080 K and 1209 K, respectively, as explained above. The first inspection of the temperature dependency of the powder pattern, as given in **Figure 4.25** (top left), confirms structural changes at the temperatures showing endothermal signals in the DSC investigations. Nevertheless, from the autocorrelation analysis additionally points of interest could be derived around 550 K and 650 K where minor changes could happen in the structure as well as between 700 K and 950 K where the $CorrNorm(1)$ parameter of the autocorrelation increases. Thereafter a strong decrease of this parameter indicates the beginning phase-transition. Finally, the last two data point well correlate with the decomposition of the phase. Rietveld refinements on the basis of the structural model were carried out for each temperature step leading to very accurate lattice parameters. Due to the shorter measurement times during the data collection in combination with a maximum data collection diffraction angle of 85° (2 Theta), which must be used for an acceptable total data collection time, in combination with the very big unit cell and high number of positional parameters the positional errors within each Rietveld refinement are too big to really derive structural changes in detail. Therefore this section concentrates on the changes of the metric parameters using Debye-Einstein-Anharmonicity (**DEA**) description for the first-order Mie-Grneisen equation of state (FO-MG-EoS) as developed in this extended way for mullite-type compounds and used in comparable systems to describe the changes of the internal energy. The harmonic, quasi-harmonic and anharmonic phonon contribution of the internal energy $U(T)$ to the metric parameter M is expressed in equation (3.2) (see **Chapter** 3.2 from **page** 30), where $M(T)$ refers to any of the temperature dependent metric parameters ($V(T)$, $a(T)$, $b(T)$ and $c(T)$), k_{Di}, k_{Ei} and k_A are thermoelastic constants contributing to Debye (U_{Di}), Einstein (U_{Ei}) and anharmonic (U_A) internal energies, respectively.

For the temperature-dependent volume development a quite complex behavior till the phase-transition was as well found as for the ***a***- and ***c***-lattice parameter, where the latter one shows significant differences. In a first step of the DEA modeling only one Debye term (d = 1, e = 0, a = 0) should be used and properly fitted to the data before increasing the complexity of the model. From these first refinements a_0 = 1168.50 pm, k_{D1}(a) = 1.21(2)$\times10^{-12}$ and a Debye temperature of θ_{D1}(a) = 416(4) K and c_0 = 4609.69 pm, k_{D1}(c) = 5.41(4)$\times10^{-12}$ and a Debye temperature of θ_{D1}(c) = 507(5) K for the ***a*** and ***c*** direction, respectively, are determined. As could be seen from the respective graphs in **Figure** 4.25 (middle left and right) this simple Debye approximations fits well with the low-temperature data up to 650 K for the ***a*** direction and 550 K for the ***c*** direction but hits also the data points evaluated for the lattice parameters of the high-temperature phase after the displacive phase transition quite well, showing the close energetic level of both the high- and low-temperature phase. For both directions a strong deviation from the Debye model could be seen around 650 K (marked with an arrow in **Figure** 4.25) leading to a much smaller expansion in the ***c*** direction and a slight negative expansion in the ***a*** direction up to around 850 K as could be seen from the thermal expansion coefficient (TEC) given as insert in the respective plots in **Figure** 4.25. This leads to the smallest thermal expansion coefficient for the volume of αV = 2.6(5) 10^{-6} K^{-1} in this temperature range. The different contribution of the lattice parameters to the volume development could best be seen in the relative change of all three parameters as shown in **Figure** 4.25 (bottom right). As described above an additional small deviations from the Debye model could be seen around 550 K for the c lattice parameter. This effect is more pronounced while plotting the ***c***/***a***-ratio versus the temperature (**Figure** 4.25 bottom left) where a slight increase of the ***c***/***a***-ratio could be seen starting around 550 K followed by a strong increase above 650 K. Nevertheless, looking to the scattering of the data below 500 K the interpretation of the data development at this temperature could also be seen as a further scattering. The effect becomes more pronounced and clear if one calculates the anisotropy of the thermal expansion coefficient. The TEC anisotropy factor changes from 4(1)$\times10^{-6}$ K^{-1} at 540 K to 16(1)$\times10^{-6}$ K^{-1} at 646 K reaching a maximum of 20(1)$\times10^{-6}$ K^{-1} at 710 K to further decrease to 12(1)$\times10^{-6}$ K^{-1} at 810 K followed by a range of a more or less constant value up to 930 K followed by a further decrease to 8(1)$\times10^{-6}$ K^{-1} at 980 K before it strongly increases towards the phase transition. Although the FO-MG-EoS gives only physical meaningful values for the volume changes and not for the respective lattice parameters one can use it to describe their behavior. Nevertheless, such a complicated expansion could not be fitted using the DEA model. But from the data evaluation one can summarized that a Debye like thermal expansion could be observed up to 500 K driven by the quasi-harmonic phonon contribution to the interatomic bond distance thermal expansion and therefore more or less similar in all directions of the $Rb_6Th_6(WO_4)_{14}O$ structure. Around 550 K a smaller increase of the thermal expansion is observed for the c lattice parameter giving rise for the assumption that a slight reorientation of the bond-system in the linkers between the six-leaved lily block layers occur. These linkers are dominated by WO_4 tetrahedra which have the expansibility in the structure and tend to tilt the earliest. Above 650 K the change of the thermal behavior in both different unit-cell directions could be interpreted as a maximum bond expansion of the six-leaved lily blocks leading to a non-expansion in the ***ab*** plane (layer plane) of the structure and a highly reduces expansion in the ***c*** directions correlated to the limited steric behavior of the linkers between the structural layers. A reason for this behavior could be an electron-phonon interaction caused by the double-bonded oxygen atoms of the WO_4 tetrahedra which cap the $[Th_6W_6O_{45}(W_2O_9)]^{36-}$ polyanion barrel shell and the neighboring Rb^+-cations, which suppresses the harmonic phonon contribution leading to a negative Einstein term. A further increase of the cell volume could only be realized if complete building blocks like octahedra, the thorium-oxygen-barrels or the six-leaved lilies are rotating or distorting which would lead to rigid-unit modes (**RUM**). At the phase-transition temperature the increase of the needed energy for this RUM behavior increases in such a strong way that an atomic reorientation is more energy efficient leading to the observed displace phase-transition. In general this total behavior should lead to a negative Einstein contribution to the thermal expansion internal energy calculation for the temperature range where the electron-phonon interaction is observed as well as a strong increase of a second Einstein term towards the phase-transition. It should be noted that due to the small energy difference between the low- and the high temperature phase the latter one is not much more stable leading to decomposition at an only 107(3) K higher temperature, which could also be seen on the slightly higher volume dependent Debye temperature of 653 K for the high-temperature phase compared to 503(32) K for the low-temperature phase.

Based on these observations the volume thermal expansion was DEA modeled using one Debye and two Einstein contributions ($d = 1$, $e = 2$, $a = 0$). A good solution for this model could be refined (**Figure 4.25 (top right)** using V_0 = 5445.92×10^6pm^3, k_{D1}(V) = 20.74(1)×10^{-12}, θ_{D1}(V) = 503(32) K, K_{E1}(V) = -459(29)×10^{-12}, θ_{E1}(V) = 4822(307) K and $k_{E2}(V)$ = 5200(331)×10^{-12}, $\theta_{E2}(V)$ = 7998(509) K. Whereas V_0 represents the big unit cell, the Debye temperature is within a normal range of quasi-harmonic phonon contributions and the slightly high thermoelastic constant k_{D1} represents the bigger absolute volume increase. As mentioned above the Einstein contributions $E1$ and $E2$ are assumed to correlate with electron-phonon and rigid-unit mode harmonic phonon contributions, respectively. To obtain the same amount of internal energy change the thermoelastic constant of an Einstein contribution must increase with increasing Einstein temperature. Therefore it is not surprising that the k_{E2} parameters are rather large because of the high respective Einstein temperature θ_{E1} and θ_{E2}. The negative K_{E1} parameter is associated with the electron-phonon interaction suppressing the harmonic phonon contribution. The second harmonic phonon contribution will be associated with a rigid-unit mode behavior which leads to an expansion behavior typical for Landau theory second-order/tricritical phase transitions as observed for example in observed for example in sodalites. This

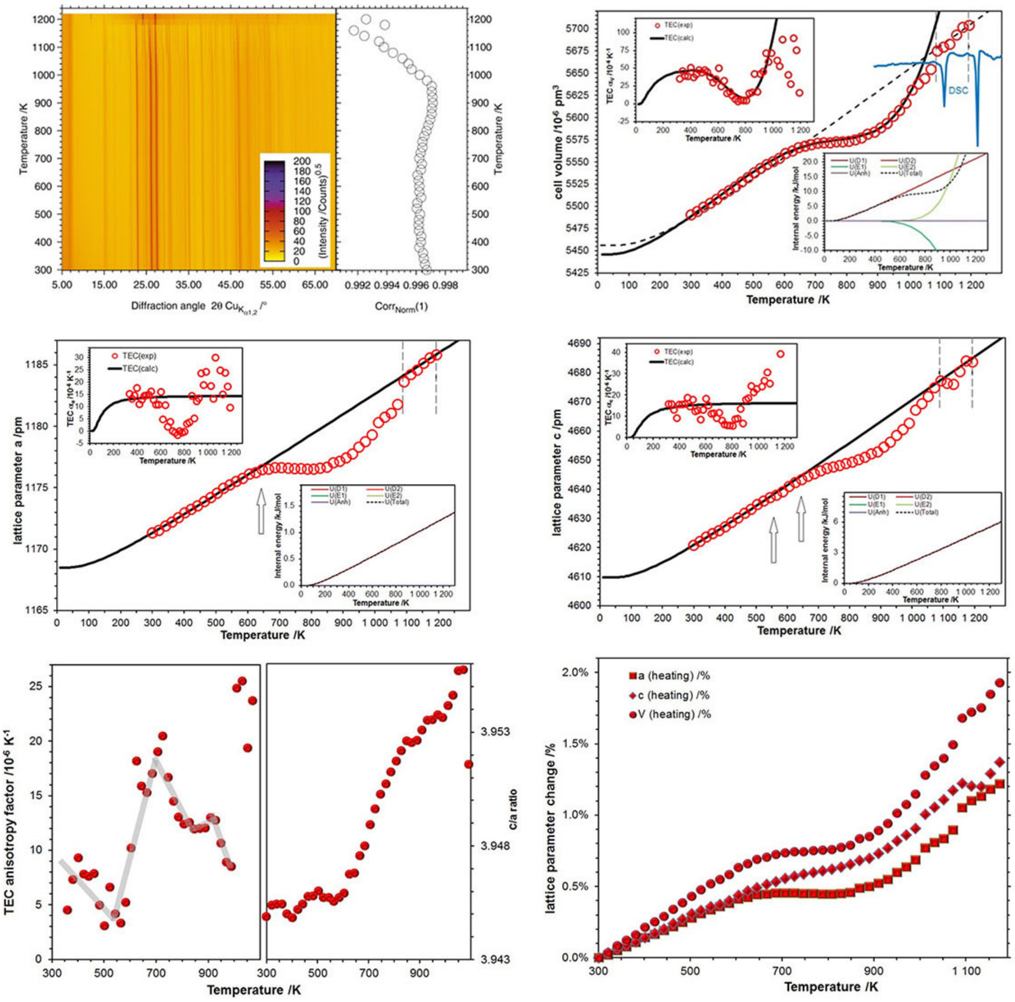

Figure 4.25: Temperature-dependent X-ray powder diffraction patterns and autocorrelation analysis results of $Rb_6Th_6(WO_4)_{14}O$ (top left) and temperature-dependent unit cell dimensions of $Rb_6Th_6(WO_4)_{14}O$ determined from high-temperature X-ray powder diffraction.

type of phase-transitions is observed for structure showing group-subgroup relations for the high-temperature to low-temperature transition which could also be assumed here.

4.3.4 Vibrational spectroscopy

The Raman spectra for $Rb_6Th_6(WO_4)_{14}O$ and $K_6Th_6(WO_4)_{14}O$ are recorded from 100 to 1100 cm^{-1}, as presented in **Figure 4.26**. For both compounds, the modes in the low-frequency region from 100 to 250 cm^{-1} are raised from the lattice vibrations, whereas the high-frequency zone from 250 to 1100 cm^{-1} is dominated by signals associated with the tungstate ions. Since the observed unit-cells are huge and W is found in various coordination geometries, that is, WO_4 tetrahedra and W_2O_9 confacial

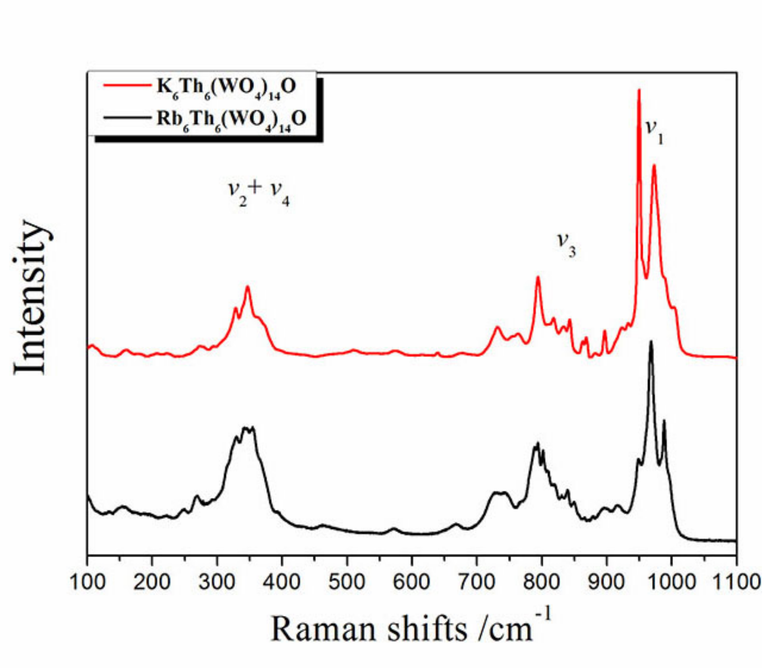

Figure 4.26: Raman shifts for $Rb_6Th_6(WO_4)_{14}O$ and $K_6Th_6(WO_4)_{14}O$, respectively.

bioctahedra, each compound reported here demonstrates a very complex vibrational pattern in the whole measured region. The vibrational modes for WO_4^{2-} are well characterized and they can be divided into internal modes (where WO_4^{2-} anion keeps the centre mass unmovable) and external modes (for which the WO_4^{2-} anion is considered as a rigid unit). The isolated WO_4^{2-} anion in aqueous solutions forms a regular tetrahedron (T_d symmetry) with four fundamental internal vibrational modes located at 928 cm^{-1} (ν_1), 320 cm^{-1} (ν_2), 833 cm^{-1} (ν_3) and 405 cm^{-1} (ν_4), respectively. In the crystals of $Rb_6Th_6(WO_4)_{14}O$ and $K_6Th_6(WO_4)_{14}O$, however, because of the significant coupling between the WO_4 anions with the vibrational modes of different cations (Rb^+/K^+ and Th^{4+}) within the unit cell, the vibrational modes in idealized symmetry T_d are split in a wider range. For both compounds, the bands value located at 925–1050 cm^{-1} is the normal symmetric stretching vibrational modes (ν_1) for a distorted tetrahedron. The Raman intensive shifts at around 800 cm^{-1} in both compounds correspond to the asymmetric stretching modes (ν_3) of the WO_4 ions, which agrees with that for free WO_4^{2-} ions in solution. The most significant feature in the Raman spectra is the bands in the region from 430 cm^{-1} to 710 cm^{-1}. Normally, in solid state compounds containing only isolated WO_4 anions, there exists a vibrational energy gap between stretching and bending modes in these compounds. Because the stretching modes ν_1 and ν_3 appear in the range of 750–1000 cm^{-1} whereas the bending modes ν_2 and ν_4 fall in the 250–430 cm^{-1} range. In this cases, bands with respect to such region are not silent because modes such as 592(4) cm^{-1} and 639(3) cm^{-1} in $K_6Th_6(WO_4)_{14}O$ and 466(3) cm^{-1} and 569(3) cm^{-1} in $Rb_6Th_6(WO_4)_{14}O$, respectively, can be detected. This may be due to the activation of the oxygen bridge vibrations, which arises from the confacial biocahedral cores (W_2O_9) in the both structures.

4.3.5 Conclusion

The thorium tungstates system bear a fascinating structural complexity. The products, $K_6Th_6(WO_4)_{14}O$ and $Rb_6Th_6(WO_4)_{14}O$, both are constructed by complex polyanions with a composition of $[Th_6W_7O_{46}(W_2O_9)]^{32-}$. The complex polyanions, having a six-leafed lily cross-section, contain a rare confacial $[W_2O_9]^{6-}$ bioctahedral core. The bond asymmetry deriving from the local C_3 out-of-center distortion geometry is observed for each WO_6 octahedron inside the bioctahedral core. Besides, a displacive phase transition is confirmed by TG-DSC and the temperature-dependent X-ray powder diffraction analysis in the compound of $Rb_6Th_6(WO_4)_{14}O$.

According to Paulings rule,[97] the presence of face sharing will lead to strong repulsive forces between the central cation of the polyhedra, therefore the more flexible configurations such as vertex- and edge-sharing become the overwhelming connections in the crystal chemistry of W(VI). It is a high likelihood that the special coordination geometries about the $[Th_6W_7O_{46}(W_2O_9)]^{32-}$ cage stabilize such uncommon $[W_2O_9]^{6-}$ bioctahedral polyhedra. The discovery of rare case of face-sharing $[W_2O_9]^{6-}$ bioctahedral core in $A_6Th_6(WO_4)_{14}O$ (A = K and Rb) may shed new light into the structural and topological chemistry of actinide tungstates.

---

[97] Linus Pauling. *J. Am. Chem. Soc.*, **51**: 1010, 1929.

Chapter 5

Crystal Chemistry of Thorium Molybdates and Tungstates Synthesized Using Solvothermal Method

In addition to the above mentioned high-temperature solid-state synthesis method, multiple synthetic routes have also been tested in an effort to further explore on the thorium molybdate family. The low-temperature molten boric acid synthetic method is one such technique that is discovered recently as a promising methodology for preparing novel actinide compounds. Compare to the traditional hydrothermal synthesis, this method uses the boric acid as a reactive flux to substitute water in a relatively low-temperature (around 200 °C) in the autoclaves, and thus allows borate to easily access to the inner-sphere coordination sites of actinide elements. Water may also be used in a tiny amount as the chemical reactant. This new synthetic strategy continues to be broadly employed in obtaining novel structures and it has already infused fresh blood into actinide borate chemistry by giving birth to a large family of uranyl borates, multi mixed-valence neptunium borates as well as a plutonium(VI) borate over the course of the past 4 years. These actinide borates adopt a wide variety of unusual topological structural types and display a vast array of fascinating properties. My motivation here was to try to find out how the melt boric acid would affect the associated reactions compared to the normal hydrothermal synthesis and also attempt to obtain a novel series of mixed-metal thorium molybdenum borate compounds.

5.1 Structural modulation of thorium molybdate architectures by water molecules

5.1.1 Crystal chemistry of thorium molybdates isolated under the solvothermal conditions

Structure of $Th_2(MoO_4)_3(NO_3)_2(H_2O)_3$

The major building block of $Th_2(MoO_4)_3(NO_3)_2(H_2O)_3$ is a 3D framework with channels constructed by corner-sharing ThO_9 and MoO_4 polyhedra, shown in **Figure 5.1**. The channels have approximate dimensionality of 2.9×5.1 Å, extending parallel along [100] direction, and are occupied by water molecules. In the framework, the ninefold Th atoms achieve a tricapped trigonal prism, by corner-sharing of six O atoms from the $MoO_4{}^{2-}$ units, two O atoms from $NO_3{}^{-}$ units, and one O atom from the aqua ligand. The ThO_9 polyhedron yields an average Th-O bond distance of 2.46 Å, in good accordance with those reported in other thorium molybdates also containing ThO_9 geometry, such as average 2.46 Å and 2.47 Å in $Th(SeO_3)(SeO_4)$[98] and $Th(V_2O_7)(H_2O)_2$[99] respectively. There are two crystallographically unique Mo atoms in $Th_2(MoO_4)_3(NO_3)_2(H_2O)_3$. Each is tetrahedrally coordinated by O with Mo-O distances from 1.750(3) to 1.779(3) Å and O-Mo-O angles from 106.6(2)° to 102.1(2)°. Each $NO_3{}^{-}$ triangle shares two O vertices with two adjacent ThO_9 polyhedra. The coordination of N is typical in the distorted $NO_3{}^{-}$ group with N-O bond distances ranging from 1.236(5) to 1.258(6) Å. Because of the low X-ray scatter factor for H atoms and high residual peaks around high atoms (Th) in the Fourier maps, the H atoms for water molecular were unable to be located. But they are confirmed by the Raman spectroscopic data.

The structure of $Th_2(MoO_4)_3(NO_3)_2(H_2O)_3$ observed here is remarkable in the fact that it consists of one-dimensional thorium nitrate chains $Th(NO_3)(H_2O)$, highlighted in **Figure 5.1**. The $Th(NO_3)(H_2O)$ chain is composed of corner-linked ThO_9 polyhedra and NO_3 triangles and stretches along [010] direction. The MoO_4 tetrahedra interlink the adjacent $Th(NO_3)(H_2O)$ chain from above and below throughout the (100) plane, completing the 3D framework structure. It is worthy of mention that such corner-shared Th-N linkage has not been reported previously for any inorganic thorium compounds so far. In general, the thorium nitrate compounds tend to form an isotropic coordination configuration with $[\mathrm{Th_x(NO_3)_y}]^{4x-y}$ (x = 1 or 2; y = 4, 5, 6) finite clusters encompassing $\mathrm{ThO_x}$ polyhedra and NO_3 triangles in face-sharing manner. **Figure 5.2** lists all types of Th-N connectivities that have been seen in the literatures. To analysis the topological structures and corresponding connectivity relationship between Th polyhedra and NO_3 triangles in these thorium nitrate compounds, here the *black and white nodal representation*[100] was adopted. Within this method, the coordination centers of Th^{4+} and N^{3-} cations are labeled by black and white nodes, respectively. Two nodes are connected by lines only if corresponding cations share at least one O atom, and the number of lines between these two nodes

---

[98] Tyler A. Sullens et al. *J. Solid State Chem.*, **179**: 1192–1201, 2006.

[99] Said Yagoubi et al. *Acta Crystallogr. Sect. E*, **67**: i60, 2011.

[100] Sergey V. Krivovichev et al. *Angew. Chem. Int. Ed.*, **117**: 1158–1160, 2005.

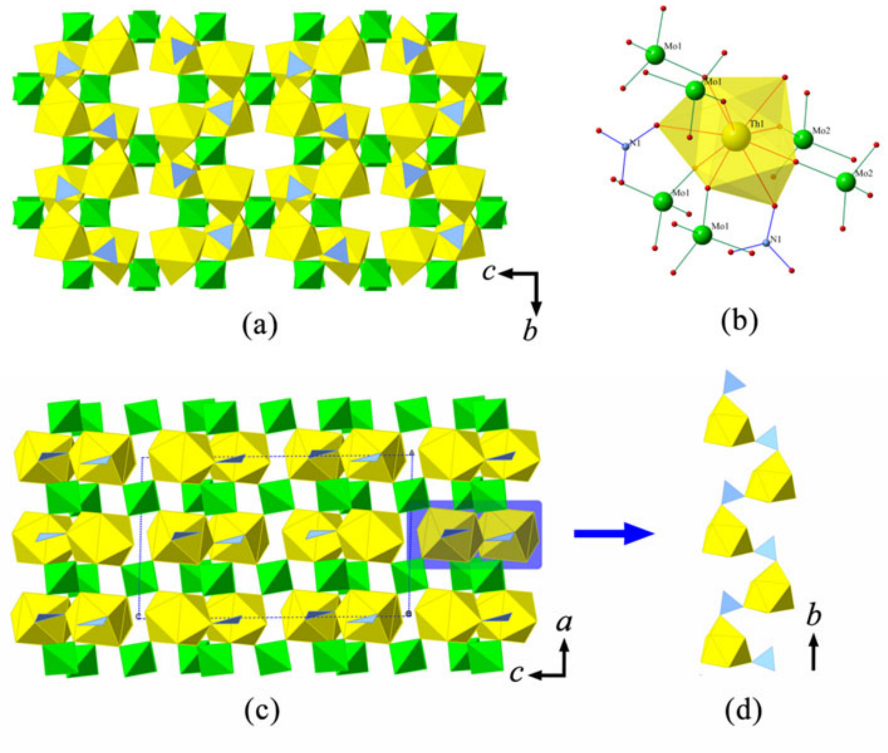

Figure 5.1: View of crystal structure of $Th_2(MoO_4)_3(NO_3)_2(H_2O)_3$.

is associated with the number of common O atoms. The cluster of $[Th(NO_3)_6]^{2-}$ containing Th in an icosahedral coordination geometry can be found in the structures of $MTh(NO_3)_6{\cdot}H_2O$(M: Mg, Mn, Co, Ni, Zn)[101] and $(NH_4)_2Th(NO_3)_6$[102]. The clusters having the same Th-N topology are observed in $Th(NO_3)_4(H_2O)_4$[103] and $Th(NO_3)_4(H_2O)_5$[104]. However, due to exist of different coordination numbers (12 and for Th in the former and latter clusters, respectively) the coordination geometries are different and one cluster cannot be transformed to the other without breaking the Th-O connections. In the compound of $Th(NO_3)_3(OH)(H_2O)_4$, the $[Th_2(NO_3)_6(OH)_2(H_2O)_6]$ cluster consisted of two ThO_{11} polyhedra with each sharing edges with three NO_3^-.

Structure of $Th(MoO_4)_2{\cdot}2\,H_2O$

$Th(MoO_4)_2{\cdot}2\,H_2O$ is crystallized in the $P\bar{1}$ space group. There are one crystallographically unique Th and two Mo sites in an asymmetric unit, and the corresponding coordination environments of these sites are shown in **Figure 5.3 (a, b, c)**. Each Th is square antiprismatically coordinated by oxygens with Th-O bond lengths ranging from 2.385(6) to 2.551(6) Å, the average value being 2.47 Å. These values are close to those observed for many other thorium molybdates which also contain ThO_8 polyhedra but were synthesized *via* high-temperature solid-state condition, such as 2.300(6)

---

[101] S Scavnicar and B Prodic. *Acta Crystallogr.*, **18**: 698–702, 1965.

[102] MR Spirlet et al. *Acta Crystallogr., Sect. C: Cryst. Struct. Commun.*, **48**: 1161–1164, 1992.

[103] P Charpin et al. *Acta Crystallogr., Sect. C: Cryst. Struct. Commun.*, **43**: 1239–1241, 1987.

[104] JC Taylor, MH Mueller, and RL Hitterman. *Acta Crystallogr.*, **20**: 842–851, 1966.

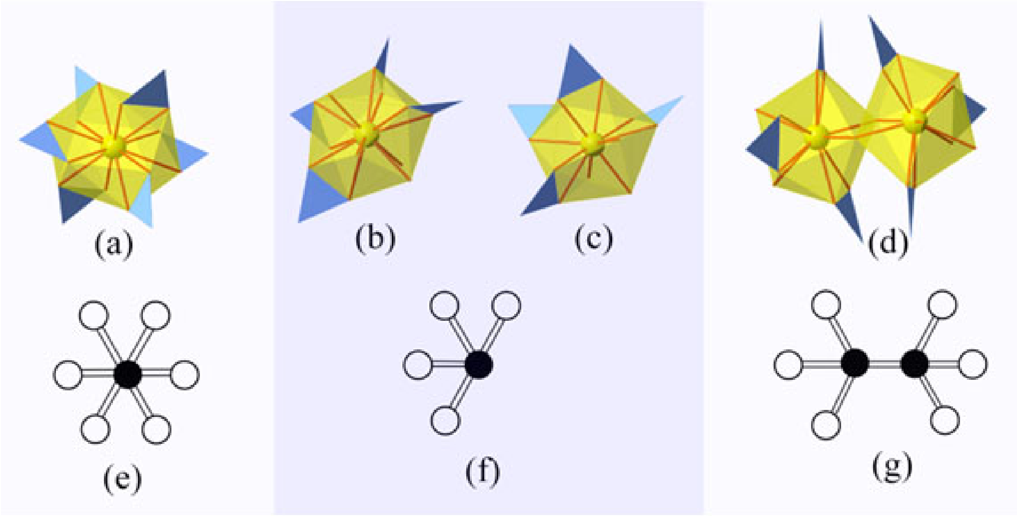

Figure 5.2: The Th-N connectiviey and the corresponding topological units among the thorium compounds. The Yellow and light blue polyhedra stand for Th and N, respectively. (a) $MTh(NO_3)_6(H_2O)_8$ (M: Mg, Mn, Co, Ni, Zn) and$(NH_4)Th(NO_3)_6$. (b) Th is an icosahedral coordination geometry in $Th(NO_3)_4(H_2O)_4$. (c) $Th(NO_3)_4(H_2O)_5$. (d) $Th_2(NO_3)_6(OH)_2(H_2O)_6$.

to 2.753(6) Å in $Cs_2Th_3(MoO_4)_7$ and 2.31(1) to 2.56 (1) Å in $Cs_2Th(MoO_4)_3$.[105] In the case of Mo sites, both are four-fold coordinated in a tetrahedral geometry with Mo-O bond distances and O-Mo-O bond angles ranging from 1.709(7) to 1.863(7) Å and 105.7(3) to 114.9(3)°, respectively.

The structure of $Th(MoO_4)_2{\cdot}2\,H_2O$ is based on 2D corrugated layers composed of ThO_8 and MoO_4 polyhedra, running propagating along ***bc*** plane (see **Figure 5.3 (d, e)**). These Th-Mo layers, separated by the water molecules in between, have electrically neutral composition of $[Th(MoO_4)_2]^0$. As can be seen from **Figure 5.3(f)**, each $[Th(MoO_4)_2]^0$ layer can be seen as based on a fundamental building fragment encompassing two ThO_8 and eight MoO_4 polyhedra. In layer, two ThO_8 square antiprisms are connected together through sharing common edges lead to Th—Th dimers that are further surrounded by two symmetrically distinct $Mo(1)O_4$and $Mo(2)O_4$tetrahedra with tridentate- and bidentate-bridging behavior, respectively. In both cases, the Mo—O bond lengths with the bridging oxygen atoms (1.743(6) Å—1.863(7) Å) are significantly longer than those with the terminal oxygen atoms (1.709(7) Å—1.743(6) Å).

A comparison of the crystal structure of $Th(MoO_4)_2{\cdot}2\,H_2O$ with the lanthanide-based $ABNd_2(MoO_4)_4$(A and B = alkaline metals) and $CLn(MoO_4)_2$ (C = alkaline metals; and Ln = rare-earth metals) structures indicates a close resemblance. All these compounds are constructed from 2D layers of $[Th(MoO_4)_2]^0$ or $[Ln(MoO_4)_2]^-$. These thorium/lanthanum molybdate layers are built from ThO_8/LnO_8 square antiprisms and MoO_4 polyhedra in exactly the same topological geometry. The only difference is that the thorium-based layers are electrically neutral while the lanthanum-based ones are not. This leads to the requirement of charge-compensating cations (the alkaline metal in this case)

---

[105] Bin Xiao et al. *Cryst. Growth Des.*, **14**: 2677–2684, 2014.

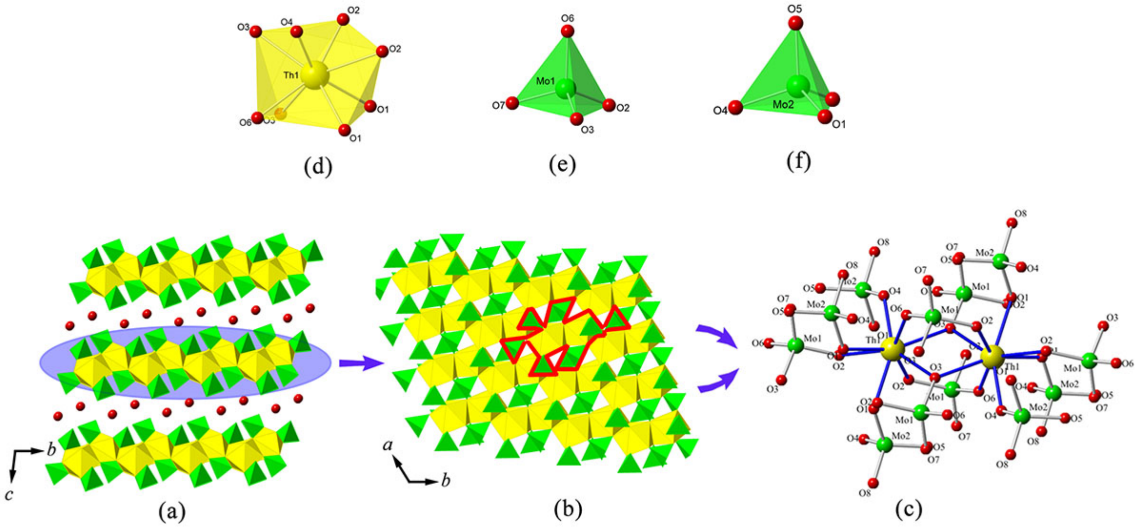

Figure 5.3: Polyhedral presentation of the layered structure of $Th(MoO_4)_2{\cdot}2\,H_2O$. (a) View along the a-axis shows the corrugated $[Th(MoO_4)_2]^0$ layers. (b) One of the layer that is taken for the structure and is shown along the c-axis. (c) The layer is based on ThO_8 square antiprisms connected with MoO_4 tetrahedra. (d) The local coordination environment of $Th(1)O_8$ square antiprism. (e) The local coordination environment of $Mo(1)O_4$ tetrahedron. (d) The local coordination environment of $Mo(2)O_4$ tetrahedron.

in lanthanide-based compounds to keep the whole formula neutrality. Such chemically different but structurally and topological identical also indicates the possibility of this structural type to host different actinide and lanthanide elements with different sizes and charges.

Structure of $(NH_4)_2Th_4(MoO_4)_9$

The compound $(NH_4)_2Th_4(MoO_4)_9$is crystallized in the non-centrosymmetric cubic space group $I\bar{4}3d$. The cubic structures are uncommon and poorly represented among the actinide oxoanion compounds. This compound represents only the third instance in the thorium molybdate family for which single-crystal structures are refined; the others being the isostructural compounds with composition of $A_2Th_4(MoO_4)_9$ ($A = Li^+$, Cu^+). $(NH_4)_2Th_4(MoO_4)_9$ is a dense, three-dimensional framework containing one crystallographically unique, nine-fold coordinated Th site with tricapped trigonal prismatic geometry as well as two crystallographically unique, four-fold coordinated MoO_4 tetrahedra. Each ThO_9 canter is surrounded by nine MoO_4 tetrahedra in corner-sharing manner. Part of the structure is shown in **Figure 5.4** with the $(NH_4)^+$ cations omitted. The $(NH_4)^+$ cations are located in small twisting interconnected cavities and channels created by corner-sharing of ThO_9 and MoO_4 polyhedra. To better describe the arrangement of these ThO_9 and MoO_4 polyhedra inside the structural framework, here the 3D framework is cut into 2D pseudo-layers. The corresponding *black-and-white topology* of this pseudo-layer consists of five-connected black (Th) and two-connected white nodes (Mo). It is easy to note that the elementary unit of this graph has a shape of rhomb that is constructed by two black and two while nodes. All the rhombs are oriented in the same direction

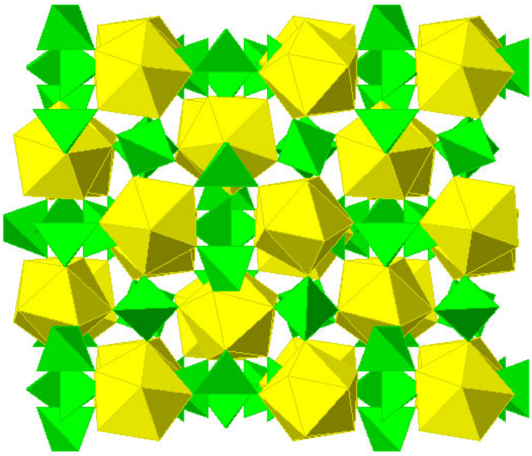

Figure 5.4: Polyhedral presentation of the framework structure of $(NH_4)_2Th_4(MoO_4)_9$.

among the pseudo-layer direction, while they are rotated by 90° related to those in the adjacent pseudo-layers. The neighboring pseudo-layers are linked together by sharing common corners form the ThO_9 and MoO_4 polyhedra to complete the structure.

The Th-O bond distances vary within a very narrow range of 2.433(8)−2.445(8) Å, with the mean value of 2.444 Å. As the case of Mo, the variation of Mo(1) to O bond distances is appreciable, from 1.738(9) to 1.760(8) Å. The O-Mo(1)-O bond angles range from 107.1(5)° to 112.6(6)°. In contrast, the local coordination environment of Mo(2) shows much less perturbed in Mo-O bond distances (1.745 Å × 4) and angles (from 109.1(3)° to 110.1(6)°) than aforementioned Mo(1) site. The bond-valence sums for Th and Mo atoms in the $(NH_4)_2Th_4(MoO_4)_9$ were calculated utilizing the data according to *Brese* and *OKeefee*[106].The results of 4.31 v.u. for Th(1), 6.13 v.u. for Mo(1) and 6.19 v.u. for Mo(2) agrees well with the expected bond-valence values.

5.2 Structural evolution from order to disorder in the thorium chromate family

With respect to thorium chromate, there are only two compounds reported in the literature. The first single crystal structure of a thorium chromate, $Th(OH)_2(CrO_4)(H_2O)$, was synthesized by *Lundgren, et al.* in 1949.[107] This compound is based on eight-coordinated Th and four-coordianted Cr connected by sharing corners with each other to form 3D framework. After this initial study, no new thorium chromate compounds were then reported until $Th(CrO_4)_2(H_2O)$ has been obtained by *Sullens, et al.* through mild hydrothermal condition in 2006.[108] $Th(CrO_4)_2(H_2O)$ is a far more complex structure encompassing Th cations in both ThO_8 dodecahedral and ThO_9 tricapped trigonal prismatic coordination geometries. In order to explore more thorium chromate compounds to further extend the

---

[106] NE Brese and M O'keeffe. *Acta Crystallographica Section B: Structural Science*, **47**: 192–197, 1991.

[107] Georg Lundgren and Lars Gunnar Sillén. *Naturwissenschaften*, **36**: 345–346, 1949.

[108] Tyler A. Sullens and Thomas E. Albrecht-Schmitt. *Acta Crystallogr. Sect. E: Struct. Rep. Online*, **62**: I258–I260, 2006.

knowledge of actinide chemistry, this section reports on the reactions of thorium nitrate with chromate under low-temperature reaction conditions (≈ 200 °C) including both mild hydrothermal and boric acid flux reaction.

5.2.1 Structural and topological discussions of thorium chromate family

Structure of $Th_2(CrO_4)_3(OH)_2$

The structure of $Th_2(CrO_4)_3(OH)_2$ is built upon one unique crystallographic site of ThO_9 and two sites of CrO_4 polyhedra. The ThO_9 polyhedron which can be best described as a monocapped square antiprism is highly distorted with one short and one slightly long Th-O bond distances of 2.36(1) Å and 2.63(1) Å, respectively. The ThO_9 polydedra are linked end to end with alternative edge and facing-sharing manner through bridging hydroxyl and oxygen anions, respectively, leading to a chain propagating along [100] direction. The Th pseudo-layers are formed by arranging these thorium chains parallel to (010) planes. It is note that the resulting Th chains are different from those observed in $Th(CrO_4)_2(H_2O)$ where the neighboring Th polyhdra are fused exclusively by facing-sharing, but analogous to the (find the Th-Th in other compounds). The CrO_4 tetrahedra are located in the interlayer space, playing a role of linkage of the thorium pseudo-layers, giving rise to form a 3D framework. Each Cr(1) has five ThO_9 polyhedra neighbours resided in the four corners of its tetrahedron, *i.e.* Cr(1)O_4 tetrahedron is chelated with two ThO_9 polyhedra in O(2) corner, and at the same time also bridged with three other ThO_9 polyhedra in respective O(3), O(4) and O(5) corners. In this case, the CrO_4 tetrahedral distortion is obvious in the O(2) direction, this being the longest Cr-O distance of 1.71(1) Å The distribution of CrO_4 bond distances are in accordance with those reported for other thorium chromates.[98,107,108]

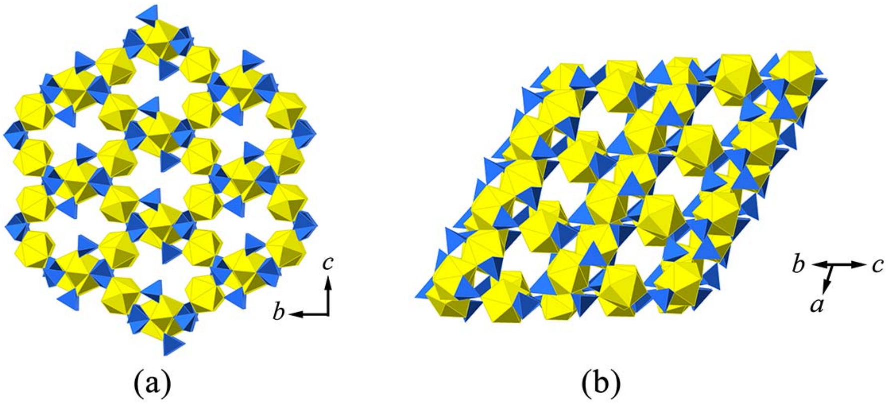

Figure 5.5: View of the structure of $Th_3(CrO_4)_6(H_2O)_8{\cdot}(H_2O)_6$.

Structure of $Th_3(CrO_4)_6(H_2O)_8{\cdot}(H_2O)_6$

The $Th_3(CrO_4)_6(H_2O)_8{\cdot}(H_2O)_6$ crystallizes in a space group $P2_1/c$, with its structure exhibiting a 3D open-framework structure, that consists of channels running through [100], [011], [01$\bar{1}$] and [01$\bar{1}$]

direction (shown in **Figure 5.5**). In the asymmetric unit there are two unique Th sites and three Cr sites. Both Th sites are coordinated by nine O atoms in a distorted monocapped square antiprismatic geometry. The average Th-O bond distance for Th(1) is 2.50 Å, and the distortion can be observed especially in the O(12) direction, this being the shortest Th-O bond distance of 2.42(1) Å. The four coordinated water molecules have Th(1)-O bond distances ranging from 2.50(2) Å to 2.58(1) Å. The Th(1)-H_2O bond distances are consistent well with those of 2.479(1) Å and 2.542(1) Å observed for $Th_3(SO_4)_6(H_2O)_6{\cdot}H_2O$, a well-known open-framework compound with 11.5 Å voids built from corner-sharing of ThO_9 and SO_4 polyhedra.[109] In comparison to Th(1) site, there is no water molecule connected to Th(2), and the Th(2)O_9 polyhedron is more distorted, which can be manifested by the wider distribution of Th-O bond distance, ranging from 2.38(1) Å to 2.62(1) Å, but is still acceptable if compared to the other compounds containing nine-coordinated thorium.[110] Moreover, the connection manner is also different between both Th sites, $i.e.$ Th(1)O_9 polyhedra are totally isolated from each other due to the lack of O linkages between neighbouring Th(1)O_9 polyhdra, while the adjacent Th(2)O_9 polyhedra are interlinked by sharing a common edge, giving rise to thorium chains stretch along [100]. All Cr atoms are tetrahedrally coordinated and they form in a +6 oxidation state confirmed by the bond valence calculation method given by Brese, and keeffe[106] (6.03 v.u. 5.94 v.u. and 5.89 v.u. for Cr(1), Cr(2) and Cr(3), respectively). However, the local coordination features are different for these three Cr sites. Cr(1)O_4 and Cr(2)O_4 polyhedra each shares all the O corners by attachment of one bidentate Th and other three monodentate Th atoms. whereas Cr(3)O_4 is bridged by three Th atom, leaving one terminal O atom which is orientated to the inner channels. It is note that the edge-sharing manner between Th and Cr has not been observed in inorganic compounds before.

The $Th_3(CrO_4)_6(H_2O)_8{\cdot}(H_2O)_6$, as mentioned above, contains interlaced channels throughout the structure. Among them, the largest one propagates through [100] direction with the internal dimensions of 6.9×1.9 Å^2, based on the nearest oxygen atoms across the channel. In order to understand the linkages of ThO_9 monocapped square antiprisms and CrO_4 tetrahedra inside the channel, the method of nodal representation is adopted to describe the topology around the cylindrical channels. This method has been applied to delineate compounds containing complex channels, such as $(NH_4)_4[(UO_2)_5(MoO_4)_7](H_2O)_5$[111] and $Cs_2Th_3(MoO_4)_7$[105]. For $Th_3(CrO_4)_6(H_2O)_8{\cdot}(H_2O)_6$, the CrO_4 and ThO_9 polyhedra are designated by white and black nodes, respectively, and two nodes are connected by line only if the corresponding polyhedra share at least a common O atom. The associated black and white node representation and the corresponding unfold version for $Th_3(CrO_4)_6(H_2O)_8{\cdot}(H_2O)_6$ are shown in **Figure 5.6**. All the white (CrO_4) nodes are three-connected, while the black nodes corresponding to Th(1)O_9 are four-connected and Th(2)O_9 are six-connected, respectively. In the ideal version, it is obvious to see pores defined by eight-member rings consisted of four ThO_9 and four CrO_4 polyhedra each. Note that the Th-Cr nodal representation is built upon fundamental units which are shown as the tapes in **Figure 5.6**. The channel can be obtained by folding equivalent points on

---

[109] Richard E. Wilson et al. *Inorg. Chem.*, **47**: 9321–9326, 2008.

[110] Tyler A. Sullens and Thomas E. Albrecht-Schmitt. *Inorg. Chem.*, **44**: 2282–2286, 2005.

[111] S. V. Krivovichev, C. L. Cahill, and P. C. Burns. *Inorg. Chem.*, **42**: 2459–2464, 2003.

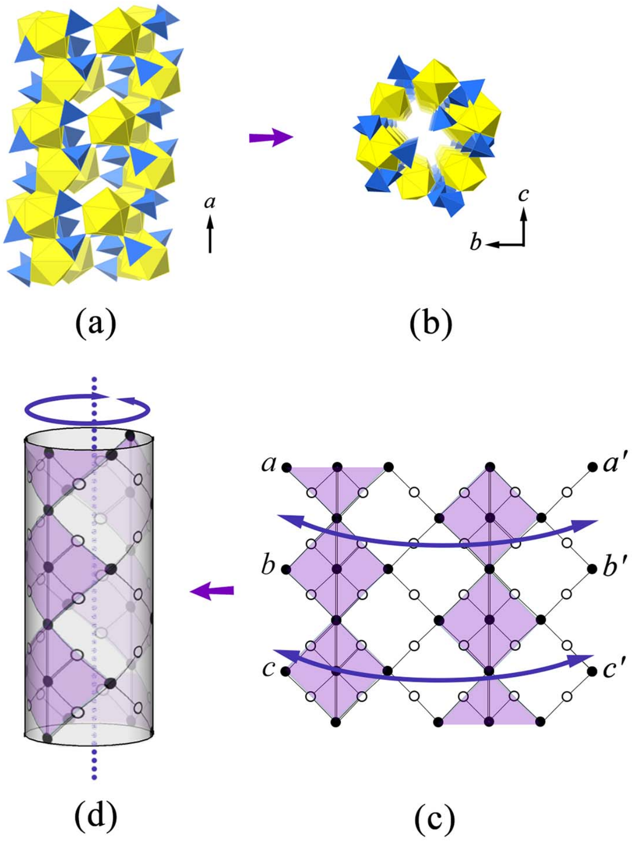

(a) (b)

(d) (c)

Figure 5.6: Channels in the structure of $Th_3(CrO_4)_6(H_2O)_8{\cdot}(H_2O)_6$.

two sides of the tapes (the equivalently opposite sides are labels as a, a'; b, b'; c, c'). In this way, the eight-member pores in the unfold version can be obviously converted to voids along [011], [01$\bar{1}$] and [0$\bar{1}$1] with the sizes of $3.9 \times 2.0\,\text{Å}^2$.

Structure of $Li_2Th_4(CrO_4)_9$

$Li_2Th_4(CrO_4)_9$ crystallizes in space group $I\bar{4}3d$. Its structural backbone can be considered as a 3D framework built from ThO_9 and MoO_4 polyhedra connected in corner-sharing manner, shown in **Figure 5.7**. There only one symmetrically unique Th cation is connected by nine O atoms to create a tricapped trigonal prismatic coordination geometry, a typical Th coordination geometry observed at a large number of inorganic thorium compounds. The positions of Li atoms were not identified owing to their low X-ray scatter efficiency and the high residual peaks in Fourier maps around center heavy Th atoms. The Th-O bond distances, ranging from 2.429(6) Å to 2.479(6) Å with the mean value of 2.450 Å is in good accordance with nine-coordinated Th atoms.[110] There are two independent Cr sites in the structure and each of them is tetrahedrally coordinated by O atoms. $Cr(1)O_4$ demonstrates an ideal tetrahedral geometry with all the Cr-O bond distance the same, *i.e.* 1.644(6) Å. For $Cr(2)O_4$, however, a slight distorted can be observed with the Cr-O bond distances between 1.643(7) and 1.669(6) and O-Cr-O angles ranging from 108.5(3)° to 1111.0(5)° The bond valence summation

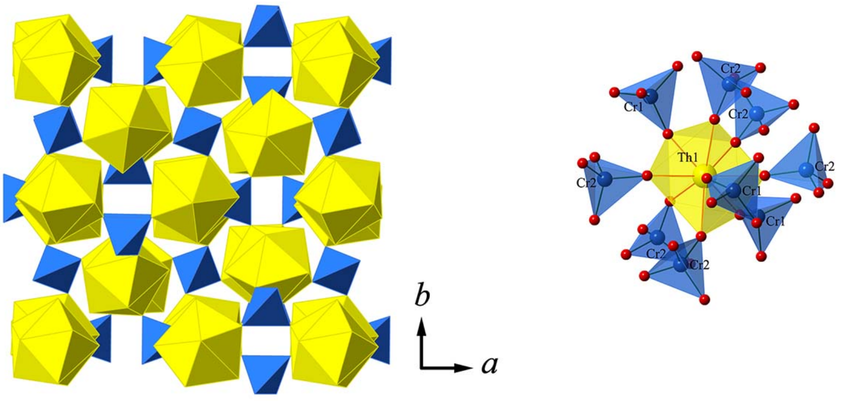

(a) (b)

Figure 5.7: View of the 3D in the structure of $Li_2Th_4(CrO_4)_9$.

calculated for Cr(1) and Cr(2) are 6.00 v.u. and 5.81 v.u. respectively, which confirms well with the 6+ oxidation state of Cr atoms. The $Li_2Th_4(CrO_4)_9$ is isostructural to the structures in the family of $A_2Th_4(MO_4)_9$ (A = Li^+, Cu^+, Tl^+; M = Mo, W) constructed by corner-sharing of ThO_9 and MO_4 polyhedra.[112] However, all the latter compounds were obtained *via* high-temperature solid state synthesis method while $Li_2Th_4(CrO_4)_9$ was synthesized by hydrothermal method. It is interesting to note that the above thorium-based compounds have a similar structural skeleton as the corresponding lanthanide family of $La_4(MoO_4)_3(ReO_4)_6$ in which the Mo^{6+} and Re^{7+} sites are statistically occupied in the same $24d$ wickoff position with the ratio of 2:1.[112]

---

[112] S. Launay et al. *J. Solid State Chem.*, **136**: 199–205, 1998.

Chapter 6

Stereochemistry of Thorium and Uranium Oxo-Selenium/-Tellurium Compounds

This chapter is mainly focusing on the thorium and uranium compounds containing lone electron pairs from Se and Te. Besides, in order to make complete structural comparison, here I also add some of the newly synthesized selenates and tellurates. For selenium compounds, due to the sublimation of Se, the crystals can only be grown from the sealed condition. In total I found four thorium selenium compounds, and the corresponding structural and Raman vibrational descriptions are given in **Chapter 6.1** from **page 82**. Due to the unstable thermal behavior of tellurium compounds, the corresponding crystals can be obtained by either performing the reaction under sealed conditions or reducing the growth temperature.[113–116] Using high-temperature/high-pressure method, several thorium and uranium tellurium compounds were successfully grown, and their structures are discussed in **Chapter 6.2** from **page 93** for thorium compounds and **Chapter 6.3** from **page 99** for uranium compounds, respectively. In fact, a large number of tellurites have been successfully synthesized by the solid-state method using a MoO_3 or WO_3 flux, which allows to grow the crystals at a relative low temperature (below 800 °C).[117,118] However, using MoO_3 or WO_3 as the flux may introduce the Mo or W as the third-party element into the studied system, as the case of my study of thorium tellurium system. I obtained several thorium tellurium compounds with mixed oxo-anions of Mo or W, and their structures and thermal behaviors are discussed in **Chapter 7.1** from **page 123**

Se and Te have extreme diverse structural properties. According to their different oxidation states,

---

[113] A. Guesdon and B. Raveau. *Chem. Mater.*, **12**: 2239–2243, 2000.

[114] Joanna Goodey, Jake Broussard, and P. Shiv Halasyamani. *Chem. Mater.*, **14**: 3174–3180, 2002.

[115] Eun Ok Chi et al. *Chem. Mater.*, **18**: 2070–2074, 2006.

[116] Jun-Ho Kim, Jaewook Baek, and P. Shiv Halasyamani. *Chem. Mater.*, **19**: 5637–5641, 2007.

[117] Weiguo Zhang et al. *Cryst. Growth Des.*, **10**: 4091–4095, 2010.

[118] Junjie Zhang et al. *CrystEngComm*, **13**: 6985–6990, 2011.

namely 4+ or 6+, selenium and tellurium compounds can be classified into two series, selenite/tellurite or selenite/tellurate, respectively. Owing to the existence of the stereochemically active lone-pair electrons in Se^{4+}, the SeO_3^{2-} ions can act as the so-called structure-directing agents to yield relatively large number of structure types with consequently promising physical properties such as second-harmonic generation (SHG), piezoelectricity, ferroelectricity, and magnetic properties.[119–121] Te(IV) can exist in diverse coordination geometries such as $Te^{IV}O_3$ trigonal pyramidal, $Te^{IV}O_4$ disphenoid and $Te^{IV}O_5$ square pyramidal.[122,123] Attributable to the second-order Jahn-Teller (SOJT) distortion, its stereochemically active lone-pair electrons are able to result in asymmetric units, which can produce the noncentrosymmetric or polar structures with interesting physical properties. The coordination geometry of Te(VI) is simpler than that of Te^{4+}, and it is normally found in ubiquitously octahedral $Te^{VI}O_6$ configuration. These TeO_x (x = 3-6) units can further polymerize to produce polytellurites or polytellurates by sharing common corners or edges. Due to the inexhaustible topological arrangements of these tellurium building units, the tellurium compounds have the potential to expand without limitation, forming a fascinating group of clusters[124,125], one-dimensional chains[122,126,127], two-dimensional sheets[128] and three-dimensional framework[129] materials.

6.1 Chemical and structural evolution in the Th-SeO_3^{2-}/SeO_4^{2-} system

While extensive success has been gained in the structural chemistry of the uranium selenium system, the synthesis and characterization of the thorium-based selenium structures are widely unexplored. Here, four new thorium selenium compounds, α-$Th(SeO_3)_2$, β-$Th(SeO_3)_2$, $Th(Se_2O_5)_2$ and $Th_3O_2(OH)_2(SeO_4)_3$ have been obtained from mild hydrothermal or low-temperature (180−220 °C) flux conditions and were subsequently structurally and spectroscopically characterized. The crystal structures of α-$Th(SeO_3)_2$ and β-$Th(SeO_3)_2$ are based on ThO_8 and SeO_3 polyhedra, respectively, featuring a three-dimensional (3D) network with selenite anions filling in the Th channels along the ***a***-axis. $Th(Se_2O_5)_2$ is a 3D framework composed of isolated ThO_8 polyhedra interconnected by $[Se_2O_5]^{2-}$ dimers. $Th_3O_2(OH)_2(SeO_4)_3$ is also a 3D framework constructed by octahedral hexathorium clusters $[Th_6(\mu_3-O)_4(\mu_3-OH)_4]^{12+}$, which are interlinked by selenate groups SeO_4^{2-}. The positions of the vibrational modes associated with both $Se(IV)O_3^{2-}$ and $Se(VI)O_4^{2-}$ units, respectively, were determined for five compounds and the Raman spectra of α- and β-$Th(SeO_3)_2$ are compared

---

[119] Philip M. Almond and Thomas E. Albrecht-Schmitt. *Inorg. Chem.*, **41**: 1177–1183, 2002.
[120] Philip M. Almond and Thomas E. Albrecht-Schmitt. *Inorg. Chem.*, **42**: 5693–5698, 2003.
[121] Fang Kong et al. *J. Am. Chem. Soc.*, **128**: 7750–7751, 2006.
[122] Hyejin Kim et al. *Z. Anorg. Allg. Chem.*, **633**: 473–477, 2007.
[123] M. K. Kim et al. *Inorg. Chem.*, **49**: 7028–7034, 2010.
[124] Song Ping Huang and Mercouri G. Kanatzidis. *J. Am. Chem. Soc.*, **114**: 5477–5478, 1992.
[125] Yu I. Smolin et al. *Crystallogr. Rep.*, **45**: 21–25, 2000.
[126] M. P. Minimol and K. Vidyasagar. *Indian J. Chem. A.*, **42**: 2244–2249, 2003.
[127] Kang Min Ok and P. Shiv Halasyamani. *J. Solid State Chem.*, **179**: 1345–1350, 2006.
[128] T. Sivakumar, Kang Min Ok, and P. Shiv Halasyamani. *Inorg. Chem.*, **45**: 3602–3605, 2006.
[129] Jian Lin et al. *Inorg. Chem.*, **51**: 10083–10085, 2012.

and discussed in detail.

All the titled thorium selenium compounds have been obtained at temperatures around 220 °C. The isolation of α- and β-Th(SeO$_3$)$_2$ from hydrothermal conditions is very likely to be driven by stoichiometry. The reagent ratio of the starting materials controls the formation of these two compounds. α-Th(SeO$_3$)$_2$ is more favored at a low Th: Se ratio and β-Th(SeO$_3$)$_2$ can be present when increasing the amount of Se. Compared to α- and β-Th(SeO$_3$)$_2$, Th(Se$_2$O$_5$)$_2$ obtained using the boric acid as the flux is characterized by a very high Th/Se ratio. This method has been proven to be an effective way to synthesize novel actinide borates in the past few years.[130–135] The borate acid which does not include into the structure of Th(Se$_2$O$_5$)$_2$ serves as the role of reaction medium, its presence, however, without a doubt plays an important role in the process of crystallization. In addition to this, the thorium selenium borates can be formed by modifying the stoichiometry ratio of the starting materials, but this will be part of another publication. Up to now, most of the thorium polynuclear complexes are synthesized *via* slow precipitation method with organic acids as reaction media. To the best of knowledge, Th$_3$O$_2$(OH)$_2$(SeO$_4$)$_3$ is the first inorganic hexanuclear thorium material prepared under hydrothermal conditions. It is noteworthy that the hydrothermal conditions lead to a Th coordination number equal 8 in Th$_3$O$_2$(OH)$_2$(SeO$_4$)$_3$, which is different from the 9-fold coordination environment in the previous reported hexanuclear thorium clusters.[136]

The synthesis process for α- and β-Th(SeO$_3$)$_2$ polymorphs was quite similar. The differences were the ratio and amount of the initial reactants. Our first attempt was to obtain thorium selenium compounds containing alkaline cations. Thus, the sodium nitrate was also included for sample synthesis. For α-Th(SeO$_3$)$_2$, 100 mg of Th(NO$_3$)$_4$·(H$_2$O)$_5$ (0.175 mmol), 58.4 mg SeO$_2$ (0.526 mmol), 74.5mg NaNO$_3$ (0.877 mmol) and 4 ml H$_2$O were weighed in. This results in a Th:Se:Na ratio of 1:3:5. For β-Th(SeO$_3$)$_2$, 100 mg of Th(NO$_3$)$_4$·(H$_2$O)$_5$ (0.175 mmol), 19.5 mg SeO$_2$ (0.175 mmol), 44.7mg NaNO$_3$ (0.526 mmol) and 4 ml H$_2$O were weighed in. This results in a Th:Se:Na ratio of 1:1:3. The mixtures were filled in 23 ml autoclaves and placed inside a program-controlled furnace (MEMMERT). They were heated up with 100 °C/h to 220 °C and held there for roughly 48 hours. The furnace was then cooled down to room temperature with a cooling rate of 4.2 °C/h. Apparently, the sodium was not incorporated into both structures. The α-Th(SeO$_3$)$_2$ crystals were colorless and shaped as long prisms, while for β-Th(SeO$_3$)$_2$, the shape however was more compact and didnt show any elongation into a specific direction.

Th(Se$_2$O$_5$)$_2$ was synthesized by the low-temperature flux method. 100 mg of Th(NO$_3$)$_4$·(H$_2$O)$_5$ (0.175 mmol), 97.3 mg SeO$_2$ (0.877 mmol) and 216.9 mg H$_3$BO$_3$ (3.5 mmol) were weighed in.

---

[130] Shuao Wang et al. *Chem. Commun.*, **46**: 3955–3957, 2010.

[131] Shuao Wang et al. *Angew. Chem. Int. Ed.*, **49**: 1057–1060, 2010.

[132] Shuao Wang et al. *Chem. Commun.*, **47**: 10874–10885, 2011.

[133] Shuao Wang et al. *Inorg. Chem.*, **50**: 2079–2081, 2011.

[134] Shuao Wang et al. *Inorg. Chem.*, **50**: 4692–4694, 2011.

[135] Shuao Wang et al. *Inorg. Chem.*, **51**: 7–9, 2012.

[136] Karah E. Knope and L. Soderholm. *Chem. Rev.*, –, 2012.

This results in a Th:Se:B ratio of 1:5:20. 100 μl of water were added. The temperature profile, however, was slightly different compared to the syntheses of α- and β-Th$(SeO_3)_2$, respectively. The filled autoclave was placed inside the furnace at room temperature and was heated up at a rate of 100 °C/h for two hours to 220 °C. After a holding time of 48 hours, the furnace was cooled down in two steps. First the temperature was gradually reduced at a rate of 1.75 °C/h down to 150 °C and then to room temperature within three hours. Apparently the boron played the part of a flux during the crystal growth process and was not incorporated into the structure.

$Th_3O_2(OH)_2(SeO_4)_3$ was obtained by using hydrothermal synthesis. An initial ratio of the reactants of 1:1 for Th:Se resulted in the reported structure. That is to say, 100 mg of $Th(NO_3)_4{\cdot}(H_2O)_5$ (0.175 mmol), 19.5 mg SeO_2 (0.175 mmol) and 0.2 ml of 1M HCl (0.2 mmol) were weighed in and the autoclave was loaded with an additional small amount of water (2 ml). The furnace containing the autoclave was heated up from room temperature to 220 °C in two hours, keeping the temperature constant for about 48 hours. Cooling down to room temperature was also done in about 48 hours at a constant cooling rate of 4.2 °C/h. The product of this synthesis resulted in, typical for Th(IV), colorless crystals.

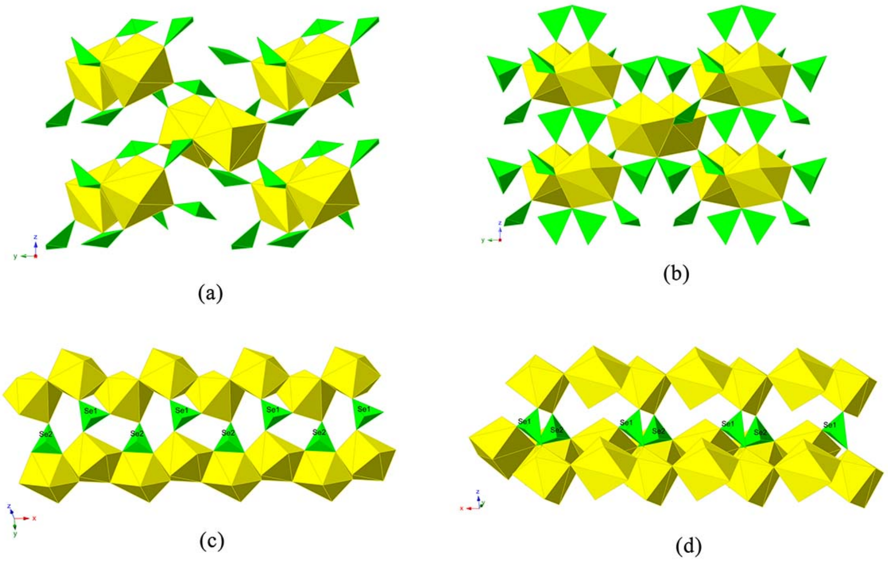

(a) (b) (c) (d)

Figure 6.1: Polyhedral representation of the structures of two polymorphs of $Th(SeO_3)_2$. (a) 3D framework in α-$Th(SeO_3)_2$. (b) 3D framework in β-$Th(SeO_3)_2$. (c) The linkage manners for Se sites in α-$Th(SeO_3)_2$. (d) The linkage manners for Se sites in β-$Th(SeO_3)_2$. Blue and orange polyhedral represent ThO_8 and SeO_3, respectively.

6.1.1 Structural and topological relationship in Th-Se family

α-Th$(SeO_3)_2$

The α-Th$(SeO_3)_2$ polymorph, crystallizing in the monoclinic system with space group $P2_1/n$, contains one independent Th position and two Se sites, as shown in **Figure 6.1 (a)**. It adopts the $CeSe_2O_6$[137] structure type, which has also been found in the compounds $CeTe_2O_6$[138], $ThTe_2O_6$, $PuTe_2O_6$[139] and $PuSe_2O_6$[140], respectively. The Th atom is coordinated by eight O atoms with an average Th-O bond distance of 2.42 Å, which fits well with other thorium compounds[105,141]. In order to determine the polyhedral geometry of Th, the shape measuring algorithm was carried out.[142] The output of the algorithm is a value S, which is the minimal variance of all dihedral angles along all edges. The lower this value, the higher is the resemblance to the ideal polyhedron. The obtained S values ($S(D_{2d})$= 18.7°, $S(C_{2v})$= 18.3°, $S(D_{4d})$ = 19.5°) demonstrate the bicapped trigonal prism geometry of the Th polyhedra. The coordination type as well as the determined bond angles are comparable to those of other inorganic Th(IV) compounds.[110,143] Se(1) and Se(2) are both coordinated by three O atoms, respectively, in a trigonal pyramid geometry with the Se atom situated at the apical vertex, exhibiting an asymmetric coordination environment which arises from the stereoactive non-bonded electron pairs. Adjacent ThO_8 polyhedra are edge connected with two O atoms, forming corrugated chains extending along the [100] direction. The chains are further linked together to construct the 3D framework with the help of trigonal pyramidal SeO_3 groups. The $Se(1)O_3$ polyhedra share all three O atoms with Th chains in corner-sharing configuration, that is, two O atoms with two ThO_8 from a single chain and the third O atom with another ThO_8 from a different chain. However, the $Se(2)O_3$ groups share a common edge with a ThO_8 polyhedron from one chain and a corner with another chain (**Figure 6.1 (c)**). The different connection geometry result in different bond length configurations for Se(1) and Se(2) despite that both are very similar in their average lengths (1.70 Å). The Se(2) polyhedra are more distorted (from 1.673(6) Å to 1.719(6) Å) compared to Se(1) polyhedra (from 1.698(6) Å to 1.703(6) Å). The related angles in Se(2) also show an abnormal behavior with one notably smaller angle for the edge sharing O atoms (91.7(3)°). The average of 98.3° for Se(2) is slightly smaller than 101.9° for Se(1), but agrees well with other reported values for compounds containing Se(IV) lone-pair electrons. [119,144]

β-Th(SeO$_3$)$_2$

The β-Th(SeO$_3$)$_2$ polymorph adopts an orthorhombic crystal system with the $Pna21$ space group. The structure of this polymorph is presented in **Figure 6.1 (b)**. Similar to α-Th(SeO$_3$)$_2$, it consists of one symmetrically independent Th position and two Se positions. The Th is also coordinated by eight O atoms with an average bond distance of 2.44 Å. Shape measure calculations for the Th polyhedron result in a distorted trigonal dodecahedron. The thorium polyhedra share one common edge with one another, leading to chains propagating along the [100] direction. Notably, there is

---

[137] C. Delage et al. *Acta Crystallogr., Sect. C*, **42**: 1475–1477, 1986.

[138] Steffen F. Meier et al. *Z. Anorg. Allg. Chem.*, **627**: 2448–2450, 2001.

[139] K. Krishnan, K. D. S. Mudher, and V. Venugopal. *J. Alloys Compd.*, **307**: 114–118, 2000.

[140] Travis H. Bray et al. *J. Solid State Chem.*, **181**: 493–498, 2008.

[105] Bin Xiao et al. *Cryst. Growth Des.*, **14**: 2677–2684, 2014.

[141] Bin Xiao et al. *Inorg. Chem.*, **53**: 3088–3098, 2014.

[142] Jide Xu et al. *Inorg. Chem.*, **39**: 4156–4164, 2000.

[110] Tyler A. Sullens and Thomas E. Albrecht-Schmitt. *Inorg. Chem.*, **44**: 2282–2286, 2005.

[143] Geng Bang Jin and L. Soderholm. *J. Solid State Chem.*, **184**: 337–342, 2011.

[144] Philip M. Almond et al. *J. Solid State Chem.*, **168**: 358–366, 2002.

a broad range of distances for the Th-O bonds from 2.32(2) to 2.77(1) Å. The average Se-O bond distances, with 1.70 Å and 1.71Å for Se(1) and Se(2), respectively, are in agreement with expected bond lengths.[119,144] Similar to α-Th(SeO_3)$_2$, both Se sites are coordinated by three O atoms forming trigonal pyramidal polyhedra. The lone pairs of the Se(2) atoms are orientated into the negative **c** direction, however, such a distinct behavior cannot be observed for Se(1) atoms owing a more cluttered distribution of their lone pairs. Similar to α-Th(SeO_3)$_2$, the SeO_3 polyhedra in β-Th(SeO_3)$_2$ also function as a linkage to bridge the Th chains to yield a 3D framework. The Se(1)O_3 polyhedra connect three different Th chains by sharing all three corners, whereas, Se(2)O_3 polyhedra share an edge with a ThO_8 polyhedron from one chain and a corner with another ThO_8 polyhedron from a different chain (**Figure 6.1 (d)**).

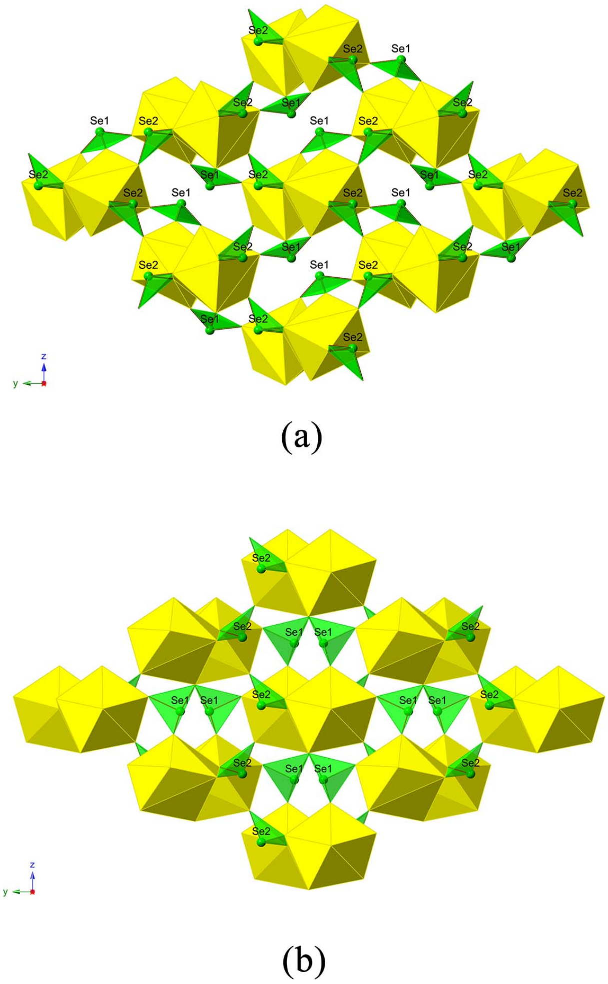

(a)

(b)

Figure 6.2: The orientation of lone pairs of SeO_3^{2-} in (a) α-Th(SeO_3)$_2$ and (b) β-Th(SeO_3)$_2$, respectively.

Comparison of α-Th(SeO_3)$_2$ and β-Th(SeO_3)$_2$

Both 3D framework polymorphs are built from the edge-sharing ThO_8 polyhedra forming chains parallel to the [100] direction, which are further connected by SeO_3 trigonal pyramids. The calculated densities for both polymorphs are rather similar (5.885 $\mathrm{g/cm^3}$ and 6.072 $\mathrm{g/cm^3}$ for α- and β-$Th(SeO_3)_2$, respectively). The symmetry of the α-polymorph, monoclinic, is lower compared to the orthorhombic β-polymorph. Using empirical parameters according to Brese and OKeefee[106], the bond valence calculations give bond valence sums for α-$Th(SeO_3)_2$ of 4.16 v.u. (valence units) for Th, 4.04 v.u. for Se(1), and 4.06 v.u. for Se(2), respectively. For β-$Th(SeO_3)_2$ bond valence calculations for Th, Se(1) and Se(2) yield 4.00 v.u. for all three elements. These values fit very well to the expected ones for Th(IV) and Se(IV).

A major difference between these two structures is the interior of the apparently empty voids between adjacent ThO_8 polyhedra chains, where the lone pairs of selenite groups ($SeO_3{}^{2-}$) are present. **Figure 6.2** shows the channels accommodated with the selenite polyhedra. For the α-polymorph, the lone pairs of both Se(1) and Se(2) sites are oriented vertically to the chain direction. For the β-polymorph, however, these lone pairs are directing parallel and vertical to the chain direction for Se(1) and Se(2), respectively. The second difference is the coordinating behavior of the $SeO_3{}^{2-}$ groups. One can see that the distance between the up-most O atoms of neighboring ThO_8 polyhedra along the Th chain direction is larger for the β-polymorph. The distance is 2.707 Å for the α-polymorph and 3.612 Å for the β-polymorph, respectively, which is too large for the $SeO_3{}^{2-}$ group to corner share these O sites in the β-polymorph.

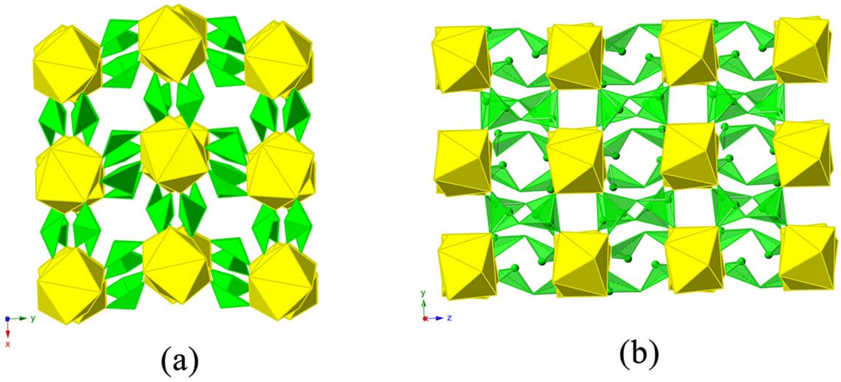

(a)
(b)

Figure 6.3: View of the structure of $Th(Se_2O_5)_2$ along the (a) [001] and (b) [100] directions, respectively demonstrating the connection of ThO_8 polyhedra and $Se_2O_5{}^{2-}$ dimers.

$Th(Se_2O_5)_2$

Using the low-temperature flux method, another new thorium selenite structure was found with the formula $Th(Se_2O_5)_2$, which is shown in **Figure 6.3**. The symmetry is orthorhombic with space group $Pbca$. The average Th-O bond length is 2.404 Å. The average Se-O bond length of 1.706 Å fits well to that of other reported selenite groups.[119,144] Shape measure calculations indicate disordered trigonal dodecahedra geometry for Th atoms. Each $SeO_3{}^{2-}$ trigonal pyramid shares two corners with two Th

---

[106] NE Brese and M O'keeffe. *Acta Crystallographica Section B: Structural Science*, **47**: 192–197, 1991.

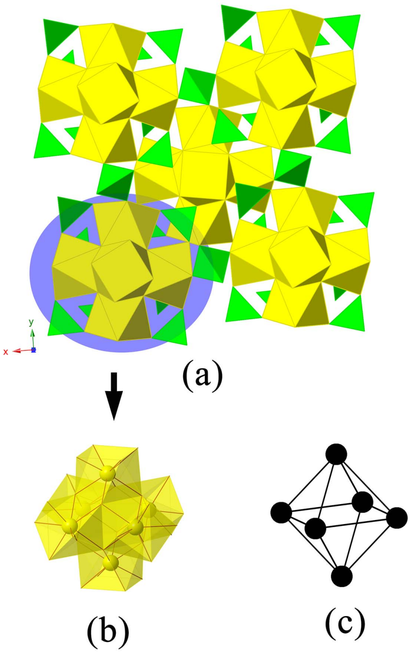

Figure 6.4: (a) View of the 3D structure $Th_3O_2(OH)_2(SeO_4)_3$ (b) The hexanuclear cluster $[Th_6(\mu_3{-}O)_4(\mu_3{-}OH)_4]^{12+}$ (c) Schematic representation of the corresponding octahedron composed by the six Th ions.

polyhedra and the third one with another selenite polyhedron to yield a $Se_2O_5{}^{2-}$ dimer. The ThO_8 polyhedra are corner-linked to $Se_2O_5{}^{2-}$ dimers, thus completing the 3D framework. The positions where the O atoms are bonded to two selenium atoms each all lie within a plane parallel to (001) (**Figure 6.3** (b)). This is the reason why the c parameter is the largest, as the ThO_8 polyhedra are connected directly by $Se_2O_5{}^{2-}$ dimers.

$Th_3O_2(OH)_2(SeO_4)_3$

Using hydrothermal acidic conditions, a new thorium selenate was found with the formula $Th_3O_2(OH)_2(SeO_4)_3$. It is interesting that $Th_3Se_3O_{14}(OH)_2$ is similar to tetravalent uranium and cerium hydroxosulfate ($U_6O_4(OH)_4(SO_4)_6$[145] and $Ce_6O_4(OH)_4(SO_4)_6$[146]respectively). The 3D framework structure adopts a tetragonal system with space group $I4/m$, consisting of $[Th_6(\mu_3{-}O)_4(\mu_3{-}OH)_4]^{12+}$ clusters put together by six Th(IV) atoms. As shown in **Figure 6.4**, these six Th atoms form a nearly regular octahedron with Th-Th distances ranging from 3.9354(6) to 3.9735(6) Å. The eight faces of the resulting octahedron are bridged by either μ_3O or μ_3OH groups. In terms of charge balance, here, the μ_3O and μ_3OH have to be present in equal numbers. Because of the low X-ray scatter efficiency and high residual peaks surrounding the heavy atoms (Th), the hydrogen positions were not determined with single crystal diffraction measurement. Besides, the vibrational frequencies at around 3000 cm^{-1} also show the evidence of OH groups (see Raman Spectra section). The existence of the protonated μ_3OH groups within the structure also agrees with the lowest energy configuration obtained by DFT calculations on the hexameric Th cores.[147] Basic structural feature which fundamentally distinguishes

---

[145] G. Lundgren. *Arkiv foer Kemi*, **5**: 349–363, 1952.

[146] G Lundgren. *Arkiv for Kemi*, **10**: 183–197, 1956.

[147] Monica Vasiliu et al. *J. Phys. Chem. A*, **116**: 6917–6926, 2012.

μ_3OH from μ_3O sites is a difference in Th-OH and Th-O bond distances. For instance, the presence of Th-μ_3OH and Th-μ_3O bond values in hexanuclear Th based cloroactate are 2.486−2.514 Å and 2.291−2.315Å, respectively.[148] However, due to the high symmetric crystal system, the observed difference for Th-μ_3O(H) bond distances in $Th_6O_4(OH)_4(SeO_4)_6$, from 2.426(11)−2.448(12) Å, are negligible. The indistinguishable Th-O/OH phenomenon is also reported in several other hexanuclear Th compounds with μ_3O/OH$^-$bridging.[148] Each Th atom achieves the eightfold coordination, by attachment of four O atoms from μ_3-O/OH and four O atoms from four $SeO_4{}^{2-}$ groups. The shape measure calculations resulted in approximating square antiprism geometry for both Th sites. Inside the clusters, the Th(1)O_8 square antiprism shares corners with four separate SeO_4 tetrahedra, two of which are Se(1) and the other two are Se(2), whereas, the Th(2)O_8 are exclusively connected with four Se(1) tetrahedra. The Se(1) tetrahedra exhibit an average bond length of 1.625 Å and bond angles ranging from 108.2(6)° to 112.7(1)°. They are within the expected range of selenate ions, since they form an almost tetrahedron with an average bond angle of 109.5°. Se(2) tetrahedra with an average bond distance of 1.639 Å and angles in the range of 107.3(3) ° to 113.8(7) ° are also in compliance with expected values. The Se(1) tetrahedra connect three different $[Th_6(\mu_3{-}O)_4(\mu_3{-}OH)_4]^{12+}$ clusters by corner sharing with two Th polyhedra from one cluster and two Th polyhedra from other two different clusters (See **Figure 6.5 (a)**). Compared to the Se(1), the Se(2) tetrahedra share all their four O vertexes connecting four separate $[Th_6(\mu_3{-}O)_4(\mu_3{-}OH)_4]^{12+}$ clusters (See **Figure 6.5 (b)**).

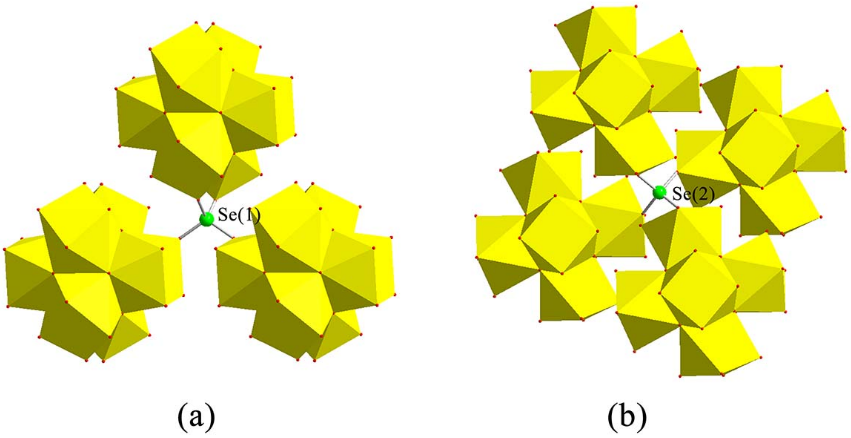

Figure 6.5: (a) Representation of the linkage of Se(1) in the structure of $Th_3O_2(OH)_2(SeO_4)_3$. (b) Representation of the linkage of Se(2) in the structure of $Th_3O_2(OH)_2(SeO_4)_3$.

Comparing already isolated hexanuclear thorium clusters,[148–150] no incorporated water was found in the crystal structure of $Th_3O_2(OH)_2(SeO_4)_3$. The fact that similar plutonium clusters $[Pu_6(OH)_4O_4]^{12+}$ have been found recently underlines the possibility for using such structures to understand the hy-

---

[148] Karah E. Knope et al. *Inorg. Chem.*, **50**: 9696–9704, 2011.

[149] Shinobu Takao et al. *Eur. J. Inorg. Chem.*, **2009**: 4771–4775, 2009.

[150] Christoph Hennig et al. *Dalton Trans.*, **41**: 12818–12823, 2012.

drolysis trends in actinide chemistry. [151]

6.1.2 Raman spectroscopic analysis

The ideal $SeO_3{}^{2-}$ trigonal pyramid has a C_{3v} symmetry consisting of four vibrational frequencies: two non-degenerate ν_1 and ν_2 modes and the other two doubly degenerate ν_3 and ν_4 modes.[152,153] For each $Th(SeO_3)_2$ polymorph, there are totally 108 normal vibrational modes ($27A_g$ + $27A_u$ + $27B_g$ + $27B_u$ and $27A_1$ + $27A_2$ + $27B_1$ + $27B_2$ for α and β polymorphs, respectively) predicted by the factor group analysis, with some of them being acoustic modes.[154] **Figure 6.6** shows the Raman spectra for both the α- and β-polymorphs of the $Th(SeO_3)_2$ in the range of 100−1050 cm^{-1}. The most intense peak, around 855 cm^{-1} in both cases, is expected to be assigned to the symmetric stretching vibration ν_1. This position is slightly shifted from 858(1) cm^{-1} for α to 854(1) cm^{-1} for β, and well consistent with that determined for a series of alkali selenites by *Cody* and *Micka*.[155] The asymmetric stretching vibration ν_3, on the other hand, behaves quite different in both polymorphs. For the α-polymorph, there are five obvious peaks at approximately 659, 682, 701, 722 and 749 cm^{-1} located in the ν_3 vibrational range whereas, for the β-polymorph only two broad bands of strong intensity (692(1) and 740(1) cm^{-1}) are observed for this mode. The difference in the bending vibration ν_2 is tiny; both consist of peaks at similar wavenumbers occurring from 450 cm^{-1} to 515 cm^{-1}. A comparison may be made with the vibrational spectra of mineral mandarinoite, in which the ν_2 modes are located between 449 and 461 cm^{-1}.[156] The ν_4 bending mode again shows a big difference. The α-polymorph shows a clear peak at 402(1) cm^{-1} while there is no corresponding peak detected for the β-polymorph. Another weak peak at around 363 cm^{-1} may also be attributed to ν_4 for the α-polymorph. The vibrations for both spectra in the range 100 to 330 cm^{-1} are mainly due to the coupling modes among O-Th-O bends and lattice vibrations.[157,158]

From **Figure 6.7**, the observed Raman shifts from 300 to 1000 cm^{-1} for $Th(Se_2O_5)_2$ are quite similar to those of $Cu(Se_2O_5)$, a compound the vibrational properties of which has been discussed by *Choi, et al.* by comparing the polarized Raman spectra at different temperatures.[159] This clearly identifies the presence of diselenite units in the compound of $Th(Se_2O_5)_2$. Similar to $Cu(Se_2O_5)$, due to the existence of a high number of crystallographically distinct Se sites in the asymmetrical unit of $Th(Se_2O_5)_2$, more vibrational bands in the stretching region (such as 769(1) and 788(1) cm^{-1}) are detected.

The Raman spectrum shown in **Figure 6.7** for the $Th_3O_2(OH)_2(SeO_4)_3$ structure was recorded in

---

[151] Karah E. Knope and L. Soderholm. *Inorg. Chem.*, **52**: 6770–6772, 2013.

[152] R. Ratheesh et al. *Spectrochim. Acta, Part A*, **51**: 1509–1515, 1995.

[153] Laurie L. Dussack, William T. A. Harrison, and Allan J. Jacobson. *Mater. Res. Bull.*, **31**: 249–255, 1996.

[154] D. L. Rousseau, R. P. Bauman, and S. P. S. Porto. *J. Raman Spectrosc.*, **10**: 253–290, 1981.

[155] C. A. Cody et al. *J. Solid State Chem.*, **26**: 281–291, 1978.

[156] Ray L. Frost and Eloise C. Keeffe. *J. Raman Spectrosc.*, **40**: 42–45, 2009.

[157] B. L. Khandelwal and V. P. Verma. *J. Inorg. Nucl. Chem.*, **38**: 763–769, 1976.

[158] Ray L. Frost and Eloise C. Keeffe. *J. Raman Spectrosc.*, **40**: 128–132, 2009.

[159] K.-Y. Choi, P. Lemmens, and H. Berger. *Phys. Rev. B*, **83**: 174413–, 2011.

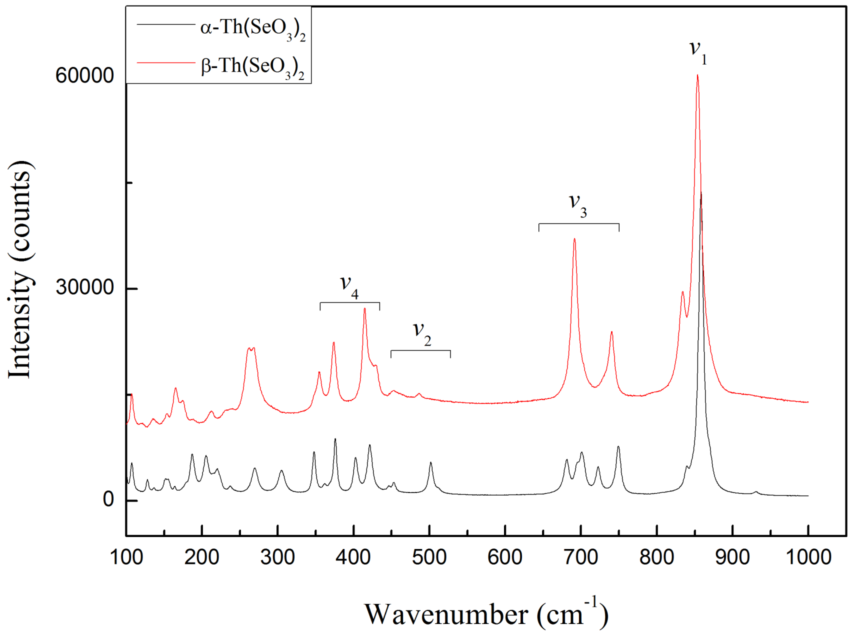

Figure 6.6: Comparison of Raman shifts for α- and β-polymorphs of the Th(SeO$_3$)$_2$.

the range 100 to 3000 cm^{-1}. For the $SeO_4{}^{2-}$ tetrahedral group, the structural appearance results in four normal modes which are all Raman active. These modes are the symmetric stretch ν_1, the asymmetric stretch ν_3 and two bending modes ν_2 and ν_4. For free $SeO_4{}^{2-}$ ions in aqueous solution, these frequencies are distributed at 833 (ν_1), 335 (ν_2), 875 (ν_3) and 432 cm^{-1} (ν_4), respectively. Within solid-state compounds, however, these modes are expected to shift due to mutual interactions and crystal-field effects.[160] The corresponding values are described by *Socrates, et al.* to be 750−830 cm^{-1} for ν_1, 300−370 cm^{-1} for ν_2, 830−935 cm^{-1} for ν_3 and 350−450 cm^{-1} for ν_4.[161] The ν_1 peak is said to be the most intense followed by ν_3, and subsequently by the bending modes. In $Th_3O_2(OH)_2(SeO_4)_3$, the spectrum can be coarsely divided into three different parts. The first part is a low-frequency part within the range of 100 to 250 cm^{-1} and it can be assigned to lattice modes. The mid-frequency range part of 300 to 1000 cm^{-1} is mostly associated with the internal motions within the $SeO_4{}^{2-}$ tetrahedra. The third part around 3000 cm^{-1} belongs to the high-frequency part showing the vibrational behavior of hydroxyl units. As can be seen in **Figure** 6.7, the Raman spectrum in the lower frequency range (from 100 to 250 cm^{-1}) has a weak signal to noise ratio, and therefore no direct information can be taken from this range. The mid-frequency range contains a lot of strong bands and these can partly be assigned to distinct modes. The bands located at 328(1) cm^{-1} and at 349(1) cm^{-1} might be assigned to the ν_2 bending mode. The ν_4 bending mode is most likely resembled by the 465(1) cm^{-1} band. The weak band at 515(1) cm^{-1} can possibly be assigned to Th-O stretching. *Knope, et al.* investigated similar clusters containing octanuclear cores and they found the Th-O stretch to be at 528 cm^{-1}.[162]

---

[160] Geng Bang Jin, S Skanthakumar, and L Soderholm. *Inorg. Chem.*, **51**: 3220–3230, 2012.

[161] George Socrates and G Socrates. *Infrared and Raman characteristic group frequencies: tables and charts*. vol. 245 Wiley Chichester, 2001.

[162] Karah E. Knope et al. *Inorg. Chem.*, **51**: 4239–4249, 2012.

The strong peak at 910(1) cm^{-1} is associated with the ν_1 stretch of the selenate ion. The two bands at 932(1) cm^{-1} and 947(1) cm^{-1} might be corresponding to the ν_3 mode of the selenate group. In general, the two assigned stretching modes appear to be at slightly higher wave numbers than those for free selenate ions. Owing to the low Raman scattering intensities property of the OH$^-$ group, bands in the high-frequency range just below 3000 cm^{-1} are low in the signal to noise ratio. These shifts are comparable to the spectra of guilleminite (observed also at around 3000 cm^{-1}).[163]

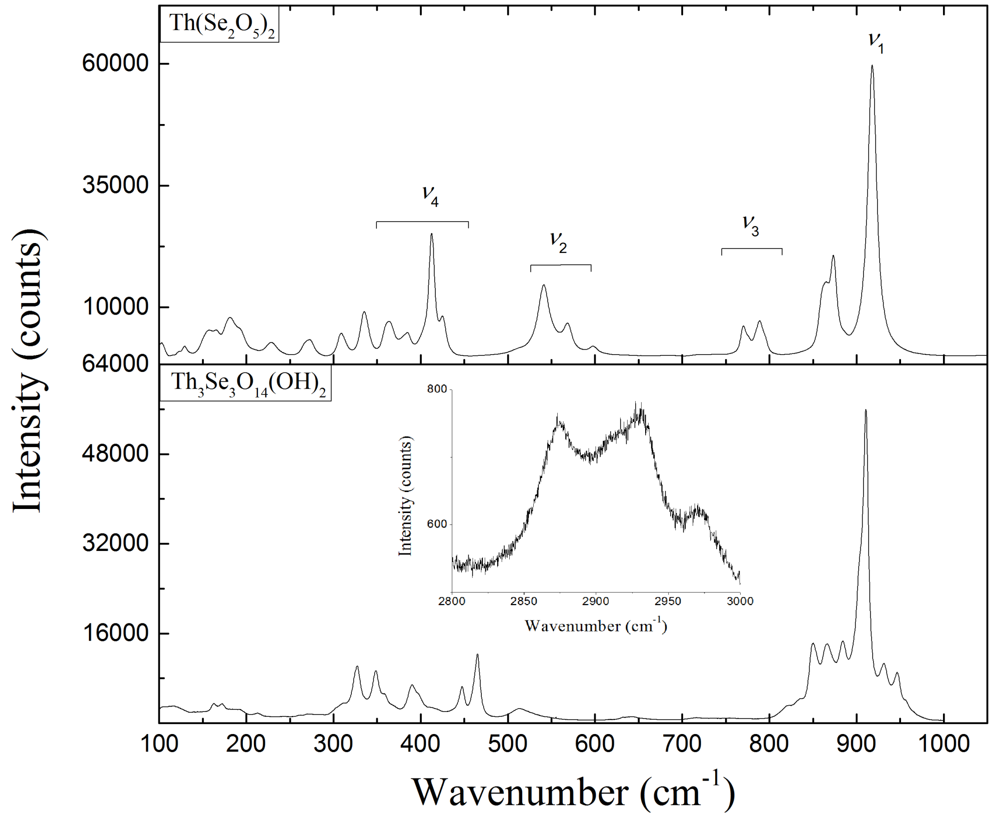

Figure 6.7: Raman shifts in the compounds of $Th(Se_2O_5)_2$ and $Th_3O_2(OH)_2(SeO_4)_3$, respectively.

6.1.3 Conclusion

The compounds discussed here, containing SeO_4^{2-}, SeO_3^{2-} and $Se_2O_5^{2-}$ units, display an outstanding diversity regarding the coordination geometry of selenium cations. α- and β-$Th(SeO_3)_2$ are based on similar structural skeletons but differ mainly with respect to the orientation of SeO_3^{2-} trigonal pyramids. It is clear that due to a lack of oxygen connections between neighboring ThO_8 polyhedra in $Th(Se_2O_5)_2$, all ThO_8 polyhedra are thoroughly isolated from each other by neighboring $Se_2O_5^{2-}$ units. $Th_3O_2(OH)_2(SeO_4)_3$ is by far the first inorganic compound containing hexanuclear thorium clusters. The Raman spectra show the typical vibrational modes for selenites and selenates in studied

---

[163] Ray L. Frost, Ji ejka, and Marilla J. Dickfos. *J. Raman Spectrosc.*, **40**: 355–359, 2009.

phases with local features respected their symmetry. These four new thorium selenium compounds, together with another previously published $Th(SeO_3)(SeO_4)$ compound become a cornerstone for studying other actinide complexation, such as Np(IV) and Pu(IV), in oxo-selenium systems. It is clear that the introduction of counter cations, such as alkali or alkaline earth metals, will generate more chemically and structurally complex phases in studied systems.

6.2 New structural features of thorium oxo-tellurium family obtained from extreme condition

The crystal structures reported for thorium oxo-tellurium family are very poor. The only representative in thorium oxo-tellurium family with refined crystal structure is $ThTe_2O_6$, which was obtained more than 30 years ago from solid-state method at a temperature of 700 °C.[164] This compound adopts the $CeSe_2O_6$[137] structural type, which has also been found in the compounds of $CeTe_2O_6$[138], $PuTe_2O_6$[139], $PuSe_2O_6$[140] and α-$ThSe_2O_6$[165]. Following this, recently, the compound $Th_{13}Te_{24}O_{74}$ was reported for the reaction of ThO_2 and TeO_2 with molar ratio of 13:24 in a sealed ampoule at 700 °C.[166] However, only its powder diffraction patterns were characterized, and no single structural analysis was performed on this material. In order to understand the structural chemistry of these compounds that may lay a basis for nuclear energy and environmental application.

All the thorium oxo-tellurium compounds are prepared form at the temperature of 1100 °C and pressure of 3.5 GPa. The detailed procedures are the same as for HT/HP$-ThMo_2O_8$ in the page of 19. Specially, $Th_2Te_3O_{11}$ was synthesized by mixing 20.0 mg of $Th(NO_3)_4(H_2O)_5$, 30.8 mg of TeO_3 and 6.1 mg of $Na_2S_2O_4$. This leads to an approximate ratio of Th: Te: S to 1: 5: 2. $Na_4Th_2(Te_3O_{15})$ was obtained using the same temperature steps as those of $Th_2Te_3O_{11}$. Loading 20.0 mg of $Th(NO_3)_4(H_2O)_5$, 11.2 mg of TeO_2 and 6.0 mg of NaNO3 into a Platinum capsule. $K_2Th(TeO_3)_3$ was prepared through mixing 20.0 mg of $Th(NO_3)_4(H_2O)_5$, 61.6 mg of TeO_3 and 78.5 mg of KCl. This leads to an approximate ratio of reactants of Th: Te: K = 1: 10: 30. $Th(TeO_3)(SO_4)$ was prepared through mixing 20.0 mg of $Th(NO_3)_4(H_2O)$, 5.6 mg of TeO_2 and 6.1 mg of $Na_2S_2O_4$. This leads to the ratio of Th: Te: S equals 1: 1: 2. β-$Th(TeO_3)(SO_4)$ was synthesized by following the similar procedures for making the $K_2Th(TeO_4)_3$. The crystals have light yellow coloration and were isolated for crystallographic studies.

6.2.1 Crystal structure analysis

$Th_2Te_3O_{11}$

The $Th_2Te_3O_{11}$ is crystallized in $P2_1/c$ space group, exhibiting a complicated 3D framework in which

---

[164] A. I. L. Botto and E. J. Baran. *Z. Anorg. Allg. Chem.*, **484**: 215–220, 1982.

[165] Bin Xiao et al. *Inorg. Chem.*, **54**: 3022–3030, 2015.

[166] SN Tripathi, SN Achary, and PN Namboodiri. *Powder Diffr.*, **17**: 32–36, 2002.

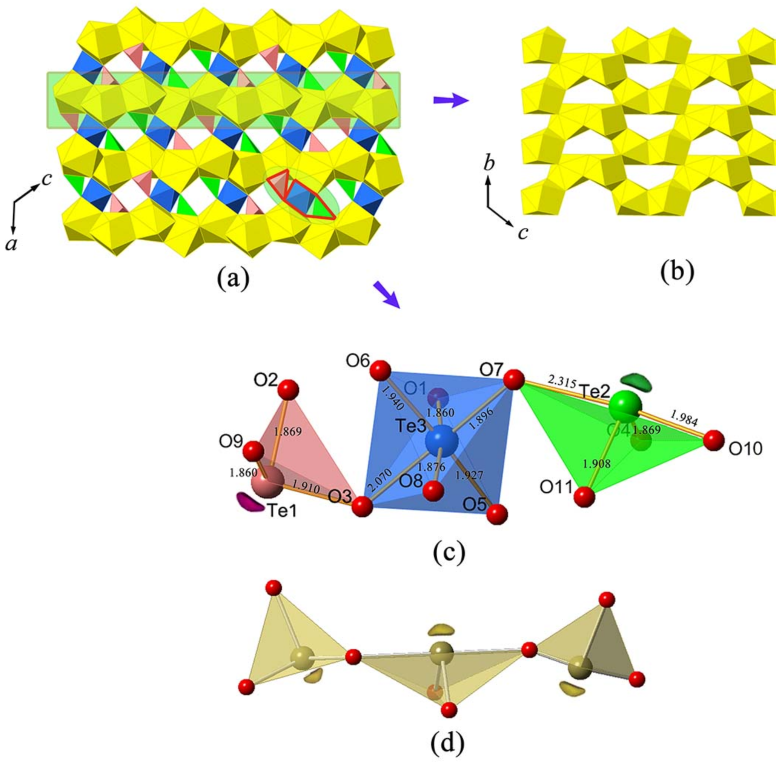

Figure 6.8: View of the structure of $Th_2Te_3O_{11}$. (a) Projection of the $Th_2Te_3O_{11}$ along [010] direction. The structure can be considered as composed of thorium sheets with tellurium fragments in between (b) View of the thorium sheets along [100] direction. (c) The local coordination environment of tellurium fragment with the formula of $[Te_3O_{11}]^{8-}$. (d) The $[Te_3O_8]^{4-}$ anion fragment observed in the lanthanide alkaline-earth tellurite of $La_2Ba(Te_3O_8)(TeO_3)_2$ bears an analog to that found in $Th_2Te_3O_{11}$.

the thorium layers are interconnected by tellurium fragments (see **Figure 6.8 (a)**). There are two crystallographically different Th and three Te sites in an asymmetric unit. Both Th sites are nine-fold coordinated, forming in a distorted capped square antiprismatic configuration. The Th(1)-O bond distances ranging from 2.210(10) to 2.649(9) Å are slight wider than those of Th(2) which range from 2.260(10) to 2.633(10) Å), but are still comparable with those in other thorium tellurium compounds.[110] These two ThO_9 polyhedra are connected with each other though common edges, resulting in corrugated Th layers that stretch along *bc* plane. It is of interest that such layers with the same topological linkages are also observed in a series of lanthanide-bearing tellurium compounds, $M_2Te_4O_{11}$ (M = La-Nd and Sm-Yb).[167] Similar to the structure of $Th_2Te_3O_{11}$, the tellurium units in these latter compounds are also found being embedded between lanthanide layers.

As the case of Te sites, the $Te^{IV}(1)$ and $Te^{IV}(2)$ are in tetravalent oxidation with lone-pair electrons, while $Te^{VI}(3)$ is observed in hexavalent oxidation. $Te^{IV}(1)$ site is coordinated by three O atoms resulting in a more frequently observed TeO_3 trigonal geometry with the lone pairs occupying the

---

[167] Steffen F Meier and Thomas Schleid. *Zeitschrift fr Naturforschung B*, **59**: 881–888, 2004.

pyramidal site. The bond distances and angles in TeO_3 are from 1.860(11) to 1.915(10) Å and from 90.1(5) to 96.0(4)°, respectively. Up to now, all the are exclusively in this geometry. The $Te^{IV}(2)$ is found to be surrounded by four oxygen atoms, forming in a disphenoidal geometry. The Te-O lengths are in the range of 1.868(10)–2.324(10) Å, which are consistent with reported Te^{IV} in fourfold coordination.[127,168] The six-coordinated $Te^{VI}(3)$ site is in a distorted octahedral geometry. The $Te^{VI}(3)$-O bond distances exhibit three short (from 1.861(11) to 1.886(10) Å) and three long Te-O (from 1.926(11) to 2.062(10) Å) bonds. It is noteworthy that $Te(3)O_6$ is highly polarized attributable to the lone-pair electrons from $Te^{IV}(1)$ cations near to this octahedral site. The distortion can be especially observed from the bonded oxygen atoms, which is denoted by the longest Te-O distance (2.062(10) Å) in this direction.

A unique feature of $Th_2Te_3O_{11}$ is the presence of mixed-valent tellurium in three different polyhedral geometries (TeO_4, TeO_5 and TeO_6). These Te polyhedra are fused together by sharing *trans*-corners of $Te^{VI}(3)O_6$ octahedron, leading into a $[Te_3O_{11}]^{8-}$ fragment, shown in **Figure 6.8 (c)**. In a construction perspective, the resulting $[Te_3O_{11}]^{8-}$ fragment is very similar to the $[Te_3O_8]^{4-}$ anion found in the lanthanide tellurite of $La_2Ba(Te_3O_8)(TeO_3)_2$ (see **Figure 6.8 (d)**).[169] In the latter structure, these anion fragments also play a role of linkage to cross-connect adjacent lanthanum-tellurium layers. It is noteworthy that the mixed-valent tellurium with three kinds of coordination geometries is the first time with respect to the tellurium chemistry. Most reported tellurium compounds contain Te cations only in one or two coordination geometries with the corresponding oxidation state of either tetravalent or hexavalent. There has been a report of two isostructural tellurium compounds, $NH_4ATe_4O_9{\cdot}2\,H_2O$ (A = Rb or Cs), which simultaneously embrace three different coordination of tellurium(+4): pyramidal TeO_3, disphenoid TeO_4 and square pyramidal TeO_5.[168] All the $Te^{IV}O_x$ polyhedra feature a stereo-active lone-pair that severely polarizes their local coordination environment. Both compounds are constructed from condensed oxo-tellurite layers that is composed of corner- and edge-sharing of $Te^{IV}O_x$ (x = 3, 4, 5) polyhedra.

The structure of $Th_2Te_3O_{11}$ can also be portrayed as based on the fundamental building block of infinite pseudo-channels, shown in **Figure 6.9 (a)**. These pseudo-channels, with elliptic-shaped cross-sections, are constructed from a skeleton of ThO_9 and TeO_6 polyhedra with a pair of either TeO_3 or TeO_4 filled in the center (see **Figure 6.9 (b)**). In order to describe the interior polyhedral linkages around the channel structure, here one can cut and unfold the associated cylindrical channel into 2D plane, exhibited in **Figure 6.9 (c, d)**. The planes shown in **Figure 6.9 (d)** are formed from an assemblage of Th_2O_{16} dimers and TeO_6 octahedra, which are connected by means of both corner- and edge-sharing manners. The corresponding nodal presentation of plane topology is shown in **Figure 6.9 (e)**. It is assembled solely from eight-membered rings. All the white (Te) nodes are three-connected, while the black (Th) nodes are two- or three-connected. Using the method of building stripes,[170] the

---

[168] Jun-Ho Kim and P. Shiv Halasyamani. *J. Solid State Chem.*, **181**: 2108–2112, 2008.

[169] Hai-Long Jiang, Fang Kong, and Jiang-Gao Mao. *J. Solid State Chem.*, **180**: 1764–1769, 2007.

[170] E. C. Kirby. In: *Recent Work on Toroidal and Other Exotic Fullerene Structures*. AlexandruT Balaban, ed. Chap. 8, 263–296. Springer US, 2002. DOI: 10.1007/0-306-46907-3_8

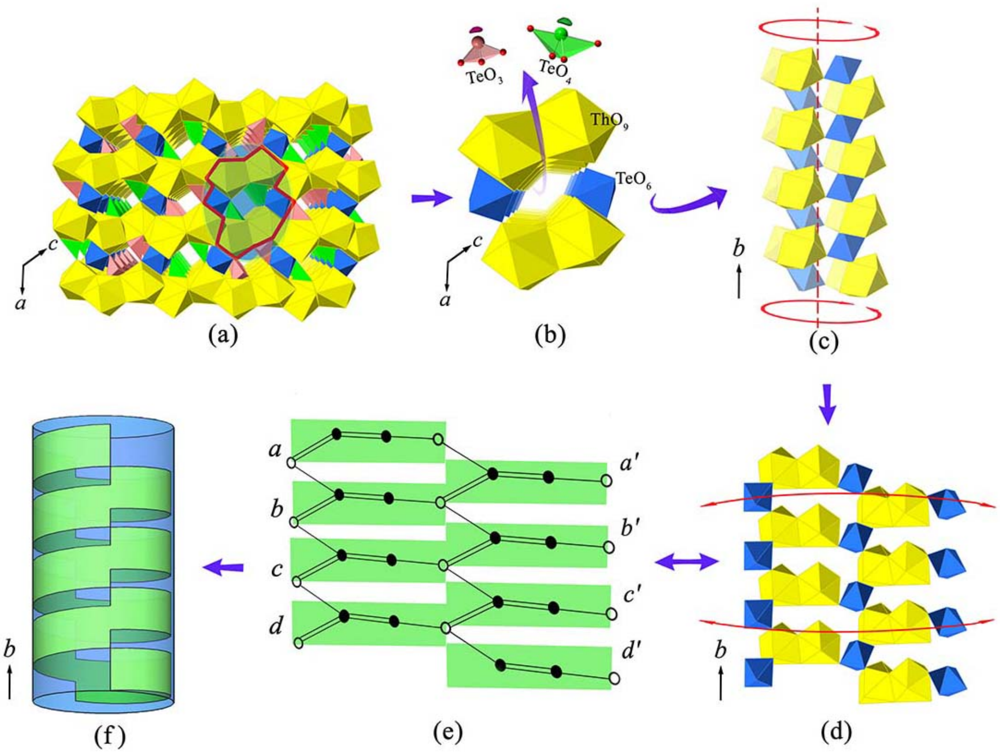

Figure 6.9: View of the channels in the structure of $Th_2Te_3O_{11}$.

idealized topological structure of $Th_2Te_3O_{11}$ can be converted *via* the folding and gluing procedure. Firstly, label the equivalent points on sides of the stripe by letters a, b, c and d. Secondly, fold the stripe by jointing the corresponding opposite sides (a–a', b–b', c–c' and d–d') to make a cylinder. It is important to note that the method of building stripes is also helpful to understand the symmetry inside the channels.[171] As can be easily detected from **Figure 6.9 (f)**, the idealized channel structure are related by a two-fold screw axis along to ***b***-axis, as required by the space group $P2_1/c$. Therefore, the corresponding cylindroid channels feature an achiral topology in this structure. Such method was also adopted by *Krivovichev, et al.* to present the linkage of U and Mo polyhedra inside the channels of an rare open-framework structure of $(NH_4)_4[(UO_2)_5(MoO_4)_7](H_2O)_5$.[172] In contrast to $Th_2Te_3O_{11}$, the equivalent points on the side of tapes for $(NH_4)_4[(UO_2)_5(MoO_4)_7](H_2O)_5$ are not opposite with each other, thus their folding procedure results in a chiral U-Mo channel topology.

$Na_4Th_2Te_3O_{15}$

The structure of $Na_4Th_2Te_3O_{15}$, as determined by single crystal X-ray diffraction study, demonstrates two crystallographically distinct Th sites and one Te site in an asymmetric unit. It is based upon a 3D $[Th_2Te_3O_{15}]^{4-}$ anionic framework which consists of Th_2O_{15} and Te_2O_{10} dimers (see **Figure 6.10 (a)**), and is charge balanced by Na^+ cations. Both Th(1) and Th(2) sites are coordinated with nine oxygen

---

[171] Shuao Wang et al. *Inorg. Chem.*, **51**: 11211–11213, 2012.

[172] Shuao Wang et al. *Chem. Mater.*, **23**: 2931–2939, 2011.

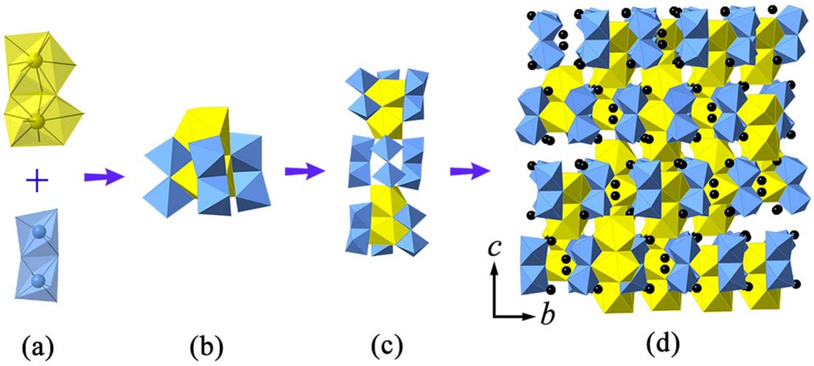

Figure 6.10: The process of forming structure of $Na_4Th_2Te_3O_{15}$.

atoms. They share a common face to give rise to a Th_2O_{15} dimer. This Th_2O_{15} dimer that resides on a three-fold rotational axis is further bounded with three Te_2O_{10} dimers, forming a $[Th_2Te_6O_{33}]_2^{2-}$ fragment with a shape similar to a flaming rocket, as shown in **Figure 6.10 (b)**. Each Te_2O_{10} dimer in the resulting thorium tellurate fragment is composed by two Te(1) in edge-sharing manner, similar to the one in the reported $AgUO_2(HTeO_5)$[173] and $(NH_4)_4(VO_2)_2[Te_2O_8(OH)_2]{\cdot}2\,H_2O$[122]. Two of such thorium tellurate fragments which are related by an inversion center are connected through sharing of corners with another three Te_2O_{10} dimers to compose a so-called fundamental building block (**FBB**) (see **Figure 6.10 (c)**). The 3D framework of $Na_4Th_2Te_3O_{15}$ is finally complete by bridging these FBBs, shown in **Figure 6.10 (d)**.

The ThO_9 tricapped trigonal prisms in $Na_4Th_2Te_3O_{15}$ are distorted with one short (Th-O(1)) and one rather long Th-O bond (Th-O(3)) with distances of 2.326(4) and 2.513(5) Å, respectively. In this case, the Th-O bond lengths in monoclinic-$ThMo_2O_8$ are less uniform compared to those in orthorhombic-$ThMo_2O_8$ (ranging from around 2.36 to 2.46 Å) but comparable to the Th-O distances in hexagonal $ThMo_2O_8$ (between about 2.30 and 2.49 Å). The values of Te-O bond lengths vary from 1.871(7) to 2.066(6) Å, with the shortest lengths being the edging-sharing oxygen atoms (O(1) and O(4)).

$K_2ThTe_3O_{12}$

The 3D compound $K_2ThTe_3O_{12}$ crystallizes in $Pnma$ space group with one Th and two Te per asymmetric unit. The main building blocks of this structure can be conceived as undulated hexagonal tellurium layers interlinked by ThO_9 polyhedra, shown in **Figure 6.11 (a)**. The charge compensating Cs^+ cations are found resided between the intervals of adjacent tellurium layers. The Th atoms, serving as an inter-layer linker, achieve a capped square antiprismatic coordination geometry by attaching nine O atoms from the tellurium layers. More specifically, each ThO_9 polyhedron shares three edges of its square face with three TeO_6 tetrahedra from one tellurium layer, and also shares one corner and two edges with other three TeO_6 tetrahedra from another tellurium layer. The variation of Th to O distances is appreciable, from 2.325(12) to 2.691(8) Å, the average distance being 2.480 Å.

---

[173] Jie Ling, Matthew Ward, and Peter C. Burns. *J. Solid State Chem.*, **184**: 401–404, 2011.

As the case of two crystallographically different Te sites, both are octahedrally coordinated by O with Te-O bond distances between 1.851(12) and 2.009(8) Å. Within each TeO_6 octahedron, a bond asymmetry is observed in the local C_2 direction. This out-of-center distortion results in two short, two normal and two long Te-O bonds. The short bond distances occur particularly in terminal O, which has Te-O bond distances of 1.851(12) and 1.873(13) Å for Te(1) and 1.858(8) and 1.883(7) Å for Te(2), respectively. In fact, this intra-octahedral distortions are quite common among those reported for HTO typed compounds. Bond valence sum calculations of $K_2ThTe_3O_{12}$ lead to values of 5.82, 5.84 and 4.07 v.u. for Te(1), Te(2) and Th(1), respectively, confirming the presence of hexavalent tellurium and tetravalent thorium.

Inside the tellurium layers, all the TeO_6 are corner shared with four other tellurium octahedra in their equatorial planes, leaving two *trans*-corners which are not involved in inter-plane linkage. As a result, the resulting tellurium layer has the formula of $[TeO_4]^{2-}$ and is propagating parallel to (100) plane (see **Figure 6.10 (b)**. These tellurium layers stack along the crystallographic ***a***-axis in a way that the hexagonal cavity of one layer is facing the triangular cavity of its next layer, forming in a ABABAB configuration. The neighboring “A” and “B” layers are related with each other by translation of the length of a ThO_9 wide along the crystallographic **c**-axis.

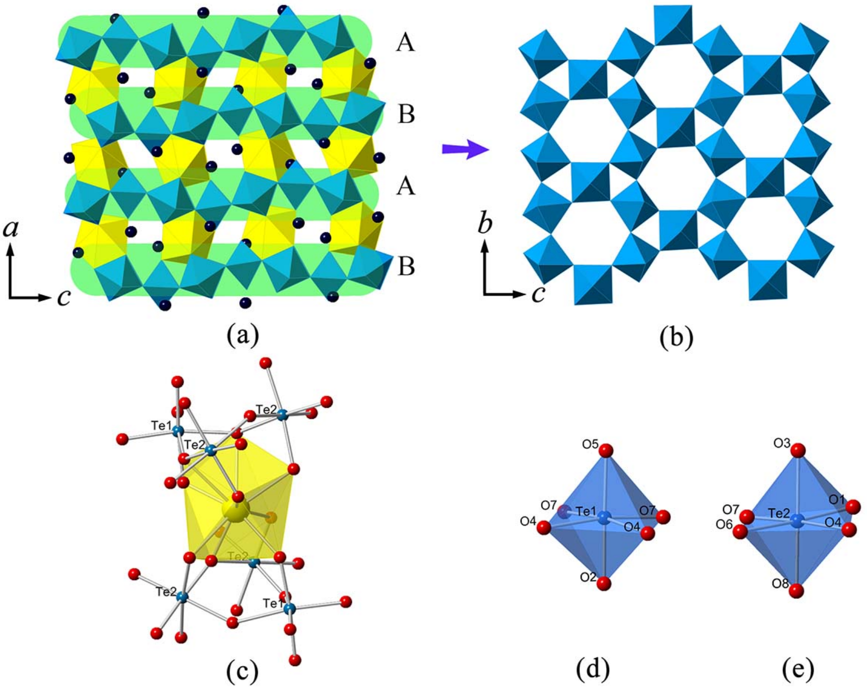

(a) (b) (c) (d) (e)

Figure 6.11: (a) View of the structure of $K_2ThTe_3O_{12}$ along b-axis. (b) The projection along [100] direction shows the HTO-like topology arrangement of TeO_6 octahedra. (c) The local coordination environment of ThO_9 capped square antiprism. (d) The coordination geometry of Te(1). (e) The coordination geometry of Te(2).

The occurrence of tellurium layers with the corner-sharing TeO_6 octahedra is usually observed among the family called hexagonal tungsten oxide bronzes (**HTO**).[174–177] Most compounds in this family are composed of three- and six-membered tunnels constructed by corner-sharing MO_6 octahedra. Typical examples are hexagonal WO_3[178] and alkali tungsten brozes A_xWO_3[179]. However, in these compounds, the neighbouring layers are further connected by sharing two $trans$ apical O atoms of the WO_6 octahedra. In $K_2ThTe_3O_{12}$, these layers are not attached together by are cross-linked by ThO_9 polyhedra. It is also noted that the structure of $K_2ThTe_3O_{12}$ also bears striking similarities with that of $RbTe_2O_6$ which may also be considered as a derivation of HTO family. In $RbTe_2O_6$, each WO_6 octahedron shares all its corner O atoms with surrounding WO_6 octahedra to create a 3D network with complex criss-crossing triangle and hexagonal cavities.

6.3 High probability of non-centrosymmetric uranyl tellurium structures achieved from high-temperature/high-pressure synthesis

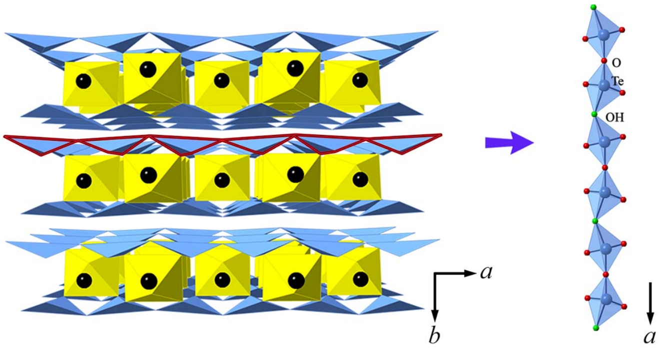

(a) (b)

Figure 6.12: (a) View of the two-dimensional structure of $\mathrm{Na[(UO_2)Te^{IV}{}_2O_5(OH)]}$. (b) The Te cations are coordinated with four O atoms to form TeO_4 polyhedra which share the alternative OH and O corners to lead to tellurium chain. The UO_6 and TeO_4 polyhedra are in yellow and blue color, respectively. Hydroxyl groups are in green nodes.

Two new sodium uranyl tellurites and two new sodium uranyl tellurates have been synthesized from high-temperature/high-pressure conditions and structurally characterized. All the uranyl oxo-tellurium compounds are prepared form at the temperature of around 1050 °C and pressure of around 3.5 GPa. The detailed procedures are the same as for $HT_/HP-ThMo_2O_8$ in the page of 19.

---

[174] J. Graham and A. D. Wadsley. *Acta Crystallogr.*, **14**: 379–383, 1961.

[175] John T. Vaughey et al. *Inorg. Chem.*, **33**: 4370–4375, 1994.

[176] N. D. Zakharov et al. *J. Solid State Chem.*, **147**: 536–544, 1999.

[177] Jeongho Yeon, Sang-Hwan Kim, and P. Shiv Halasyamani. *Inorg. Chem.*, **49**: 6986–6993, 2010.

[178] Michel Figlarz. *Prog. Solid State Chem.*, **19**: 1–46, 1989.

[179] A Hussain, R Gruehn, and CH Rscher. *Journal of alloys and compounds*, **246**: 51–61, 1997.

For $\mathrm{Na[(UO_2)Te^{IV}{}_2O_5(OH)]}$, $(UO_2)(NO_3)_2 \cdot 6\,H_2O$ (20.0 mg, 0.0398 mmol), TeO_2 (19.1 mg, 0.119 mmol) H_6TeO_6 (18.3 mg, 0.0797 mmol) and $Na_2S_2O_4$ (41.6 mg, 0.239 mmol) were weighed out. In the case of $\mathrm{Na[(UO_2)Te^{IV}{}_6O_{13}(OH)]}$, UO_3 (20.0 mg, 0.0699 mmol), TeO_2 (11.2 mg, 0.0699 mmol) H_6TeO_6 (48.2 mg, 0.2098 mmol) and Na_2NO_3 (17.8 mg, 0.2098 mmol) were weighed out. This results in a U: Te: Na ratio of 1: 4: 3. UO_3 (20.0 mg, 0.0699 mmol), TeO_2 (22.4 mg, 0.1398 mmol) and Na_2NO_3 (17.8 mg, 0.2098 mmol) were weighed out for $\mathrm{Na_2[(UO_2)(Te^{VI}{}_2O_8)]}$. This results in a U: Te: Na ratio of 1: 2: 3. For $\mathrm{Na_2[(UO_2)Te^{VI}O_5]}$ $(UO_2)(NO_3)_2 \cdot 6\,H_2O$ (20.0 mg, 0.0398 mmol), TeO_2 (25.4 mg, 0.1593 mmol) and Na_2NO_3 (41.0 mg, 0.1992 mmol) were weighed out.

Under extreme condition, the Na-U-Te family appears to be favorable in non-centrosymmetric structures, as three out of four uranyl tellurium compounds, $\mathrm{Na[(UO_2)Te^{IV}{}_2O_5(OH)]}$, $\mathrm{Na_2[(UO_2)(Te^{VI}{}_2O_8)]}$ and $\mathrm{Na_2[(UO_2)Te^{VI}O_5]}$, are crystallized in a non-centrosymmetric space group. The crystal structure of $\mathrm{Na[(UO_2)Te^{IV}{}_2O_5(OH)]}$ is based on two-dimensional $[UO_2Te_2O_5(OH)]^-$ corrugated sheets, which are charge balanced by guest Na^+ cations. The structure of $Na_2[(UO_2)Te^{VI}{}_2O_8]$ is constructed from $[(UO_2)_2Te_2O_8]^{2+}$ anionic layers composed of UO_7 pentagonal bipyramids and TeO_6 octahedra. $Na_2[(UO_2)(Te^{VI}O_5)]$ is a new type of three-dimensional anionic open framework built from the interconnection of UO_7 pentagonal bipyramids and TeO_6 octahedra with different types of interlacing channels within the U-Te anionic framework. $\mathrm{Na[(UO_2)Te^{IV}{}_6O_{13}(OH)]}$, as the only centrosymmetric compound isolated in Na-U-Te family, is crystallized in space group $Pa\bar{3}$, and the structure of which is highly related to that of cliffordite that is composed from UO_8 hexagonal bipyramids and TeO_5 tetragonal pyramids. The vibrational modes associated with U-O, Te^{IV}-O and $Te^{VI}-O$ bonds were discussed and the Raman spectra of the four compounds are characterized for signature bands.

6.3.1 Structural and topological relationship in sodium uranyl tellurium family

Structure of $\mathrm{Na[(UO_2)Te^{IV}{}_2O_5(OH)]}$

The structure of $\mathrm{Na[(UO_2)Te^{IV}{}_2O_5(OH)]}$ consists of two-dimensional $[UO_2Te_2O_5(OH)]^-$ corrugated sheets, which are charge balanced by guest Na^+ cations, as shown in **Figure 6.12 (a)**. It is noteworthy that the structure type based upon two-dimensional anionic sheets interlinked by additional charge-compensation agents is typical among mineral and synthetic inorganic U(VI) compounds.[180] $\mathrm{Na[(UO_2)Te^{IV}{}_2O_5(OH)]}$ has one crystallographic Te and one U site. Each Te cation forms in a distorted disphenoidal geometry (TeO_4), linked by sharing alternating OH^- and O^{2-} corners to result in tellurium chains with Th-O-Te-OH-Te bonding configuration (see **Figure 6.12 (b)**). The Te-O and Te-OH bond distances are 1.96(2) Å and 2.25(2) Å, respectively. The assignment of hydroxyl unit is based on the long bond distance and the bond valence sum of 1.1 u.v. for this O atom. The charge neutrality requirement also indicates the existence of OH^- unit. Besides, the vibrational bands at around 3000 cm^{-1} further supports this being protonated O (see Raman section). The $UO_2{}^{2+}$ cation is coordinated with five O atoms, yielding a UO_7 pentagonal bipyramid. As most of uranyl compounds,

---

[180] Peter C. Burns. *Can. Mineral.*, **43**: 1839–1894, 2005.

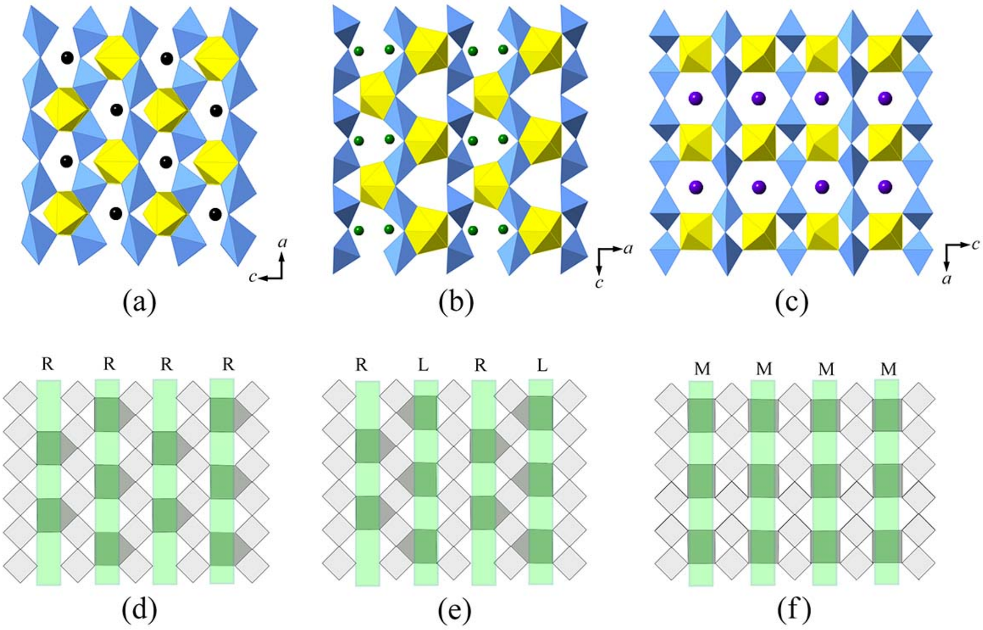

Figure 6.13: Comparison of uranyl-tellurium sheets in the structures of (a) $\mathrm{Na[(UO_2)Te^{IV}{}_2O_5(OH)]}$, (b) $Tl_3(UO_2)_2[Te_2O_5(OH)](Te_2O_6)\cdot 2\,H_2O$ and (c) $K[UO_2Te_2O_5(OH)]$, respectively. Note that the uranyl cations are formed in UO_7 pentagonal bipyramidal coordination in the first two structures while UO_6 tetrahedral bipyramids can be found in the third one. The corresponding anion topologies are shown in (d) for $Na[UO_2Te_2O_5(OH)]$, (e) for $Tl_3(UO_2)_2[Te_2O_5(OH)](Te_2O_6)\cdot 2\,H_2O$ and (d) for $K[UO_2Te_2O_5(OH)]$, respectively. The difference of linkage manners of uranyl cations is highlighted by the sequence of "right" (= R), "left" (= L) and "middle" (= M) of uranyl cations among each sheet.

the $\mathrm{UO_2}^{2+}$ has approximately linear geometry with an O=U=O angle of 175(1)°, and U=O distances of 1.80(1) Å and 1.82(4) Å. The four equatorial U-O bond distances between 2.23(3) Å and 2.75(6) Å are within the normal range.[181–187]

The $[UO_2Te_2O_5(OH)]^-$ sheets in $Na[UO_2TeO_5(OH)]$, extending in the (010) plane, are comprised of tellurium chains which are fused together by linking with UO_7 pentagonal bipyramids. It is worthy to note that the structure of $\mathrm{Na[(UO_2)Te^{IV}{}_2O_5(OH)]}$ is significantly reminiscent of $K[UO_2Te_2O_5(OH)]$and $Tl_3(UO_2)_2[Te_2O_5(OH)](Te_2O_6)\cdot 2\,H_2O$,[188] which are also based on uranium tellurite sheets, shown in **Figure 6.13**. In all three uranium tellurite compounds, the connection of uranyl cations with tellurium chains creates small hexagonal-shaped cavities that are filled with different A^+ cation-

---

[181] Evgeny V. Alekseev et al. *Z. Anorg. Allg. Chem.*, **633**: 1979–1984, 2007.

[182] Evgeny V. Alekseev, Sergey V. Krivovichev, and Wulf Depmeier. *Z. Anorg. Allg. Chem.*, **633**: 1125–1126, 2007.

[183] Evgeny V. Alekseev, Sergey V. Krivovichev, and Wulf Depmeier. *Angew. Chem. Int. Ed.*, **47**: 549–551, 2008.

[184] Evgeny V. Alekseev, Sergey V. Krivovichev, and Wulf Depmeier. *J. Solid State Chem.*, **182**: 2074–2080, 2009.

[185] Evgeny V. Alekseev, Sergey V. Krivovichev, and Wulf Depmeier. *J. Mater. Chem.*, **19**: 2583–2587, 2009.

[186] Evgeny V. Alekseev, Sergey V. Krivovichev, and Wulf Depmeier. *J. Solid State Chem.*, **182**: 2977–2984, 2009.

[187] Evgeny V. Alekseev, Sergey V. Krivovichev, and Wulf Depmeier. *Cryst. Growth Des.*, **11**: 3295–3300, 2011.

[188] Philip M. Almond and Thomas E. Albrecht-Schmitt. *Inorg. Chem.*, **41**: 5495–5501, 2002.

s (A = Na^+, K^+ and Tl^+). In order to further analysis the U-Te arrangement among each sheet, the method of anion topology is adopted, which can represent the topological connection of anions within the sheet.[189] As can be seen from **Figure 6.13**, the UO_2^{2+} cations in all three compounds are equatorially bond with four TeO_4 polyhedra. Obviously, in $Na[(UO_2)Te^{IV}{}_2O_5(OH)]$ and $Tl_3(UO_2)_2[Te_2O_5(OH)](Te_2O_6)\cdot 2\,H_2O$, all UO_2^{2+} cation are formed in UO_7 pentagonal bipyramidal geometry and are connected with tellurium chains using both corner- and edge-sharing behavior. In contrast, the UO_6 tetragonal bipyramids in the structure of $K[UO_2Te_2O_5(OH)]$are found to be only corner-shared with tellurium chains. One can image that, due to the presence of more isotropic coordination environment around UO_6 polyhedra, the sheets in K-based structure experience less bent conformation. As a result, the resulting cavities in the $K[UO_2Te_2O_5(OH)]$are bigger, 5.67 Å, compared to that of 3.0 Å in $Na[UO_2Te^{IV}O_5(OH)]$ and 4.7 Å in $Tl_3(UO_2)_2[Te_2O_5(OH)](Te_2O_6)\cdot 2\,H_2O$, measured as the two closest O atoms across the corresponding cavities. In addition, the orientations of edge-sharing linkages between uranyl and TeO_4 polyhedra within the sheets are different, which are highlighted by the sequence of "right" (= R), "left" (= L) and "middle" (= M) in **Figure 6.13 (d, e, f)**. For $Na[(UO_2)Te^{IV}{}_2O_5(OH)]$, all the UO_7 polyhedra are unanimously inclined to "right" side to share common edges with TeO_4 polyhedra. However, for $Tl_3(UO_2)_2[Te_2O_5(OH)](Te_2O_6)\cdot 2\,H_2O$, the corresponding UO_7 polyhedra have their edge-sharing sides orientated in opposite directions with respective to one another on each side of the tellurium chains. As the case of $K[UO_2Te_2O_5(OH)]$, no edge-sharing is observed and the corner-sharing UO_6 polyhedra can be considered as pointing to nowhere (thus indicates as "middle").

Structure of $Na[(UO_2)Te^{IV}{}_6O_{13}(OH)]$

The $Na[(UO_2)Te^{IV}{}_6O_{13}(OH)]$, shown in **Figure 6.14 (a)**, crystallizing in space group $Pa\bar{3}$, is highly related to the structure of cliffordite. The mineral cliffordite was first reported by *Gaines* in 1969 as a uranium(IV)-based compound (UTe_3O_8).[190] Later, based on the investigation of the UO_3-TeO_2 system, *Meunier* and *Galy* unraveled the correct formula of cliffordite as $UO_2(Te_3O_7)$ *via* ensuring the presence of U(VI) instead of U(IV).[191] Following on this, the more accurate structure determination was done by *Brandstaetter* in 1981 using the 3D diffractometer data reported by *Meunier* and *Galy*. Due to the partially occupied site of U(1), *Brandstaetter* pointed out a non-stoichiometric composition, $U_{0.91}Te_3O_{8.85}$, where he supposed that the excess negative charge might be compensated by introducing certain counter-cations or by substituting O^{2-} with OH^-. Continuing on this, with the help of high-temperature/high-pressure technique, this speculation can be confirmed through successfully isolated the alkaline-based uranyl tellurite $Na[(UO_2)Te^{IV}{}_6O_{13}(OH)]$, a first cliffordite-related compound with all sites being fully occupied. Due to the high symmetry of U site (S_6) in $Na[(UO_2)Te^{IV}{}_6O_{13}(OH)]$, the U=O bond distances equals 1.809(16) Å and the equatorial U-O are all in 2.433(9) Å. The only non-centrosymmetric Te site is coordinated by five oxygen atoms in square pyramidal geometry, with its electron lone pairs pointing towards the square base. The Te-O band distances, varying from 1.880(9) to 2.338(9) Å, are within the range seen in other tellurites which

---

[189] P. C. Burns. *Rev. Mineral.*, **38**: 23–23, 1999.

[190] RV Gaines. *Am. Mineral.*, **54**: 697–701, 1969.

[191] J. Galy and G. Meunier. *Acta Crystallogr., Sect. B: Struct. Sci*, **27**: 608–616, 1971.

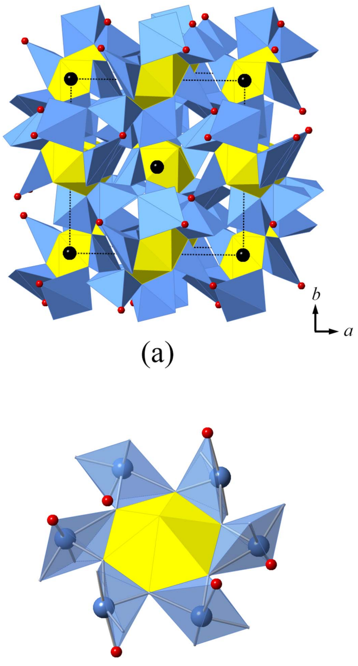

(a)

(b)

Figure 6.14: (a) View of the structure of cliffordite-related $Na[(UO_2)Te^{IV}{}_6O_{13}(OH)]$. (b) The building ring of $[(UO_2)Te_6O_{13}(OH)]^-$ which is constructed from six TeO_5 polyhedra fused corner by corner with a UO_8 hexagonal bipyramid located in middle.

also contain TeO_5 polyhedra.[123,192] The structure of $Na[(UO_2)Te^{IV}{}_6O_{13}(OH)]$ can be described as based on $[(UO_2)Te_6O_{13}(OH)]^-$ rings, where six TeO_5 polyhedra enclose a hexagonal cavity in which a UO_8 polyhedron is located, exhibited in **Figure 6.14 (b)**. The adjacent rings are interlinked through corner-sharing of hydroxyl to complete a 3D network structure. Bond valence summation was performed and the result of 1.13 v.u. indicates the presence of protonated O(4) site. The vibrational frequencies at around 3000 cm^{-1} also show the evidence of OH^- groups (see Raman Spectra section).

The structure of $Na[(UO_2)Te^{IV}{}_6O_{13}(OH)]$ is remarkably similar to that of $UO_2(Te_3O_7)$, both structures crystallize in a cubic system (space group: $Pa\bar{3}$) composed of UO_8 hexagonal bipyramids and TeO_5 square pyramids. The difference originates form the number of UO_8 polyhedra and their arrangement in each unit cell. Two crystallographically distinct U sites are found in the structure of $UO_2(Te_3O_7)$, whereas only one U site is observed in $K_2[(UO_2)Te_4O_{14}]$. For $UO_2(Te_3O_7)$, there are 27 UO_8 hexagonal bipyramids resided in an unit cell, shown in **Figure 6.15 (a)**. The topology arrangement can be easily described by the graphical approach as based upon regular **pcu** (primitive cubic lattice) net, shown in **Figure 6.15 (c)**. In the case of $Na[(UO_2)Te^{IV}{}_6O_{13}(OH)]$, however, only 13 U atoms are found in one unit cell, given in **Figure 6.15 (b)**, and they are arranged into a cuboctahedral conformation with **fcu-a** (face-centered cubic lattice) topology (see **Figure 6.15 (e)**). Analysis of the resulting graphs demonstrates that their topologies can be converted from one to another using simple topological transformation. **Figure 6.15 (d)** shows U arrangement in $Na[(UO_2)Te^{IV}{}_6O_{13}(OH)]$ can be obtained by removing the 8 corners and 6 face-centers from $UO_2(Te_3O_7)$ based topology.

---

[192] Dongrong Xiao et al. *J. Solid State Chem.*, **176**: 159–164, 2003.

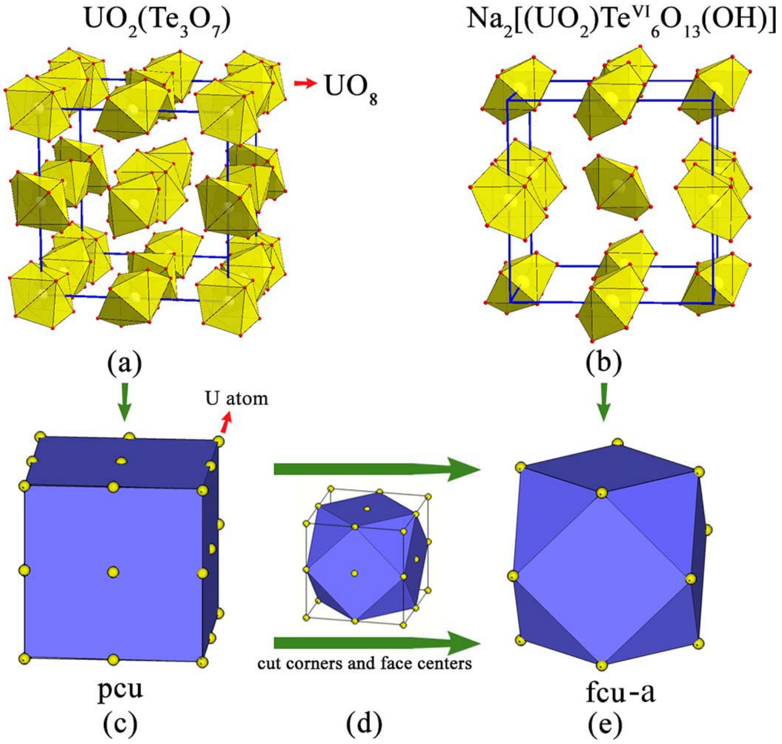

Figure 6.15: Arrangement of UO_8 hexagonal pyramids in one unit cell for (a) cliffordite $UO_2(Te_3O_7)$ and (b) $\mathrm{Na[(UO_2)Te^{IV}{}_6O_{13}(OH)]}$, respectively. (c, e) The corresponding topologies of pcu and fcu-a net for $UO_2(Te_3O_7)$ and $\mathrm{Na[(UO_2)Te^{IV}{}_6O_{13}(OH)]}$, respectively. (d) Topological transformation of U arrangement from pcu observed in $\mathrm{Na[(UO_2)Te^{IV}{}_6O_{13}(OH)]}$ to fcu-a observed in $UO_2(Te_3O_7)$ can be achieved by removing the 8 corners and 6 face-centers. UO_8 hexagonal bipyramids are shown in yellow polyhedra.

Structure of $Na_2[(UO_2)Te^{VI}{}_2O_8]$

The structure of $Na_2[(UO_2)Te^{VI}{}_2O_8]$, exhibiting 2D $[(UO_2)_2Te_2O_8]^{2+}$ anionic layers, is shown in **Figure 6.16 (a)**. The 2D layers are composed of UO_7 pentagonal bipyramids and TeO_6 octahedra, and stack along the crystallographic-***a*** direction, with Na^+ cations residing between the layers. The only U site is in seven-coordinated UO_7 pentagonal bipyramidal coordination. These UO_7 pentagonal bipyramids are linked end-to-end to make 1D U chains which has one UO_7 polyhedral wide, similar to that reported in $AgUO_2(HTeO_5)$.[173] The two crystallographically unique Te sites, hereafter referred to as Te(1) and Te(2), share a common edge to form a Te_2O_{10} dimer. Adjacent Te_2O_{10} dimers are further connected to give rise to double tellurium chains propagating along ***b*** direction, which in turn are linked with U chains, completing the above mentioned $[(UO_2)_2Te_2O_8]^{2+}$ anionic layers.

The UO_7 polyhedron is greatly distorted if observing from its equatorial plane, which can be shown by the largestO_{eq}-U-O_{eq} of 114(4)°. The distortion is attributable from bidentate chelating bond with two TeO_6 octahedra (see **Figure 6.16 (c)**). The bond distance variation of U to equatorial O is appreciable, from 2.25(5) Å to 2.76(4) Å, with the mean distance being around 2.37 Å, but is still falling into the

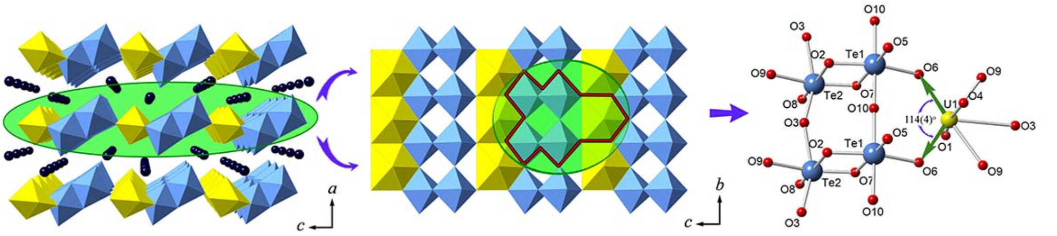

(a) (b) (c)

Figure 6.16: (a) View of structure of $Na_2[(UO_2)Te^{VI}{}_2O_8]$ along the crystallographic b-axis. (b) One layer extracted from $Na_2[(UO_2)Te^{VI}{}_2O_8]$. (c) The local coordination of Te_2O_{10} dimers and distorted UO_7 pentagonal bipyramid.

range of typical uranyl compounds containing UO_7 pohydedra.[193] As for the TeO_6 octahedra, both Te sites demonstrate significant lengthening along the edge-sharing O direction (O(2)-O(7)) with respect to other Te-O bonds. The bond distances for Te(1)-O range from 1.73(2) to 2.33(8) Å, while the Te(2)-O bonds distances range from 1.73(9) to 2.27(6) Å. Bond valence calculations for the U and Te cations result in values are 5.77 v.u. and 6.22−6.23 v.u., respectively, indicating that all the U and Te cations are presented in hexavalent oxidation state.

The structure of $Na_2[(UO_2)Te^{VI}{}_2O_8]$ is strongly related to those of a series of uranyl tungstates with the general formula of $A_2[(UO_2)W_2O_8]$ (A = Na, K, Ag,)[194,195] which are also constructed from similar infinite U and Te chains (see **Figure 6.17 (b)**). In $Na_2[(UO_2)Te^{VI}{}_2O_8]$, the neighboring U and Te chains are connected in alternative corner- and edge-sharing manners. In contrast, $A_2[(UO_2)W_2O_8]$ are formed exclusively by corner-sharing of corresponding U and Te chains. It is noted that both structures can be easily transformed by turning half of the UO_7 pentagonal bipyramids 180° along the layer plane, as demonstrated in **Figure 6.17**.

Structure of $Na_2[(UO_2)(Te^{VI}O_5)]$

The compound $Na_2[(UO_2)(Te^{VI}O_5)]$, containing only one kind of crystallographically unique U and one Te site, is crystallized in the space group $Ama2$. It is a new type of 3D anionic open framework that is constructed from the interconnection of UO_7 pentagonal bipyramids and TeO_6 octahedra (in **Figure 6.18 (a)**). A main feature of the crystal structure is that different types of interlacing channels can be obviously observed in the directions of [100] [100], [10$\bar{1}$] and [1$\bar{1}$0] within the U-Te anionic framework. These channels are resided by the Na^+ cations which play the role of maintaining charge neutrality. Among them, the largest one with a cylindrical shaped appearance, shown in **Figure 6.18 (b)**, extends propagating along [010] direction. This channel has a formula of $[(UO_2)(TeO_5)]^{2-}$ and can be seen as a fundamental building block (**FBB**) to compose the framework of $Na_2[(UO_2)(Te^{VI}O_5)]$.

In order to easily elucidating the U-Te linkages inside the channel structure, the channel is expanded

---

[193] Evgeny V. Alekseev et al. *Inorg. Chem.*, **46**: 8442–8444, 2007.

[194] Sergey V. Krivovichev and Peter C. Burns. *Solid State Sci.*, **5**: 373–381, 2003.

[195] S. Obbade et al. *J. Solid State Chem.*, **172**: 305–318, 2003.

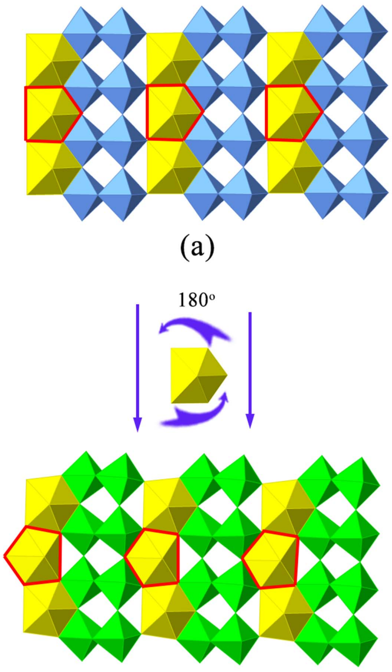

(a)

(b)

Figure 6.17: (a) The layers observed in $\mathrm{Na_2[(UO_2)Te^{VI}{}_2O_8]}$. (b) The layers observed in $\mathrm{A_2[(UO_2)W_2O_8]}$ (A = Na, K, Ag,). Note that these two layers can be converted from one to the other *via* turning half of the $\mathrm{UO_7}$ pentagonal bipyramids (highlighted in red lines) 180º along the layer plane.

into a 2D sheet, which are shown in **Figure 6.19 (a, b)**. From **Figure 6.19 (b)** one can see that each $\mathrm{UO_7}$ pentagonal bipyramid is equatorially connected with four $\mathrm{TeO_6}$ octahedra, two of them are found in corner-sharing manner and the other two are in edge-sharing linkage. The tellurium chains are formed along the direction of ***b***-axis *via* polymerization of $\mathrm{TeO_6}$ octahedra through common corners. The 2D unfolding channel is completed by further connecting adjacent tellurium chains with the help of $\mathrm{UO_7}$ polyheda. Inside the anionic channel $\mathrm{[(UO_2)(TeO_5)]^{2-}}$, the uranyl U=O bond distances of the $\mathrm{UO_7}$ pentagonal bipyramid are 1.82(2) and 1.83(1) Å, which are typical to those in other uranyl tellurite compounds.[196,197] The equatorial bond lengths of $\mathrm{UO_7}$ polyhedra demonstrate significant variation, ranging from 2.23(1) to 2.57(1) Å. This distortion is originated from the differences of linkage behavior associated with the $\mathrm{TeO_6}$ octahedra, that is, corner-sharing versus edge-sharing. The edge-sharing U-O bonds produce the longer equatorial bonds than the corner-sharing ones. The topological graph of the resulting unfolding channel can be plotted using the method of *black and white nodal representation*. This method allows recognizing the internal U-Te connections along the channel structure. The black and white nodes symbolize U and Te polyhedra, respectively. The neighboring nodes are connected by single or double lines only when the corresponding polyhedra are linked through corner- or edge-manner, respectively. As can be seen in **Figure 6.19 (c)**, each white node is two-connected with adjacent two black nodes while the black nodes are exclusively four-connected with four nearest white nodes. It is obvious that its topology can be seen as composed of the so-called basic building tapes (highlighted in **Figure 6.19 (c)**), the concept of which has already been widely

---

[196] George H. Swihart et al. *Am. Mineral.*, **78**: 835–839, 1993.

[197] Philip M. Almond, Michael L. McKee, and Thomas E. Albrecht-Schmitt. *Angew. Chem. Int. Ed.*, **41**: 3426–3429, 2002.

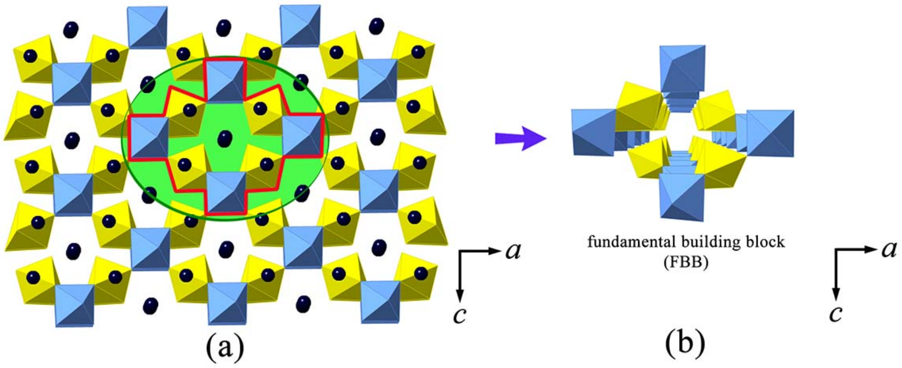

Figure 6.18: (a) View of the structure of $Na_2[(UO_2)(Te^{VI}O_5)]$ along the crystallographic b direction. (b) The fundamental building block (FBB) extracted from $Na_2[(UO_2)(Te^{VI}O_5)]$.

adopted to demonstrate the tubular units formed in many other actinide compounds, such as uranyl selenate tubules $[(UO_2)_3(SeO_4)_5]^{4-}$ and thorium molybdate channels $[Th_3(MoO_4)_7]^{2-}$.[100,105] The adjacent building tapes are joined together by connecting the white nodes. To obtain the cylindrical channels observed in the structure of $Na_2[(UO_2)(Te^{VI}O_5)]$, one only needs to fold and glue the corresponding building tapes in the following procedures: Firstly, label the equivalent points on the sides of tapes by letters a, b, c, d, e, f and g. Then fold the tape by jointing the associated opposite sides (a–a', b–b', c–c', d–d', e–e', f–f' and g–g'), as demonstrated in **Figure 6.19 (c, d)**.

6.3.2 Raman spectroscopic analysis

The Raman spectra of as-prepared uranyl tellurites/tellurates in the region of 100 to 1050 cm^{-1} are shown in **Figure 6.20**. These vibrational spectra are characterized by motions from linearity of uranyl (UO_2^{2+}) and trigonal pyramid of tellurite ($Te^{IV}O_3$) or octahedron of tellurate ($Te^{VI}O_6$). The vibrational data on tellurites/tellurates are well-established in the literature.[198] However, very little research has been undertaken on the vibrational spectroscopy of uranyl tellurates/tellurites. The infrared spectrum studies of schmitterite (UO_2TeO_3) and cliffordite ($UO_2(Te_3O_7)$) were reported by *Botto, et al.*[199], and Raman vibrational studies of schmitterite (UO_2TeO_3)[200] and moctezumite ($Pb(UO_2)(TeO_3)_2$)[201] were discussed by *Frost, et al.*.

Due to the structural complexity of these compounds which contain overlapping bands from uranyl and tellurium units ($Te^{IV}O_3$ or $Te^{VI}O_6$), here, only signature peaks are assigned. The ideal uranyl (UO_2^{2+}) unit has $D_{\infty h}$ symmetry. It has three normal modes in aqueous solution, that is, ν_1 symmet-

---

[100] Sergey V. Krivovichev et al. *Angew. Chem. Int. Ed.*, **117**: 1158–1160, 2005.
[198] J. Hanuza et al. *Spectrochim. Acta, Part A*, **71**: 68–72, 2008.
[199] I. L. Botto and E. J. Baran. *Z. anorg. allg. Chem.*, **484**: 210–214, 1982.
[200] Ray L. Frost et al. *J. Raman Spectrosc.*, **37**: 816–821, 2006.
[201] Ray L. Frost, Ji ejka, and Marilla J. Dickfos. *J. Raman Spectrosc.*, **40**: 38–41, 2009.

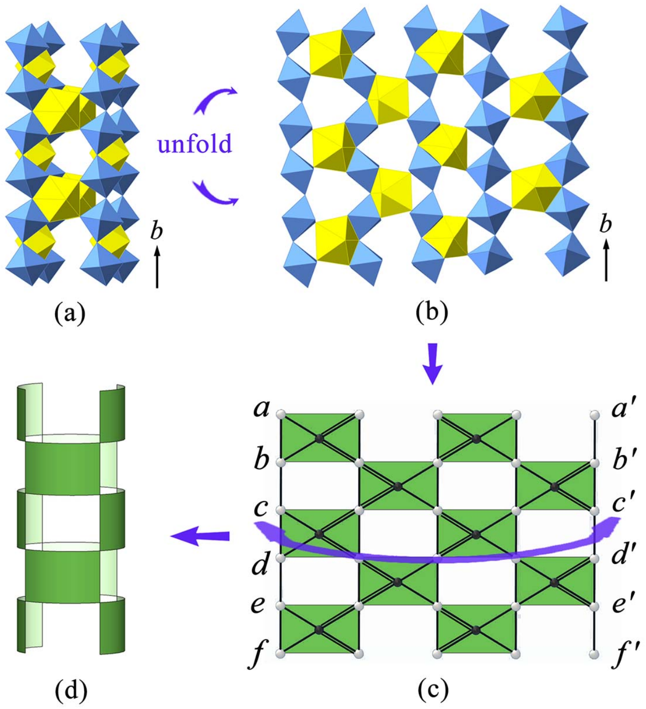

Figure 6.19: (a) The $[(UO_2)(TeO_5)]^{2-}$ cylindrical shaped fundamental building block (FBB) channel extending along the b-axis of the $Na_2[(UO_2)(Te^{VI}O_5)]$. (b) The corresponding unfold version of cylindrical channel. (c) The idealized topological connection of U-Te inside the unfold channel structure. Note that the basic building tapes are highlighted with the green rectangles. (d) The ideal fold version of channel structure can be obtained from gluing the associated two ends of the basic tapes.

ric stretching mode (from 860 to 880 cm^{-1}), ν_3 anti-symmetrical stretching (from 930 to 960 cm^{-1}), and the ν_2 bending mode (from 199 to 210 cm^{-1}).[202,203] The relationship of ν_1 and ν_3 modes in the solid-state uranyl compounds can be related by the equation posted by *Bagnall, et al.* as $\nu_1 = 0.912\nu_3$ 1.04 cm^{-1}[204] The free tellurite ($Te^{IV}O_3{}^{2-}$) unit with C_{3v} symmetry has four vibrational modes, namely $2A_1$ and $2E$. Famer states their locations at 758 cm^{-1} for ν_1 (A_1), 703 cm^{-1} for ν_3 (E), 364 cm^{-1} for ν_2 (A_1) and 326 cm^{-1} for $\nu_4(E)$. The ideal $Te^{VI}O_6$ octahedron has three kinds of Raman active vibrational bands, $\nu_1(A_{1g})$, $\nu_2(E_g)$ and v5(F_{2g}), and the stretching and bending vibrations for mostly tellurate compounds are distributed in the range of 550−750 and 350−450 cm^{-1}, respectively.[205] The vibrational data for all four uranyl compounds are quite similar. The high frequency bands ranging from 600 to 1050 cm^{-1} are all characterized by the one single high-intensive band accompanied with several individual small bands. These high frequency bands can be attributed to the stretching vibrations of Te-O and U-O, primarily associated with the motions of O atoms.[205–207] In contrast, the lower range of the spectra, from 200 to 450 cm^{-1}, are all featured by rather broad bands with lower intensity, which may correspond to the vibrations coupling of Te-O and U-O, because this is an overlapping region for these vibrations.[200,201] The spectral range below 200 cm^{-1} is dominated by the presence

---

[202] Llewellyn H. Jones. *Spectrochim. Acta, Part A*, **10**: 395–403, 1958.

[203] David D. Schnaars and Richard E. Wilson. *Inorg. Chem.*, **52**: 14138–14147, 2013.

[204] K. W. Bagnall and M. W. Wakerley. *J. Inorg. Nucl. Chem.*, **37**: 329–330, 1975.

[205] G. Sekar, V. Ramakrishnan, and G. Aruldhas. *Infrared Phys.*, **27**: 253–256, 1987.

[206] Ray L. Frost, Ji ejka, and Marilla J. Dickfos. *J. Raman Spectrosc.*, **39**: 779–785, 2008.

[207] Ray L. Frost. *Spectrochim. Acta, Part A*, **72**: 903–906, 2009.

of partially overlapping bands, mainly contributed from the motions of the “lattice skeleton”.[208,209] Specifically, for $\mathrm{Na[(UO_2)Te^{IV}{}_2O_5(OH)]}$, the highest peak of 707(1) cm^{-1} can be attributed to the symmetric stretching mode (ν_1) of Te^{IV}-O. The weak peaks situated near 860 cm^{-1} are perhaps due to the U-O symmetric stretching vibrations, which are comparable to those observed in schmitterite.[210] The Te^{IV}-O symmetric stretching mode (ν_1) of $\mathrm{Na[(UO_2)Te^{IV}{}_6O_{13}(OH)]}$ is shifted to 664(1) cm^{-1} and becomes boarder. This broader feature of vibrational spectrum also indicates a high degree of overlapping bands attributable from the cubic crystal symmetry. Owing to OH$^-$ stretching vibrations, both uranyl tellurite compounds have weak broad bands located from 2800 to 3100 cm^{-1}. These bonds are comparable to those found in many tellurite minerals, such as sonoraite ($\mathrm{Fe^{III}Te^{IV}O_3(OH){\cdot}H_2O}$)[211] and yecoraite ($\mathrm{Bi_5Fe_3O_9(Te^{IV}O_3)(Te^{VI}O_4)_2{\cdot}9\,H_2O}$)[212] A close resemblance between the Raman spectra of $\mathrm{Na_2[(UO_2)(Te^{VI}{}_2O_8)]}$ and $\mathrm{Na_2[(UO_2)Te^{VI}O_5]}$ can be detected. The highest peak around 738(1) and 729(1) cm^{-1} for $\mathrm{Na_2[(UO_2)(Te^{VI}{}_2O_8)]}$ and $\mathrm{Na_2[(UO_2)Te^{VI}O_5]}$, respectively, can be attributed to the stretching mode (ν_1) of Te^{VI}-O. Such small change in ν_1 of octahedral $\mathrm{TeO_6}$ unit is probably due to the combination of electronic and vibrational interactions, as described in many other tellurates.[213]

6.3.3 Conclusion

Herein, this section describes the high-temperature/high-pressure synthesis, crystal structures and spectroscopic investigations of four sodium uranyl tellurium compounds. The uranyl tellurites $\mathrm{Na[(UO_2)Te^{IV}{}_2O_5(OH)]}$ and $\mathrm{Na[(UO_2)Te^{IV}{}_6O_{13}(OH)]}$ are based on $\mathrm{Te^{IV}O_3}$ trigonal pyramids while the uranyl tellurates $\mathrm{Na_2[(UO_2)(Te^{VI}{}_2O_8)]}$ and $\mathrm{Na_2[(UO_2)Te^{VI}O_5]}$ are constructed from $\mathrm{Te^{VI}O_6}$ octahedra. Compared to all existing uranyl tellurium compounds isolated at atmosphere pressure or mild hydrothermal conditions, the Na-U-Te family is facile to form in non-centrosymmetric structures under the extreme synthesis condition. Except for $\mathrm{Na[(UO_2)Te^{IV}{}_6O_{13}(OH)]}$ which has the same structural skeleton as mineral cliffordite ($\mathrm{UO_2(Te_3O_7)}$), all the others are crystallized in non-centrosymmetric space group. In this case, the utilization of high-temperature/high-pressure synthesis method which serves as an opportunity to paint a portrait on a much larger canvas, which may aid in the design of novel nonlinear optical materials. However, could this significant non-centrosymmetry percentage found in Na-based uranyl tellurium family also apply to other U-Te families? Future attempts through the preparation of ongoing studies with incorporation of other alkaline metal countercations into uranyl tellurium family will answer this question.

---

[208] J. Hanuza, M. Maczka, and J. H. van der Maas. *J. Mol. Struct.*, **348**: 349–352, 1995.

[209] K. Hermanowicz et al. *J. Lumin.*, **92**: 151–159, 2000.

[210] Ray L. Frost et al. *Spectrochim. Acta, Part A*, **65**: 571–574, 2006.

[211] Ray L. Frost and Eloise C. Keeffe. *J. Raman Spectrosc.*, **40**: 133–136, 2009.

[212] Ray L. Frost and Eloise C. Keeffe. *J. Raman Spectrosc.*, **40**: 1117–1120, 2009.

[213] W. Levason. *Coord. Chem. Rev.*, **161**: 33–79, 1997.

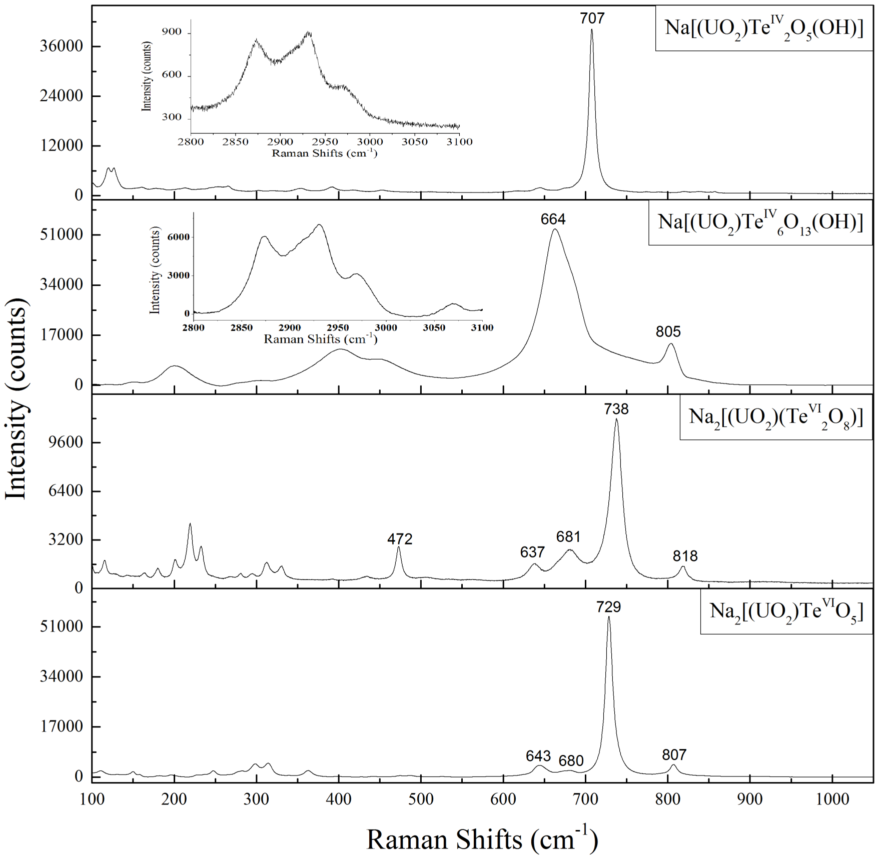

Figure 6.20: Raman Shifts of $\mathrm{Na[(UO_2)Te^{IV}{}_2O_5(OH)]}$, $\mathrm{Na[(UO_2)Te^{IV}{}_6O_{13}(OH)]}$, $\mathrm{Na_2[(UO_2)(Te^{VI}{}_2O_8)]}$ and $\mathrm{Na_2[(UO_2)Te^{VI}O_5]}$, respectively.

6.4 Flexible structural dimensionality of potassium uranyl oxo-tellurium

In spite of the promising application potentials for open framework materials, detailed studies associated with a targeted design are barely reported. Recently, our group addressed that the formation of 3D framework can be directly affected by the reaction condition such as temperature and pressure.[214] Follow on this, this section discusses the influence of high-temperature/high-pressure conditions on the formation of atypical structural features present in the solid-state uranium compounds.[215] This extreme condition plays an important role in enhancing and improving the structural diversity and complexity that uranium can adopt. Under high-temperature (up to 1200 °C) and high-pressure (near 2.5 GPa) condition, a totally novel family of uranyl borates where UO_6, UO_7, and UO_8 tetragonal,

---

[214] Shijun Wu et al. *Chem. Eur. J.*, **18**: 4166–4169, 2012.

[215] Shijun Wu et al. *Inorg. Chem.*, **51**: 3941–3943, 2012.

pentagonal, and hexagonal bipyramids are all within one compound were prepared.[216] In addition, this method is also helpful for yielding structural features that have not been observed with traditional synthesis conditions, as exemplified by the isolation of the first thorium compound with mixed-valent oxoarsenic(III)/arsenic(V),[217] as well as the first actinide aluminoborate.[214] Continuing with this direction, here, the uranyl tellurium family is studied through the application of high-temperature/high-pressure route that yields four new potassium uranyl tellurium compounds, $K_2[(UO_2)_3(Te^{IV}O_3)_4]$, $K_2[(UO_2)Te^{IV}{}_6O_{14}]$, α-$K_2[(UO_2)Te^{VI}O_5]$ and β- $K_2[(UO_2)Te^{VI}O_5]$.

In contrast to most of reported uranyl compounds which are favorable in layered structures, under extreme condition, the potassium uranyl tellurium compounds prefer in three-dimensional (3D) framework with complex structural topologies. All the uranyl oxo-tellurium compounds are prepared form at the temperature of around 1050 °C and pressure of around 3.5 GPa. The detailed procedures are the same as for $HT/HP-ThMo_2O_8$ in the page of 19. The raw chemicals used were A. R. grade of UO_3, KNO_3 (Alfa-Aesar), TeO_2 (Alfa-Aesar) and H_6TeO_6 (Alfa-Aesar) without further purification. The starting materials were 20.0 mg (0.0699 mmol) UO_3, 14.1 mg (0.1398 mmol) KNO_3, 33.5 mg (0.2098 mmol) TeO_2, and 16.1 mg (0.0699 mmol) H_6TeO_6 for $K_2[(UO_2)_3(TeO_3)_4]$. For $K_2[(UO_2)Te_6O_{14}]$, the starting materials were 20.0 mg (0.0699 mmol) UO_3, 28.3 mg (0.2796 mmol) KNO_3, 67.0 mg (0.4196 mmol) TeO_2, and 16.1 mg (0.0699 mmol) H_6TeO_6. The starting materials were 20.0 mg (0.0699 mmol) UO_3, 14.1 mg (0.1398 mmol) KNO_3, and 16.1 mg (0.0699 mmol) H_6TeO_6 for $K_2[(UO_2)_3(TeO_3)_4]$. The starting materials were 20.0 mg (0.0699 mmol) UO_3, 14.1 mg (0.1398 mmol) KNO_3, and 48.3 mg (0.2097 mmol) H_6TeO_6 for β-$K_2[(UO_2)_3(TeO_3)_4]$.

Anion topology analysis indicates that the tellurite anionic framework observed in $K_2[(UO_2)_3(Te^{IV}O_3)_4]$ are attributable to the additional linkages of TeO_3 polyhedra connecting with TeO_4 disphenoids from neighboring U-Te layers. The structure of $K_2[(UO_2)Te^{IV}{}_6O_{14}]$ can be described as based on $[UTe_6O_{26}]^{22-}$ clusters, where six TeO_5 polyhedra enclose a hexagonal cavity in which a UO_8 polyhedron is located. The $[UTe_6O_{26}]^{22-}$ clusters are further linked by TeO_5 square pyramids to form the 3D network. As the case of uranyl tellurates, both α-$K_2[(UO_2)Te^{VI}O_5]$ and β-$K_2[(UO_2)Te^{VI}O_5]$ contain TeO_6 octahedra which share a common face to form a dimeric Te_2O_{10} unit. However, in α-$K_2[(UO_2)Te^{VI}O_5]$, these Te_2O_{10} units connect with UO_6 tetragonal bipyramids to result in a 3D structural framework, while in β-$K_2[(UO_2)Te^{VI}O_5]$, the same Te_2O_{10} dimers are observed to link with UO_7 pentagonal bipyramids, forming 2D layers. In addition, Raman measurements were carried out and the vibrations related to Te^{IV}-O, Te^{VI}-O and U^{VI}-O bonds are discussed.

6.4.1 Structural and topological relationship in potassium uranyl tellurium family

$K_2[(UO_2)_3(Te^{IV}O_3)_4]$

$K_2[(UO_2)_3(Te^{IV}O_3)_4]$ crystallizes in the triclinic space group $P\bar{1}$, and forms a 3D U-Te anionic frame-

---

[216] Shijun Wu et al. *Inorg. Chem.*, **52**: 5110–5118, 2013.

[217] Na Yu et al. *Inorg. Chem.*, **53**: 8194–8196, 2014.

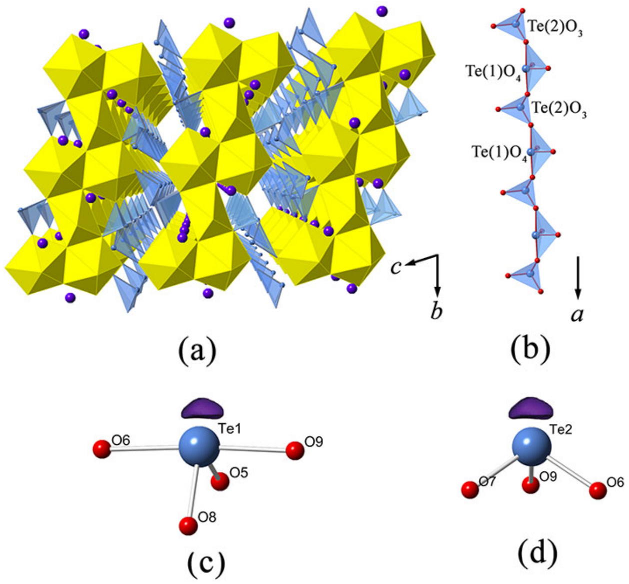

Figure 6.21: Representation of structure of $K_2[(UO_2)_3(Te^{IV}O_3)_4]$. (a) Illustration of the anionic uranyl tellurite framework which is charge balanced by K^+. (b) View of the $[TeO_3]^{2-}$ chain comprised by alternating connections of TeO_3 and TeO_4 polyhedra. (c) The local coordination environment of Te(1). (d) The local coordination environment of Te(2). Legends: UO_7 pentagonal bipyramids are shown in yellow. TeO_3 polyhedra are in light blue and their long pairs are shown in purple. K^+ cations are in blue nodes.

work which is charge balanced by K^+ cations. It contains two symmetrically unique U^{6+} sites (U(1) and U(2)) and two different Te^{4+} sites (Te(1) and Te(2)) in the asymmetric unit. Both uranium sites are coordinated with two nearly linear *trans* oxygen atoms at the axial positions, forming a uranyl ($UO_2{}^{2+}$) unit. U(1) forms in a highly distorted UO_6 tetragonal bipyramidal geometry by binding with four equatorial O atoms, a less common coordination environment for uranium. The U=O bond distance of U(1) is 1.812 Å (× 2), which falls in the typical range of uranyl coordination.[180] Its equatorial U-O distances, with an average value of 2.310 Å, are obviously distorted in the O(4) direction, this being the shortest U-O distance of 2.198(9) Å. U(2) is found in a UO_7 pentagonal bipyramidal configuration with the U=O bond distances from 1.817(9) to 1.820(9) Å. Compared to U(1), U(2) experiences less perturbed within its equatorial plane, but still shows a slight variation, which ranges from 2.268(8) to 2.383(9) Å.

Te(1) is in the form of a disphenoidal geometry (TeO_4). It is coordinated with four oxygen atoms, with its electron lone pairs pointing towards the cross corner (see **Figure 6.21 (c)**). Whereas, Te(2) is surrounded with three oxygen atoms in a trigonal pyramidal configuration (TeO_3). The Te(2) atom is off-centered from the triangular base (see **Figure 6.21 (d)**). It is noted that such fourfold ($Te^{IV}O_4$) or threefold ($Te^{IV}O_3$) coordination is quite common among the tellurite structures.[113,218,219] The Te(1)-O bond lengths vary within a considerably wide range from 1.845(9) to 2.171(9) Å, the mean value being around 1.999 Å. In contrast, the $Te(2)O_3$ trigonal pyramid is less distorted, but still show substantial variations in Te-O bond lengths and O-Te-O angles, which range from 1.853(9) to 1.890(9) Å and from 87.8(4)° to 103.0(4)°, respectively.

---

[218] Vidyavathy and K. Vidyasagar. *Inorg. Chem.*, **38**: 1394–1400, 1999.

[219] Seong-eun Bang et al. *J. Solid State Chem.*, **208**: 65–70, 2013.

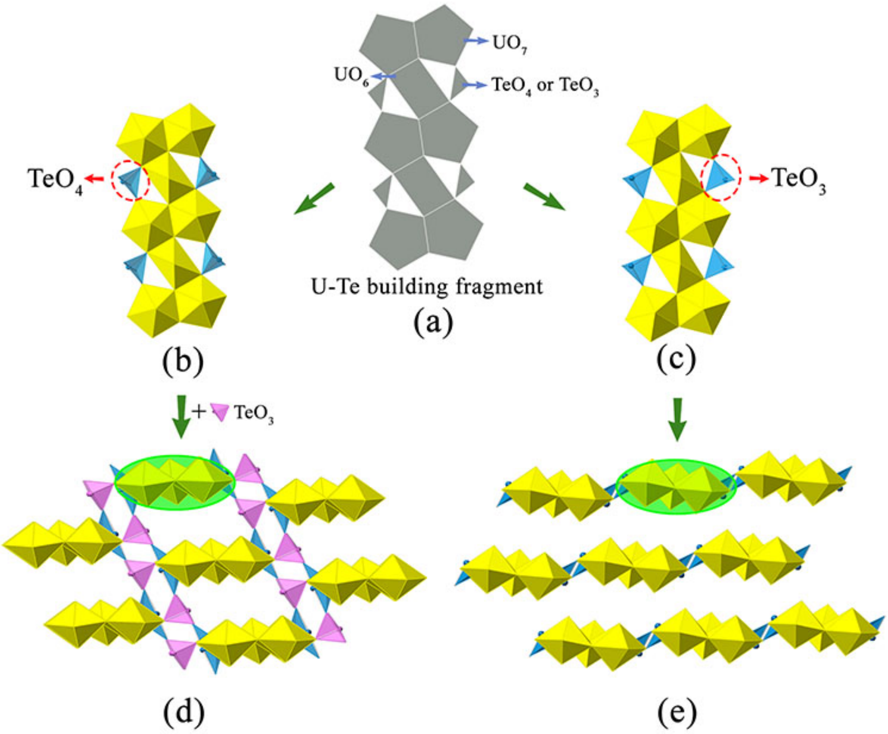

Figure 6.22: Structural comparison between 3D $K_2[(UO_2)_3(Te^{IV}O_3)_4]$ and 2D $A_2[(UO_2)_3(TeO_3)_2O_2]$ (A = K, Rb, Cs).(a) The anion topology of uranyl tellurite building block. (b) The uranyl tellurite building block observed in $K_2[(UO_2)_3(Te^{IV}O_3)_4]$. (c) The uranyl tellurite building block observed in $A_2[(UO_2)_3(TeO_3)_2O_2]$ (A = K, Rb, Cs). (d) 3D framework in $K_2[(UO_2)_3(Te^{IV}O_3)_4]$ formed by connecting uranyl tellurite building blocks with additional TeO_3 linkers (the TeO_3 linkers are highlighted in pink). (e) 2D layered structure in $A_2[(UO_2)_3(TeO_3)_2O_2]$ (A = K, Rb, Cs) composed by linking uranyl tellurite building blocks side-by-side in a plane. Legends: UO_7 pentagonal bipyramids are shown in yellow. TeO_x (x = 3 or 4) polyhedra are in light blue and pink, respectively.

In $K_2[(UO_2)_3(Te^{IV}O_3)_4]$, two U(2) pentagonal bipyramids share a common edge, leading to a U_2O_{12} dimer. Neighboring U_2O_{12} dimers are fused together *via* sharing four vertexes with four equatorial corners from a UO_6 polyhedra, resulting in a uranyl ribbon running in the [010] direction (**Figure 6.21 (a)**). The Te(1)O_4 disphenoids and Te(2)O_3 trigonal pyramids are connected alternatively by sharing common corners to form infinite $[TeO_3]^{2-}$ chains propagating along ***a***-axis direction (**Figure 6.21 (b)**). The lone electron pairs of Te(1) and Te(1) polyhedra are arranged exclusively vertical to the chain direction. Finally, these $[TeO_3]^{2-}$ chains further link with above mentioned uranyl ribbons in corner-sharing manner, completing the $[(UO_2)_3Te_4O_{12}]^{2-}$ framework. Bond valence calculation results in 4.05 and 3.97 v.u. for Te(1) and Te(2), respectively, both of which are consistent with Te in tetravalent oxidation.

It is noteworthy that the structure of $K_2[(UO_2)_3(Te^{IV}O_3)_4]$ is closely related to that of $A_2[(UO_2)_3(TeO_3)_2O_2]$ (A = K, Rb, Cs). Both can be seen as based on similar U-Te building fragment, shown in

Figure 6.22 (b and c). The local linkages inside such building fragment can be described using the method of *anion topology* and the result is shown in **Figure 6.22** (a). In this anion topology, the triangles are filled with Te polyhedra (TeO_3 or TeO_4) while the squares and pentagons are occupied by UO_6 and UO_7, respectively. In the former structure, the observed U-Te building fragments are fused together, with the linkage of additional TeO_3 polyhedra, resulting in a terraced configuration (**Figure 6.22 (d)**). Whereas the adjacent U-Te building fragments in the latter compounds are fused side-by-side within a plane (**Figure 6.22 (f)**). As the result, $A_2[(UO_2)_3(TeO_3)_2O_2]$ (A = K, Rb, Cs) crystallize in a 2D layered structural type while the $K_2[(UO_2)_3(Te^{IV}O_3)_4]$ forms in a 3D framework conformation. It is obvious to see that this dimensionality difference is due to the coordination requirements of Te polyhedra inside the respective U-Te building fragment. As mentioned above, the anion topology of both structural types contains triangles that represent Te polyhedra. In $K_2[(UO_2)_3(Te^{IV}O_3)_4]$, the corresponding triangular area in the anion topology graph cannot be exactly occupied by a four-coordinated TeO_4 disphenoid. In this case, the remaining two oxygen corners of this TeO_4 which do not participate in triangle composition can be further linked “up” and “down” relative to the U-Te building plane with additional TeO_3 units (highlighted in **Figure 6.22 (c)** in pink color). In contrast, for $A_2[(UO_2)_3(TeO_3)_2O_2]$ (A = K, Rb, Cs), the corresponding triangle in anion topology can be exactly filled by three oxygen atoms of a TeO_3 trigonal pyramid.

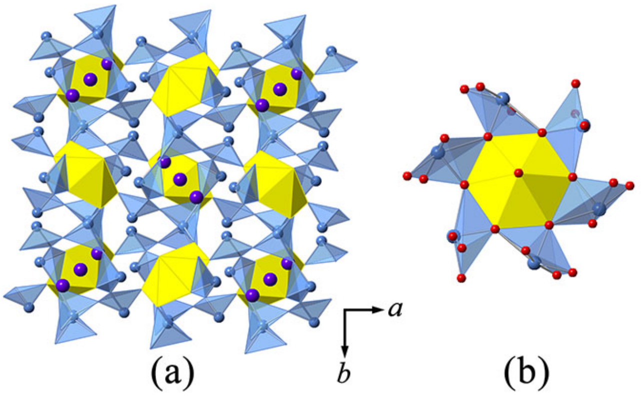

Figure 6.23: (a) A view of the three-dimensional $K_2[(UO_2)Te^{IV}{}_6O_{14}]$ extending along the c-axis. (b) The local coordination geometry of $[UTe_6O_{26}]^{22-}$ clusters in $K_2[(UO_2)Te^{IV}{}_6O_{14}]$. UO_8 hexagonal bipyramids are shown in yellow. TeO_5 polyhedra are in light blue. K^+ cations are blue nodes.

$K_2[(UO_2)Te^{IV}{}_6O_{14}]$

The structure analysis reveals that the 3D framework of $K_2[(UO_2)Te^{IV}{}_6O_{14}]$ is formed by edge-sharing of UO_8 and TeO_5 polyhedra (shown in **Figure 6.23 (a)**). The asymmetric unit contains one crystallographically independent U and one Te atoms. The U(1) atom is formed in an almost ideal hexagonal bipyramid, with U=O bond distances of 1.788(10) Å (× 2), and the O=U=O angle of 180.0(0)°. The equatorial U-O bond distances are all equal to 2.445(6) Å. As given in **Figure 6.23 (b)**, each U shares all six edges with six TeO_5 polyhedra in the equatorial plane, giving rise to a $[UTe_6O_{26}]^{22-}$ cluster. Each Te(1) site is coordinated by five oxygen atoms with the electron lone pairs pointing towards the square base, creating a distorted square pyramidal coordination geometry. The resulting Te(1)O_5 polyhedron has one μ_2-O atom linked with another Te(1), and four μ_3-O atoms, two of which are linked with one Te(1) and one U(1) and another two are linked with two Te(1) atoms. The Te-O band distances varying from 1.873(6) to 2.363(6) Å are within the range seen in other tellurites containing TeO_5 polyhedra.[123,192] Finally, the TeO_5 square pyramids further bridge with $[UTe_6O_{26}]^{22-}$ clusters to complete the 3D network structure of $K_2[(UO_2)Te^{IV}{}_6O_{14}]$. Bond valence sum calculations are consistent with U^{VI} and Te^{IV}, providing the values of 6.0 and 3.9 v.u., respectively.

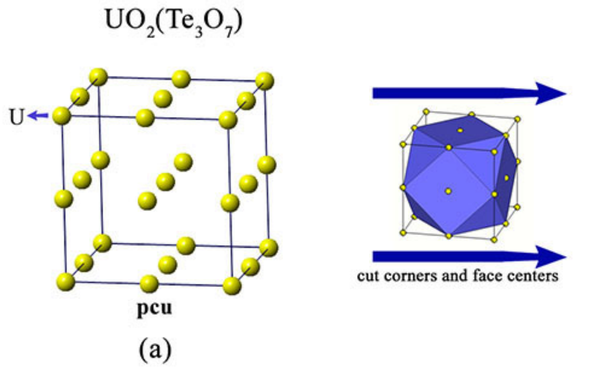

Figure 6.24: Arrangement of UO_8 hexagonal pyramids in one unit cell for (a) cliffordite $UO_2(Te_2O_7)$ and (b) $K_2[(UO_2)Te^{IV}{}_6O_{14}]$, respectively. The corresponding topologies of pcu and fcu-a net for $UO_2(Te_2O_7)$ and $K_2[(UO_2)Te^{IV}{}_6O_{14}]$, respectively. Topological transformation of U arrangement from pcu observed in $K_2[(UO_2)Te^{IV}{}_6O_{14}]$ to fcu-a observed in $UO_2(Te_2O_7)$can be achieved by removing the 8 corners and 6 face-centers. UO8 hexagonal bipyramids are shown in yellow nodes.

The structure of $K_2[(UO_2)Te^{IV}{}_6O_{14}]$ is highly related to that of cliffordite ($UO_2(Te_2O_7)$). Both are constructed from the same structural building units of UO_8 hexagonal bipyramids and TeO_5 square pyramids. Their structural difference comes from the number and arrangement of the UO_8 polyhedra in each structural unit. As shown in **Figure 6.24**, only one U site is observed in $K_2[(UO_2)Te^{IV}{}_6O_{14}]$. However, two symmetrically independent U sites are found in the structure of cliffordite, one of which is partial occupied and the other is fully occupied. For cliffordite, 27 UO_8 hexagonal bipyramids resided in each unit cell, forming regular **pcu** (primitive cubic lattice) net. In contrast, only 13 U atoms are found in one unit cell for $K_2[(UO_2)Te^{IV}{}_6O_{14}]$, and they are arranged into a cuboctahedral conformation with **fcu-a** (face-centered cubic lattice) topology. In fact, the U arrangement in $K_2[(UO_2)Te^{IV}{}_6O_{14}]$ and cliffordite can be transformed from one to another by removing the 8 corners and 6 face-centers from califfordite- based topology.

α-$K_2[(UO_2)Te^{VI}O_5]$

The 3D framework of α-$K_2[(UO_2)Te^{VI}O_5]$ (**Figure 6.25 (a, b)**) is crystallized in $P2_1/n$ space group. It contains one symmetrically independent U^{6+} which is strongly bonded to two O atoms, resulting in a linear uranyl unit $UO_2{}^{2+}$. The bond lengths of the uranyl cation are 1.824(8)-1.829(9) Å for U=O, and 2.221(10)-2.246(9) Å are observed for equatorial U-O_{eq}. One symmetrically distinct Te^{6+}

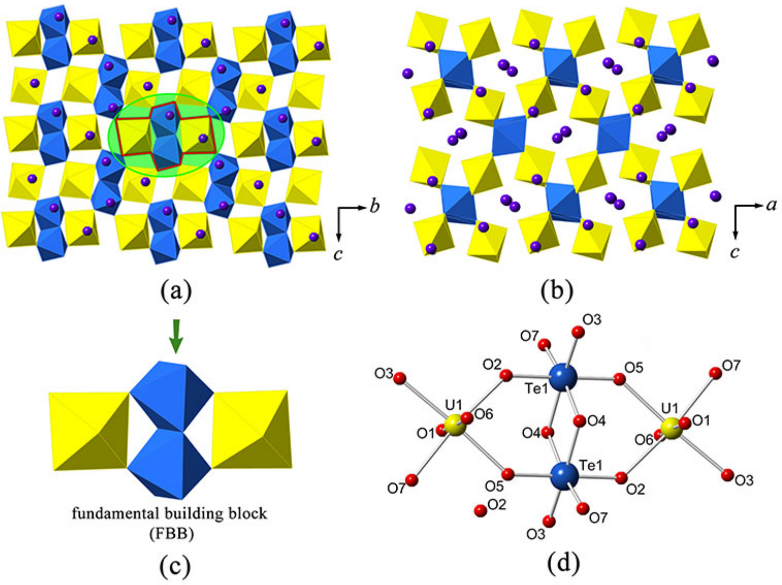

Figure 6.25: View of the structure of α-$K_2[(UO_2)Te^{VI}O_5]$.

cation, with BVS result of 5.97 v.u., is present in TeO_6 octaheral coordination. The bond angles are 78.9(4)-99.9(4)° and 169.3(4)-179.5(4)° for Te-O in cis- and $trans$- configurations, respectively.

The fundamental building block (**FBB**) in the 3D structural framework of α-$K_2[(UO_2)Te^{VI}O_5]$ is composed of two TeO_6 octahedra and two UO_6 tetragonal bipyramids, shown in **Figure 6.25 (c, d)**. Within it, the $[Te_2O_{10}]^{4-}$ anions, formed by two edge-sharing TeO_6 octahedra, share four corners linking with two UO_6 tetragonal bipyramids. The bridging Te-O(4), with a bond length of 1.995(9) Å, shows significant lengthening with respect to the remaining Te-O bonds, which range from 1.869(10) to 1.911(9) Å. The Te-O-Te angles in $[Te_2O_{10}]^{4-}$ anions are around 101°. It is noted that the $[Te_2O_{10}]^{4-}$ anions can also be found in several inorganic tellurates.[173,220] The FBBs link together via corner-sharing manner to form a complex 3D system of channels. When viewing from **c**-axis, one can find that the largest channel runs though the U-Te lattice (highlighted in **Figure 6.26 (a)**). This channel, with eight-ring pore opening, is resided by charge compensating K^+ cations. It has a cross-section of elliptic shape and the dimensions of around 5.4 Å × 3.2 Å. Besides, additional smaller interlacing channels can also be detected propagating in the [101], $[10\bar{1}]$ and [110] directions. In order to describe the connection behavior of uranium and tellurium polyhedra along the channel direction, the *black-and-white nodal representation* is adopted. The UO_6 tetragonal bipyramids and TeO_6 octahedra are simplified as black and white nodes, respectively. The nodes are connected by single or double lines if the corresponding polyhedra share corner or edge with each other. This method permits to elucidate the local topological feature inside the channel structure and has been widely used to describe the open-framework actinide compounds containing tubular units, such as uranyl selenate $[(UO_2)_3(SeO_4)_5]^{4-}$,[100] uranyl

---

[220] Matthias Weil. *Z. Anorg. Allg. Chem.*, **633**: 1217–1222, 2007.

molybdate $[(UO_2)_5(MoO_4)]^{4-}$[111] and thorium molybdate $[Th_3(MoO_4)_7]^{2-}$[105]. The largest channels propagating along ***c***-axis is shown in **Figure 6.26 (b and c)**. The corresponding topological net is given in **Figure 6.26 (d)**. Form the idealized unfold topology (see **Figure 6.26 (e)**), one can note that the infinite U-Te channel is assembled from seven- and three-membered rings. Due to the existence of a twofold rotational axis, the topological net is achiral, which is consistent with the space group $P2_1/n$. Each uranium polyhedron (black node) is four-connected while each tellurium polyhedron (white node) is three-connected. It is noted that this channel structure can be re-constructed using a folding and gluing procedure. First, label the equivalent points on sides of the tap by letters a, b and c. Then fold the tape by jointing the corresponding opposite sides (a–a', b–b' and c–c') to make a cylinder. The idealized topological structure for the tubular unit in α-$K_2[(UO_2)Te^{VI}O_5]$ is demonstrated in **Figure 6.26 (f)**.

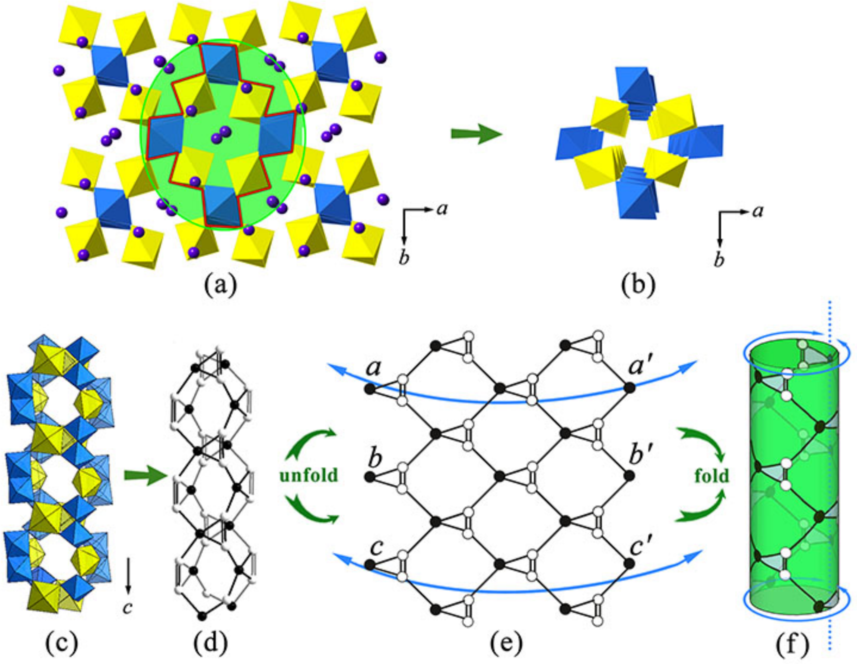

Figure 6.26: Channels in the structure of α-$K_2[(UO_2)Te^{VI}O_5]$. The structure can be considered as consisting of cylinder unit.

Structure of β-$K_2[(UO_2)Te^{VI}O_5]$

The 2D structure of β-$K_2[(UO_2)Te^{VI}O_5]$ consists of $[UTeO_7]^{2-}$ anionic layers propagating along bc plane. These two-dimensional anionic layers are shown in **Figure 6.27 (a)**. They are separated from each other by K^+ cations playing the role of maintaining charge neutrality. As shown in **Figure 6.27 (b, c)**, each $[UTeO_7]^{2-}$ anionic layer is formed from one crystallographically unique U site and one Te site. The U cation is coordinated by two-terminal oxo-groups, creating the uranyl moiety. The U-O bond lengths range from 1.799(5) to 1.807(5) Å for U=O bonds of the uranyl unit, and from

---

[111] S. V. Krivovichev, C. L. Cahill, and P. C. Burns. *Inorg. Chem.*, **42**: 2459–2464, 2003.

2.241(5) to 2.541(5) Å for the U-O in equatorial plane. These UO_7 polyhedra share common edges with each other to result in infinite chains, with one UO_7 polyhedron wide, running along the **c**-axis. In fact, these U chains have been commonly observed among many mineral and synthetic uranium tellurites/tellurates, such as moctezumite $Pb[(UO_2)(TeO_3)_2]$[196], and $UTeO_5$[221]. As for the Te site, it exhibits a slightly distorted octahedral environment. The distortion can be best shown from the *cis* O-Te-O angles in the range of 80.0(2)° to 95.4(2)°. The Te-O bond distances vary within an appreciable range of 1.886(4) to 1.983(5) Å, the average distance being 1.929 Å. The bond valence sum calculations give the values of 5.9 v.u. for U site, and 5.8 v.u. for Te site, respectively, confirming that all the U and Te are all in +6 oxidation state.

As shown in **Figure 6.27 (c)**, two TeO_6 octahedra share a common edge, O(6)-O(6)′, leading to a Te_2O_{10} dimmer, similar to the one reported in a series of compounds with formula of $A_2[Te_3O_8(OH)_4]$ (A = Na, K, Rb, Cs).[126] However, the Te_2O_{10} dimers have different coordination environments in both structures. In β-$K_2[(UO_2)Te^{VI}O_5]$, these Te_2O_{10} dimers are embedded into above mentioned $[UTeO_7]^{2-}$ anionic layers by sharing one edge (O(3) and O(5)) and one corner (O(7)) from each TeO_6 octahedron. In contrast, the corresponding Te_2O_{10} dimers in $A_2[Te_3O_8(OH)_4]$ are further fused together through corners to result in infinite chains.

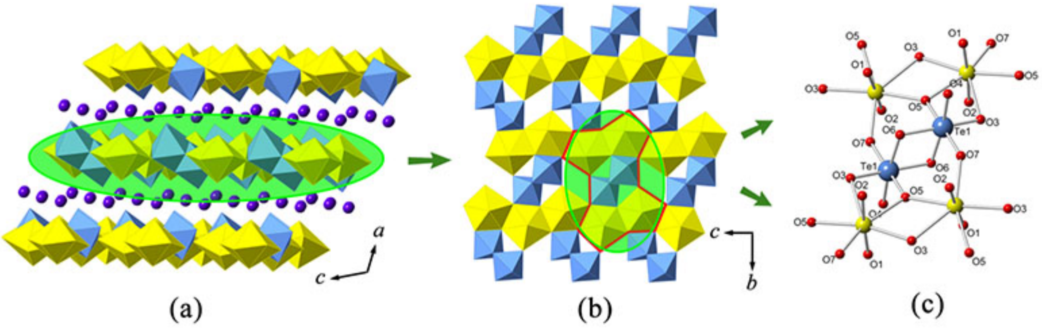

Figure 6.27: View of layered structure of β-$K_2[(UO_2)Te^{VI}O_5]$.

6.4.2 Raman spectroscopic analysis

The Raman spectra for all four uranyl tellurium compounds are presented in **Figure 6.28**. It is noteworthy to mention that the vibrational data on tellurites/tellurates are well-established in the literature,[198] however, very little research has been undertaken on the vibrational spectroscopy of actinide tellurates/tellurites. The infrared spectrum studies of schmitterite (UO_2TeO_3) and cliffordite

---

[221] K Krishnan et al. *Journal of nuclear materials*, **254**: 49–54, 1998.

(UTe_3O_9) were reported by *botto, et al.*, and Raman vibrational studies of schmitterite (UO_2TeO_3)[200] and moctezumite ($Pb(UO_2)(TeO_3)_2$)[201] were recently discussed by *Frost, et al.*.

The Raman spectra for all the above discussed uranyl tellurium compounds are characterized by motions from uranyl ($UO_2{}^{2+}$) linearity and tellurite ($Te^{IV}O_3$) trigonal pyramid or tellurate ($Te^{VI}O_6$) octahedron. The ideal uranyl ($UO_2{}^{2+}$) unit with $D_{\infty h}$ symmetry has three normal modes in aqueous solution, that is, ν_1 symmetric stretching mode (approximately from 860 to 880 cm^{-1}), ν_3 antisymmetrical stretching (approximately from 930 to 960 cm^{-1}), and ν_2 bending mode (approximately from 199 to 210 cm^{-1}).[202,203] The free $Te^{IV}O_3$ trigonal pyramid has the C_{3v} symmetry, with motions being assigned as $A_1(\nu_1)$, $A_1(\nu_2)$, E(ν_3) and E(ν_4), where ν_1, ν_2, ν_3 and ν_4 modes are denoted as non-degenerated symmetric stretching, non-degenerated symmetric bending, doubly degenerated asymmetric stretching and asymmetric bending vibrations, respectively. In aqueous solution, these modes are observed to be located at 758 cm^{-1} for ν_1, 703 cm^{-1} for ν_3, 364 cm^{-1} for ν_2 and 326 cm^{-1} for ν_4, respectively.[222] The ideal $Te^{VI}O_6$ octahedron has three kinds of Raman active vibrational bands, $\nu_1(A_{1g})$, $\nu_2(E_g)$ and $\nu_5(F_{2g})$, and the stretching and bending vibrations for mostly tellurate compounds are distributed in the range of 550−750 cm^{-1} and 350−450 cm^{-1}, respectively.[205]

For all four uranyl compounds, the high frequency bands between 600 and 800 cm^{-1} are mainly attributed to the stretching vibrations of U-O and Te-O, whereas the low frequency part below 250 cm^{-1} is correspond to the motions of the crystal lattice. Due to the large number of atoms in the unit cell and to the relatively overlapping vibrational regions of U-O and Te-O, here I only assign the signature peaks for uranyl tellurium compounds. The assignment of the vibrational bands were mainly based on the comparison of two uranyl mineral schmitterite(UO_2TeO_3)[200] and moctezumite ($Pb(UO_2)(TeO_3)_2$)[201]. For $K_2[(UO_2)_3(Te^{IV}O_3)_4]$, the very strong peak at 678 cm^{-1} may be assigned to the symmetric stretching of ν_1 $Te^{IV}O_3$. The corresponding band is shift to higher frequency for $K_2[(UO_2)Te^{IV}{}_6O_{14}]$ (at 702 cm^{-1}), but still agrees well with that in schmitterite which is also observed as the strongest peak in Raman spectrum at 724 cm^{-1}[200]. The Raman spectra for $K_2[(UO_2)Te^{IV}{}_6O_{14}]$ is characterized by the presence of board, partially overlapping bands. Band located at 846 cm^{-1} may be assigned to the ν_1 $UO_2{}^{2+}$ symmetric stretching vibration, which can be compared with 823 cm^{-1} in calcurmolite ($Ca(UO_2)_3(MoO_4)_3(OH)_2{\cdot}H_2O$)[206] and 826 cm^{-1} in moctezumite[201], respectively. The presence of different peaks in α- and β-$K_2[(UO_2)(Te^{VI}O_5)]$ reflects the structural differences in both modifications. The largest peak which can be assigned as ν_1 of $Te^{VI}O_6$ is lower for α-$K_2[(UO_2)(Te^{VI}O_5)]$ (at 715 cm^{-1}) than that for β modification (at 748 cm^{-1}), but still comparable well with most tellurate compounds.[223,224]

---

[222] K. V. Domoratskii et al. *Phys. Solid State*, **42**: 1443–1446, 2000.

[223] S. Raman. *Inorg. Chem.*, **3**: 634–638, 1964.

[224] Jaime Llanos et al. *J. Alloys Compd.*, **485**: 565–568, 2009.

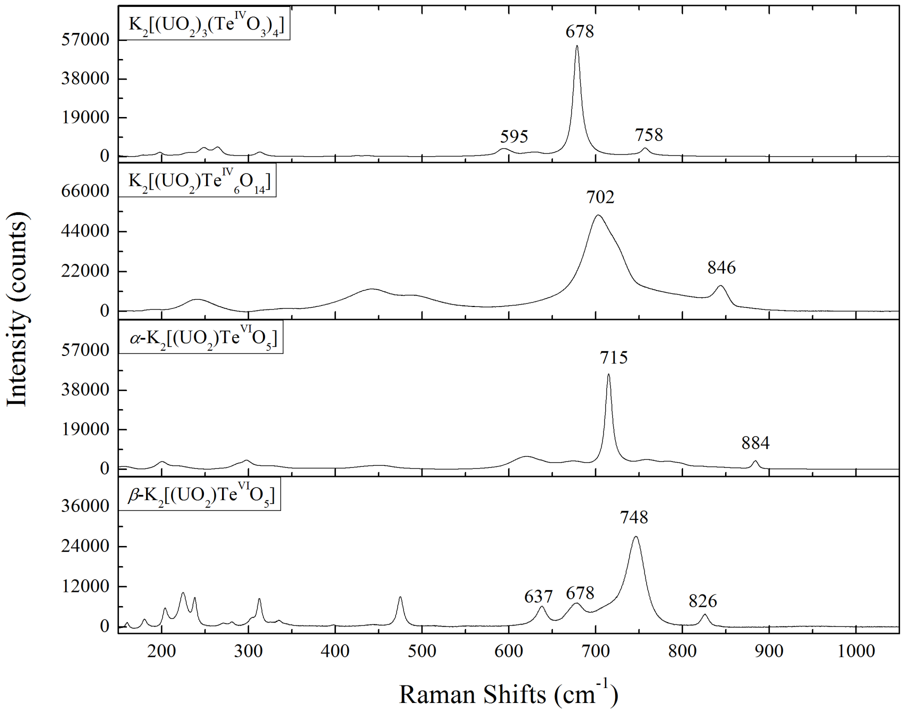

Figure 6.28: Raman shifts from 150 to 1050 cm^{-1} for $K_2[(UO_2)_3(Te^{IV}O_3)_4]$, $K_2[(UO_2)Te^{IV}{}_6O_{14}]$, α-$K_2[(UO_2)(Te^{VI}O_5)]$, β-$K_2[(UO_2)(Te^{VI}O_5)]$.

6.4.3 Conclusion

This work enhances the poorly investigated area of application the high-temperature/high-pressure technology in studying of actinide chemistry. Among all the synthetic uranyl tellurium compounds in the literature, most were isolated *via* employing mild hydrothermal (around 200 °C) condition in a Teflon-lined autoclave, and a few were synthesized at high-temperature (around 800 °C) using alkaline chloride as flux.[225,226] The obtained novel uranyl tellurium compounds in this work are structurally more complex than those produced under atmosphere pressure or mild hydrothermal conditions.

The structures of the titled compounds demonstrate the considerable flexibility of tellurium polyhedral geometries ($Te^{IV}O_3$ trigonal pyramid, $Te^{IV}O_4$ disphenoid, $Te^{IV}O_5$ square pyramid and $Te^{VI}O_6$ octahedron) in forming diverse structural topologies. Specifically, $Te^{IV}O_3$ trigonal pyramids and $Te^{IV}O_4$ disphenoids are connected in $[TeO_3]^{2-}$ chains extending along the $\boldsymbol{a}$-axis in $K_2[(UO_2)_3(Te^{IV}O_3)_4]$. $Te^{IV}O_5$ square pyramids play the role of structural linkers to connect $[UTe_6O_{26}]^{22-}$ clusters into

---

[225] Jonathan D. Woodward, Philip M. Almond, and Thomas E. Albrecht-Schmitt. *J. Solid State Chem.*, **177**: 3971–3976, 2004.

[226] Jonathan D. Woodward and Thomas E. Albrecht-Schmitt. *J. Solid State Chem.*, **178**: 2922–2926, 2005.

$K_2[(UO_2)Te^{IV}{}_6O_{14}]$, and $Te^{VI}O_6$ octahedra are found to form Te_2O_{10} dimers among both and α- and β-$K_2[(UO_2)Te^{VI}O_5]$. Moreover, three out of four uranyl compounds, $K_2[(UO_2)_3(Te^{IV}O_3)_4]$, $K_2[(UO_2)Te^{IV}{}_6O_{14}]$ and α-$K_2[(UO_2)Te^{VI}O_5]$ are isolated in 3D framework, which is a sharp contrast to the dominant 2D layered structures among uranyl compounds synthesized under regular conditions. Thus, it is clear that the extreme condition allows for the formation of atypical structure types with structures more complex and dimensionalities more variable than expected.

Chapter 7

Crystal Chemistry of Thorium Compounds with Mixed Oxo-Anions

Recent interest in new tellurite compounds in the solid-state chemistry has mainly focused on mixed oxo-anions including d^0 transition metals such as W^{6+} and Mo^{6+} that are susceptible to second-order Jahn-Teller (**SOJT**) distortions, with a clear effort to design new noncentrosymmetric materials.[114,118,227,228] Similarly, the coordination geometry of Mo^{6+}/W^{6+} cations are equally versatile, with four to six oxygen atoms being found to form tetrahedral, square pyramidal, trigonal bipyramidal or octahedral polyhedra. Considerable accomplishments have been gained in this regard in recent years. From these compounds, $BaTeM_2O_9$ (M = Mo^{6+}, W^{6+})[227], $A_2TeM_3O_{12}$ (A = ${NH_4}^+$, Rb^+, Cs^+; M = Mo^{6+}, W^{6+}) and $(NH_4)_2Te_2WO_8$[116] exhibit potential application in developing new devices in laser systems due to their satisfactory outcomes in the properties of piezoelectricity, pyroelectricity and second-harmonic generation. The inclusion of rare earth metals into this system is of high interest due to the excellent luminescence and alexandrite effect of rare earth metals.[229] $Nd_2MoTe_3O_{12}$, for example, is considered as a possible luminescent candidate for 1.06 μm emission.[230]

However, comparing to a vast number of molybdate tellurites and tungstate tellurites containing alkali, alkaline earth, transition and even rare earth metals, the study of actinide molybdate tellurites or tungstate tellurites remains in deep freeze, and until now there is no crystal structure reported in this family. Because of the versatility of coordination geometries of actinide elements,[231] it is expected that this family also possesses fascinating topological structural types. This chapter will fill this gap by introducing four new compounds that simultaneously contain MoO_4/WO_6 and Te^{4+} groups, namely,

---

[114] Joanna Goodey, Jake Broussard, and P. Shiv Halasyamani. *Chem. Mater.*, **14**: 3174–3180, 2002.

[118] Junjie Zhang et al. *CrystEngComm*, **13**: 6985–6990, 2011.

[227] H. S. Ra, K. M. Ok, and P. S. Halasyamani. *J. Am. Chem. Soc.*, **125**: 7764–7765, 2003.

[228] Junjie Zhang et al. *Chem. Mater.*, **23**: 3752–3761, 2011.

[116] Jun-Ho Kim, Jaewook Baek, and P. Shiv Halasyamani. *Chem. Mater.*, **19**: 5637–5641, 2007.

[229] Jian Lin et al. *Inorg. Chem.*, **52**: 13278–13281, 2013.

[230] Yue-Ling Shen et al. *Inorg. Chem.*, **44**: 9314–9321, 2005.

[231] Peter C. Burns, Rodney C. Ewing, and Frank C. Hawthorne. *Can. Mineral.*, **35**: 1551–1570, 1997.

$ThWTe_2O_9$, $Th(WO_4)(TeO_3)$, $ThMoTe_2O_9$ and $Th_2(MoO_4)(TeO_3)_3$.

7.1 Incorporation Te(IV) oxo-anions into thorium molybdate/tungsten systems

The exploration of phase formation in the Th-Mo/W-Te systems has resulted in four mixed oxo-anion compounds from high-temperature solid-state reactions: For $ThWTe_2O_9$, $Th(WO_4)(TeO_3)$, $ThMoTe_2O_9$ and $Th_2(MoO_4)(TeO_3)_3$. For $ThWTe_2O_9$, $Th(NO_3)_4 \cdot (H_2O)_5$ (50 mg, 0.0877 mmol), TeO_2 (42.0 mg, 0.263 mmol) and WO_3 (61.0 mg, 0.259 mmol) were weighed in. This results in a Th: Te: W ratio of 1:3:3. The mixture was fully ground and transferred into a 5 ml Pt crucible. After a holding time of 3 hours at 780 °C for homogeneous melting, the furnace was cooled down in two steps. First the temperature was gradually decreased by 5 °C/h to 250 C, then to room temperature (RT) within three hours. Brown colored crystals were found on the wall of the crucible and were hand-picked for further analyses. The yield cannot be calculated because the broken glassy pieces and crystals are indistinguishable. The molar ratio of Th: Te: W: Li = 1: 2: 4: 3 for $Th(WO_4)(TeO_3)$. The Th: Te: Mo molar ratio of 1: 4: 4 for $ThMoTe_2O_9$ and a Th: Te: Mo molar ratio of 1: 2: 4 for $Th_2(MoO_4)(TeO_3)_3$, respectively.

All four compounds contain edge-sharing thorium polyhedra linked by MoO_4/WO_6 and different tellurium oxo-groups to form three-dimensional frameworks. In $ThWTe_2O_9$, each helical Th based chain is connected by four tungstotellurite clusters resulting in a building fragment which has a cross-section of four-leafed clovers. The structure of $Th(WO_4)(TeO_3)$ exhibits a multilayer-sandwich framework composed by thorium tellurite layers with tungsten chains in between. In the case of the molybdate family, $ThMoTe_2O_9$ and $Th_2(MoO_4)(TeO_3)_3$, are built from puckered Th-Te sheets which are further interconnected by MoO_4 tetrahedral linkers. The DSC-TG technique was performed to gain insight into the thermal behavior of the synthesized compounds. Raman spectra of as-prepared phases were obtained and analyzed for signature peaks.

Due to the unstable thermal behavior of tellurium compounds, the corresponding crystals can be obtained by either reducing the growth temperature or performing the reaction under sealed conditions. [113–116] In fact, a large number of molybdate/tungstate tellurites have been successfully synthesized by the solid-state method using a MoO_3 or TeO_2 flux, which allows to grow the crystals at a relative low temperature (below 800 °C).[117,118] These significant achievements encouraged us to take such a method into first consideration. During experiment, it is found that a high TeO_2 ratio always led to high viscosity of the melted mixture promoting glass formation, while a low ratio could result in low yields or in phases not involving the Te element. The results of different synthesis experiments

---

[113] A. Guesdon and B. Raveau. *Chem. Mater.*, **12**: 2239–2243, 2000.

[115] Eun Ok Chi et al. *Chem. Mater.*, **18**: 2070–2074, 2006.

[117] Weiguo Zhang et al. *Cryst. Growth Des.*, **10**: 4091–4095, 2010.

demonstrate that these mixed oxo-anion crystals are preferable to be grown with Mo(W): Te ratios from 1:1 to 2:1.

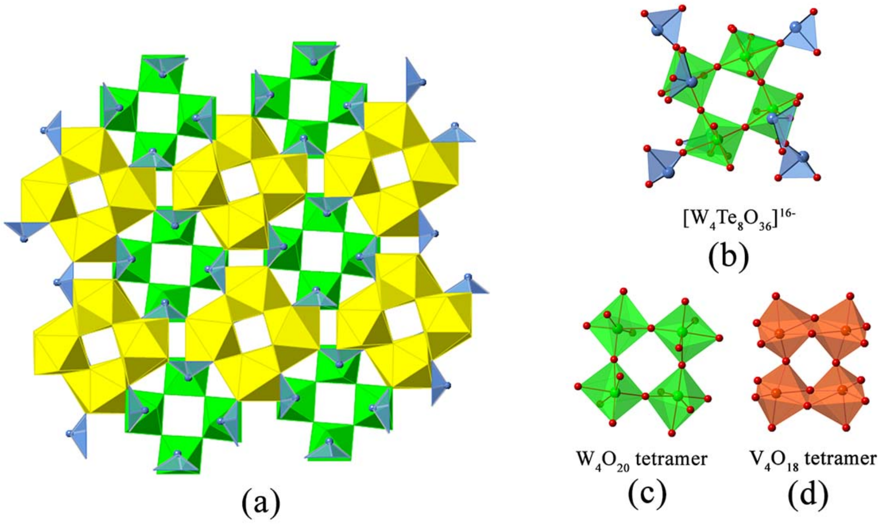

(a)

$[W_4Te_8O_{36}]^{16-}$
(b)

W_4O_{20} tetramer
(c)

V_4O_{18} tetramer
(d)

Figure 7.1: Polyhedral presentation of the structure of $ThWTe_2O_9$.

It is noteworthy that the formation of these four compounds is stoichiometrically sensitive, which implies that different structural building blocks can be formed by changing the molar ratio of raw materials. We found that $Th(WO_4)(TeO_3)$ and $Th_2(MoO_4)(TeO_3)_3$, where all oxo-anions are separated from each other, were favored in the reactions which had a slightly lower Mo(W)/Te ratio. By comparison, the other two compounds $ThWTe_2O_9$ and $ThMoTe_2O_9$ which contain the Te-O-W or Te-O-Mo linkages can be isolated from the reactions of a higher Mo(W)/Te ratio.

7.1.1 Crystal structure analysis

$ThWTe_2O_9$

The $ThWTe_2O_9$ is built from a complex 3D framework composed of ThO_9, TeO_3 and WO_6 polyhedra with the space group $I4_1/a$ (**Figure 7.1 (a)**). It contains one symmetrically independent Th site, which is nine-coordinated by O atoms from two neighboring Th, six Te and two W cations, creating an environment around the center thorium atom that can be best described as a monocapped square antiprism. The Th-O bond distances fall in the range of 2.27(1)−2.64(1) Å. There are two Te sites and each is coordinated by three O atoms in a trigonal pyramidal geometry. For Te(1), the Te-O bond distances range from 1.83(1) Å to 1.94(1) Å, while the $Te(2)O_3$ shows slightly less perturbation with the variation in Te-O bonds in the range from 1.86(1) Å to 1.94(1) Å. These two TeO_3 groups exhibit quite similar coordination features, *i.e.* all of them are pentadentate and each TeO_3 polyhedron forms one bidentate chelation with one Th atom and also bridges with two other Th and one W atoms. Finally, the only octahedral WO_6 site is significantly distorted. The distortion is manifested as a movement toward the face of the octahedron along the local C_3 direction, producing three long (1.74(1)−1.80(1) Å) and three short W-O bonds (2.05(1)−2.12(1) Å). This out-of-center distortion is common for octahedrally coordinated W^{6+} cations attributable to the second-order Jahn-Teller (**SOJT**) distortions.[114,232,233] The O-W-O bond angles are also observed to deviate from the ideal octahedral geometry, *i.e.* being in the range of 77.7(4)° to 103.6(5)° for *cis* O-W-O bonds and from 161.4(4)° to 168.3(4)° for *trans* ones. As being noted in many molybdenum/tungsten selenite/tellurite compounds, the MO_6 (M = W, Mo) octahedra are distorted more from the O atoms bonded to the Te^{4+}, owing to the lone pair electrons.[234] The bond valence calculation based on the Th-O, Te-O and W-O bond distances were calculated to be 4.03, 3.61−3.80 and 6.31 v.u. respectively, and they are consistent with the ideal values asked for Th(IV), Te(IV) and W(VI).

The octahedral tetramer, as shown in **Figure 7.1 (c)**, formed by four WO_6 octahedra interlinking *via* equatorial corners, is remarkable as it has not been found in other actinide tungstate compounds. Similar four-membered rings with equal topological configuration can be observed in the structure of $V_2O_3(XO_3)_2$ (X = Se, S) (**Figure 7.1 (d)**).[235] However, in the latter structure, such tetramer is composed of two pairs of edge-shared octahedra by connecting octahedral corners. The W_4O_{20} tetramer is connected by four $Te(1)O_3$ and four $Te(2)O_3$ to result in a tungstotellurite cluster $[W_4Te_8O_{36}]^{16-}$ with complex topology (**Figure 7.1 (b)**). It is noteworthy to mention that the term "tungstotellurite" is typically used to name phases groups are directly linked with tellurite groups. In contrast, compounds consist of isolated tungstate and tellurite groups are denoted as "tungstate tellurite".[236,237] Due to containing clusters of $[W_4Te_8O_{36}]^{16-}$, here the $ThWTe_2O_9$ becomes the first tugnstotellurite compound among all actinide families.

The most extraordinary aspect of the structure of $ThWTe_2O_9$ lies at the helical Th chains constructed by edge-sharing of neighboring ThO_9 polyhedra along the **c**-axis (**Figure 7.2 (a, d)**). The Th-Th bond distance of 4.12(0) Å, is in good agreement with those observed in other reported thorium tungstate compounds.[143] To the best of knowledge, no solid-state compounds containing such a helical Th structural configuration have been reported. Each Th chain lies on a four-fold screw axis, as required by the space group $I4_1/a$, and is further linked with four tungstotellurite clusters in a spiral fashion to complete the $ThWTe_2O_9$ framework, as shown in **Figure 7.2 (b, e)**. Due to the four-fold screw axis, when viewed along the **c**-axis, the resulting structural fragment has a cross-section of four-leafed clovers (see **Figure 7.2 (c, f)**). In $ThWTe_2O_9$, each WO_6 octahedron in the W_4O_{20} tetramer shares one edge with a ThO_9 polyhedron within one thorium chain and a corner with another ThO_9 polyhedron in a neighboring thorium chain. As the case of TeO_3 groups, the $Te(2)O_3$ polydedra are bidentate and monodentate between every fourth ThO_9 polyhedron along the chain length, respectively, whereas

---

[232] Joanna Goodey et al. *J. Solid State Chem.*, **175**: 3–12, 2003.
[233] Sau Doan Nguyen and P. Shiv Halasyamani. *Inorg. Chem.*, **51**: 9529–9538, 2012.
[234] Su-Yun Zhang and Jiang-Gao Mao. *Inorg. Chem.*, **50**: 4934–4943, 2011.
[235] A. P. Tyutyunnik et al. *Russ. J. Inorg. Chem.*, **55**: 501–507, 2010.
[236] Rdiger Kniep, Holger Engelhardt, and Cornelia Hauf. *Chem. Mater.*, **10**: 2930–2934, 1998.
[237] Bastian Ewald, Ya-Xi Huang, and Rdiger Kniep. *Z. Anorg. Allg. Chem.*, **633**: 1517–1540, 2007.
[143] Geng Bang Jin and L. Soderholm. *J. Solid State Chem.*, **184**: 337–342, 2011.

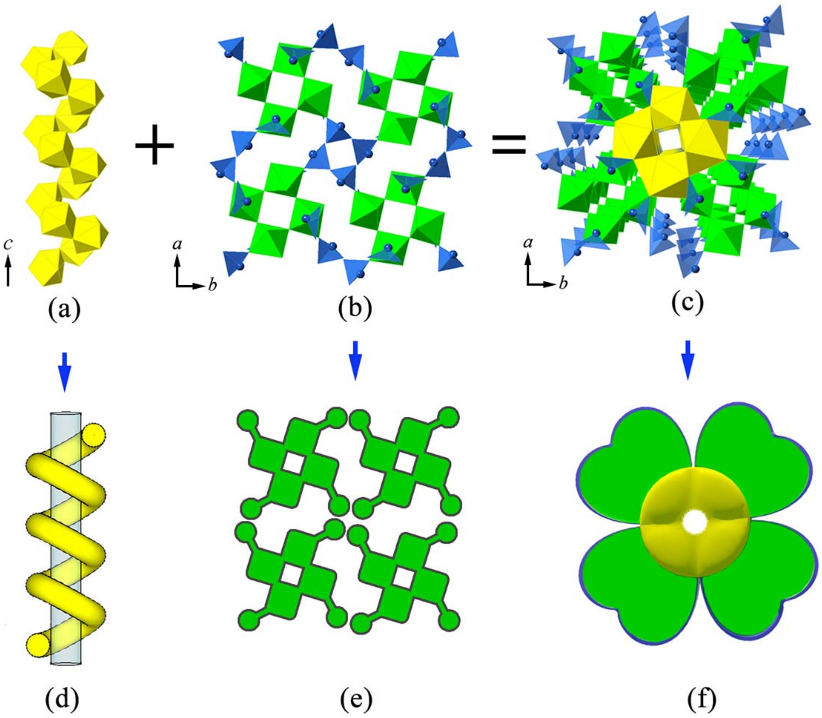

Figure 7.2: A representation of $ThWTe_2O_9$ composed by the helical thorium chains and tungstotellurite clusters. (a, d) The thorium chains in the structure of $ThWTe_2O_9$ constructed by edge-sharing of ThO_9 polyhedra along the c-axis. (b, e) Four tungstotellurite clusters in a spiral fashion. (c, f) Due to the four-fold screw axis, when viewing along the c-axis, the resulting structural fragment has a cross-section similar to four-leafed clovers.

the $Te(1)O_3$ polydedra which are not involved in the thorium chain play a role in fusing adjacent thorium chains. The lone pairs, for the Te(1) atoms, which are arranged in alternate order along the spiral direction, are oriented parallel to the (001) plane, whereas for the $Te(2)O_3$ trigonal pyramids, all the lone pairs point approximately into the [001] direction.

$Th(WO_4)(TeO_3)$

The structure of $Th(WO_4)(TeO_3)$ crystallizes in the space group $P2_1/c$. It is built upon ThO_9 monocapped square antiprisms, TeO_4 polyhedra and WO_6 octahedra. The ThO_9 monocapped square antiprisms are bound by common edges to create chains extending along the [010] direction. These Th chains are found to be most similar to those in $ThTe_2O_6$ where the Th chains are connected by TeO_3 and TeO_4 polyhedra. In $Th(WO_4)(TeO_3)$, however, the thorium chains are not interlinked by TeO_3 trigonal pyramids, but rather they are fused together along the [100] direction, creating 2D Th sheets which are inlaid with TeO_3 polyhedra (**Figure 7.3 (a, b)**). The Th-O bond distance, ranging from 2.36(1) to 2.73(1) Å with an average value of 2.48 Å, fits well with the typical nine-coordinated

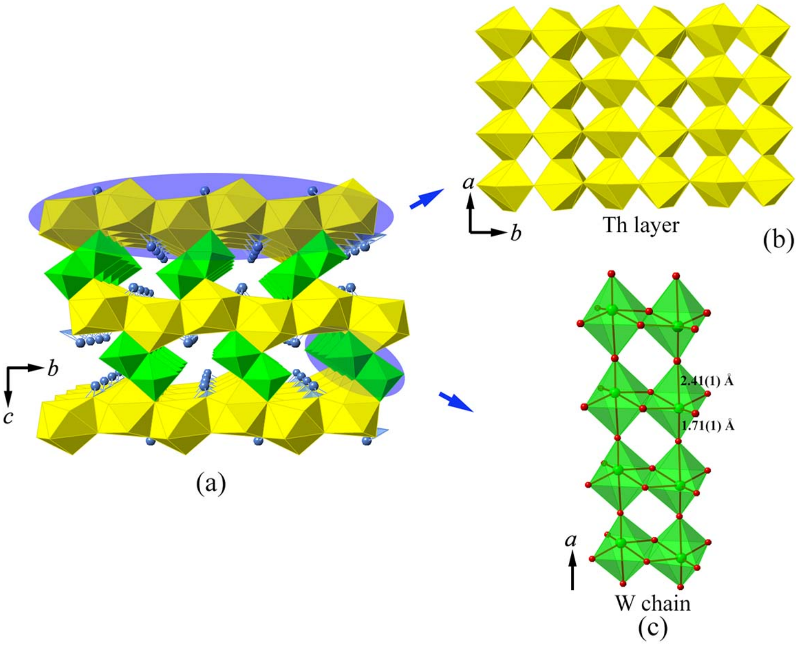

Figure 7.3: View of the structure of $Th(WO_4)(TeO_3)$.

thorium in other compounds.[141,217] The only Te site in TeO_4 polyhedral configuration, with BVS result of 4.04 v.u., is bidentatedly chelated by four Th atoms with the lone pairs located on the opposite sides of the sheets. The bond distances of Te-O range from 1.88(1) Å to 2.45(1) Å with an average value of 2.03 Å. In the case of W sites, two WO_6 octahedra are bound together by a common edge, forming a W_2O_{10} dimer. If viewing along [100] direction, one can observe such W_2O_{10} dimers are interconnected in a corner-sharing manner, shown in **Figure 7.3 (c)**. This results in an alternating short (1.71(1) Å) and long (2.41(1) Å) W-O bond distance for two apical O atoms in $trans$-configuration. The remaining W-O bond distances involved in the equatorial plane range from 1.78(1) to 2.08(1) Å. Similar tungsten chains have also been observed in a series of lanthanide compounds $Ln(WO_4)_2$ (A = K and Cs; Ln = La, Gd, Lu, and Y).[238,239] Finally, the above mentioned Th-Te sheets are connected together with these tungsten chains in between, resulting in a multilayer-sandwich framework of $Th(WO_4)(TeO_3)$. The joining of the Th-Te sheets with tungsten chains also leads to channels filled with lone pairs of electrons propagating in the [100] direction.

$ThMoTe_2O_9$

$ThMoTe_2O_9$, forming in the $C2/c$ space group, features a 3D framework structural type constructed by the linkages of ThO_9, MoO_4 and TeO_4 polyhedra (**Figure 7.4 (a)**). The only Th site in $ThMoTe_2O_9$ is again coordinated with nine O atoms,forming a distorted tricapped trigonal prismatic coordination geometry. The bond distances for Th-O are in the range of 2.295(3) Å to 2.876(4) Å with the average

---

[141] Bin Xiao et al. *Inorg. Chem.*, **53**: 3088–3098, 2014.
[217] Na Yu et al. *Inorg. Chem.*, **53**: 8194–8196, 2014.
[238] C. C. Torardi et al. *J. Solid State Chem.*, **69**: 171–178, 1987.
[239] E. Gallucci et al. *J. Alloys Compd.*, **306**: 227–234, 2000.

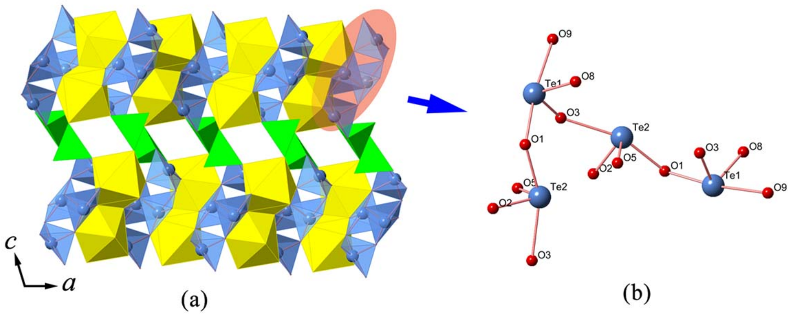

(a) (b)

Figure 7.4: Projection of the structure of $ThMoTe_2O_9$ along the b-axis.

value of around 2.497 Å, and are comparable with other reported thorium compounds.[240,241]. Two ThO_9 polyhedra are interconnected to a Th_2O_{16} dimer by sharing a common edge. In $ThMoTe_2O_9$ two TeO_4 polyhedra, Te(1)O_4 and Te(2)O_4, are interlinked *via* O(3) and O(1) atoms with their lone pairs orientated roughly in opposite directions, producing $[Te_2O_5]^{2-}$ infinite chains along the **c**-axis, presented in **Figure 7.4 (b)**. The Te-O bond distances, between 1.842(3) Å and 2.395 (3) Å, fall in the typical range required for TeO_4 geometry.[242] It is noted that such tellurium chains have not been observed in telluride compounds containing actinide elements. The Te-Te distance within the chain, 3.645(3) Å, is comparable with that in other telluride compounds.[129] The Th_2O_{16} dimers are incorporated into the above tellurium chains to generate $[Th(Te_2O_5)]^{2+}$ thorium tellurite sheets extending parallel to the (001) plane. Due to the lone pairs, the thorium tellurite sheets themselves are puckered and they are further interconnected by MoO_4 tetrahedra, resulting in the formation of a 3D framework. The Mo-O bond distance for Mo-O-Te, is relatively short, 1.738(3) Å, compared to those involved in the ThO_9 connection (between 1.759(3) Å and 1.813 (4) Å).

$Th_2(MoO_4)(TeO_3)_3$

$Th_2(MoO_4)(TeO_3)_3$ crystallizes in the $P2_1/c$ space group with two crystallographically different Th sites, three different Te sites and one Mo site. It is a 3D framework where the Th polyhedra are interconnected by TeO_3, TeO_4 and MoO_4 polyhedra. The Th(1) cations are nine-coordinated with O atoms, featuring a monocapped square antiprismatic coordination geometry, whereas Th(2) cations form distorted square antiprisms by linking with eight O atoms. It is to be noted, that up to now, among all the inorganic thorium molybdates available in literature, only two compounds, orthorhombic-$Th(MoO_4)_2$[243] and $Cs_2Th_3(MoO_4)_7$[141], are found to contain more than one kind of thorium-oxygen polyhedral. The Th-O bond distances vary from 2.357(5) Å to 2.842(6) Å with the average value of 2.46 Å, which is comparable with that found in $ThMoTe_2O_9$. The coordination geometry around Te(1) is disphenoid (TeO_4), while Te(2) and Te(3) can be demonstrated as trigonal pyramids (TeO_3) with

---

[240] M. Huyghe et al. *Acta Crystallogr., Sect. C: Cryst. Struct. Commun.*, **47**: 244–246, 1991.

[241] Amanda J. Albrecht et al. *J. Solid State Chem.*, **184**: 1591–1597, 2011.

[242] Matthias Weil. *Z. Anorg. Allg. Chem.*, **640**: 128–135, 2014.

[129] Jian Lin et al. *Inorg. Chem.*, **51**: 10083–10085, 2012.

[243] T. L. Cremers, P. G. Eller, and R. A. Penneman. *Acta Crystallogr., Sect. C: Cryst. Struct. Commun.*, **39**: 1165–1167, 1983.

lone pairs occupying the pyramidal sites. The bond valence calculations for Te(1) and Te(2) are 3.95 v.u. and 3.82 v.u. respectively, confirming that all the Te atoms are in the oxidation state of +4. The Te-O bond distances are in the range of 1.864(5) Å to 2.275(5) Å. As in most thorium molybdate compounds, the Mo atoms are in a slightly distorted tetrahedral geometry with O-Mo(1)-O angles ranging from 102.6(3)° to 113.0(3)°. More specifically, the shortest Mo(1)-O(13) bond, 1.733(6) Å, is terminal while the three long Mo(1)-O bonds from 1.770(6) Å to 1.796(6) Å are further linked to Th(1) cations. As shown in **Figure 7.5 (a)**, the adjacent Th(2)O_8 square antiprisms in $Th_2(MoO_4)(TeO_3)_3$ share two common edges to result in chains which are one polyhedron wide and run along the [010] direction. These chains are interconnected into a zigzag thorium sheet by sharing edges with Th(1)O_9 monocapped square antiprisms which are located by the sequence of "up and down" between the neighboring Th(2)O_8 chains (**Figure 7.5 (b)**). The resulting thorium sheet displays a rather loose configuration, and the space of which is filled with TeO_3 and TeO_4 polyhedra, leading to a thorium tellurite sheet $[Th_2(TeO_3)_3]^{2+}$ parallel to the (100) plane (**Figure 7.5 (c)**). Unlike the compound of $ThMoTe_2O_9$ where the Te atoms are constructed into infinite chains, in $Th_2(MoO_4)(TeO_3)_3$ they are isolated or constructed into dimers. As can be seen from **Figure 7.5**, among the thorium tellurite sheet, the Te(3)O_3 and Te(1)O_4 polyhedra share one common O atom to form a $[Te_2O_6]^{4-}$ dimer. The resulting $[Te_2O_6]^{4-}$ dimer chelates bidentately with one Th(2) atom and also bridges with one Th(1) and another two Th(2). The Te(2)O_3 polyhedra are found to bidentately chelate with one Th(1) atom and bridge with two Th(2) and another Th(1) atom. The $[Th_2(TeO_3)_3]^{2+}$ sheets are further linked into a 3D framework with the help of MoO_4 tetrahedra which serve as a role of inter-layer linkers. Each MoO_4 linker shares three of its corner O atoms with surrounding Th(1)O_8 polyhedra. Note that the adjacent MoO_4 tetrahedra are orientated in an opposite direction from each other by the sequence of the non-shared O corners. The unshared O atoms of these MoO_4 tetrahedra, with alternative [001] and [00$\bar{1}$] orientations, are located parallel to the direction of thorium tellurite sheets. The 3D framework, from **Figure 7.5 (d)**, possesses small voids observed in the [010] direction which are filled with the lone pairs of the Te(3)O_3 polyhedra.

The connection manner for MoO_4 tetrahedra in $ThMoTe_2O_9$ is different from that of $Th_2(MoO_4)(TeO_3)_3$. In the latter, each MoO_4 tetrahedron shares only 3 O atoms hooking on adjacent thorium tellurite sheets, while there is no terminal O atom for MoO_4 tetrahedra in the former structure. Each MoO_4 tetrahedron in $ThMoTe_2O_9$ shares two of its corners with two ThO_9 tricapped trigonal prisms from one $[Th(Te_2O_5)]^{2+}$ sheet, one corner with one ThO_9 polyhedron from the opposite thorium tellurite sheet and another corner with a Te(2)O_4 tetrahedron. Another difference is the connection manner of the hexavalent oxo-anions. In $Th_2(MoO_4)(TeO_3)_3$ all MoO_4 tetrahedra are completely separated from tellurium units, whereas the MoO_4 octahedra are linked directly with TeO_4 units to give rise to a Mo-O-Te linkage. As a result, $ThMoTe_2O_9$ can be named as "molybdotellurite" while $Th_2(MoO_4)(TeO_3)_3$ should be called "molybdate tellurite".[236,237] It can clearly be seen that the tungstotellurite $ThWTe_2O_9$ and molybdotellurite $ThMoTe_2O_9$ are based on the same chemical stoichiometric ratio (Th:W/Mo:Te = 1:1:2). However, there is a remarkable contrast between their structures. In this case, one can note how critical the oxo-ainons affect the formation of crystal structures. In $ThWTe_2O_9$, tungstotellurites fragments are constructed from corner-sharing WO_6 octahedra and TeO_3 units which are further

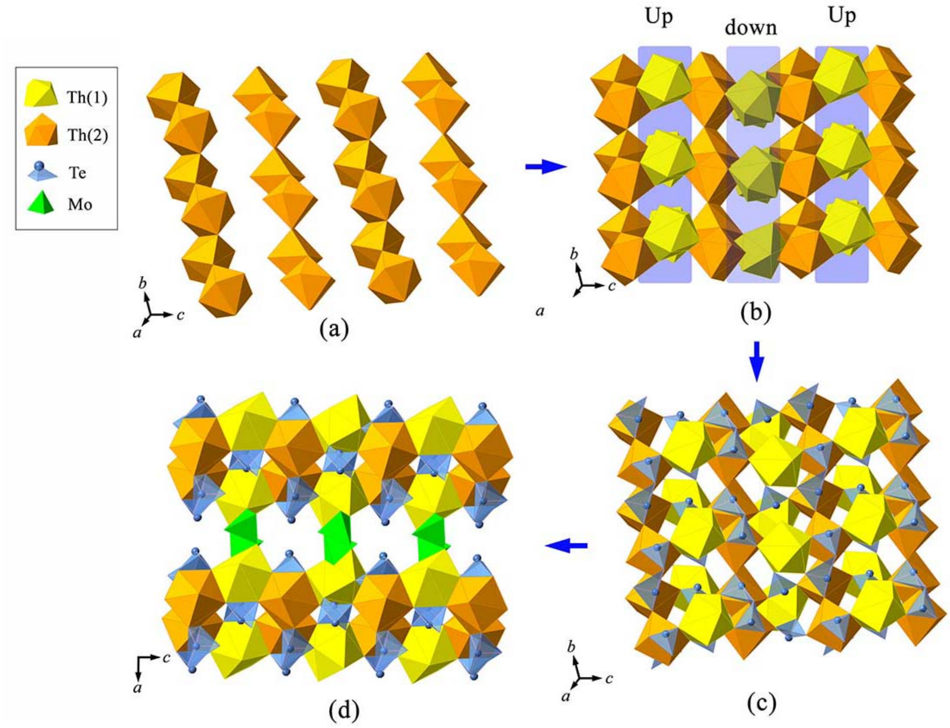

Figure 7.5: The proposed construction procedure of the structure of $Th_2(MoO_4)(TeO_3)_3$.

connected by a spiral Th chain to from complex four-leafed clover fragments. Whereas, $ThMoTe_2O_9$ is built from $Th(Te_2O_5)^{2+}$ thorium tellurite sheets which are further interconnected by MoO_4 tetrahedra.

7.1.2 Thermal behavior

DSC and TG measurements were performed simultaneously for as-synthesized pure polycrystalline samples from room temperature to 1200 °C. The DSC curves for $ThWTe_2O_9$ and $ThMoTe_2O_9$ are quite similar. Both samples have two sharp endothermic peaks. In the case of $ThWTe_2O_9$ (**Figure 7.6 (a)**), the first peak with onset at around 835 °C exhibits a characteristic of large mass loss, which indicates the sample is melting and decomposing. The major phase that is indicated by powder XRD for the decomposing products is ThW_2O_8. A considerable amount of the material decomposes continuously when further heated to nearly 1000 °C, which is accompanied by the second endothermic DSC effect starting at 975(7) °C. Two endothermic peaks were observed during the heating of $ThMoTe_2O_9$, with onset at 745(7) °C and 965(7) °C, respectively, shown in **Figure 7.6 (c)**. The higher temperature peak, without a doubt, associated with a solid-liquid transformation behavior. Of special interest is the first peak ranging from 745(7) °C to 805(7) °C for $ThMoTe_2O_9$. Since there is no appreciable variation of weight observed in this region, it is possible to make a hypothesis of solid-solid phase transition. However, considering the thermal instability of most molybdate tellurite compounds at high

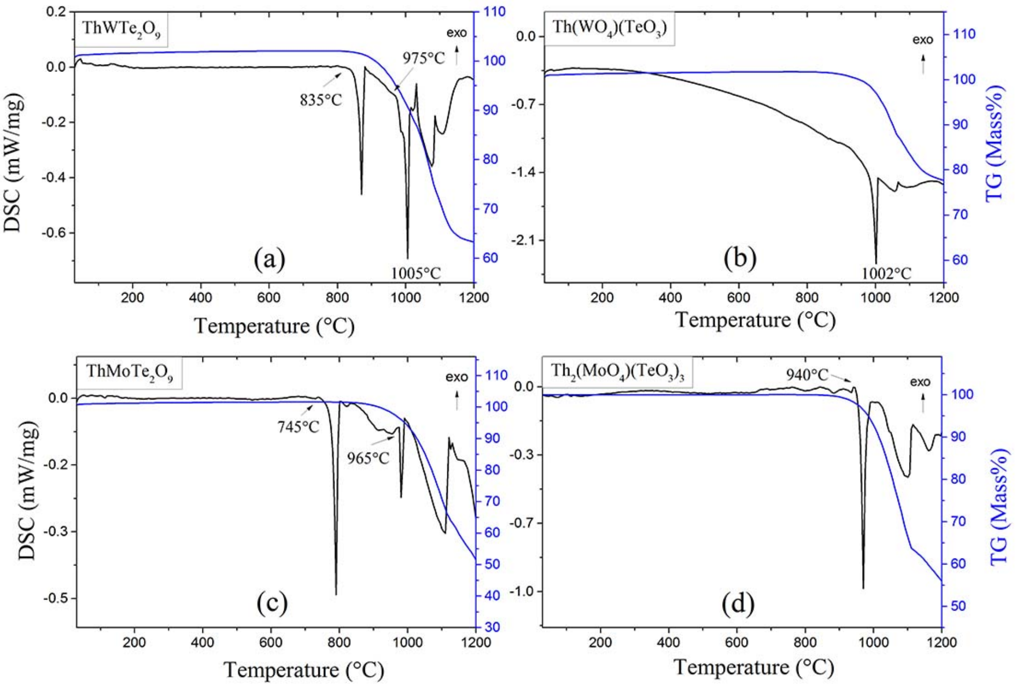

Figure 7.6: DSC and TG diagram of (a) $ThWTe_2O_9$, (b) $Th(WO_4)(TeO_3)$, (c) $ThMoTe_2O_9$ and (d) $Th_2(MoO_4)(TeO_3)_3$, respectively.

temperature (≈ 800 °C)[244,245], this assumption is speculative. From the powder XRD measurements, which were collected after heating the polycrystalline samples of $ThMoTe_2O_9$ slightly above the first peak for 5 h, one was able to identify the orthorhombic-$ThMo_2O_8$ and $MoTe_2O_7$ as the dominant phases. This means, that the corresponding peak should be assigned to the sample decomposition. Only one endothermic peak appears during the heating of $Th(WO_4)(TeO_3)$, with maxima at 1002(3) °C (**Figure 7.6 (b)**), which is related to the melting point, as evidenced by powder XRD technique after heating the corresponding sample slightly across this temperature peak. The thermal behavior for $Th_2(MoO_4)(TeO_3)_3$ presents a similar pattern, with only one melting peak starting at around 940 °C (**Figure 7.6 (d)**).

7.1.3 Raman spectroscopic analysis

The Raman spectra of all the above described thorium compounds are presented in **Figure 7.7**. Nevertheless, very few vibrational spectra of thorium contained molybdates/tungstates or tellurites have been published. The ideal $MoO_4{}^{2-}$ has the T_d symmetry with the 4 normal motions being assigned as $A_1(\nu_1)$; $E(\nu_2)$; $F_1(rot)$, $F_2(trans, \nu_3, \nu_4)$ where A_1, E and F_2 are Raman permitted while F_2 is

---

[244] J. C. J. Bart, G. Petrini, and N. Giordano. *Z. Anorg. Allg. Chem.*, **412**: 258–270, 1975.

[245] G. Petrini and J. C. J. Bart. *Z. Anorg. Allg. Chem.*, **474**: 229–232, 1981.

IR active. The ν_1, ν_2, ν_3 and ν_4 modes are denoted as non-degenerated symmetric stretching, doubly degenerated symmetric bending, triply degenerated asymmetric stretching and asymmetric bending vibrations, respectively. The stretching vibrations of ν_1 and ν_3 in free MoO_4^{2-} are placed in the region of 700 $cm^{-1}$$-$100 cm^{-1}, while the bending vibrations (ν_2 and ν_4) are situated in the scope of 300 $cm^{-1}$$-$500 cm^{-1}. For WO_6 octahedra, the ν_1 mode is always observed as the strongest Raman line around 800 $cm^{-1}$$-$950 cm^{-1}. In comparison, the ν_2 mode of WO_6 is less clear in the spectra and often gives rise to very weak signals in broad wavenumber range from 500 $cm^{-1}$$-$770 cm^{-1}. The ideal TeO_3^{2-} trigonal pyramid has a C_{3v} symmetry consisting of four vibrational frequencies: two non-degenerate ν_1 and ν_2 modes and the other two doubly degenerate ν_3 and ν_4 modes.[152,153]

Because of the complexity of reported compounds, here one can assign only selected frequencies based on a comparison of literature. For all the Raman spectra, the high frequency bands ranging from 600 to 950 cm^{-1} are characterized by the presence of individual bands, among which are rather loose bands with high intensity. These bands can be attributed to the stretching vibrations of Te-O and Mo(W)-O, primarily associated with the motions of O atoms.[222,246] The lower range of the spectra, from 200 to 450 cm^{-1}, are characterized by broad overlapping bands with lower intensity, which may correspond to one or a conjunction of the vibrations of Te-O and Mo(W)-O, because this is an overlapping region for these vibrations.[247] The spectral range below 200 cm^{-1} is dominated by the presence of partially overlapping bands, mainly contributed from the motions of the “lattice skeleton”.[208,209] For $Th(WO_4)(TeO_3)$, the highest peak of 910(1) cm^{-1} can be unambiguously attributed to the symmetric stretching mode (ν_1) of W-O. However, this peak is shifted to 901(1) cm^{-1} and becomes the second highest peak for $ThWTe_2O_9$. A close resemblance between the Raman spectra of $ThMoTe_2O_9$ and $Th_2(MoO_4)(TeO_3)_3$ can be detected. Similarly, the highest peak around 903(1) and 906(1) cm^{-1} for $ThMoTe_2O_9$ and $Th_2(MoO_4)(TeO_3)_3$, respectively, can be attributed to the stretching mode (ν_1) of Mo-O.[209]

7.1.4 Conclusion

We demonstrate that tetravalent chalcogenes can be combined with oxo-anions of hexavalent transition elements within the actinide bearing compounds. Structural study of obtained materials reveals the influence of tetravalent tellurium cations on the crystal chemistry of thorium molybdates or tungstates. All the as-synthesized compounds are built from thorium polyhedra bridged through tetrahedral MoO_4 (or octahedral WO_6) and tellurium units (TeO_3 or TeO_4). One exception, the $Th_2(MoO_4)(TeO_3)_3$, contains both ThO_9 and ThO_8 polyhedra, all other phases are composed exclu-

---

[152] R. Ratheesh et al. *Spectrochim. Acta, Part A*, **51**: 1509–1515, 1995.

[153] Laurie L. Dussack, William T. A. Harrison, and Allan J. Jacobson. *Mater. Res. Bull.*, **31**: 249–255, 1996.

[222] K. V. Domoratskii et al. *Phys. Solid State*, **42**: 1443–1446, 2000.

[246] A. P. Mirgorodsky et al. *J. Phys. Chem. Solids*, **63**: 545–554, 2002.

[247] Vidyavathy and K. Vidyasagar. *Inorg. Chem.*, **37**: 4764–4774, 1998.

[208] J. Hanuza, M. Maczka, and J. H. van der Maas. *J. Mol. Struct.*, **348**: 349–352, 1995.

[209] K. Hermanowicz et al. *J. Lumin.*, **92**: 151–159, 2000.

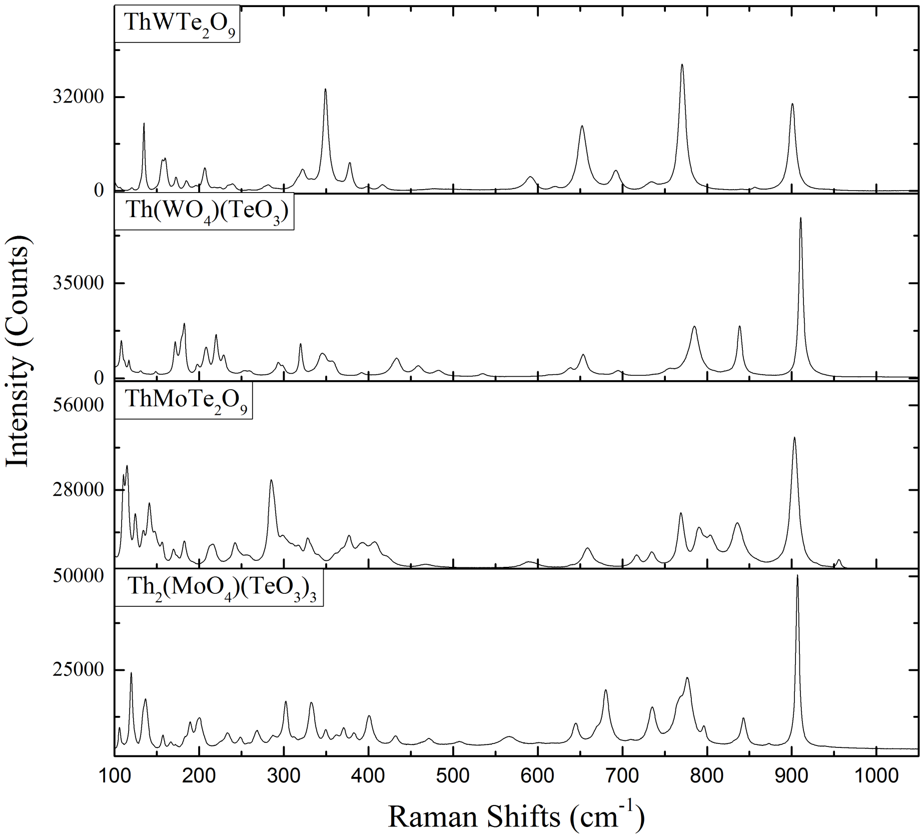

Figure 7.7: Raman spectra of (a) $ThWTe_2O_9$, (b) $Th(WO_4)(TeO_3)$, (c) $ThMoTe_2O_9$ and (d) $Th_2(MoO_4)(TeO_3)_3$, respectively.

sively by ThO_9 polyhedra. The $ThWTe_2O_9$ and $ThMoTe_2O_9$ have the same stoichiometric composition, but crystallize in utterly different structures. The structure of $ThWTe_2O_9$ can be seen as based on complex four-leafed clover fragments constructed by a center spiral Th chain interlinked with four tungstotellurite clusters around its corners. $ThMoTe_2O_9$, however, is built from $Th(Te_2O_5)^{2+}$ thorium tellurite sheets which are further interconnected by MoO_4 tetrahedra.

The structures of titled thorium compounds containing tetravalent molybdate/tungstate oxo-anions are fundamentally different from those observed in ThM_2O_8; M = Mo or W. The presence of tetravalent Te in these four compounds substantially complicates the original Th-O-Mo(W) uniformity, making the corresponding structural linkages rather complex. Moreover, in order to sustain charge neutrality, the replacement of $Mo(VI)O_4$/$W(VI)O_6$ polyhedra by $Te(IV)O_x$ (x = 3, 4, 5) oxo-anions results in a low amount of hexavalent cations (Mo/W), which considerably increases the Th/Mo(W) ratio and further makes the structures of thorium molybdates/tungstates more complex. In conclusion, the basic thorium molybdate/tungstate tellurites shown in this report may help guide future research on the actinide chemistry, as it is expected that more and more compounds with new topological structures and interesting properties will be further prepared by introducing the alkali or alkaline earth metals into this family.

Chapter 8

New Synthetic Methods for Preparation of U and Th Compounds

Actinides show a great diversity in their chemistry due to the complex structure of $5f$ electron shells.[248–250] One of the most remarkable properties of actinides is a multivalence which has a very strong influence on their chemical and physical properties. Uranium is an important element from the actinides series and it is widely used for energy production. It owns valences from II to VI in the solid state where IV and VI are the most usual and stable.[251,252] The pentavalent U(V), containing only single $5f$ electron, has the simplest electron configuration, and therefore provides a practical model for not only simplifying theoretical calculations but also fundamental understanding of f electronic behavior of actinides.[253,254] In spite of the environmental importance and fundamental interest, the report of pentavalent uranium remains rare. Only until past few years have some pentavalent uranium systems been synthesized and characterized.[254–256] The rational synthetic methods of pentavalent uranium materials are still a great challenge.

---

[248] Fabien Burdet, Jacques Pcaut, and Marinella Mazzanti. *J. Am. Chem. Soc.*, **128**: 16512–16513, 2006.

[249] Bin Xiao et al. *Chem. Eur. J.*, **21**: 7629–7629, 2015.

[250] Bin Xiao et al. *Inorg. Chem.*, **54**: 5981–5990, 2015.

[251] Tyler A. Sullens et al. *J. Am. Chem. Soc.*, **126**: 2676–2677, 2004.

[252] Matthew R. MacDonald et al. *J. Am. Chem. Soc.*, **135**: 13310–13313, 2013.

[253] C. S. Chen, S. F. Lee, and K. H. Lii. *J. Am. Chem. Soc.*, **127**: 12208–12209, 2005.

[254] Christopher R. Graves and Jaqueline L. Kiplinger. *Chem. Commun.*, 3831–3853, 2009.

[255] Louise Natrajan et al. *J. Am. Chem. Soc.*, **128**: 7152–7153, 2006.

[256] Lucile Chatelain et al. *Chem. Sci.*, **3**: 1075–1079, 2012.

8.1 New route for synthesizing uranyl compound involved in cation-cation interaction

Recent studies among the explosive growth of uranium compounds provide some unprecedented results that are competing and expanding the understanding of such typical uranium (VI) geometry.[257–259] In particular, the cation-cation interactions (referred to herein as CCIs), a term used to describe direct binding of one actinyl dioxo ion ($AO_2{}^{n+}$) with another actinide group, have always gained prominence.[193,251,260] CCIs provide a means of U polyhedral linkage with anomalous connectivity and enabled the development of novel structural features. Firstly found in aqueous solution studies, CCIs became the key feature of solid-state and molecular actinide chemistry and are particularly well-characterized in Np(V) and U(V) compounds.[134,261] CCIs, however, are quite uncommon and account only for about 2 % of all uranyl crystal structures.[134,262–265] The most prevailing formation of CCIs occurs in two-centers where an axial O atom of one actinyl group behaves as an equatorial ligand in order to coordinate with only one other actinide unit.[193] The number of known compounds with multi-centered CCIs has increased steadily in response to the active research in actinide chemistry during the past decade. Up to now, 15 different types of CCIs among uranyl ions are recognized.[260] CCIs can serve as effective routes to diversify the linkages of uranyl groups and increase the dimensional complexity of uranium compounds. Compared to the overwhelming majority of 2D sheet structures of uranyl moieties, the uranyl compounds containing CCIs prefer to adopt 3D frameworks. While the influence of CCIs on the increase of the uranyl moiety dimensionality has attracted extensive attention, considerably few 3D frameworks have been found to be directly constructed by low dimensional uranyl compounds through CCIs. $A_5(UO_2)_{20}(UO_6)_2O_{16}(OH)_6(H_2O)_6$[266] and its NH_4 analogue[267], have been reported as rare examples of 3D frameworks constructed *via* pseudo-sheets, which are topologically similar to the well-established 2D β-U_3O_8 structure, formed by CCIs of $UO_2{}^{2+}$ cations. This section will discuss the structural and spectroscopic properties of a novel 3D framework, $Cs_4[(UO_2)_7(WO_5)_3O_3]$ (**CsUW-2**). It consists of a new type of CCIs and can be formed directly by 2D sheets of the uranyl compound $Cs_4[(UO_2)_4(WO_5)(W_2O_8)O_2]$ (**CsUW-1**) *via* cation-cation interaction of uranyl polyhedra. We will demonstrate a facile synthetic route for new 3D uranium compounds with CCIs and its significant influence on the structural architecture of uranium chemistry.

---

[257] William J Evans, Stosh A Kozimor, and Joseph W Ziller. *Science*, **309**: 1835–1838, 2005.
[258] Polly L Arnold et al. *Nature*, **451**: 315–317, 2008.
[259] Cheng-Shiuan Lee et al. *Angew. Chem. Int. Ed.*, **49**: 4254–4256, 2010.
[193] Evgeny V. Alekseev et al. *Inorg. Chem.*, **46**: 8442–8444, 2007.
[260] V. N. Serezhkin et al. *Radiochemistry*, **56**: 115–133, 2014.
[134] Shuao Wang et al. *Inorg. Chem.*, **50**: 4692–4694, 2011.
[261] Victor Mougel et al. *Nature Chemistry*, **4**: 1011–1017, 2012.
[262] Chia-Hui Lin et al. *Inorg. Chem.*, **47**: 4445–4447, 2008.
[263] Victor Mougel et al. *Chem. Eur. J.*, **16**: 14365–14377, 2010.
[264] Shuao Wang et al. *Chem. Mater.*, **22**: 5983–5991, 2010.
[265] Shuao Wang et al. *Inorg. Chem.*, **51**: 7016–7018, 2012.
[266] Karrie-Ann Kubatko and Peter C. Burns. *Inorg. Chem.*, **45**: 10277–10281, 2006.
[267] Yaping Li, Christopher L Cahill, and Peter C Burns. *Chem. Mater.*, **13**: 4026–4031, 2001.

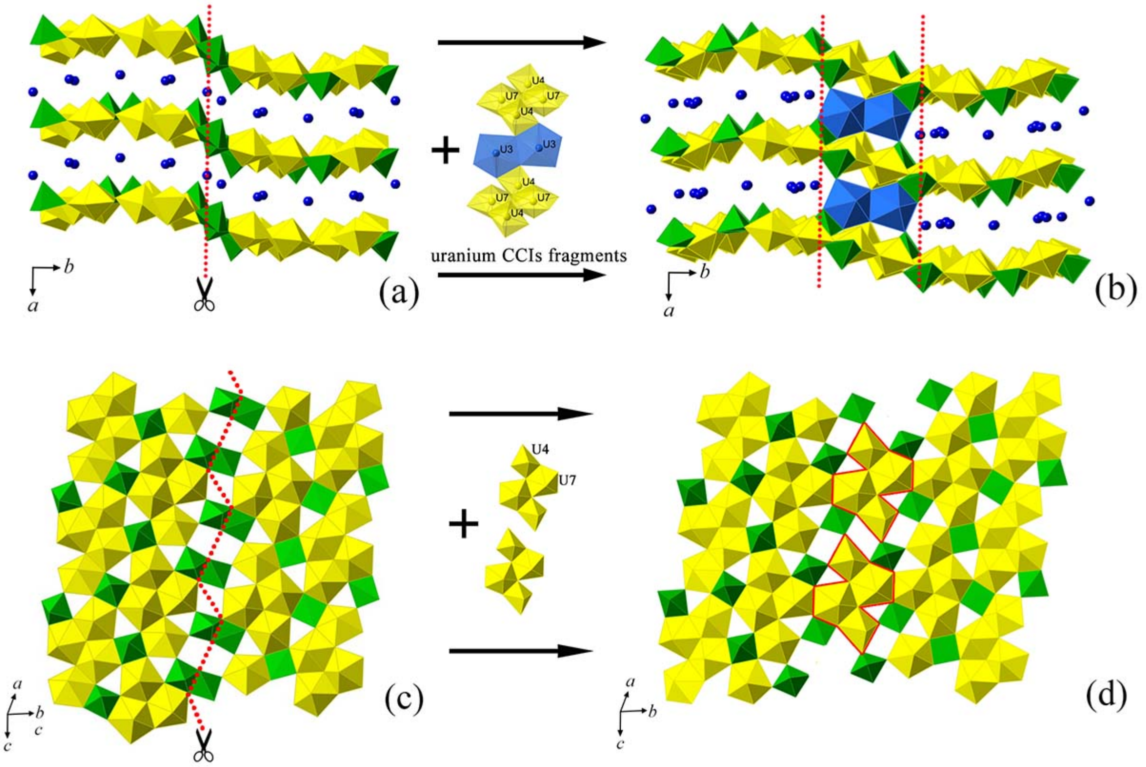

Figure 8.1: View of the crystal structures of CsUW-1 and CsUW-2.

Two uranyl tungstates, $Cs_4[(UO_2)_4(WO_5)(W_2O_8)O_2]$ (**CsUW-1**) and $Cs_4[(UO_2)_7(WO_5)_3O_3]$ (**CsUW-2**), were obtained *via* the high-temperature solid-state synthesis method by reacting uranyl nitrate with WO_3 in the presence of cesium nitrate. **CsUW-1** crystallizes in space group $P2_1/n$, adopting a two-dimensional (2D) sheet structure. **CsUW-2** forms a three-dimensional (3D) framework constructed by complex 2D sheets linked by cation-cation interactions of $UO_2{}^{2+}$ groups. The cation-cation interactions fragment presented in **CsUW-2** involves the 2D $\rightarrow$ 3D transformation of the uranyl tungstate network and acts as an intermediate part by bridging the structures of **CsUW-1** and **CsUW-2**. We demonstrate that the chemical and structural transformation from **CsUW-1** to **CsUW-2** is possible *via* adding a suitable amount of UO_3 oxide. Besides, the DSC-TG technique was carried out to gain insight into the thermal behavior of the synthesized compounds. Raman spectra of titled compounds were obtained and analyzed for signature peaks.

Crystal structure of $Cs_4[(UO_2)_4(WO_5)(W_2O_8)O_2]$ (CsUW-1)

CsUW-1 crystallizes in the monoclinic system with space group $P2_1/c$. The crystal structure is based upon 2D sheets constructed from four symmetrically independent linear $UO_2{}^{2+}$ molecules and three W^{6+} sites. All $UO_2{}^{2+}$ ions, with U=O bond distances in the range of 1.80(1)-1.82(1) Å, are coordinated by five O atoms in each equatorial plane with U-O bond lengths between 2.20(1) and 2.55(1) Å, respectively, resulting in the formation of slightly distorted UO_7 pentagonal bipyramids. Four of such UO_7 pentagonal bipyramids connect together *via* sharing equatorial edges to form a tetramer $[U_4O_{21}]$

that has a width of two polyhedra, as shown in **Figure 8.1 (c)**. Adjacent tetramers are bridged by sharing common O corners from both sides, generating infinite chains that are oriented perpendicular to the ***b***-axis. The resulting uranium chains are connected to $[(UO_2)_4(WO_5)(W_2O_8)O_2]^{4-}$ corrugated sheets parallel to the ***b***-axis, by edge-shared W_2O_8 dimers on the one side and by WO_5 square pyramids on the other side (**Figure 8.1 (c)**). The alkali metal cations, Cs^+, are disorderedly located in the interlayers to balance the charge, creating overall 2D layered structures. The bond lengths for all three W-O, from 1.71(1) to 2.12(0) Å, are in good agreement with previous results concerning well-refined uranyl tungstates,[194,195,268,269] with a clear difference displayed between bridging W-O (around 1.86 Å on average) and terminal W-O bond lengths (around 1.72 Å on average).

Crystal structure of $Cs_4[(UO_2)_7(WO_5)_3O_3]$ (CsUW-2)

CsUW-2 was also refined in space group $P2_1/c$, containing seven crystallographically different U sites, six of which are seven-fold coordinated, forming UO_7 pentagonal bipyramids, and the remaining one is six-fold coordinated, forming UO_6 tetragonal bipyramids. The variation of U=O distances is appreciable, from 1.76(3) to 1.99(2) Å and the U-O bonds occur from 2.09(2) to 2.53(2) Å. The five-fold coordinated environment of the W sites observed in **CsUW-2** is quite similar to that of **CsUW-1** with the W-O bond distances differing from 1.73(3) to 2.05(2) Å, and the average being 1.84 Å. **CsUW-2** is based on a 3D framework and is structurally directly related to **CsUW-1**. The former is constructed by 2D corrugated uranium-tungstate layers, which are further interlinked by additional uranium polyhedra as CCIs, shown in **Figure 8.1 (b, d)**. Similar to **CsUW-1**, the Cs^+ counteractions playing the role of maintaining charge neutrality are also found resided between the adjacent layers of **CsUW-2**. The interlayer behaviors are different between these two compounds. The additional uranium polyhedra between adjacent sheets in **CsUW-2** result in larger interlayer distances (roughly 8.6 Å) in comparison to that of **CsUW-1** (roughly 8.2 Å)

8.1.1 Structural aspects of cesium uranyl tungstate compounds

The crystal structures of **CsUW-1** and **CsUW-2** differ only in one important respect, the containment of complex U(VI) CCIs fragments. The uranium CCIs fragments among neighboring sheets consist of six UO_7 pentagonal bipyramids and two UO_6 tetragonal bipyramids. **Figure 8.1** highlights such uranium CCIs fragments and the associated structural transition from 2D **CsUW-1** to 3D **CsUW-2**. In **CsUW-2**, two $U(7)O_7$ pentagonal bipyramids share a common edge to form a pentagonal dimeric unit that is further surrounded by two $U(4)O_6$ tetragonal bipyramids in an edge-sharing manner, leading to a uranium tetramer $[U_4O_{21}]$ with the direction corresponding to the sheet plane. Two such tetramers sit on the upper and lower sheets, respectively, each sharing one edge with a central uranium dimer $[U(3)_2O_{12}]$ in order to create such CCIs fragments. The most significant

---

[194] Sergey V. Krivovichev and Peter C. Burns. *Solid State Sci.*, **5**: 373–381, 2003.

[195] S. Obbade et al. *J. Solid State Chem.*, **172**: 305–318, 2003.

[268] Evgeny V. Alekseev et al. *Angew. Chem. Int. Ed.*, **45**: 7233–7235, 2006.

[269] Evgeny V. Alekseev et al. *Z. Kristallogr.*, **222**: 391–395, 2007.

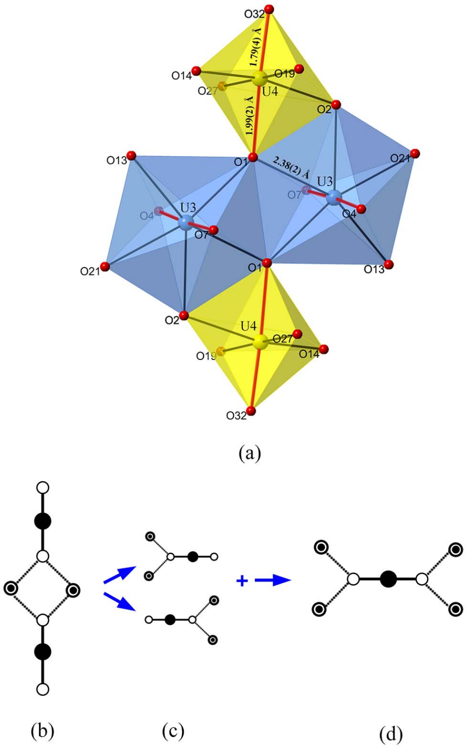

Figure 8.2: (a) Local coordination geometry of the cation-cation interaction distances in the structure of CsUW-2. The uranyl bonds are highlighted by red sticks. (b) Schematic view of uranyl groups in CsUW-2. (c, d) The process of topological reconstruction from CCI fragments observed in CsUW-2 to those of γ-UO_3. The U and O ions are depicted in black and white nodes, respectively.

part of this CCIs fragment, as illustrated in **Figure 8.2 (a)**, is a four-membered uranyl unit which connects the adjacent sheets. Having cation-cation bonds above and below the layered structure effectively forces $U(4)O_6$ and $U(3)O_7$ to be perpendicular to each other, forming two mutual vertical sheets and thereby resulting in a 3D architecture. Note that the uranyl O(1) of $U(4)O_6$ tetragonal bipyramid simultaneously belongs to the equatorial vertices of two $U(3)O_7$ pentagonal bipyramids, that is to say, each $U(4)O_6$ donors a cation-cation bond to two $U(3)O_7$ polyhedra, exhibiting a three-centered cation-cation bond feature. For this reason, the resulting linked configuration between these four-membered uranium polydedra can be considered as a conformation of doubled three-centered CCIs, which is revealed for the first time in uranyl chemistry (See **Figure 8.2 (b)**). Such remarkable configuration is satisfied by the essentially extended U(4)-O(1) bond distance of 1.99(2) Å. This distance is not common to the uranyl oxo-atoms without involving CCIs, but comparable to that in other three-centered donor O atoms, such as around 1.94 Å in $Li_4[(UO_2)_{10}O_{10}(Mo_2O_8)]$[193] and 1.967(9)Å in $Sr_5(UO_2)_{20}(UO_6)_2O_{16}(OH)_6(H_2O)_6$[266], respectively. The bond-valence sum calculations for U(3) and U(4) that participate in CCIs are 5.85 and 5.95 valence units, respectively, which are in good agreement with the expected value for U(VI).

As mentioned above, apart from the CCIs fragment, the remaining structural part of **CsUW-2** shows an equivalent coordination geometry compared to that in **CsUW-1**. For the purpose of understanding the linkage relationship of U and W polyhedra within these two structures, the approach of anion-topology is adopted to compare the sheet of **CsUW-1** with the single-layered sheet extracted from

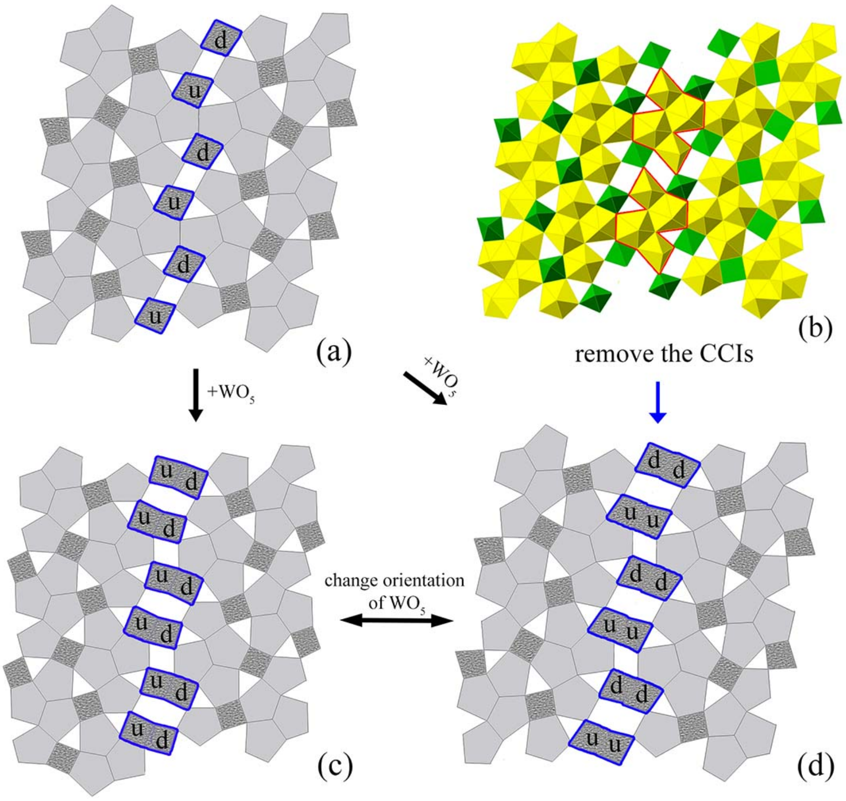

Figure 8.3: Anion topology describing structural transformation among three cesium uranium tungstates. (a) Anion topology of sheets in $Cs_2U_2WO_{10}$. (b) polyhedral view of pseudo-sheets inCsUW-2. (c) Anion topology of sheets in CsUW-1. (d) Anion topology of sheets in CsUW-2 without the CCIs fragment. Note that figures (c) and (d), having exactly the same topology, only differ by the orientation of the labelled WO_5 tetragonal pyramids.

CsUW-2 (without regard to the CCIs fragment, hereafter called a reformed **CsUW-2** sheet). This method is especially convenient for the representation of complex 2D uranium architectures.[189] As shown in **Figure 8.3 (c,d)**, both sheets share the same topology, where the pentagons and squares are occupied by UO_7 and WO_5, respectively. Therefore, one can assume that the 2D → 3D transformation only involves “cut” and “glue” procedures, without any reconstruction of the polyhedral connectivity among the sheets. However, further analysis of the polydedral diagrams shown in **Figure 8.3 (c, d)** indicates that the orientations of WO_5 square pyramids along the joint line are fundamentally distinct. The reason for the deviation is the following: in both structures, each WO_5 square pyramid shares four corner O atoms in the equatorial plane with surrounding polyhedra, leaving one non-shared apical O atom that can be oriented either “up” and “down”, corresponding to the plane of the sheet without involving intra-sheet polymerization. In **CsUW-1**, two WO_5 square pyramids are oriented in opposite directions composing a W_2O_8 dimer, whereas the corresponding dimer in a reformed **CsUW-2** sheet

---

[189] P. C. Burns. *Rev. Mineral.*, **38**: 23–23, 1999.

is linked by two WO_5, pointing to the same direction. It is worth mentioning that such structural fragments are commonly observed in uranyl tungstates, such as $Rb_6[(UO_2)_7(WO_5)_2(W_3O_{13})O_2]$[270] and $Cs_2U_2WO_{10}$.[271] The structural motif of $Cs_2U_2WO_{10}$ only differs between **CsUW-1** and reformed **CsUW-2** sheets by the presence of W_2O_8 dimers. The anion topologies among these three sheets can be easily converted to each other by the simple topological transformation procedure shown in **Figure 8.3**.

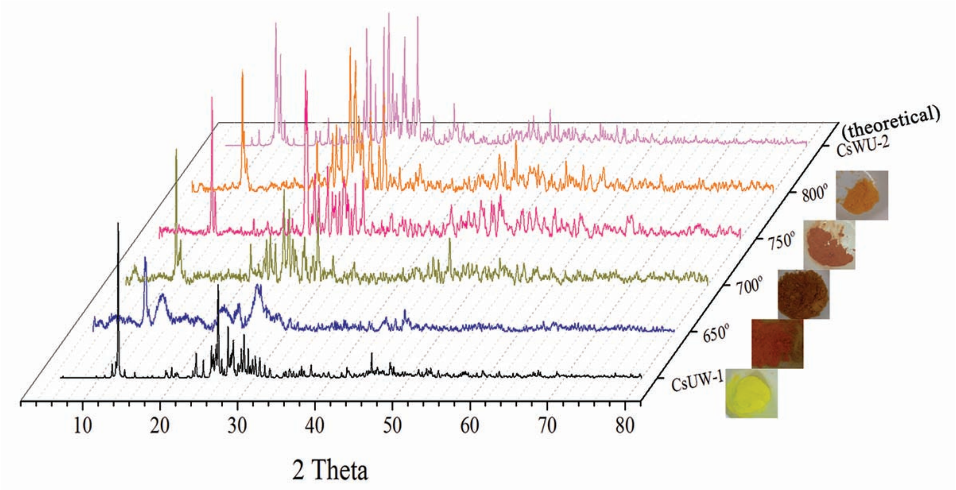

Figure 8.4: Experimental PXRD diagrams for the temperature evolution from CsUW-1 to CsUW-2.

Direct chemical transformation from **CsUW-1** into **CsUW-2** *via* UO_3 intercalation Based on the above analysis, it is reasonable to expect that **CsUW-2** can be synthesized directly through **CsUW-1** by adding the required amount of γ-UO_3, since these two compounds only differ by CCIs units of uranium polydedra. Therefore, a series of synthesis experiment was carried out for **CsUW-2** in order to get a deeper insight into the phase evolution from **CsUW-1** to **CsUW-2** associated with the CCIs. The detailed procedure is described in the Experimental Section. As a first step, pure **CsUW-1** was synthesized and was subsequently used as a starting material for the formation of **CsUW-2** *via* high-temperature solid-state treatment under different temperature conditions, following the sequence

$$4CsNO_3 + 4(UO_2)(NO_3)_2(H_2O)_6 + 3WO_3 \rightarrow Cs_4[(UO_2)_4(WO_5)(W_2O_8)O_2] \tag{8.1}$$

$$Cs_4[(UO_2)_4(WO_5)(W_2O_8)O_2] + 3\gamma\text{-}UO_3 \rightarrow Cs_4[(UO_2)_7(WO_5)_3O_3] \tag{8.2}$$

The measured PXRD patterns show the evolution course from mixed **CsUW-1** and UO_3 to the single **CsUW-2** phase (**Figure 8.4**). The first observed PXRD pattern after annealing at 650 °C shows overlapping peaks of **CsUW-1** and γ-UO_3. With increasing temperature, the PXRD patterns develop more and more to that of **CsUW-2** pattern. Finally, the PXRD peaks observed at 800 °C are totally consistent with those expected for **CsUW-2**. This indicates that **CsUW-2** is the only phase synthesized

---

[270] Andrey N. Seliverstov et al. *Dalton Trans.*, **41**: 8512–8514, 2012.

[271] E. V. Alekseev et al. *J. Struct. Chem.*, **47**: 881–886, 2006.

by reaction 8.2 at 800 °C, concluding that **CsUW-2** can be prepared directly from **CsUW-1** by adding the corresponding molar weight of γ-UO_3.

It has to be noted that the CCIs fragments observed in the structure of **CsUW-2** reveal a dramatic similarity to those found in γ-UO_3, the latter also containing three-centered CCIs fragments.[260] The detailed examination of these structural fragments shows that they can be transformed into one another by simple "cut" and "glue" topological reconstruction (see **Figure** 8.2). The suggestion may be confirmed, that reaction pathway includes the most stable fragments of both **CsUW-1** and γ-UO_3, resulting in the structure of **CsUW-2** as a superposition. It is quite similar to that of classical syntheses of organic molecular materials.

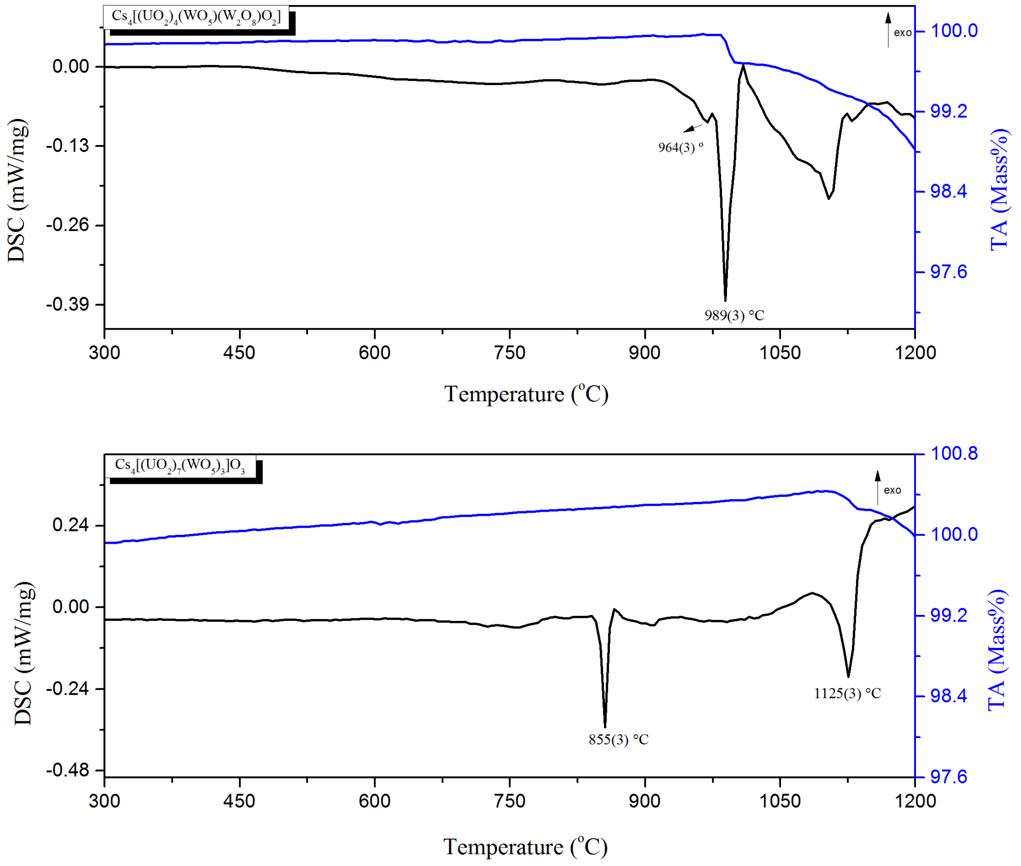

Figure 8.5: DSC and TG curves for (a) CsUW-1 and (b) CsUW-2, respectively.

8.1.2 Thermal analysis

The DSC-TG curves of **CsUW-1** and **CsUW-2** powders in the temperature range from 300 to 1200 °C are shown in **Figure** 8.5. The endothermic onset around 914 °C observed in the DSC measurement of **CsUW-1** corresponds to its melting point. A small peak located at 964(3) °C beside it demonstrates the sample decomposition. Accompanied by a small weight loss in the TG curve in this range, this reveals an incongruent melting behavior of **CsUW-1**. As for the case of **CsUW-2**, the thermal decomposition could be divided into 2 steps. The first step, starting at a temperature of around 840(8) °C up to 870(8) °C, but not obvious in the TG curve as a mass loss, shows a strong endothermic effect, which is related to sample melting. This is confirmed by heating bulk polycrystalline **CsUW-2** powders across the corresponding peak (855(3) °C). The PXRD technique shows the dark black melting products are dominated by U_3O_8. At higher temperatures, the second endothermic peak at around 1125(3) °C can be explained by the evaporation of the thermal decomposition products.

8.1.3 Raman spectroscopic analysis

The Raman spectra for as-synthesized uranium tungstates measured in the range of 100−1100 cm^{-1} region are displayed in **Figure 8.6**. It is obvious to coarsely divide the spectra into two frequency parts; a low frequency part between 100 cm^{-1} and 250 cm^{-1} where the modes are contributed from the vibrations of the "lattice skeleton", and a high-frequency part from 300 cm^{-1} to 1100 cm^{-1}, which are are dominated by modes from the uranium and tungstate polyhedra. Jones demonstrated that the uranium unit can be simplified as a linear triatomic molecule $\mathrm{UO_2}^{2+}$ with $D_{\infty h}$ symmetry owing to lack of coupling between the vibrational frequencies of equatorial ligands and those of the uranyl moiety. In aqueous solution, the characteristic vibrations of $\mathrm{UO_2}^{2+}$ are three normal modes, that is, ν_1 symmetric stretching mode (from 860−880 cm^{-1}), ν_3 anti-symmetrical stretching (from 930−960 cm^{-1}), and the ν_2 bending mode (from 199−210 cm^{-1}).[202,203] Both compounds only contain W ions that are five-fold coordinated (WO_5 square pyramids). Some of the modes for $\mathrm{UO_2}^{2+}$ and WO_5 mentioned above can be recognized in **Figure 8.6**. However, band positions will shift and split associated with a symmetry change specific for the respective the crystalline environment.[154] Due to the overlapping modes of the U and W polydedra[272], respectively, and because hardly any reference data for vibrational modes of WO_5 polyhedra are available in the literature, here only the main frequencies are discussed.

The differences between the structures of **CsUW-1** and **CsUW-2** (**Figure 8.6**) have an obvious impact on the vibrational properties of these compounds. The peaks obtained for the compound **CsUW-2** at 828(2) cm^{-1}, 871(1) cm^{-1} and 879(1) cm^{-1} are almost absent for **CsUW-1**, which can be presumed to result from the vibrations of U-O inside the CCIs unit. The anti-symmetrical stretching mode of $\mathrm{UO_2}^{2+}$ shows a shift to lower frequencies from **CsUW-1** to **CsUW-2** in the region 930−960 cm^{-1}. This deviation might be explained as a consequence of the different U-O terminal bond distances.[273] Owing to CCIs, the U-O bond distances are more abnormal in **CsUW-2** (U-O terminal ranging from

---

[202] Llewellyn H. Jones. *Spectrochim. Acta, Part A*, **10**: 395–403, 1958.
[203] David D. Schnaars and Richard E. Wilson. *Inorg. Chem.*, **52**: 14138–14147, 2013.
[154] D. L. Rousseau, R. P. Bauman, and S. P. S. Porto. *J. Raman Spectrosc.*, **10**: 253–290, 1981.
[272] P. Shiv Halasyamani et al. *Inorg. Chem.*, **38**: 271–279, 1998.
[273] Ray L. Frost et al. *J. Raman Spectrosc.*, **40**: 1816–1821, 2009.

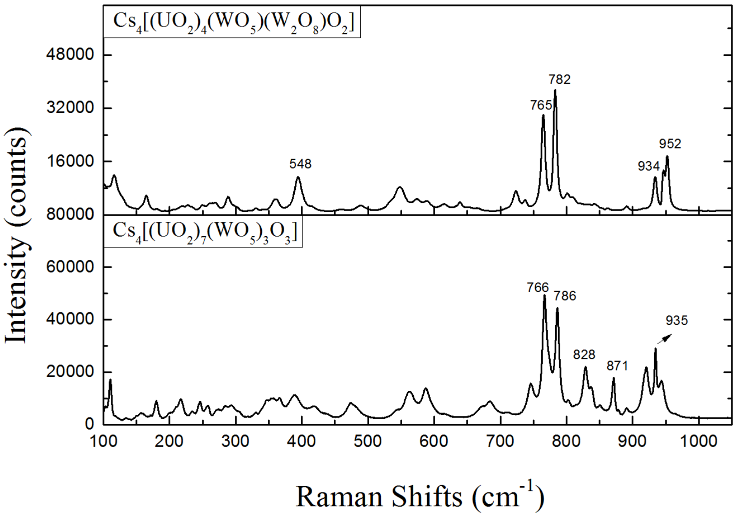

Figure 8.6: Raman spectra of (a) CsUW-1 and (b) CsUW-2, respectively.

1.80(1) Å to 1.82(1) Å for **CsUW-1** whereas, from 1.76(2) Å to 1.99(2) Å for **CsUW-2**). The peaks between 750 and 800 cm^{-1} for both compounds could be assigned to the symmetric stretching (ν_1) of UO_2^{2+}.[274] The stretching modes for W_2O_8 dimers (with W-O-W connection) in **CsUW-1** increase up to 1002(6) cm^{-1}. In **CsUW-2** where there is no such W_2O_8 dimers geometry, and therefore there are no stretching modes beyond 955(7) cm^{-1}. This phenomenon is also demonstrated in many lanthanide tungstate compounds, as the bridging of WO_x (x = 4, 5, 6) polydedra in the structure will result in a wider distribution of vibrational frequencies.[275]

8.1.4 Conclusion

CsUW-1 and **CsUW-2** are rare in actinides chemistry, since they are associated with each other *via* introducing of a CCIs based on UO_2^{2+}. The CCI topology observed in **CsUW-2**, to our knowledge, is revealed for the first time in uranyl chemistry. It is composed by four-membered uranium polyhedra with the connection that can be considered as a conformation of doubled three-centered CCIs. The structural transformation from 2D **CsUW-1** to 3D **CsUW-2** indicates the role of CCIs in forming a 3D framework by the unusual uranium connection geometry. Overall, the sharing of axial O atoms between uranyl polyhedra in general demonstrates that CCIs can provide 3D linkages between 2D sheets of uranyl compounds. This leads to more structural flexibility of complexation compared to the exclusive sharing of equatorial O atoms, enhancing the possibility of more diversifying structural themes.

CsUW-2 contains structural discrete units which are commonly observed among uranium compounds including **CsUW-1**. The question is what is the mechanism of **CsUW-2** formation in reaction between

---

[274] Valrie Vallet, Ulf Wahlgren, and Ingmar Grenthe. *J. Phys. Chem. A*, **116**: 12373–12380, 2012.

[275] V. I. Tsaryuk and V. F. Zolin. *Spectrochim. Acta Mol. Biomol*, **57**: 355–359, 2001.

CsUW-1 and γ-UO_3? We suppose that, at high temperature region, complex structural recombination is occurred between U-W layers of **CsUW-1** and CCIs fragments of γ-UO_3. We expect that U-W fragments which were observed in both **CsUW-1** and **CsUW-2** are the most stable aggregations of uranyl and oxo-tungstate groups at elevated temperatures. Ideologically this process is quite similar to the reactions between organic molecules where different ligands or functional groups bonded together to form a new material. In this way, both U-W fragments from **CsUW-1** and CCIs fragments from γ-UO_3 can be considered as "functional groups" which are combined together to form **CsUW-2**. This speculation is also supported by the existence of numerous uranyl compounds with similar U-W fragments obtained from similar temperature conditions.[270],[271] From topological point of view, **CsUW-2** can be considered as being composed from known structural pieces by an approach similar to a "jigsaw puzzle". The pieces of the "puzzle", represented by the layered fragments of **CsUW-1** and CCI parts of γ-UO_3, are locked together to complete the structure of **CsUW-2** at suitable temperature.

Of course, more studies are needed to be done before one can make a solid conclusion regarding on the generality of this method. Nonetheless, this report exhibits a potential way that is helpful for designing of actinyl compounds *via* introducing of CCI fragments at elevated temperatures. All in all, given the dominance of 2D sheets appearing in the crystal chemistry of U(VI), the ability of CCIs in increasing the dimensionality of uranium structures is remarkable, and there is a high possibility that it can originate novel U(VI) topologies.

8.2 First alkaline- and rare-earth thorium molybdates

Four novel thorium molybdates containing alkaline-earth or rare-earth metals were isolated from high-temperature solid-state synthesis. For $K_2MgTh_3(MoO_4)_8$, $Th(NO_3)_4 \cdot 5\,H_2O$ (A.R. grade), KNO_3 (A.R. grade), $Mg(NO_3)_2$ (A.R. grade) and MoO_3 (A.R. grade) with a molar ratio of 1: 1: 2: 2 were loaded into a Pt crucible after being fully ground. The mass weights of the reactants were 100.0 mg for $Th(NO_3)_4 \cdot 5\,H_2O$, 17.7 mg for KNO_3, 52.0 mg for $Mg(NO_3)_2$ and 50.5 mg for MoO_3, respectively. The Pt crucible was heated up to 1000 °C within 4 h in a furnace (CARBOLITE CWF 1300) and held constant at 1000 °C for 2 h in order to melt homogeneously. Afterwards, the mixture was cooled to 400 °C at a rate of 6.5 °C/h, followed by quenching. The resulting products were washed with hot water and bulk colorless crystals of good quality were obtained. Due to the undistinguishable optical behavior of synthesized crystals and glassy pieces, the yield couldn't be calculated. For $K_2SrTh_2(MoO_4)_6$, The reactants $Th(NO_3)_4 \cdot 5\,H_2O$ (100.0 mg), KNO_3 (53.2 mg), $Sr(NO_3)_2$ (148.5 mg) and MoO_3 (50.5 mg) with a molar ratio of 1: 3: 4: 2 were loaded into a Pt crucible. The mixture was ground and heated in a furnace at 950 °C for 3 h. The heating rate was 500 °C/h and the cooling rate was 5 °C/h. The resultant mixture in the crucible consisted of well-formed colorless prisms of $K_2SrTh_2(MoO_4)_6$ as well as crystals of K_2MoO_4 and other undefined amorphous products. For $Nd_2Th_3(MoO_4)_9$, $Th(NO_3)_4 \cdot 5\,H_2O$ (100.0 mg), Nd_2O_3 (23.6 mg) and MoO_3 (20.2 mg) with a molar ratio of 5:2:4 were loaded into a Pt crucible after being fully ground in an agate mortar. The crucible was then heated in a furnace for 6 h at 1100 °C, and slowly cooled to 400 °C at a rate of 5 °C /h followed by quenching. The resulting products consisted of $Nd_2Th_3(MoO_4)_9$ crystals and a glassy mass that was subsequently isolated. The yield couldn't be determined because of the similar shapes between crystals and glass pieces.

The incorporation of divalent and trivalent cations into the thorium molybdate system results in complex structural topologies. $A_2MgTh_3(MoO_4)_8$ (A = K, Rb) which crystallizes in space group $C2/c$ is the first instance among the thorium molybdate family that incorporates alkaline-earth metals. Its crystal structure is based on complex channels composed of ThO_8 square antiprisms and MoO_4 tetrahedra in a corner-sharing manner. $K_2SrTh_2(MoO_4)_6$, as the first thorium polymolybdate compound, is constructed by ThO_8 square antiprisms and Mo_4O_{16} tetramers. The Mo_4O_{16} tetramers, laying in the (001) plane, are built from four edge-sharing MoO_6 octahedra $Nd_2Th_3(MoO_4)_9$ is the first thorium molybdate containing rare-earth cations. The resemblance of $Nd_2Th_3(MoO_4)_9$ with hexagonal-$ThMo_2O_8$ reveals its potential as a host for different trivalent transuranium elements. Raman spectra analysis shows that the different Mo polyhedral geometries (MoO_4 tetrahedra and MoO_6 octahedra) have significant effects on the vibrational bands of these compounds. In addition, the TG-DSC technique was carried out to gain insight into the thermal behavior of the synthesized compounds.

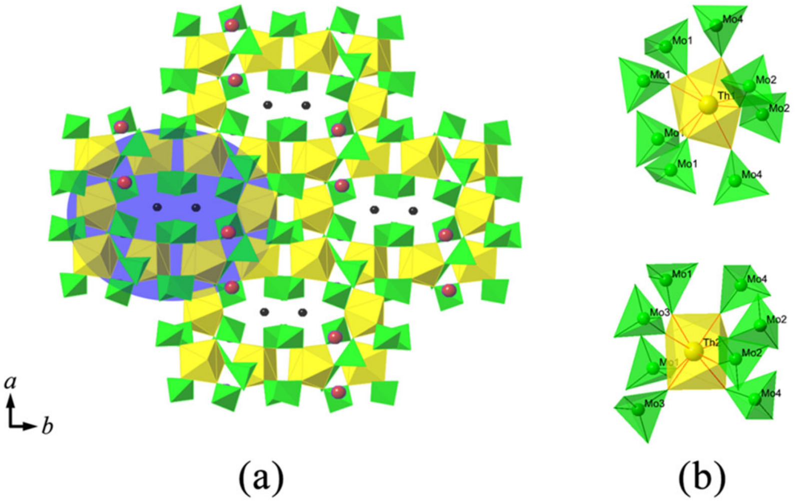

Figure 8.7: (a) Crystal structure of $A_2MgTh_3(MoO_4)_8$ (A = K, Rb) projected along the c axis. The channels with elliptical cross-section are highlighted with blue color. (b) The local connection of ThO_8 and MoO_4 polyhedra in the crystal structure of $K_2MgTh_3(MoO_4)_8$. The yellow and green polyhedra represent Th and Mo, respectively. Mg cations are shown as black nodes. The alkaline metals (K or Rb) are shown in red.

Crystal structure of $A_2MgTh_3(MoO_4)_8$ (A = K, Rb)

$A_2MgTh_3(MoO_4)_8$ (A = K, Rb) features a 3D open-framework network, as shown in **Figure 8.7 (a)**. It contains two Th and four Mo anions in an asymmetrical unit. As being observed in most thorium molybdate compounds, the Th and Mo atoms in $A_2MgTh_3(MoO_4)_8$ (A = K, Rb) are eight- and four-fold coordinated, forming a distorted square antiprismatic and tetrahedral geometry, respectively. For both phases the Th-O distances range from 2.346(4) to 2.513(4) Å. This range is typically observed in other inorganic thorium molybtates reported previously.[276,277] In $K_2MgTh_3(MoO_4)_8$, the Mo-O(1) bond distance (1.790(4) Å) is the longest one, which is further connected to Th(1), and the shortest bond distance is Mo-O(16) (1.687(4) Å), where O(16) is a terminal oxygen atom. For $Rb_2MgTh_3(MoO_4)_8$, the Mo-O bond distances range from 1.699(7) to 1.788(6) Å, with an average value of 1.757(6) Å, which is comparable to that found in potassium-based structure (1.759(8) Å). The Th-O-Mo angles in both structures are in the range from 129.6(2)° to 176.9(2)°, demonstrating quite flexible linkages between the ThO_8 and MoO_4 polyhedra. In the structure of $A_2MgTh_3(MoO_4)_8$ (A = K, Rb), all ThO_8 square antiprisms are eight-fold coordinated by MoO_4 tetrahedra. The local coordination environment of ThO_8 in $K_2MgTh_3(MoO_4)_8$ that is chosen as an example is exhibited in **Figure 8.7 (b)**. All O atoms of the Mo(1)O_4tetrahedra are bridging oxygen atoms to ThO_8 polyhedra, whereas Mo(2)$O_4$and Mo(4)O_4each share three O atoms with ThO_8 polyhedra, and Mo(3)O_4only shares two O atoms with adjacent ThO_8 polyhedra. As one can easily imagine, these non-shared terminal O atoms in Mo(2)O_4, Mo(3)$O_4$and Mo(4)O_4directly lead to an open-framework structure with channels running along [001] direction. The resulting channels, having an elliptical cross-section, are filled by Mg^{2+} cations. As can be seen from **Figure 8.7 (a)**, additional small voids within the framework that are created by ThO_8 square antiprisms corner sharing with MoO_4 polyhedra are accompanied by K^+ cations.

The most notable feature of $A_2MgTh_3(MoO_4)_8$ (A = K, Rb) are unusual complex channels, highlighted in **Figure 8.7 (a)**. **Figure 8.8 (a, b)** shows the local connections of ThO_8 and MoO_4 polyhedra inside the cylindroid channels. Using the black and white nodal representation, the idealized unfolding version of topological graph for such Th-Mo channel is shown in **Figure 8.8 (c)**. It is assembled with four-connected black nodes (Th) and two-connected white nodes (Mo). It is obvious that its topology is composed of so-called basic building tapes (highlighted in **Figure 8.8 (c)**).[278] The adjacent building tapes are joined by Mo(3) cations. In order to obtain the channels observed in the structure of $A_2MgTh_3(MoO_4)_8$, one needs to fold and glue the corresponding building tapes by the following procedure: As a first step, label the equivalent points on the sides of the tapes by the letters a, b, c, d, e, f, g and h. Then fold the tape by jointing the associated opposite sides (a-a', b-b', c-c', d-d', e-e', f-f', g-g' and h-h'), as demonstrated in **Figure 8.8 (c, d)**. It is notable that the method of basic building tapes not only allows us to recognize the internal Th-Mo polyhedral connections along the channels, but is also helpful to understand the symmetry inside the channels.[171] The basic tapes are related by a two-fold screw axis perpendicular to the channel direction. Due to the inversion center, as required by the space group $C2/c$, the cylindroid channels demonstrate an achiral cylindroid topology within this structure. Such method was also adopted by *Krivovichev, et al.* to present the linkage of U and Mo polyhedra inside the channels of a rare open-framework structure

---

[276] Ping Yu et al. *Angew. Chem. Int. Ed.*, **49**: 5975–5977, 2010.

[277] Shuao Wang et al. *Adv. Funct. Mater.*, **22**: 2241–2250, 2012.

[278] Shuao Wang et al. *Chem. Mater.*, **22**: 2155–2163, 2010.

[171] Shuao Wang et al. *Inorg. Chem.*, **51**: 11211–11213, 2012.

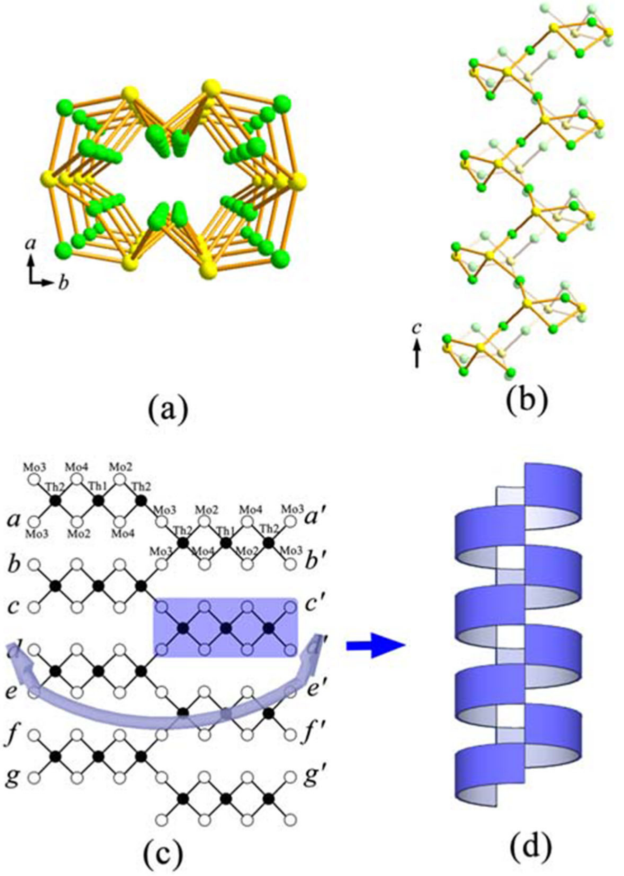

Figure 8.8: Representation of the cylindroid channels in the structure of $A_2MgTh_3(MoO_4)_8$ (A = K, Rb). (a, b) Construction of the channels connected by Th and Mo atoms. (c) Black and white nodal presentation of strips of Th and Mo polyhedra. The basic building strip is highlighted. (d) The idealized cylindroid channel is formed by folding the building strips around the c axis.

of $(NH_4)_4[(UO_2)_5(MoO_4)_7](H_2O)_5$.[172] In contrast to $A_2MgTh_3(MoO_4)_8$, the equivalent points on the sides of the tapes for $(NH_4)_4[(UO_2)_5(MoO_4)_7](H_2O)_5$ are not oppositely orientated to each other, thus their folding procedure results in a chiral U-Mo channel topology.

8.2.1 Structural and topological relationship in alkaline- and rare-earth thorium molybdate family

Structure of $K_2SrTh_2(MoO_4)_6$

The complex framework of $K_2SrTh_2(MoO_4)_6$ crystallizes in space group $P\bar{1}$, consisting of ThO_8 square antiprisms and Mo_4O_{16} tetramers. The crystal structure of $K_2SrTh_2(MoO_4)_6$ is exhibited in **Figure 8.9**. There are six crystallographically unique Mo sites and two distinct Th sites. Each Mo

---

[172] Shuao Wang et al. *Chem. Mater.*, **23**: 2931–2939, 2011.

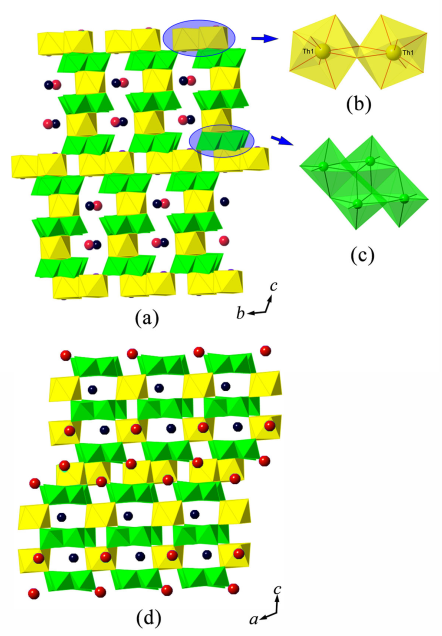

Figure 8.9: View of the crystal structure of $K_2SrTh_2(MoO_4)_6$. (a) Projection along the a axis. (b) The Th_2O_{14} thorium dimers. (c) The Mo_4O_{16} tetramers laying in the ab plane. (d) Projection along the b axis shows the rectangular voids occupied by Sr^{2+} cations. The Th and W polyhedra are shown in yellow and green, respectively. The K and Sr atoms are presented as red and black nodes, respectively.

cation is coordinated by six O atoms forming a MoO_6 octahedral configuration. Th(1) and Th(2), with square antiprismatic coordination geometry, reveal varying Th-O bond distances ranging from 2.34(1) Å to 2.56(2) Å, with the mean value being 2.44 Å, which is slightly larger than that observed in $Cs_2Th(MoO_4)_3$ (average Th-O = 2.41 Å)[105], but agrees well with the values reported for many molybdates containing eight-fold coordinated Th.[240,243,279] In $K_2SrTh_2(MoO_4)_6$, two $Th(1)O_8$ polyhedra, related by an inversion center, share a common O(8)-O(8) edge to construct a $Th(1)_2O_{14}$ dimeric unit, whereas the $Th(2)O_8$ polyhedra are found to be isolated from neighboring ThO_8 polyhedra.

The most interesting structural feature of $K_2SrTh_2(MoO_4)_6$ are Mo_4O_{16} tetramers laying in the ab plane. They are built by four MoO_6 octahedra connecting with each other in an edge-sharing manner. Each Mo_4O_{16} tetramer contains two kinds of bridging oxygen atoms, that is, μ_2-oxo and μ_3-oxo groups, respectively. The Mo-O bond distances within the MoO_6 octahedra vary from 1.72(2) Å to 2.44(2) Å. The average Mo-O bond distance is 1.96 Å, with some lengthening observed for Mo-μ_3O (around 2.15 Å). The O-Mo-O bond angles for O atoms in *cis* positions vary from 76.4(2)° to 106.4(3)°, and are thus far from an ideal right angle. In general, such Mo_4O_{16} tetramer has not been reported in any actinide family before. However, it can be typically found in polyoxomatellate compounds,[280,281] where Mo can be aggregated in corner-, edge- and even face-sharing environments to form large and complex 3D frameworks. It also has been reported as a fundamental structural unit in some simple

---

[105] Bin Xiao et al. *Cryst. Growth Des.*, **14**: 2677–2684, 2014.

[240] M. Huyghe et al. *Acta Crystallogr., Sect. C: Cryst. Struct. Commun.*, **47**: 244–246, 1991.

[243] T. L. Cremers, P. G. Eller, and R. A. Penneman. *Acta Crystallogr., Sect. C: Cryst. Struct. Commun.*, **39**: 1165–1167, 1983.

[279] M. Huyghe et al. *Acta Crystallogr., Sect. C: Cryst. Struct. Commun.*, **49**: 950–954, 1993.

[280] Adam J. Bridgeman and Germn Cavigliasso. *Polyhedron*, **21**: 2201–2206, 2002.

[281] Junwei Zhao et al. *CrystEngComm*, **13**: 3462–3469, 2011.

structures, such as $Ag_2Mo_2O_7$.[282]

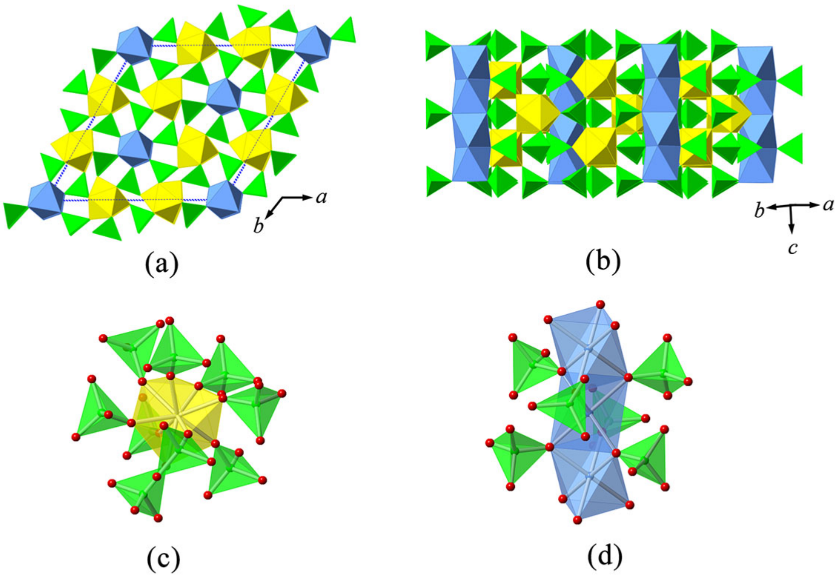

(a) (b)
(c) (d)

Figure 8.10: View of the crystal structure of $Nd_2Th_3(MoO_4)_9$ along the c axis in (a) and along [110] in (b) respectively. The local coordination environment of Th and Nd polyhedra are shown in (c) and (d), respectively. Blue symbolizes NdO_6 octahedra, yellow and green represent ThO_9 and MoO_4 polyhedra, respectively.

Each Mo_4O_{16} tetrameter shares 14 O atoms by attachment to three $Th(1)_2O_{14}$ dimers on the one hand side (two of them forming an unidentate configuration and the other one forming a bidentate fashion) and two $Th(2)O_8$ square antiprisms on the other side (one being involved in the unidentate and the other forming the bidentate configuration, respectively). As a result, two types of channels can be found in the crystal structure of $K_2SrTh_2(MoO_4)_6$. The first one, with interior dimensions of approximately 11.5 × 1.9 Å, is formed propagating in [100] direction. These channels are located within the Th-O-Mo anionic network and are occupied by charge-compensating K^+ and Sr^{2+} cations. Viewing along [010] direction, another small channel with rectangular shape occupied by Sr^{2+} cations become apparent. These two kinds of channels intersect with each other, resulting in an open-framework structure.

Structure of $Nd_2Th_3(MoO_4)_9$

The compound $Nd_2Th_3(MoO_4)_9$ crystallizes in space group $P6_3/m$ with a 3D framework structure, as shown in **Figure 8.10**. The structure of $Nd_2Th_3(MoO_4)_9$ consists of one ThO_9 site, two independent NdO_6 sites, and three independent MoO_4 sites. Each Th atom, coordinating to nine O atoms, connects to nine MoO_4 tetrahedra forming a distorted and capped square antiprism coordination. The Th-O bond distances range from 2.42(1) to 2.51(1) Å, with an average bond distance equal 2.44 Å. This bond distance is slightly shorter than those found in other synthetic thorium molybdates owing nine-

---

[282] Bryan M Gatehouse and Peter Leverett. *Dalton Trans.*, 1316–1320, 1976.

fold coordinated Th polyhedra, such as 2.46 Å in hexagonal $ThMo_2O_8$,[283] but is still consistent with the ionic radii reported by Shannon.[284] The Nd atoms which are six-coordinated in a highly distorted octahedral geometry are linked to chains by sharing two octahedral faces with each other (Figure 4(b) and **Figure 8.11 (a)**). As given in **Figure 8.11 (c)**, each NdO_6 octahedron is polarized by a three-fold rotation axis running through its two parallel triangular faces. As a result, the Nd^{3+} cations move towards the octahedral face. This distortion is obviously reflected by a *cis* O-Nd-O configuration diverging from the ideal angle of 90°, exhibiting small (around 83°) and large (around 97°) angles. Each MoO_4 tetrahedron is four-fold connected to both types of polyhedra, *i.e.* ThO_9 and NdO_6. The variation of Mo-O bond distances is appreciable, ranging from 1.70(1) to 1.81(1) Å, the average distance being 1.75 Å. This is in good agreement to previous results of thorium molybdates in MoO_4 tetrahedra.[240,243]

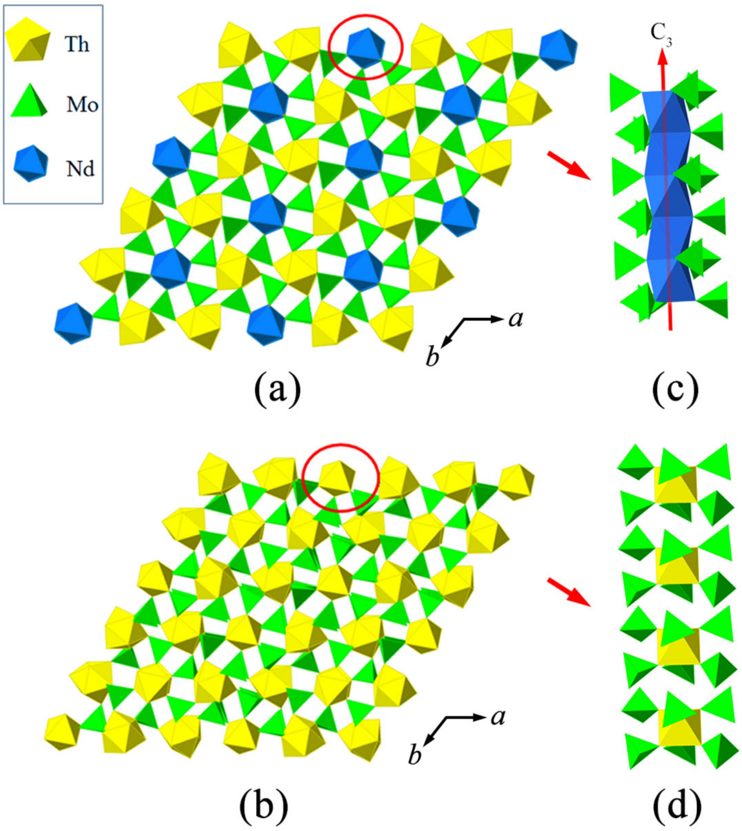

Figure 8.11: Comparison of the crystal structures of $Nd_2Th_3(MoO_4)_9$ and hexagonal $ThMo_2O_8$, respectively. (a and b) The polyhedral representations in $Nd_2Th_3(MoO_4)_9$ and hexagonal $ThMo_2O_8$, respectively. (c) Face-sharing NdO_6-NdO_6 chain in $Nd_2Th_3(MoO_4)_9$. (d) Isolated ThO_6 octahedra in hexagonal $ThMo_2O_8$.

---

[283] E. M. Larson et al. *Acta Crystallogr., Sect. C: Cryst. Struct. Commun.*, **45**: 1669–1672, 1989.

[284] R. D. Shannon. *Acta Cryst. A*, **32**: 751–767, 1976.

The structures of a series of compounds $Ln_2M_3(MoO_4)_9$ (Ln = La-Lu, Y, Sc; M = Zr, Hf)[285,286] own a similar stoichiometric composition compared to $Nd_2Th_3(MoO_4)_9$. Both can be derived from the octahedral-tetrahedral framework of the mineral kosnarite ($NaZr_2(PO_4)_3$), a structure type that has been proposed as a nuclear waste form due to its capacity of accommodating large variety of radionuclides present in high-level wastes.[287] $Ln_2M_3(MoO_4)_9$ is also based upon a 3D framework composed of three kinds of corner-sharing polyhedra: MoO_4 tetrahedra, MO_6 octahedra and nine-fold coordinated LnO_9. One of the interesting features of $Ln_2M_3(MoO_4)_9$ compounds is that they have been demonstrated as an acceptant for immobilizing tri- and tetravalent actinides, which elucidates the chemical behavior of actinides in processes for the treatment and disposal of radioactive waste.[288] As a new member of this big family, $Nd_2Th_3(MoO_4)_9$ may also become a potential waste form, but further investigation is necessary in order to confirm this hypothesis.

It is also noteworthy that there is a close structural resemblance between $Nd_2Th_3(MoO_4)_9$ and hexagonal $ThMo_2O_8$. Both compounds show similar unit-cell parameters. The ***a*** and ***b*** parameters of $Nd_2Th_3(MoO_4)_9$ are shorter than those of hexagonal $ThMo_2O_8$, and this shortening can be explained by the inclusion of the smaller Nd^{3+} cation. **Figure** 8.11 shows the polyhedral representations of both compounds. The similarity can best be demonstrated by projecting $Nd_2Th_3(MoO_4)_9$ and hexagonal-$ThMo_2O_8$ along each crystallographic **c**-axis. However, further structural analysis reveals that all six-coordinated sites (NdO_6 octahedra) in $Nd_2Th_3(MoO_4)_9$ are connected *via* face-sharing, while the corresponding sites (ThO_6 octahedra) observed in hexagonal $ThMo_2O_8$ are completely separated. (Figure 5(c) and (d) respectively). For this reason, the associated Nd-Nd bond distance in $Nd_2Th_3(MoO_4)_9$ is remarkably short, *i.e.* only around 3.1 Å. The fact that $Nd_2Th_3(MoO_4)_9$ and hexagonal-$ThMo_2O_8$ are based on a similar structural framework while containing different cations, indicates that Th^{4+} cations can be partially substituted by trivalent ions while keeping the same structural skeleton. This means that such a framework has the ability to host diverse cations of various radii as well as valences without a considerable change of geometric parameters. Therefore, $Nd_2Th_3(MoO_4)_9$ can be used as a host phase for rare-earth elements and minor actinides (Am^{3+}, Cm^{3+}...).

8.2.2 Raman spectroscopic analysis

The Raman spectra of all thorium molybdates shown in **Figure** 8.12 can be coarsely divided into two parts; a low frequency part between 100 cm^{-1} and 250 cm^{-1} among which the bands are associated with lattice phonon modes, and a high-frequency part from 250 cm^{-1} to 1000 cm^{-1}, which is assigned

---

[285] R. F. Klevtsova et al. *J. Struct. Chem.*, **41**: 280–284, 2000.

[286] B. G. Bazarov et al. *J. Struct. Chem.*, **50**: 566–569, 2009.

[287] Rodney C Ewing and LuMin Wang. *Reviews in mineralogy and geochemistry*, **48**: 673–699, 2002.

[288] Tatiana A. Vereshchagina et al. *J. Mater. Chem.*, **21**: 12001–12007, 2011.

to the internal motions of oxo-anion groups ($MoO_4{}^{2-}$ tetrahedron or $MoO_6{}^{2-}$ octahedron).[76,208,209,289] As discussed in the structure analysis part, except for $K_2SrTh_2(MoO_4)_6$ which contains Mo_4O_{16} tetramers constructed from edge-sharing of four MoO_6 octahedra, all remaining units are based on separated $MoO_4{}^{2-}$ groups. For the $MoO_4{}^{2-}$ group, the vibrational data are well defined by a large number of available references.[208] However, very little research has been undertaken so far on actinide molybdate materials. The free $MoO_4{}^{2-}$ tetrahedron has T_d symmetry and four normal modes which are assigned as $A_1(\nu_1)$; $E(\nu_2)$; $F_1(rot)$, $F_2(trans, \nu_3, \nu_4)$, where A_1, E and F_2 are Raman permitted whereas F_2 is also IR active. ν_1, ν_2, ν_3 and ν_4 are denoted as non-degenerated symmetrical stretching mode, double degenerated symmetrical bending mode, and triple degenerated anti-symmetrical stretching and anti-symmetrical bending vibrations, respectively. The stretching vibrations ν_1 and ν_3 in ideal $MoO_4{}^{2-}$ are located in the region 700 cm^{-1}$-$1000 cm^{-1}, while the bending vibrations (ν_2 and ν_4) are situated in the region 300 cm^{-1}$-$500 cm^{-1}.[76] When it comes to a specific structure, however, due to crystal field effects, the $MoO_4{}^{2-}$ groups are distorted, and therefore the number of possible modes is increased. Because of having a large number of atoms in an asymmetrical unit ($e.g.$ 35 crystallographically different atoms observed in $K_2SrTh_2(MoO_4)_6$) the vibrational properties are remarkable complex for reported compounds.

Like most of the reported molybdate compounds containing MoO_4 tetrahedral units, strong vibrational bands for $K_2MgTh_3(MoO_4)_8$, $Rb_2MgTh_3(MoO_4)_8$ and $Nd_2Th_3(MoO_4)_9$, respectively are observed related to the symmetric stretching modes (ν_1), while the asymmetric stretches (ν_3) are relatively weak. The Raman spectra of the isostructural compounds $K_2MgTh_3(MoO_4)_8$ and $Rb_2MgTh_3(MoO_4)_8$ are virtually identical. Both have totally 276 normal vibrational modes ($68A_g + 68A_u + 70B_g + 70B_u$) predicted by factor group analysis.[154] Only minor vibrational differences occur between these two compounds. In particular, the highest peak located at 953(1) cm^{-1} in $K_2MgTh_3(MoO_4)_8$ can be assigned to the ν_1 of MoO_4, while it is shifted to a lower frequency (951(1) cm^{-1}) in $Rb_2MgTh_3(MoO_4)_8$. Such distinction is mainly originated from different Mo-O bond distances, which has been elucidated in detail by Hardcastle and Wachs.[290] The most significant feature of $Nd_2Th_3(MoO_4)_9$ are strong bands in the region from 750 cm^{-1} to 1000 cm^{-1}. The high and sharp peak located at 965(1) cm^{-1} can be assigned to the symmetrical stretching mode ν_1 of the $MoO_4{}^{2-}$ tetrahedron. As for $K_2SrTh_2(MoO_4)_6$, because of containing a huge number of atoms in an asymmetrical unit and Mo-O-Mo connections, the Raman profile shows complex broad and overlapping bands, originated by varying Mo-O bond distances and Mo-O-Mo bond angles.[291] The stretching modes of $K_2SrTh_2(MoO_4)_6$ occur at wavenumbers from 700 to 1000 cm^{-1}, and bending modes from 250 to 450 cm^{-1}, which is comparable to other molybdates containing MoO_6 octahedra.[291–293]

---

[76] V.P. Mahadevan Pillai et al. *Spectrochim. Acta, Part A*, **53**: 867–876, 1997.

[208] J. Hanuza, M. Maczka, and J. H. van der Maas. *J. Mol. Struct.*, **348**: 349–352, 1995.

[209] K. Hermanowicz et al. *J. Lumin.*, **92**: 151–159, 2000.

[289] J. Hanuza et al. *J. Raman Spectrosc.*, **41**: 424–430, 2010.

[290] Franklin D. Hardcastle and Israel E. Wachs. *J. Raman Spectrosc.*, **21**: 683–691, 1990.

[291] V. O. Sokolov et al. *J. Non-Cryst. Solids*, **355**: 239–251, 2009.

[292] G. A. Nazri and C. Julien. *Solid State Ionics*, **5356, Part 1**: 376–382, 1992.

[293] L. Seguin et al. *Spectrochim. Acta, Part A*, **51**: 1323–1344, 1995.

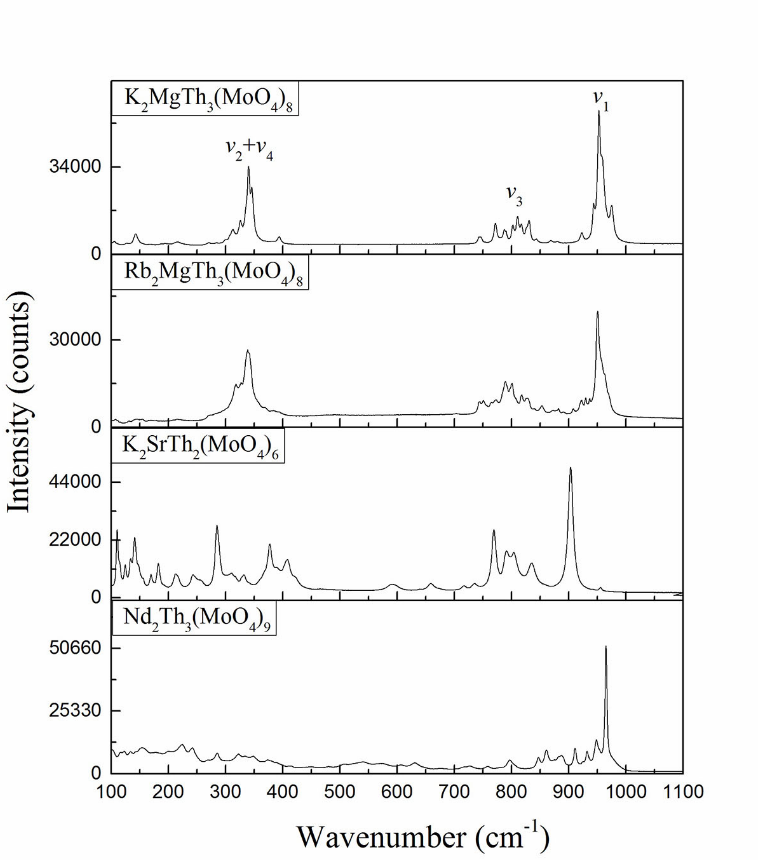

Figure 8.12: Raman shifts of $K_2MgTh_3(MoO_4)_8$, $Rb_2MgTh_3(MoO_4)_8$, $K_2SrTh_2(MoO_4)_6$ and $Nd_2Th_3(MoO_4)_9$, respectively.

8.2.3 Discussion of thermal analysis

Figure 8.13 shows DSC and TG measurements of as-synthesized pure thorium molybdate phases. Black lines relate to DSC curves and blue lines to the percentage mass loss (TG), respectively. The DSC curves exhibit different profiles for thorium molybdates containing different types of cations. The thermal behavior of $K_2MgTh_3(MoO_4)_8$ is quite similar to that of alkaline thorium molybdates, such as $Rb_4Th_5(MoO_4)_{12}$[141] and $Na_4Th(MoO_4)_4$[294]. $K_2MgTh_3(MoO_4)_8$ reveals two endothermic peaks, at around 921(5) °C and 1116(5) °C, respectively. The first peak indicates sample melting, and the broad and weak one, appearing immediately after the starting of mass loss, shows the incongruent melting behavior. A similar thermal evolution has also been observed for the isostructural counterpart $Rb_2MgTh_3(MoO_4)_8$. For $K_2SrTh_2(MoO_4)_6$ the DSC curve shows a strong endothermic peak at 985(5) °C indicating decomposition. For $Nd_2Th_3(MoO_4)_9$ decomposition seems to start at 667(5) °C, detectable by powder X-ray diffraction while heating the sample across this temperature. The main decomposition products can be indexed as hexagonal $ThMo_2O_8$. The associated mass loss in this

---

[141] Bin Xiao et al. *Inorg. Chem.*, **53**: 3088–3098, 2014.

[294] N. D. Dahale, Meera Keskar, and K. D. Singh Mudher. *J. Alloys Compd.*, **415**: 244–250, 2006.

range can serve as an additional proof.

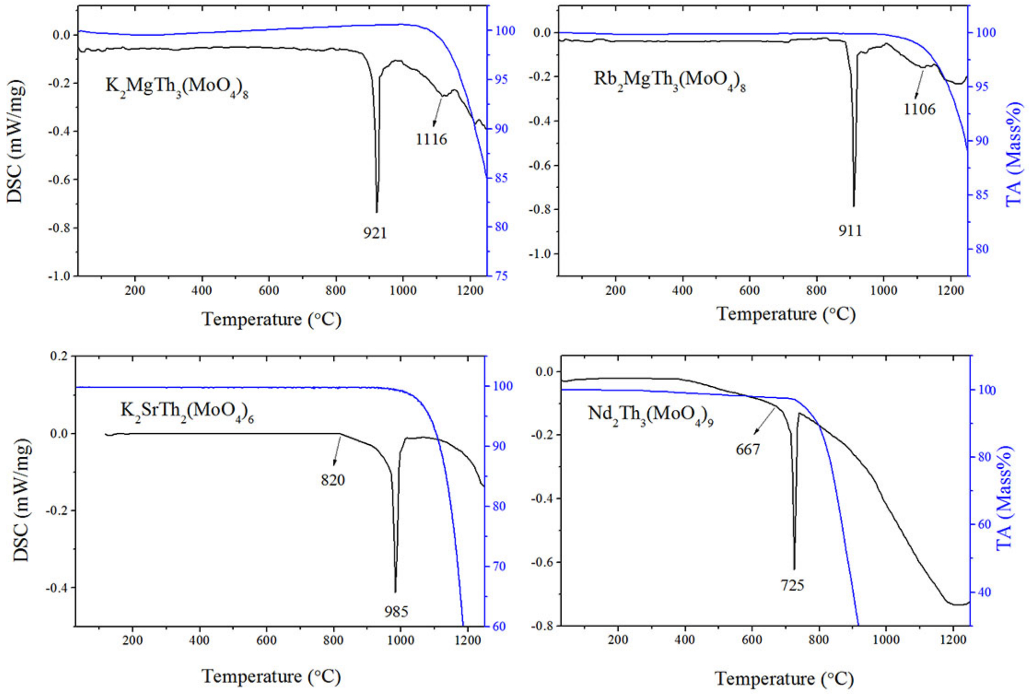

Figure 8.13: DSC and TG behavior of $K_2MgTh_3(MoO_4)_8$, $Rb_2MgTh_3(MoO_4)_8$, $K_2SrTh_2(MoO_4)_6$ and $Nd_2Th_3(MoO_4)_9$, respectively.

8.2.4 Conclusion

The incorporation of the multi-valent metal cations into the Th-Mo family leads to a remarkable topological diversity, substantially expanding the structural chemistry of thorium molybdates. Compared to alkaline thorium molybdates, the thorium molybdate compounds containing alkaline-earth or rare-earth metals are more complex. The structural disparity between these thorium molybdates is strongly attributed to the radii and valences of the cations. $A_2MgTh_3(MoO_4)_8$ (A = K, Rb) are based on unusual complex cylindroid channels composed by ThO_8 square antiprisms and MoO_4 tetrahedra. Up to now, all known thorium molybdates are exclusively built by MoO_4 tetrahedra. $K_2SrTh_2(MoO_4)_6$ is the first phase being constructed by MoO_6 octahedral units. $Nd_2Th_3(MoO_4)_9$, comparable to octahedral-tetrahedral based natural kosnarite, has a structure similar to that of hexagonal $ThMo_2O_8$ but with NdO_6 instead of ThO_6 octahedra. The lanthanide to actinide substitution observed within the $Nd_2Th_3(MoO_4)_9$ framework may be an indication for the potential of this structure as a matrix for the immobilization of actinides.

Conclusions

This dissertation reports the synthesis, phase studies and physicochemical properties of a large family of novel thorium and uranium compounds containing elements from the Group VI (S, Se, Te, Cr, Mo, W) of the Periodic Table (compounds are listed in **Table** 2.2 from the **page** 15). These compounds exhibit an exceeding diversity in the structural topologies, which ranges from infinite clusters to unprecedented complex frameworks. The purpose of this dissertation is to study the crystal chemistry of novel inorganic actinides which may aid in understanding the chemical behaviors of actinides in the areas of nuclear energy, storage and separations. General conclusions are highlighted based on the studies of synthetic routes and crystal chemical analysis presented in this dissertation.

Regarding the synthetic aspect, in total, 4 methods are used in this study: room-temperature slow evaporation method, mild-hydrothermal method, high-temperature (HT) solid-state method and high-temperature and high-pressure (HT/HP) method (detailed descriptions are in **Chapter** 2.1 from **page** 11). Among them, the high-temperature/high-pressure method, an excellent technique to obtain atypical structural features, was applied to systematically investigate the chemical behaviors of thorium and uranium tellurium families. In comparison with traditional synthetic methods, the extreme synthesis condition plays an important role in enhancing and improving the structural diversity and complexity that actinide can adopt. Moreover, during the research of mixed-oxoanion (Mo/W-Te) system, it is noted that a high tellurium ratio always led to high viscosity of the melted mixture promoting glass formation, while a low ratio could result in low yields or in phases not involving the Te element. The results of different synthesis experiments showed that the thorium system with mixed oxo-anions of Te-Mo(W) are preferable to be formed with Mo(W): Te ratios from 1: 1 to 2: 1.

By applying the above mentioned synthetic methods, the obtained uranium and thorium compounds in this dissertation have rich and fascinating crystal chemistry in all regards. Generally, most of the actinide compounds described above contain TO_4 tetrahedra (T = S, Cr, Se, Te, W, Mo). These TO_4 tetrahedra can further connect through corner-, edge-, or face-sharing manners with actinide polyhedra to create clusters, one-dimensional chains, two-dimensional sheets and three-dimensional framework structures. More specifically, all the thorium molybdates and tungstates can be seen as based on a “father” compound $ThMo_2O_8$. This compound is seemingly simple in formula appearance, yet considerably complicated in chemical behavior. This simple thorium molybdate has totally four polymorphs. Among them, three polymorphs were prepared at the ambient pressure. The fourth phase was formed under high temperature and high pressure condition by significantly changing the structural volume and crystal topology of the ambient polymorph. compound. Additionally, a large number of actinide tellurium compounds prepared at HT/HP condition exhibit some unprecedent structure features, such as the unusual high dimensionality and noncentrosymmetric crystal system observed in the uranyl tellurium family and diverse coordination geometries mixed-valent oxo-anions found in thorium tellurium family. Besides, we note that some uranyl tungstate compounds with different structural dimensionalities are connected with each other only by the cation-cation interactions. These compounds can be structurally converted form one to another by adding or removing the cation-cation interactions. This shows the remarkable ability of cation-cation interactions in affecting the dimensionality of uranium structures.

Finally, a large number of uranium and thorium compounds with elements from group VI of the periodic table were synthesized and studied in this work. Some of these elements such as Mo, Se and Te are important fission products created in a nuclear reactor. As a consequence, the formation of these actinide compounds may play an important role in the behavior of spent nuclear fuel in final disposal sites. Moreover, U(IV) and Th(IV) are often used as the surrogates to study the chemical and structural behavior of more toxic and radioactive Np(IV) and Pu(IV) in reducing condition. Thus, the data on formation and properties of U(IV) and Th(IV) compounds obtained in this work can be used for nuclear safety assessment with processes including Pu and Np.

Many Th(IV), Np(IV) and Pu(IV) compounds such as $AnMo_2O_8$, $A_2An(MO_4)_3$ and $A_4An(MO_4)_4$ (An = Th(IV), Np(IV) or Pu(IV); A = alkaline metals; M = Mo or W) are based on identical crystal structures. However, in this dissertation we have also observed some thorium tungstate compounds with very complex topological structures. Based on this, we may ask, whether the corresponding analogues can be found in Np(IV) and Pu(IV) families and how closely their physicochemical properties are related to each other in respect to the different $5f$-shells structure. These questions are raised from the different electronic configurations among these actinides, and it will be necessary to make further experiment with transuranic (IV) elements in order to answer them.

As a conclusion, a large number of uranium and thorium compounds with elements from group VI of the periodic table were synthesized and studied in this work. Some of these elements such as Mo, Se and Te are important fission products created in a nuclear reactor. As a consequence, the formation of these actinide compounds may play an important role for investigating and understanding their influence on the spent nuclear fuel. Moreover, due to the fact that U(IV) and Th(IV) are often used as surrogates to study the chemical behaviors of more toxic and radioactive Np(IV) and Pu(IV) in a reducing condition, the stabilities and thermodynamic data in this work can be used for nuclear safety assessment.

References

[1] Sergey V. Krivovichev and Peter C. Burns. “Chapter 4 - Actinide compounds containing hexavalent cations of the VI group elements (S, Se, Mo, Cr, W)” in: *Structural Chemistry of Inorganic Actinide Compounds* ed. by Sergey V. KrivovichevPeter C. BurnsIvan G. Tananaev. Amsterdam: Elsevier, 2007. 95–182 (see **page** 1)

[2] Robert Finch and Takashi Murakami. Systematics and paragenesis of uranium minerals. *Reviews in Mineralogy and Geochemistry*, **38**: 91–179, 1999. (see **pages** 1, 7)

[3] G.H. Swihart, PK Sen Gupta, E.O. Schlemper, M.E. Back, and R.V. Gaines. The crystal structure of moctezumite [PbUO2](TeO3) 2. *Am. Mineral.*, **78**: 835–839, 1993. (see **pages** 1, 7)

[4] D.Yu. Pushcharovsky, R.K. Rastsvetaeva, and H. Sarp. Crystal structure of deloryite, Cu4(UO2)[Mo2O8](OH)6. *J. Alloys Compd.*, **239**: 23–26, 1996. (see **page** 1)

[5] A.A. chernikov. *Behaviour of Uranium in the Hypergene Zone.* Nedra, Moscow, Russia (in Russ.), 1981. (see **page** 1)

[6] Peter C Burns. U6+ minerals and inorganic compounds: insights into an expanded structural hierarchy of crystal structures. *Can. Mineral.*, **43**: 1839–1894, 2005. (see **pages** 1–3, 61)

[7] S. V. Krivovichev, C. L. Cahill, and P. C. Burns. Syntheses and Crystal Structures of Two Topologically Related Modifications of Cs2[(UO2)2(MoO4)3]. *Inorg. Chem.*, **41**: 34–39, 2001. DOI: `10.1021/ic010345y` (see **pages** 1, 6)

[8] Jonathan A. Webb and Indrajit Charit. Monte Carlo criticality analysis of simple geometries containing tungsten-rhenium alloys engrained with uranium dioxide and uranium mononitride. *Nucl. Eng. Des.*, **241**: 2968–2973, 2011. (see **page** 2)

[9] Bin Xiao, Eike Langer, Jakob Dellen, Hartmut Schlenz, Dirk Bosbach, Evgeny V. Suleimanov, and Evgeny V. Alekseev. Chemical and Structural Evolution in the Th-SeO32-/SeO42- System: from Simple Selenites to Cluster-Based Selenate Compounds. *Inorg. Chem.*, **54**: 3022–3030, 2015. DOI: `10.1021/acs.inorgchem.5b00133` (see **page** 2)

[10] Richard E. Wilson, S. Skanthakumar, Karah E. Knope, Christopher L. Cahill, and L. Soderholm. An Open-Framework Thorium Sulfate Hydrate with 11.5 ÅVoids. *Inorg. Chem.*, **47**: 9321–9326, 2008. DOI: `10.1021/ic800931f` (see **page** 2)

[11] Grégory Nocton, Pawel Horeglad, Valentina Vetere, Jacques Pécaut, Lionel Dubois, Pascale Maldivi, Norman M. Edelstein, and Marinella Mazzanti. Synthesis, Structure, and Bonding of Stable Complexes of Pentavalent Uranyl. *J. Am. Chem. Soc.*, **132**: 495–508, 2010. DOI: `10.1021/ja9037164` (see **page** 3)

[12] Liam P. Spencer, Eric J. Schelter, Ping Yang, Robyn L. Gdula, Brian L. Scott, Joe D. Thompson, Jaqueline L. Kiplinger, Enrique R. Batista, and James M. Boncella. Cation-Cation Interactions, Magnetic Communication, and Reactivity of the Pentavalent Uranium Ion [U(NtBu)2]+. *Angew. Chem. Int. Ed.*, **48**: 3795–3798, 2009. (see **page** 3)

[13] Chih-Shan Chen, Shang-Fan Lee, and Kwang-Hwa Lii. K(UO)Si2O6: A PentavalentUranium Silicate. *J. Am. Chem. Soc.*, **127**: 12208–12209, 2005. DOI: `10.1021/ja0543853` (see **page** 3)

[14] Shuao Wang, Juan Diwu, Evgeny V. Alekseev, Laurent J. Jouffret, Wulf Depmeier, and Thomas E. Albrecht-Schmitt. Cation-Cation Interactions between Neptunyl(VI) Units. *Inorg. Chem.*, **51**: 7016–7018, 2012. DOI: 10.1021/ic3009305 (see **page** 3)

[15] Monica Vasiliu, Karah E. Knope, L. Soderholm, and David A. Dixon. Spectroscopic and Energetic Properties of Thorium(IV) Molecular Clusters with a Hexanuclear Core. *J. Phys. Chem. A*, **116**: 6917–6926, 2012. DOI: 10.1021/jp303493t (see **page** 3)

[16] Clément Falaise, Jean-Sébastien Charles, Christophe Volkringer, and Thierry Loiseau. Thorium Terephthalates Coordination Polymers Synthesized in Solvothermal DMF/H2O System. *Inorg. Chem.*, –, 2015. DOI: 10.1021/ic502725y (see **page** 4)

[17] Karah E. Knope, Monica Vasiliu, David A. Dixon, and L. Soderholm. Thorium(IV)-Selenate Clusters Containing an Octanuclear Th(IV) Hydroxide/Oxide Core. *Inorg. Chem.*, **51**: 4239–4249, 2012. DOI: 10.1021/ic202706s (see **pages** 4, 7)

[18] Karah E. Knope, Richard E. Wilson, Monica Vasiliu, David A. Dixon, and L. Soderholm. Thorium(IV) Molecular Clusters with a Hexanuclear Th Core. *Inorg. Chem.*, **50**: 9696–9704, 2011. DOI: 10.1021/ic2014946 (see **page** 4)

[19] Patrick Woidy and Florian Kraus. [Th10(-F16)(3-O4)(4-O4)(NH3)32](NO3)819.6 NH3 - the Largest Thorium Complex from Solution known to Date. *Z. Anorg. Allg. Chem.*, **640**: 1547–1550, 2014. (see **page** 4)

[20] Alexander P. Novikov, Stepan N. Kalmykov, Satoshi Utsunomiya, Rodney C. Ewing, Franois Horreard, Alex Merkulov, Sue B. Clark, Vladimir V. Tkachev, and Boris F. Myasoedov. Colloid Transport of Plutonium in the Far-Field of the Mayak Production Association, Russia. *Science*, **314**: 638–641, 2006. DOI: 10.1126/science.1131307 eprint: http://www.sciencemag.org/content/314/5799/638.full.pdf (see **page** 4)

[21] J. J. Berzelius. *Poggendorf'sAnn.*, **16**: 385–415, 1829. (see **page** 5)

[22] Hyun Sun Ahn, Dong Woo Lee, and Kang Min Ok. From an Open Framework to a Layered and a Hexagonal Tungsten Oxide Structure: Controlled Transformation Reactions of an Extended Solid-State Material, Cs3Ga7(SeO3)12 to Ga(OH)(SeO3) and KGa3(SeO4)2(OH)6. *Inorg. Chem.*, **52**: 12726–12730, 2013. DOI: 10.1021/ic402274s (see **page** 5)

[23] Sang-Hwan Kim, Jeongho Yeon, and P. Shiv Halasyamani. Noncentrosymmetric Polar Oxide Material, Pb3SeO5: Synthesis, Characterization, Electronic Structure Calculations, and StructureProperty Relationships. *Chem. Mater.*, **21**: 5335–5342, 2009. DOI: 10.1021/cm902639p (see **page** 5)

[24] Sergey V. Krivovichev, Volker Kahlenberg, Reinhard Kaindl, Edgar Mersdorf, Ivan G. Tananaev, and Boris F. Myasoedov. Nanoscale Tubules in Uranyl Selenates. *Angew. Chem. Int. Ed.*, **117**: 1158–1160, 2005. (see **pages** 5, 23)

[25] Fang Kong, Xiang Xu, and Jiang-Gao Mao. A Series of New Ternary and Quaternary Compounds in the LiIGaIIITeIVO System. *Inorg. Chem.*, **49**: 11573–11580, 2010. DOI: 10.1021/ic101843g (see **page** 5)

[26] Jian Lin, Juan Diwu, Justin N. Cross, Eric M. Villa, and Thomas E. Albrecht-Schmitt. Cerium(IV) Tellurite Halides [Ce2Te7O17]X2 (X = Cl- or Br-): The First Cerium-Containing Cationic Frameworks. *Inorg. Chem.*, **51**: 10083–10085, 2012. DOI: 10.1021/ic301628q (see **page** 5)

[27] Jun-Ho Kim and P. Shiv Halasyamani. A rare multi-coordinate tellurite, NH4ATe4O92H2O (ARb or Cs): The occurrence of TeO3, TeO4, and TeO5 Polyhedra in the same material. *J. Solid State Chem.*, **181**: 2108–2112, 2008. (see **page** 5)

[28] Oleg I. Siidra, Evgeny V. Nazarchuk, Anna N. Suknotova, Roman A. Kayukov, and Sergey V. Krivovichev. Cr(VI) Trioxide as a Starting Material for the Synthesis of Novel Zero-, One-, and Two-Dimensional Uranyl Dichromates and Chromate-Dichromates. *Inorg. Chem.*, **52**: 4729–4735, 2013. DOI: 10.1021/ic400341q (see **page** 5)

[29] Evgeny V. Alekseev, Sergey V. Krivovichev, Thomas Malcherek, and Wulf Depmeier. One-Dimensional Array of Two- and Three-Center CationCation Bonds in the Structure of Li4[(UO2)10O10(Mo2O8)]. *Inorg. Chem.*, **46**: 8442–8444, 2007. DOI: 10.1021/ic7009385 (see **page** 6)

[30] Chuan-De Wu, Can-Zhong Lu, Hong-Hui Zhuang, and Jin-Shun Huang. Hydrothermal Assembly of a Novel Three-Dimensional Framework Formed by [GdMo12O42]9- Anions and Nine Coordinated GdIII Cations. *J. Am. Chem. Soc.*, **124**: 3836–3837, 2002. DOI: 10.1021/ja017782w (see **page** 6)

[31] P.C. Burns, K.M. Deely, and L.A. Hayden. The crystal chemistry of the zippeite group. *Can. Mineral.*, **41**: 687–706, 2003. (see **page** 7)

[32] P.C. Burns. A new uranyl sulfate chain in the structure of uranopilite. *Can. Mineral.*, **39**: 1139–1146, 2001. (see **page** 7)

[33] Karah E. Knope, Richard E. Wilson, S. Skanthakumar, and L. Soderholm. Synthesis and Characterization of Thorium(IV) Sulfates. *Inorg. Chem.*, **50**: 8621–8629, 2011. DOI: 10.1021/ic201175u (see **page** 7)

[34] Georg Lundgren and LarsGunnar Sillén. Die Kristallstruktur von Th (OH)2 CrO4 H2O. Die Th (OH)2-Kette, ein neues Strukturelement. *Naturwissenschaften*, **36**: 345–346, 1949. DOI: 10.1007/BF00596797 (see **page** 7)

[35] Tyler A. Sullens, Philip M. Almond, Jessica A. Byrd, James V. Beitz, Travis H. Bray, and Thomas E. Albrecht-Schmitt. Extended networks, porous sheets, and chiral frameworks. Thorium materials containing mixed geometry anions: Structures and properties of Th(SeO3)(SeO4), Th(IO3)2(SeO4)(H2O)3H2O, and Th(CrO4)(IO3)2. *J. Solid State Chem.*, **179**: 1192–1201, 2006. DOI: 10.1016/j.jssc.2006.01.017 (see **pages** 7, 53)

[36] R. W. M. D'Eye, P. G. Sellman, and J. R. Murray. 485. The thorium-selenium system. *J. Chem. Soc.*, 2555–2562, 1952. (see **page** 7)

[37] RV Gaines. CLIFFORDITE-A NEW TELLURITE MINERAL FROM MOCTEZUMA. *Am. Mineral.*, **54**: 697–701, 1969. (see **page** 7)

[38] G. Meunier and J. Galy. Structure cristalline de la schmitterite synthetique UTeO5. *Acta Crystallogr., Sect. B: Struct. Sci*, **29**: 1251–1255, 1973. DOI: 10.1107/S0567740873004334 (see **page** 7)

[39] Kang Min Ok and P. Shiv Halasyamani. New Selenites: Syntheses, Structures, and Characterization of Centrosymmetric Al2(Se2O5)3 and Ga2(Se2O5)3 and Non-centrosymmetric In2(Se2O5)3. *Chem. Mater.*, **14**: 2360–2364, 2002. DOI: 10.1021/cm011694t (see **page** 8)

[40] Philip M. Almond, Michael L. McKee, and Thomas E. Albrecht-Schmitt. Unusual Uranyl Tellurites Containing [Te2O6]4 Ions and Three-Dimensional Networks. *Angew. Chem. Int. Ed.*, **41**: 3426–3429, 2002. (see **page** 8)

[41] J. D. Woodward, P. M. Almond, and T. E. Albrecht-Schmitt. Synthesis and crystal structures of the layered uranyl tellurites A(2)[(UO2)3(TeO3)(2)O-2] (A = K, Rb, Cs). *J. Solid State Chem.*, **177**: 3971–3976, 2004. DOI: 10.1016/j.jssc.2004.06.054 (see **page** 8)

[42] Jie Ling, Matthew Ward, and Peter C. Burns. Hydrothermal syntheses and structures of the uranyl tellurates AgUO2(HTeO5) and Pb2UO2(TeO6). *J. Solid State Chem.*, **184**: 401–404, 2011. DOI: 10.1016/j.jssc.2010.12.007 (see **page** 8)

[43] Sergey V. Krivovichev and Peter C. Burns. Synthesis and Structure of Ag6[(UO2)3O(MoO4)5]: A Novel Sheet of Triuranyl Clusters and MoO4 Tetrahedra. *Inorg. Chem.*, **41**: 4108–4110, 2002. DOI: 10.1021/ic025662z (see **pages** 8, 36)

[44] Alain Tabuteau and Monique Pages. Identification and crystal chemistry of double molybdates of alkali metals (K, Rb, Cs) and transuranium elements (Np, Pu, Am). *Journal of Inorganic and Nuclear Chemistry*, **42**: 401–403, 1980. (see **page** 8)

[45] A. Tabuteau, M. Pags, and W. Freundlich. Sur les phases de structure scheelite dans les systems molyboate de plutonium – Molybdate de lithium ou sodium. *Mater. Res. Bull.*, **7**: 691–697, 1972. (see **page** 8)

[46] J. THORET. Comparative-study of the Influence of the Substitution of A Earth-alkaline (calcium Or Strontium) By A Tetravalent Element (cerium, Thorium Or Uranium) On the Crystallographic and Dielectric-properties of Phases With the Tetragonal Tungsten Bronze Structure. *Comptes Rendus De L Academie Des Sciences Serie Ii*, **302**: 707–709, 1986. (see **page** 8)

[47] N.D. Dahale, Meera Keskar, and K.D. Singh Mudher. Structural and thermal studies on Na2Th(MoO4)3, Na2Pu(MoO4)3, Na4Th(MoO4)4 and Na4Pu(MoO4)4. *J. Alloys Compd.*, **415**: 244–250, 2006. DOI: `10.1016/j.jallcom.2005.07.066` (see **pages** 8, 40)

[48] Paolo Orlandi, Cristian Biagioni, Luca Bindi, and Stefano Merlino. Nuragheite, Th (MoO4) 2 H2O, The Second Natural Thorium Molybdate And Its Relationships To Ichnusaite And Synthetic Th (MoO4) 2. *Am. Mineral.*, **100**: 267–273, 2015. (see **pages** 9, 21)

[49] Paolo Orlandi, Cristian Biagioni, Luca Bindi, and Fabrizio Nestola. Ichnusaite, Th (MoO4) 2 3H2O, the first natural thorium molybdate: Occurrence, description, and crystal structure. *Am. Mineral.*, **99**: 2089–2094, 2014. (see **pages** 9, 21)

[50] Evgeny V. Alekseev, Sergey V. Krivovichev, Wulf Depmeier, Oleg I. Siidra, Karsten Knorr, Evgeny V. Suleimanov, and Evgeny V. Chuprunov. Na2Li8[(UO2)(11)O-12(WO5)(2)]: Three different uranyl-ion coordination geometries and cation-cation interactions. *Angew. Chem. Int. Ed.*, **45**: 7233–7235, 2006. DOI: `10.1002/anie.200601207` (see **page** 9)

[51] Andrey N. Seliverstov, Evgeny V. Suleimanov, Evgeny V. Chuprunov, Nikolay V. Somov, Elena M. Zhuchkova, Maxim I. Lelet, Konstantin B. Rozov, Wulf Depmeier, Sergey V. Krivovichev, and Evgeny V. Alekseev. Polytypism and oxo-tungstate polyhedra polymerization in novel complex uranyl tungstates. *Dalton Trans.*, **41**: 8512–8514, 2012. DOI: `10.1039/c2dt31000g` (see **page** 9)

[52] F. Albert Cotton and Sanjay K. Mandal. New halogen-bridged dinuclear edge-sharing and face-sharing bioctahedral tungsten(III) complexes, W2X6(PR3)n, where X = Cl or Br, PR3 = PMe3, PMe2Ph, PBu3, and n = 4 or 3: crystal structures of W2Cl6(PMe2Ph)4, W2Cl6(PMe2Ph)3 and W2Br6(PMe2Ph)3. *Inorg. Chem.*, **31**: 1267–1274, 1992. DOI: `10.1021/ic00033a026` (see **page** 9)

[53] Shuao Wang, Evgeny V. Alekseev, Jared T. Stritzinger, Wulf Depmeier, and Thomas E. Albrecht-Schmitt. Crystal Chemistry of the Potassium and Rubidium Uranyl Borate Families Derived from Boric Acid Fluxes. *Inorg. Chem.*, **49**: 6690–6696, 2010. DOI: `10.1021/ic100728s` (see **page** 12)

[54] Shuao Wang, Evgeny V. Alekseev, Jie Ling, S. Skanthakumar, L. Soderholm, Wulf Depmeier, and Thomas E. Albrecht-Schmitt. Neptunium Diverges Sharply from Uranium and Plutonium in Crystalline Borate Matrixes: Insights into the Complex Behavior of the Early Actinides Relevant to Nuclear Waste Storage. *Angew. Chem. Int. Ed.*, **49**: 1263–1266, 2010. DOI: `10.1002/anie.200906127` (see **page** 12)

[55] Shuao Wang, Evgeny V. Alekseev, Hannah M. Miller, Wulf Depmeier, and Thomas E. Albrecht-Schmitt. Boronic Acid Flux Synthesis and Crystal Growth of Uranium and Neptunium Boronates and Borates: A Low-Temperature Route to the First Neptunium(V) Borate. *Inorg. Chem.*, **49**: 9755–9757, 2010. DOI: `10.1021/ic101678d` (see **page** 12)

[56] Shuao Wang, Evgeny V. Alekseev, Jared T. Stritzinger, Wulf Depmeier, and Thomas E. Albrecht-Schmitt. How are Centrosymmetric and Noncentrosymmetric Structures Achieved in Uranyl Borates? *Inorg. Chem.*, **49**: 2948–2953, 2010. DOI: `10.1021/ic902480n` (see **page** 12)

[57] Shuao Wang, Evgeny V. Alekseev, Juan Diwu, William H. Casey, Brian L. Phillips, Wulf Depmeier, and Thomas E. Albrecht-Schmitt. NDTB-1: A Supertetrahedral Cationic Framework That Removes TcO4- from Solution. *Angew. Chem. Int. Ed.*, **49**: 1057–1060, 2010. DOI: `10.1002/anie.200906397` (see **page** 12)

[58] Shijun Wu, Shuao Wang, Matthew Polinski, Oliver Beermann, Philip Kegler, Thomas Malcherek, Astrid Holzheid, Wulf Depmeier, Dirk Bosbach, Thomas E. Abrecht-Schmitt, and Evgeny V. Alekseev. High Structural Complexity of Potassium Uranyl Borates Derived from High-Temperature/High-Pressure Reactions. *Inorg. Chem.*, **52**: 5110–5118, 2013. DOI: `10.1021/ic400016z` (see **page** 13)

[59] Na Yu, Vladislav V. Klepov, Philip Kegler, Dirk Bosbach, Thomas E. Albrecht-Schmitt, and Evgeny V. Alekseev. Th(AsIII4AsV4O18): a Mixed-Valent Oxoarsenic(III)/arsenic(V) Actinide Compound Obtained under Extreme Conditions. *Inorg. Chem.*, **53**: 8194–8196, 2014. DOI: `10.1021/ic5013704` (see **page** 14)

[60] Shijun Wu, Matthew J. Polinski, Thomas Malcherek, Ulrich Bismayer, Martina Klinkenberg, Giuseppe Modolo, Dirk Bosbach, Wulf Depmeier, Thomas E. Albrecht-Schmitt, and Evgeny V. Alekseev. Novel Fundamental Building Blocks and Site Dependent Isomorphism in the First Actinide Borophosphates. *Inorg. Chem.*, **52**: 7881–7888, 2013. DOI: `10.1021/ic400214x` (see **page** 14)

[61] Mujid Kazimi. Thorium Fuel for Nuclear Energy An unconventional tactic might one day ease concerns that spent fuel could be used to make a bomb. *AmSci*, **91**: 408–15, 2003. (see **page** 17)

[62] Christy De Meyer, Francoise Bouree, John S. O. Evans, Klaartje De Buysser, Els Bruneel, Isabel Van Driessche, and Serge Hoste. Structure and phase transition of Sn-substituted Zr(1-x)SnxW2O8. *J. Mater. Chem.*, **14**: 2988–2994, 2004. (see **page** 18)

[63] Prangya Parimita Sahoo, Sumithra S., Giridhar Madras, and T. N. Guru Row. Synthesis, Characterization, and Photocatalytic Properties of ZrMo2O8. *J. Phys. Chem. C*, **113**: 10661–10666, 2009. DOI: `10.1021/jp901897s` (see **page** 18)

[64] F. Monroy-Guzmn, L.V. Daz-Archundia, and A. Contreras Ramrez. Effect of Zr:Mo ratio on 99mTc generator performance based on zirconium molybdate gels. *Applied Radiation and Isotopes*, **59**: 27 –34, 2003. DOI: `http://dx.doi.org/10.1016/S0969-8043(03)00150-7` (see **page** 18)

[65] R.F. Klevtsova, Zh.G. Bazarova, L.A. Glinskaya, V.I. Alekseev, S.I. Arkhincheeva, B.G. Bazarov, P.V. Klevtsov, and K.N. Fedorov. Synthesis of ternary potassium, magnesium, and zirconium molybdates. The crystal structure of K5(Mg0.5Zr1.5)(MoO4)6. **35**: 286–290–, 1994. (see **page** 18)

[66] T. A. Mary, J. S. O. Evans, T. Vogt, and A. W. Sleight. Negative Thermal Expansion from 0.3 to 1050 Kelvin in ZrW2O8. *Science*, **272**: 90–92, 1996. DOI: `10.1126/science.272.5258.90` (see **page** 18)

[67] J. D. Jorgensen, M. A. Beno, D. G. Hinks, L. Soderholm, K. J. Volin, R. L. Hitterman, J. D. Grace, Ivan K. Schuller, C. U. Segre, K. Zhang, and M. S. Kleefisch. Oxygen ordering and the orthorhombic-to-tetragonal phase transition in YBa2Cu3O7x. *Phys. Rev. B*, **36**: 3608–3616, 1987. (see **page** 18)

[68] Simon Allen, Rebecca J. Ward, Matthew R. Hampson, Richard K. B. Gover, and John S. O. Evans. Structures and phase transitions of trigonal ZrMo2O8 and HfMo2O8. *Acta Crystallogr., Sect. B: Struct. Sci*, **60**: 32–40, 2004. DOI: `10.1107/S0108768103025138` (see **page** 18)

[69] Bin Xiao, Thorsten M. Gesing, Lars Robben, Dirk Bosbach, and Evgeny V. Alekseev. Dinuclear Face-Sharing Bi-octahedral Tungsten(VI) Core and Unusual Thermal Behavior in Complex Th Tungstates. *Chem. Eur. J.*, **21**: 7746–7754, 2015. (see **page** 19)

[70] Bin Xiao, Thorsten M. Gesing, Philip Kegler, Giuseppe Modolo, Dirk Bosbach, Hartmut Schlenz, Evgeny V. Suleimanov, and Evgeny V. Alekseev. High-Temperature Phase Transitions, Spectroscopic Properties, and Dimensionality Reduction in Rubidium Thorium Molybdate Family. *Inorg. Chem.*, **53**: 3088–3098, 2014. DOI: `10.1021/ic403003f` (see **page** 19)

[71] Bin Xiao, Jakob Dellen, Hartmut Schlenz, Dirk Bosbach, Evgeny V. Suleimanov, and Evgeny V. Alekseev. Unexpected Structural Complexity in Cesium Thorium Molybdates. *Cryst. Growth Des.*, **14**: 2677–2684, 2014. DOI: `10.1021/cg500418e` (see **pages** 19, 21)

[72] NE Brese and M O'keeffe. Bond-valence parameters for solids. *Acta Crystallographica Section B: Structural Science*, **47**: 192–197, 1991. (see **page** 20)

[73] T. L. Cremers, P. G. Eller, and R. A. Penneman. Orthorhombic thorium(IV) molybdate, Th(MoO4)2. *Acta Crystallogr., Sect. C: Cryst. Struct. Commun.*, **39**: 1165–1167, 1983. DOI: `10.1107/S0108270183007775` (see **page** 21)

[74] Geng Bang Jin and L. Soderholm. Syntheses and single-crystal structures of CsTh(MoO4)2Cl and Na4Th(WO4)4. *J. Solid State Chem.*, **184**: 337–342, 2011. DOI: `10.1016/j.jssc.2010.12.003` (see **page** 21)

[75] D.V. Pushkin, E.V. Peresypkina, L.B. Serezhkina, A.V. Savchenkov, A.V. Virovets, and V.N. Serezhkin. Synthesis and study of (CN3H6)2[(UO2)2(C2O4)(SeO3)2] by IR spectroscopy and X-ray diffraction. *Russ. J. Inorg. Chem.*, **57**: 175–180, 2012. (see **page** 25)

[76] V.P. Mahadevan Pillai, T. Pradeep, M.J. Bushiri, R.S. Jayasree, and V.U. Nayar. Vibrational spectroscopic studies of FeClMoO4, Na2MoO4 and Na2MoO42H2O/D2O. *Spectrochim. Acta, Part A*, **53**: 867–876, 1997. (see **pages** 33, 153)

[77] Christopher C. Underwood, Matthew Mann, Colin D. McMillen, and Joseph W. Kolis. Hydrothermal Descriptive Chemistry and Single Crystal Structure Determination of Cesium and Rubidium Thorium Fluorides. *Inorg. Chem.*, **50**: 11825–11831, 2011. DOI: `10.1021/ic2019555` (see **page** 36)

[78] Evgeny V. Suleimanov, Aleksey V. Golubev, Evgeny V. Alekseev, Charles A. Geiger, Wulf Depmeier, and Vladimir G. Krivovichev. A calorimetric and thermodynamic investigation of uranyl molybdate UO2MoO4. *J. Chem. Thermodyn.*, **42**: 873–878, 2010. DOI: `10.1016/j.jct.2010.02.011` (see **page** 36)

[79] M. Huyghe, M.-R. Lee, S. Jaulmes, and M. Quarton. Structure de K8Th(MoO4)6. *Acta Crystallogr., Sect. C: Cryst. Struct. Commun.*, **49**: 950–954, 1993. DOI: `10.1107/S0108270192012204` (see **page** 38)

[80] M. Huyghe, M.-R. Lee, M. Quarton, and F. Robert. Structure cristalline de K2Th(MoO4)3. *Acta Crystallogr., Sect. C: Cryst. Struct. Commun.*, **47**: 244–246, 1991. DOI: `10.1107/S0108270190008435` (see **page** 39)

[81] Yi Yu, Yisheng Huang, Lizhen Zhang, Zhoubin Lin, and Guofu Wang. Growth and Spectral Assessment of Yb3+-Doped KBaGd(MoO4)3 Crystal: A Candidate for Ultrashort Pulse and Tunable Lasers. *PLoS ONE*, **8**: e54450, 2013. DOI: `10.1371/journal.pone.0054450` (see **page** 39)

[82] C. de Mello Donega, M.J.D. Crombag, A. Meijerink, and G. Blasse. Vibronic transitions in the luminescence spectra of Pr3+ in Na5La(MoO4)4. *Journal of Luminescence*, **6061**: International Conference on Luminescence, 74 –77, 1994. DOI: `http://dx.doi.org/10.1016/0022-2313(94)90097-3` (see **page** 41)

[83] S Launay, S Jaulmes, F Lucas, and MLong Quarton. Cu2Th4(MoO4)9: Un nouveau squelette structural. *J. Solid State Chem.*, **136**: 199–205, 1998. DOI: `10.1006/jssc.1997.7678` (see **page** 42)

[84] Jeffrey R. Long, Logan S. McCarty, and R. H. Holm. A Solid-State Route to Molecular Clusters: Access to the Solution Chemistry of [Re6Q8]2+ (Q = S, Se) Core-Containing Clusters via Dimensional Reduction. *J. Am. Chem. Soc.*, **118**: 4603–4616, 1996. DOI: `10.1021/ja960216u` (see **page** 42)

[85] Evgeny V. Alekseev, Sergey V. Krivovichev, Thomas Armbruster, Wulf Depmeier, Evgeny V. Suleimanov, Evgeny V. Chuprunov, and Alexei V. Golubev. Dimensional reduction in alkali metal uranyl molybdates: Synthesis and structure of Cs-2[(UO2)O(MoO4)]. *Z. Anorg. Allg. Chem.*, **633**: 1979–1984, 2007. DOI: `10.1002/zaac.200700270` (see **page** 43)

[86] D. L. Rousseau, R. P. Bauman, and S. P. S. Porto. Normal mode determination in crystals. *J. Raman Spectrosc.*, **10**: 253–290, 1981. (see **page** 43)

[87] Jr. Barker A. S. Infrared Lattice Vibrations in Calcium Tungstate and Calcium Molybdate. *Phys. Rev.*, **135**: A742–A747, 1964. (see **page** 44)

[88] S. A. Klimin, M. N. Popova, B. N. Mavrin, P. H. M. van Loosdrecht, L. E. Svistov, A. I. Smirnov, L. A. Prozorova, H.-A. Krug von Nidda, Z. Seidov, A. Loidl, A. Ya. Shapiro, and L. N. Demianets. Structural phase transition in the two-dimensional triangular lattice antiferromagnet RbFe(MoO4)2. *Phys. Rev. B*, **68**: 174408–, 2003. (see **page** 46)

[89] Franklin D. Hardcastle and Israel E. Wachs. Determination of molybdenum-oxygen bond distances and bond orders by Raman spectroscopy. *J. Raman Spectrosc.*, **21**: 683–691, 1990. (see **page** 47)

[90] Miguel A. Salvad, Pilar Pertierra, Anatoly I. Bortun, Camino Trobajo, and José R. Garca. New Hydrothermal Synthesis and Structure of Th2(PO4)2(HPO4)H2O:the First Structurally Characterized Thorium Hydrogenphosphate. *Inorg. Chem.*, **44**: 3512–3517, 2005. DOI: `10.1021/ic048216f` (see **page** 52)

[91] Olga D. Chimitova, Victor V. Atuchin, Bair G. Bazarov, Maxim S. Molokeev, and Zhibzema G. Bazarova. The formation and structural parameters of new double molybdates RbLn(MoO4)2 (Ln = Pr, Nd, Sm, Eu). *Proc. SPIE*, **8771**: 87711A–87711A–9, 2013. DOI: `10.1117/12.2017816` (see **page** 52)

[92] T. A. Sullens and T. E. Albrecht-Schmitt. Structure and properties of the thorium vanadyl tellurate, Th(VO2)2 (TeO6)(H2O)2. *Inorg. Chem.*, **44**: 2282–2286, 2005. DOI: `10.1021/IC048256j` (see **page** 53)

[93] R. D. Shannon. Revised effective ionic radii and systematic studies of interatomic distances in halides and chalcogenides. *Acta Cryst. A*, **32**: 751–767, 1976. (see **page** 55)

[94] G.D. Saraiva, W. Paraguassu, P.T.C. Freire, M. Maczka, and J. Mendes Filho. Temperature-dependent Raman scattering study of K2MoO4. *Vib. Spectrosc.*, **58**: 87–94, 2012. (see **page** 56)

[95] S. P. S. Porto and J. F. Scott. Raman Spectra of CaWO4, SrWO4, CaMoO4, and SrMoO4. *Phys. Rev.*, **157**: 716–719, 1967. (see **page** 56)

[96] BN Ganguly, Frank G Ullman, Roger D Kirby, and John R Hardy. Raman spectrum of gadolinium molybdate at 80 K. *Phys. Rev. B*, **13**: 1344, 1976. (see **page** 57)

[97] Linus Pauling. *J. Am. Chem. Soc.*, **51**: 1010, 1929. (see **page** 70)

[98] Tyler A. Sullens, Philip M. Almond, Jessica A. Byrd, James V. Beitz, Travis H. Bray, and Thomas E. Albrecht-Schmitt. Extended networks, porous sheets, and chiral frameworks. Thorium materials containing mixed geometry anions: Structures and properties of Th(SeO3)(SeO4), Th(IO3)2(SeO4)(H2O)3·H2O, and Th(CrO4)(IO3)2. *J. Solid State Chem.*, **179**: 1192–1201, 2006. (see **pages** 72, 77)

[99] Said Yagoubi, Lahcen El Ammari, Abderrazzak Assani, and Mohamed Saadi. Thorium divanadate dihydrate, Th(V2O7)(H2O)2. *Acta Crystallogr. Sect. E*, **67**: i60, 2011. DOI: `10.1107/S1600536811039584` (see **page** 72)

[100] Sergey V. Krivovichev, Volker Kahlenberg, Reinhard Kaindl, Edgar Mersdorf, Ivan G. Tananaev, and Boris F. Myasoedov. Nanoscale Tubules in Uranyl Selenates. *Angew. Chem. Int. Ed.*, **117**: 1158–1160, 2005. (see **pages** 72, 107, 116)

[101] S Scavnicar and B Prodic. The crystal structure of double nitrate octahydrates of thorium and bivalent metals. *Acta Crystallogr.*, **18**: 698–702, 1965. (see **page** 73)

[102] MR Spirlet, J Rebizant, C Apostolidis, B Kanellakopulos, and E Dornberger. Structure of bis (ammonium) hexanitratoplutonium (IV) and bis (ammonium) hexanitratothorium (V). *Acta Crystallogr., Sect. C: Cryst. Struct. Commun.*, **48**: 1161–1164, 1992. (see **page** 73)

[103] P Charpin, G Chevrier, M Lance, M Nierlich, D Vigner, J Livet, and C Musikas. Structure du nitrate de thorium (IV) tetrahydrate. *Acta Crystallogr., Sect. C: Cryst. Struct. Commun.*, **43**: 1239–1241, 1987. (see **page** 73)

[104] JC Taylor, MH Mueller, and RL Hitterman. Crystal structure of thorium nitrate pentahydrate by neutron diffraction. *Acta Crystallogr.*, **20**: 842–851, 1966. (see **page** 73)

[105] Bin Xiao, Jakob Dellen, Hartmut Schlenz, Dirk Bosbach, Evgeny V. Suleimanov, and Evgeny V. Alekseev. Unexpected Structural Complexity in Cesium Thorium Molybdates. *Cryst. Growth Des.*, **14**: 2677–2684, 2014. DOI: `10.1021/cg500418e` (see **pages** 74, 78, 85, 107, 117, 149)

[106] NE Brese and M O'keeffe. Bond-valence parameters for solids. *Acta Crystallographica Section B: Structural Science*, **47**: 192–197, 1991. (see **pages** 76, 78, 87)

[107] Georg Lundgren and Lars Gunnar Sillén. Die Kristallstruktur von Th (OH) 2 CrO 4 H 2 O. Die Th (OH) 2-Kette, ein neues Strukturelement. *Naturwissenschaften*, **36**: 345–346, 1949. (see **pages** 76, 77)

[108] Tyler A. Sullens and Thomas E. Albrecht-Schmitt. Thorium(IV) chromate(VI) monohydrate. *Acta Crystallogr. Sect. E: Struct. Rep. Online*, **62**: I258–I260, 2006. DOI: `10.1107/S1600536806047416` (see **pages** 76, 77)

[109] Richard E. Wilson, S. Skanthakumar, Karah E. Knope, Christopher L. Cahill, and L. Soderholm. An Open-Framework Thorium Sulfate Hydrate with 11.5 Voids. *Inorg. Chem.*, **47**: 9321–9326, 2008. DOI: `10.1021/ic800931f` (see **page** 78)

[110] Tyler A. Sullens and Thomas E. Albrecht-Schmitt. Structure and Properties of the Thorium Vanadyl Tellurate, Th(VO2)2 (TeO6)(H2O)2. *Inorg. Chem.*, **44**: 2282–2286, 2005. DOI: `10.1021/ic048256j` (see **pages** 78, 79, 85, 94)

[111] S. V. Krivovichev, C. L. Cahill, and P. C. Burns. A Novel Open Framework Uranyl Molybdate: Synthesis and Structure of (NH4)4[(UO2)5(MoO4)7](H2O)5. *Inorg. Chem.*, **42**: 2459–2464, 2003. DOI: `10.1021/ic020516e` (see **pages** 78, 117)

[112] S. Launay, S. Jaulmes, F. Lucas, and M. Quarton. Cu2Th4(MoO4)9: Un nouveau squelette structural. *J. Solid State Chem.*, **136**: 199–205, 1998. (see **page** 80)

[113] A. Guesdon and B. Raveau. A Series of Mo(VI) Monophosphates Involving the Lone Pair Cation Te(IV):A2TeMo2O6 (PO4)2 (A = K, Rb, Tl, Cs). *Chem. Mater.*, **12**: 2239–2243, 2000. DOI: `10.1021/cm000035y` (see **pages** 81, 112, 123)

[114] Joanna Goodey, Jake Broussard, and P. Shiv Halasyamani. Synthesis, Structure, and Characterization of a New Second-Harmonic-Generating Tellurite: Na2TeW2O9. *Chem. Mater.*, **14**: 3174–3180, 2002. DOI: `10.1021/cm020087i` (see **pages** 81, 122, 123, 125)

[115] Eun Ok Chi, Kang Min Ok, Yetta Porter, and P. Shiv Halasyamani. Na2Te3Mo3O16: A New Molybdenum Tellurite with Second-Harmonic Generating and Pyroelectric Properties. *Chem. Mater.*, **18**: 2070–2074, 2006. DOI: `10.1021/cm052614e` (see **pages** 81, 123)

[116] Jun-Ho Kim, Jaewook Baek, and P. Shiv Halasyamani. (NH4)2Te2WO8: A New Polar Oxide with Second-Harmonic Generating, Ferroelectric, and Pyroelectric Properties. *Chem. Mater.*, **19**: 5637–5641, 2007. DOI: `10.1021/cm7019334` (see **pages** 81, 122, 123)

[117] Weiguo Zhang, Feng Li, Sang-Hwan Kim, and P. Shiv Halasyamani. Top-Seeded Solution Crystal Growth and Functional Properties of a Polar Material–Na2TeW2O9. *Cryst. Growth Des.*, **10**: 4091–4095, 2010. DOI: `10.1021/cg100762b` (see **pages** 81, 123)

[118] Junjie Zhang, Zhonghan Zhang, Youxuan Sun, Chengqian Zhang, and Xutang Tao. Bulk crystal growth and characterization of a new polar polymorph of BaTeMo2O9: alpha-BaTeMo2O9. *CrystEngComm*, **13**: 6985–6990, 2011. (see **pages** 81, 122, 123)

[119] Philip M. Almond and Thomas E. Albrecht-Schmitt. Hydrothermal Syntheses, Structures, and Properties of the New Uranyl Selenites Ag2(UO2)(SeO3)2, M[(UO2)(HSeO3)(SeO3)] (M = K, Rb, Cs, Tl), and Pb(UO2)(SeO3)2. *Inorg. Chem.*, **41**: 1177–1183, 2002. DOI: `10.1021/ic0110732` (see **pages** 82, 85–87)

[120] Philip M. Almond and Thomas E. Albrecht-Schmitt. Do Secondary and Tertiary Ammonium Cations Act as Structure-Directing Agents in the Formation of Layered Uranyl Selenites? *Inorg. Chem.*, **42**: 5693–5698, 2003. DOI: `10.1021/ic034308d` (see **page** 82)

[121] Fang Kong, Shu-Ping Huang, Zhong-Ming Sun, Jiang-Gao Mao, and Wen-Dan Cheng. Se2(B2O7): A New Type of Second-Order NLO Material. *J. Am. Chem. Soc.*, **128**: 7750–7751, 2006. DOI: `10.1021/ja0620991` (see **page** 82)

[122] Hyejin Kim, Yoonsuk Cho, Hoseop Yun, and Junghwan Do. Hydrothermal synthesis of a new vanadium tellurate(VI) with a novel chain structure: (NH4)(4)(VO2)(2)[Te2O8(OH)(2)]center dot 2H(2)O. *Z. Anorg. Allg. Chem.*, **633**: 473–477, 2007. (see **pages** 82, 97)

[123] M. K. Kim, S. H. Kim, H. Y. Chang, P. S. Halasyamani, and K. M. Ok. New Noncentrosymmetric Tellurite Phosphate Material: Synthesis, Characterization, and Calculations of Te2O(PO4)(2). *Inorg. Chem.*, **49**: 7028–7034, 2010. (see **pages** 82, 103, 115)

[124] Song Ping Huang and Mercouri G. Kanatzidis. [Ru6(Te2)7(CO)12]2-: hydrothermal synthesis of a novel ruthenium-tellurium Ru2+/Te22- cluster and its relationship to RuTe2. *J. Am. Chem. Soc.*, **114**: 5477–5478, 1992. DOI: `10.1021/ja00039a099` (see **page** 82)

[125] Yu I. Smolin, Yu F. Shepelev, A. E. Lapshin, and E. A. Vasilłva. Structure of selenium and tellurium clusters in cavities of NaX zeolite. *Crystallogr. Rep.*, **45**: 21–25, 2000. DOI: `10.1134/1.171130` (see **page** 82)

[126] M. P. Minimol and K. Vidyasagar. Hydrothermal synthesis and characterization of new one-dimensional tellurates, A(2)[Te3O8(OH)(4)] (A = Cs, Rb, K, Na). *Indian Journal of Chemistry Section A-inorganic Bio-inorganic Physical Theoretical; Analytical Chemistry*, **42**: 2244–2249, 2003. (see **pages** 82, 118)

[127] Kang Min Ok and P. Shiv Halasyamani. Synthesis, structure, and characterization of a new one-dimensional tellurite phosphate, Ba2TeO(PO4)2. *J. Solid State Chem.*, **179**: 1345–1350, 2006. (see **pages** 82, 95)

[128] T. Sivakumar, Kang Min Ok, and P. Shiv Halasyamani. Synthesis, Structure, and Characterization of Novel Two- and Three-Dimensional Vanadates: Ba2.5(VO2)3(SeO3)4·H2O and La(VO2)3(TeO6)·3H2O. *Inorg. Chem.*, **45**: 3602–3605, 2006. DOI: `10.1021/ic052103u` (see **page** 82)

[129] Jian Lin, Juan Diwu, Justin N. Cross, Eric M. Villa, and Thomas E. Albrecht-Schmitt. Cerium(IV) Tellurite Halides [Ce2Te7O17]X2 (X = Cl- or Br-): The First Cerium-Containing Cationic Frameworks. *Inorg. Chem.*, **51**: 10083–10085, 2012. DOI: `10.1021/ic301628q` (see **pages** 82, 128)

[130] Shuao Wang, Evgeny V. Alekseev, Wulf Depmeier, and Thomas E. Albrecht-Schmitt. Further insights into intermediate- and mixed-valency in neptunium oxoanion compounds. *Chem. Commun.*, **46**: 3955–3957, 2010. (see **page** 83)

[131] Shuao Wang, Evgeny V. Alekseev, Juan Diwu, William H. Casey, Brian L. Phillips, Wulf Depmeier, and Thomas E. Albrecht-Schmitt. NDTB-1: A Supertetrahedral Cationic Framework That Removes TcO4- from Solution. *Angew. Chem. Int. Ed.*, **49**: 1057–1060, 2010. (see **page** 83)

[132] Shuao Wang, Evgeny V. Alekseev, Wulf Depmeier, and Thomas E. Albrecht-Schmitt. Recent progress in actinide borate chemistry. *Chem. Commun.*, **47**: 10874–10885, 2011. (see **page** 83)

[133] Shuao Wang, Evgeny V. Alekseev, Wulf Depmeier, and Thomas E. Albrecht-Schmitt. Surprising Coordination for Plutonium in the First Plutonium(III) Borate. *Inorg. Chem.*, **50**: 2079–2081, 2011. (see **page** 83)

[134] Shuao Wang, Evgeny V. Alekseev, Wulf Depmeier, and Thomas E. Albrecht-Schmitt. K(NpO2)3(H2O)Cl4: A Channel Structure Assembled by Two- and Three-Center Cation-Cation Interactions of Neptunyl Cations. *Inorg. Chem.*, **50**: 4692–4694, 2011. DOI: `10.1021/ic200549f` (see **pages** 83, 136)

[135] Shuao Wang, Evgeny V. Alekseev, Wulf Depmeier, and Thomas E. Albrecht-Schmitt. New Neptunium(V) Borates That Exhibit the Alexandrite Effect. *Inorg. Chem.*, **51**: 7–9, 2012. (see **page** 83)

[136] Karah E. Knope and L. Soderholm. Solution and Solid-State Structural Chemistry of Actinide Hydrates and Their Hydrolysis and Condensation Products. *Chem. Rev.*, –, 2012. DOI: `10.1021/cr300212f` (see **page** 83)

[137] C. Delage, A. Carpy, A. H'Naifi, and M. Goursolle. Structure du seleniate(IV) de cerium. *Acta Crystallogr., Sect. C*, **42**: 1475–1477, 1986. DOI: `doi:10.1107/S0108270186091795` (see **pages** 85, 93)

[138] Steffen F. Meier, Frank A. Weber, Roger J. Glser, and Thomas Schleid. Einkristalle des Cer(IV)xotellurats(IV) CeTe2O6. *Z. Anorg. Allg. Chem.*, **627**: 2448–2450, 2001. DOI: `10.1002/1521-3749(200111)627:11<2448::aid-zaac2448>3.0.co;2-e` (see **pages** 85, 93)

[139] K. Krishnan, K. D. S. Mudher, and V. Venugopal. Structural and thermal studies on PuTe2O6. *J. Alloys Compd.*, **307**: 114–118, 2000. DOI: `http://dx.doi.org/10.1016/S0925-8388(00)00841-0` (see **pages** 85, 93)

[140] Travis H. Bray, S. Skanthakumar, L. Soderholm, Richard E. Sykora, Richard G. Haire, and Thomas E. Albrecht-Schmitt. Hydrothermal synthesis, structure, and magnetic properties of Pu(SeO3)2. *J. Solid State Chem.*, **181**: 493–498, 2008. DOI: `http://dx.doi.org/10.1016/j.jssc.2007.12.020` (see **pages** 85, 93)

[141] Bin Xiao, Thorsten M. Gesing, Philip Kegler, Giuseppe Modolo, Dirk Bosbach, Hartmut Schlenz, Evgeny V. Suleimanov, and Evgeny V. Alekseev. High-Temperature Phase Transitions, Spectroscopic Properties, and Dimensionality Reduction in Rubidium Thorium Molybdate Family. *Inorg. Chem.*, **53**: 3088–3098, 2014. DOI: `10.1021/ic403003f` (see **pages** 85, 127, 128, 154)

[142] Jide Xu, Emil Radkov, Marco Ziegler, and Kenneth N. Raymond. Plutonium(IV) Sequestration: Structural and Thermodynamic Evaluation of the Extraordinarily Stable Cerium(IV) Hydroxypyridinonate Complexes1. *Inorg. Chem.*, **39**: 4156–4164, 2000. DOI: `10.1021/ic000063i` (see **page** 85)

[143] Geng Bang Jin and L. Soderholm. Syntheses and single-crystal structures of CsTh(MoO4)2Cl and Na4Th(WO4)4. *J. Solid State Chem.*, **184**: 337–342, 2011. (see **pages** 85, 125)

[144] Philip M. Almond, Shane M. Peper, Eric Bakker, and Thomas E. Albrecht-Schmitt. Variable Dimensionality and New Uranium Oxide Topologies in the Alkaline-Earth Metal Uranyl Selenites AE[(UO2)(SeO3)2] (AE=Ca, Ba) and Sr[(UO2)(SeO3)2] · 2H2O. *J. Solid State Chem.*, **168**: 358–366, 2002. (see **pages** 85–87)

[145] G. Lundgren. *Arkiv foer Kemi*, **5**: 349–363, 1952. (see **page** 88)

[146] G Lundgren. The crystal structure of Ce6O4 (OH) 4 (SO4) 6. *Arkiv for Kemi*, **10**: 183–197, 1956. (see **page** 88)

[147] Monica Vasiliu, Karah E. Knope, L. Soderholm, and David A. Dixon. Spectroscopic and Energetic Properties of Thorium(IV) Molecular Clusters with a Hexanuclear Core. *J. Phys. Chem. A*, **116**: 6917–6926, 2012. DOI: `10.1021/jp303493t` (see **page** 88)

[148] Karah E. Knope, Richard E. Wilson, Monica Vasiliu, David A. Dixon, and L. Soderholm. Thorium(IV) Molecular Clusters with a Hexanuclear Th Core. *Inorg. Chem.*, **50**: 9696–9704, 2011. DOI: `10.1021/ic2014946` (see **page** 89)

[149] Shinobu Takao, Koichiro Takao, Werner Kraus, Franziska Emmerling, Andreas C. Scheinost, Gert Bernhard, and Christoph Hennig. First Hexanuclear UIV and ThIV Formate Complexes - Structure and Stability Range in Aqueous Solution. *Eur. J. Inorg. Chem.*, **2009**: 4771–4775, 2009. (see **page** 89)

[150] Christoph Hennig, Shinobu Takao, Koichiro Takao, Stephan Weiss, Werner Kraus, Franziska Emmerling, and Andreas C. Scheinost. Structure and stability range of a hexanuclear Th(iv)-glycine complex. *Dalton Trans.*, **41**: 12818–12823, 2012. DOI: `10.1039/c2dt31367g` (see **page** 89)

[151] Karah E. Knope and L. Soderholm. Plutonium(IV) Cluster with a Hexanuclear [Pu6(OH)4O4]12+ Core. *Inorg. Chem.*, **52**: 6770–6772, 2013. DOI: `10.1021/ic4007185` (see **page** 90)

[152] R. Ratheesh, G. Suresh, M. J. Bushiri, and V. U. Nayar. Infrared and polarized Raman spectra of Cu(HSeO3)2 · H2O single crystal. *Spectrochim. Acta, Part A*, **51**: 1509–1515, 1995. (see **pages** 90, 132)

[153] Laurie L. Dussack, William T. A. Harrison, and Allan J. Jacobson. Hydrothermal syntheses and characterization of two layered molybdenum selenites, Rb2(MoO3)3SeO3 and Tl2MoO3)3SeO3. *Mater. Res. Bull.*, **31**: 249–255, 1996. (see **pages** 90, 132)

[154] D. L. Rousseau, R. P. Bauman, and S. P. S. Porto. Normal mode determination in crystals. *J. Raman Spectrosc.*, **10**: 253–290, 1981. (see **pages** 90, 143, 153)

[155] C. A. Cody, R. C. Levitt, Rampur S. Viswanath, and Philip J. Miller. Vibrational spectra of alkali hydrogen selenites, selenous acid, and their deuterated analogs. *J. Solid State Chem.*, **26**: 281–291, 1978. (see **page** 90)

[156] Ray L. Frost and Eloise C. Keeffe. Raman spectroscopic study of the selenite mineral mandarinoite Fe2Se3O9·6H2O. *J. Raman Spectrosc.*, **40**: 42–45, 2009. (see **page** 90)

[157] B. L. Khandelwal and V. P. Verma. Liquid-liquid distribution, spectrophotometric, thermal, IR and Raman studies on selenito uranylates. *J. Inorg. Nucl. Chem.*, **38**: 763–769, 1976. (see **page** 90)

[158] Ray L. Frost and Eloise C. Keeffe. Raman spectroscopic study of the tellurite minerals: graemite CuTeO3·H2O and teineite CuTeO3·2H2O. *J. Raman Spectrosc.*, **40**: 128–132, 2009. (see **page** 90)

[159] K.-Y. Choi, P. Lemmens, and H. Berger. Critical spin dynamics of the S=1/2 spin chain compound CuSe2O5. *Phys. Rev. B*, **83**: 174413–, 2011. (see **page** 90)

[160] Geng Bang Jin, S Skanthakumar, and L Soderholm. Three New Sodium Neptunyl (V) Selenate Hydrates: Structures, Raman Spectroscopy, and Magnetism. *Inorg. Chem.*, **51**: 3220–3230, 2012. (see **page** 91)

[161] George Socrates and G Socrates. *Infrared and Raman characteristic group frequencies: tables and charts*. vol. 245 Wiley Chichester, 2001. (see **page** 91)

[162] Karah E. Knope, Monica Vasiliu, David A. Dixon, and L. Soderholm. Thorium(IV)-Selenate Clusters Containing an Octanuclear Th(IV) Hydroxide/Oxide Core. *Inorg. Chem.*, **51**: 4239–4249, 2012. DOI: `10.1021/ic202706s` (see **page** 91)

[163] Ray L. Frost, Ji ejka, and Marilla J. Dickfos. Raman spectroscopic study of the mineral guilleminite Ba(UO2)3 (SeO3)2(OH)4 3H2O. *J. Raman Spectrosc.*, **40**: 355–359, 2009. (see **page** 92)

[164] A. I. L. Botto and E. J. Baran. Darstellung und eigenschaften von CeTe2O6 und ThTe2O6, verbindungen mit einer neuen berstruktur des fluorit-typs. *Z. Anorg. Allg. Chem.*, **484**: 215–220, 1982. (see **page** 93)

[165] Bin Xiao, Eike Langer, Jakob Dellen, Hartmut Schlenz, Dirk Bosbach, Evgeny V. Suleimanov, and Evgeny V. Alekseev. Chemical and Structural Evolution in the Th-SeO32-/SeO42- System: from Simple Selenites to Cluster-Based Selenate Compounds. *Inorg. Chem.*, **54**: 3022–3030, 2015. DOI: `10.1021/acs.inorgchem.5b00133` (see **page** 93)

[166] SN Tripathi, SN Achary, and PN Namboodiri. X-ray powder diffraction studies of a new compound: Th 13 Te 24 O 74. *Powder Diffr.*, **17**: 32–36, 2002. (see **page** 93)

[167] Steffen F Meier and Thomas Schleid. Oxotellurate (IV) Der Lanthanide: I. Die Isotype Reihe M2Te4O11 (M= LaNd, SmYb)/Oxotellurates (Iv) of Lanthanides: I. The Isotopic Series M2Te4O11 (M= LaNd, SmYb). *Zeitschrift fr Naturforschung B*, **59**: 881–888, 2004. (see **page** 94)

[168] Jun-Ho Kim and P. Shiv Halasyamani. A rare multi-coordinate tellurite, NH4ATe4O9·2H2O (ARb or Cs): The occurrence of TeO3, TeO4, and TeO5 Polyhedra in the same material. *J. Solid State Chem.*, **181**: 2108–2112, 2008. (see **page** 95)

[169] Hai-Long Jiang, Fang Kong, and Jiang-Gao Mao. Synthesis, crystal and band structures, and optical properties of a new lanthanidelkaline earth tellurium (IV) oxide: La 2 Ba (Te 3 O 8)(TeO 3) 2. *J. Solid State Chem.*, **180**: 1764–1769, 2007. (see **page** 95)

[170] E. C. Kirby. In: *Recent Work on Toroidal and Other Exotic Fullerene Structures*. AlexandruT Balaban, ed. Chap. 8, 263–296. Springer US, 2002. DOI: `10.1007/0-306-46907-3_8` (see **page** 95)

[171] Shuao Wang, T. Gannon Parker, Daniel J. Grant, Juan Diwu, Evgeny V. Alekseev, Wulf Depmeier, Laura Gagliardi, and Thomas E. Albrecht-Schmitt. Elucidation of Tetraboric Acid with a New Borate Fundamental Building Block in a Chiral Uranyl Fluoroborate. *Inorg. Chem.*, **51**: 11211–11213, 2012. (see **pages** 96, 147)

[172] Shuao Wang, Evgeny V. Alekseev, Juan Diwu, Hannah M. Miller, Allen G. Oliver, Guokui Liu, Wulf Depmeier, and Thomas E. Albrecht-Schmitt. Functionalization of Borate Networks by the Incorporation of Fluoride: Syntheses, Crystal Structures, and Nonlinear Optical Properties of Novel Actinide Fluoroborates. *Chem. Mater.*, **23**: 2931–2939, 2011. (see **pages** 96, 148)

[173] Jie Ling, Matthew Ward, and Peter C. Burns. Hydrothermal syntheses and structures of the uranyl tellurates AgUO2(HTeO5) and Pb2UO2(TeO6). *J. Solid State Chem.*, **184**: 401–404, 2011. (see **pages** 97, 104, 116)

[174] J. Graham and A. D. Wadsley. A crystallographic examination of tungsten trioxide whiskers. *Acta Crystallogr.*, **14**: 379–383, 1961. DOI: `10.1107/S0365110X61001285` (see **page** 99)

[175] John T. Vaughey, William T. A. Harrison, Laurie L. Dussack, and Allan J. Jacobson. A New Layered Vanadium Selenium Oxide with a Structure Related to Hexagonal Tungsten Oxide: NH4(VO2)3(SeO3)2. *Inorg. Chem.*, **33**: 4370–4375, 1994. DOI: `10.1021/ic00097a027` (see **page** 99)

[176] N. D. Zakharov, P. Werner, I. P. Zibrov, V. P. Filonenko, and M. Sundberg. Intergrowth tungsten bronze structures of PrxWO3, formed at 50 kbar: An HRTEM study. *J. Solid State Chem.*, **147**: 536–544, 1999. (see **page** 99)

[177] Jeongho Yeon, Sang-Hwan Kim, and P. Shiv Halasyamani. A(3)V(5)O(14) (A = K+, Rb+, or TI+), New Polar Oxides with a Tetragonal Tungsten Bronze Related Structural Topology: Synthesis, Structure, and Functional Properties. *Inorg. Chem.*, **49**: 6986–6993, 2010. (see **page** 99)

[178] Michel Figlarz. New oxides in the WO3-MoO3 system. *Prog. Solid State Chem.*, **19**: 1–46, 1989. DOI: `http://dx.doi.org/10.1016/0079-6786(89)90005-8` (see **page** 99)

[179] A Hussain, R Gruehn, and CH Rscher. Crystal growth of alkali metal tungsten brozes M x WO 3 (M K, Rb, Cs), and their optical properties. *Journal of alloys and compounds*, **246**: 51–61, 1997. (see **page** 99)

[180] Peter C. Burns. U6+ minerals and inorganic compounds: insights into an expanded structural hierarchy of crystal structures. *Can. Mineral.*, **43**: 1839–1894, 2005. (see **pages** 100, 112)

[181] Evgeny V. Alekseev, Sergey V. Krivovichev, Thomas Armbruster, Wulf Depmeier, Evgeny V. Suleimanov, Evgeny V. Chuprunov, and Alexei V. Golubev. Dimensional reduction in alkali metal uranyl molybdates: Synthesis and structure of Cs-2[(UO2)O(MoO4)]. *Z. Anorg. Allg. Chem.*, **633**: 1979–1984, 2007. (see **page** 101)

[182] Evgeny V. Alekseev, Sergey V. Krivovichev, and Wulf Depmeier. K-2[(UO2)As2O7] - the first uranium polyarsenate. *Z. Anorg. Allg. Chem.*, **633**: 1125–1126, 2007. (see **page** 101)

[183] Evgeny V. Alekseev, Sergey V. Krivovichev, and Wulf Depmeier. A Crown Ether as Template for Microporous and Nanostructured Uranium Compounds. *Angew. Chem. Int. Ed.*, **47**: 549–551, 2008. DOI: `10.1002/anie.200703295` (see **page** 101)

[184] Evgeny V. Alekseev, Sergey V. Krivovichev, and Wulf Depmeier. Rubidium uranyl phosphates and arsenates with polymeric tetrahedral anions: Syntheses and structures of Rb-4[(UO2)6(P2O7)4(H2O)], Rb-2[(UO2)3(P2O7)P4O12] and Rb[(UO2))(AS3O10)]. *J. Solid State Chem.*, **182**: 2074–2080, 2009. (see **page** 101)

[185] Evgeny V. Alekseev, Sergey V. Krivovichev, and Wulf Depmeier. Novel layered uranyl arsenates, Ag6[(UO2)2(As2O7)(As4O13)] and AI6[(UO2)2 (AsO4)2(As2O7)] (AI-Ag and Na): first observation of a linear As4O136- anion and structure type evolution. *J. Mater. Chem.*, **19**: 2583–2587, 2009. (see **page** 101)

[186] Evgeny V. Alekseev, Sergey V. Krivovichev, and Wulf Depmeier. Crystal chemistry of anhydrous Li uranyl phosphates and arsenates. II. Tubular fragments and cation-cation interactions in the 3D framework structures of Li-6[(UO2)(12)(PO4)(8)(P4O13)], Li-5[(UO2)(13)(AsO4)(9)(As2O7)], Li[(UO2)(4)(AsO4)(3)] and Li-3[(UO2)(7)(AsO4)(5)O)]. *J. Solid State Chem.*, **182**: 2977–2984, 2009. (see **page** 101)

[187] Evgeny V. Alekseev, Sergey V. Krivovichev, and Wulf Depmeier. Structural Complexity of Barium Uranyl Arsenates: Synthesis, Structure, and Topology of Ba4[(UO2)2(As2O7)3], Ba3[(UO2)2(AsO4)2(As2O7)], and Ba5Ca[(UO2)8(AsO4)4O8]. *Cryst. Growth Des.*, **11**: 3295–3300, 2011. DOI: `10.1021/cg200592s` (see **page** 101)

[188] Philip M. Almond and Thomas E. Albrecht-Schmitt. Expanding the Remarkable Structural Diversity of Uranyl Tellurites:ydrothermal Preparation and Structures of K[UO2Te2O5(OH)], Tl3(UO2)2[Te2O5(OH)](Te2O6)·2H2O, -Tl2[UO2(TeO3)2], and Sr3[UO2(TeO3)2](TeO3)2. *Inorg. Chem.*, **41**: 5495–5501, 2002. DOI: `10.1021/ic025820m` (see **page** 101)

[189] P. C. Burns. *Rev. Mineral.*, **38**: 23–23, 1999. (see **pages** 102, 140)

[190] RV Gaines. CLIFFORDITE-A NEW TELLURITE MINERAL FROM MOCTEZUMA. *Am. Mineral.*, **54**: 697–701, 1969. (see **page** 102)

[191] J. Galy and G. Meunier. A propos de la cliffordite UTe3O8. Le systeme UO3-TeO2 a 700degreesC. Structure cristalline de UTe3O9. *Acta Crystallogr., Sect. B: Struct. Sci*, **27**: 608–616, 1971. DOI: `doi:10.1107/S0567740871002632` (see **page** 102)

[192] Dongrong Xiao, Shutao Wang, Enbo Wang, Yu Hou, Yangguang Li, Changwen Hu, and Lin Xu. Hydrothermal synthesis and crystal structure of a three-dimensional vanadium tellurite V4Te4O18. *J. Solid State Chem.*, **176**: 159–164, 2003. (see **pages** 103, 115)

[193] Evgeny V. Alekseev, Sergey V. Krivovichev, Thomas Malcherek, and Wulf Depmeier. One-Dimensional Array of Two- and Three-Center Cationation Bonds in the Structure of Li4[(UO2)10O10(Mo2O8)]. *Inorg. Chem.*, **46**: 8442–8444, 2007. DOI: `10.1021/ic7009385` (see **pages** 105, 136, 139)

[194] Sergey V. Krivovichev and Peter C. Burns. A novel rigid uranyl tungstate sheet in the structures of Na2[(UO2)W2O8] and Ag2[(UO2)W2O8]. *Solid State Sci.*, **5**: 373–381, 2003. (see **pages** 105, 138)

[195] S. Obbade, C. Dion, E. Bekaert, S. Yagoubi, M. Saadi, and F. Abraham. Synthesis and crystal structure of new uranyl tungstates M2(UO2)(W2O8) (M=Na, K), M2(UO2)2(WO5)O (M=K, Rb), and Na10(UO2)8(W5O20)O8. *J. Solid State Chem.*, **172**: 305–318, 2003. (see **pages** 105, 138)

[196] George H. Swihart, Pradip K. Sen Gupta, Elmer O. Schlemper, Malcolm E. Back, and Richard V. Gaines. The crystal structure of moctezumite [PbUO 2](TeO 3) 2. *Am. Mineral.*, **78**: 835–839, 1993. (see **pages** 106, 118)

[197] Philip M. Almond, Michael L. McKee, and Thomas E. Albrecht-Schmitt. Unusual Uranyl Tellurites Containing [Te2O6]4 Ions and Three-Dimensional Networks. *Angew. Chem. Int. Ed.*, **41**: 3426–3429, 2002. (see **page** 106)

[198] J. Hanuza, M. Mczka, J. Lorenc, A. A. Kaminskii, L. Bohaty, and P. Becker. Polarised IR and Raman spectra of non-centrosymmetric Na3Li(SeO4)2·6H2O crystal new Raman laser material. *Spectrochim. Acta, Part A*, **71**: 68–72, 2008. DOI: `http://dx.doi.org/10.1016/j.saa.2007.11.008` (see **pages** 107, 118)

[199] I. L. Botto and E. J. Baran. Die IR-Spektren der Phasen A1/2IIIB1/2VTe3O8 (A = Fe, In, Sc; B = Nb, Ta) und UTe3O9. *Z. anorg. allg. Chem.*, **484**: 210–214, 1982. (see **page** 107)

[200] Ray L. Frost, Matt L. Weier, B. Jagannadha Reddy, and Ji ejka. A Raman spectroscopic study of the uranyl selenite mineral haynesite. *J. Raman Spectrosc.*, **37**: 816–821, 2006. (see **pages** 107, 108, 119)

[201] Ray L. Frost, Ji ejka, and Marilla J. Dickfos. Raman spectroscopic study of the uranyl tellurite mineral moctezumite PbUO2(TeO3)2. *J. Raman Spectrosc.*, **40**: 38–41, 2009. (see **pages** 107, 108, 119)

[202] Llewellyn H. Jones. Systematics in the vibrational spectra of uranyl complexes. *Spectrochim. Acta, Part A*, **10**: 395–403, 1958. DOI: `http://dx.doi.org/10.1016/0371-1951(58)80107-1` (see **pages** 108, 119, 143)

[203] David D. Schnaars and Richard E. Wilson. Structural and Vibrational Properties of U(VI)O2Cl42- and Pu(VI)O2Cl42- Complexes. *Inorg. Chem.*, **52**: 14138–14147, 2013. DOI: `10.1021/ic401991n` (see **pages** 108, 119, 143)

[204] K. W. Bagnall and M. W. Wakerley. Infrared and Raman spectra of the uranyl ion. *J. Inorg. Nucl. Chem.*, **37**: 329–330, 1975. DOI: `http://dx.doi.org/10.1016/0022-1902(75)80194-1` (see **page** 108)

[205] G. Sekar, V. Ramakrishnan, and G. Aruldhas. Vibrational spectra of Te(OH)6·X2SO4 (X = Tl, Na). *Infrared Phys.*, **27**: 253–256, 1987. (see **pages** 108, 119)

[206] Ray L. Frost, Ji ejka, and Marilla J. Dickfos. Raman and infrared spectroscopic study of the molybdate-containing uranyl mineral calcurmolite. *J. Raman Spectrosc.*, **39**: 779–785, 2008. (see **pages** 108, 119)

[207] Ray L. Frost. Tlapallite H6(Ca,Pb)2(Cu,Zn)3SO4(TeO3)4TeO6, a multi-anion mineral: A Raman spectroscopic study. *Spectrochim. Acta, Part A*, **72**: 903–906, 2009. DOI: `http://dx.doi.org/10.1016/j.saa.2008.12.008` (see **page** 108)

[208] J. Hanuza, M. Maczka, and J. H. van der Maas. Polarized IR and Raman spectra of tetragonal NaBi(WO4)2, NaBi(MoO4)2 and LiBi(MoO4)2 single crystals with scheelite structure. *J. Mol. Struct.*, **348**: 349–352, 1995. (see **pages** 109, 132, 153)

[209] K. Hermanowicz, M. Mczka, P. J. Dere, J. Hanuza, W. Strek, and H. Drulis. Optical properties of chromium(III) in trigonal KAl(MoO4)2 and monoclinic NaAl(MoO4)2 hosts. *J. Lumin.*, **92**: 151–159, 2000. (see **pages** 109, 132, 153)

[210] Ray L. Frost, Ji ejka, Matt Weier, and Godwin A. Ayoko. A Raman spectroscopic study of the uranyl tellurite mineral schmitterite. *Spectrochim. Acta, Part A*, **65**: 571–574, 2006. DOI: `http://dx.doi.org/10.1016/j.saa.2005.12.013` (see **page** 109)

[211] Ray L. Frost and Eloise C. Keeffe. Raman spectroscopic study of the tellurite mineral: sonoraite Fe3+Te4+O3(OH)·H2O. *J. Raman Spectrosc.*, **40**: 133–136, 2009. (see **page** 109)

[212] Ray L. Frost and Eloise C. Keeffe. Raman spectroscopic study of the mixed anion mineral yecoraite. *J. Raman Spectrosc.*, **40**: 1117–1120, 2009. (see **page** 109)

[213] W. Levason. The coordination chemistry of periodate and tellurate ligands. *Coord. Chem. Rev.*, **161**: 33–79, 1997. (see **page** 109)

[214] Shijun Wu, Oliver Beermann, Shuao Wang, Astrid Holzheid, Wulf Depmeier, Thomas Malcherek, Giuseppe Modolo, Evgeny V. Alekseev, and Thomas E. Albrecht-Schmitt. Synthesis of Uranium Materials under Extreme Conditions: UO2[B3Al4O11(OH)], a Complex 3D Aluminoborate. *Chem. Eur. J.*, **18**: 4166–4169, 2012. (see **pages** 110, 111)

[215] Shijun Wu, Philip Kegler, Shuao Wang, Astrid Holzheid, Wulf Depmeier, Thomas Malcherek, Evgeny V. Alekseev, and Thomas E. Albrecht-Schmitt. Rich Coordination of Nd3+ in Mg2Nd13(BO3)(8)(SiO4)(4)(OH)(3), Derived from High-Pressure/High-Temperature Conditions. *Inorg. Chem.*, **51**: 3941–3943, 2012. (see **page** 110)

[216] Shijun Wu, Shuao Wang, Matthew Polinski, Oliver Beermann, Philip Kegler, Thomas Malcherek, Astrid Holzheid, Wulf Depmeier, Dirk Bosbach, Thomas E. Abrecht-Schmitt, and Evgeny V. Alekseev. High Structural Complexity of Potassium Uranyl Borates Derived from High-Temperature/High-Pressure Reactions. *Inorg. Chem.*, **52**: 5110–5118, 2013. (see **page** 111)

[217] Na Yu, Vladislav V. Klepov, Philip Kegler, Dirk Bosbach, Thomas E. Albrecht-Schmitt, and Evgeny V. Alekseev. Th(AsIII4AsV4O18): a Mixed-Valent Oxoarsenic(III)/arsenic(V) Actinide Compound Obtained under Extreme Conditions. *Inorg. Chem.*, **53**: 8194–8196, 2014. DOI: `10.1021/ic5013704` (see **pages** 111, 127)

[218] Vidyavathy and K. Vidyasagar. Hydrothermal Synthesis and Characterization of Novel One-Dimensional Tellurites of Molybdenum(VI), A4Mo6TeO22·2H2O (A = NH4, Rb). *Inorg. Chem.*, **38**: 1394–1400, 1999. DOI: `10.1021/ic980957r` (see **page** 112)

[219] Seong-eun Bang, Zhi Pan, Yeong Hun Kim, Dong Woo Lee, and Kang Min Ok. Y2MoSe3O12 and Y2MoTe3O12: Solid-state synthesis, structure determination, and characterization of two new quaternary mixed metal oxides containing asymmetric coordination environment. *J. Solid State Chem.*, **208**: 65–70, 2013. (see **page** 112)

[220] Matthias Weil. New Silver Tellurates - The Crystal Structures of a Third Modification of Ag2Te2O6 and of Ag4TeO5. *Z. Anorg. Allg. Chem.*, **633**: 1217–1222, 2007. (see **page** 116)

[221] K Krishnan, GA Rama Rao, KD Singh Mudher, and V Venugopal. Thermal stability and vapour pressure studies on UTe 3 O 9 (s) and UTeO 5 (s). *Journal of nuclear materials*, **254**: 49–54, 1998. (see **page** 118)

[222] K. V. Domoratskii, V. I. Pastukhov, A. Yu Kudzin, L. Ya Sadovskaya, V. M. Rizak, and V. A. Stefanovich. Raman scattering in the Bi2TeO5 single crystal. *Phys. Solid State*, **42**: 1443–1446, 2000. DOI: `10.1134/1.1307049` (see **pages** 119, 132)

[223] S. Raman. Crystal Structure of KTeO(OH)5.H2O. *Inorg. Chem.*, **3**: 634–638, 1964. DOI: `10.1021/ic50015a006` (see **page** 119)

[224] Jaime Llanos, Rodrigo Castillo, Daniel Barrionuevo, Daro Espinoza, and Sergio Conejeros. The family of Ln2TeO6 compounds (Ln = Y, La, Sm and Gd): Characterization andí¡p¿synthesis by the Pechini solel process. *J. Alloys Compd.*, **485**: 565–568, 2009. (see **page** 119)

[225] Jonathan D. Woodward, Philip M. Almond, and Thomas E. Albrecht-Schmitt. Synthesis and crystal structures of the layered uranyl tellurites A2[(UO2)3(TeO3)2O2] (A=K, Rb, Cs). *J. Solid State Chem.*, **177**: 3971–3976, 2004. (see **page** 120)

[226] Jonathan D. Woodward and Thomas E. Albrecht-Schmitt. Molten salt flux synthesis and structure of the new layered uranyl tellurite, K4[(UO2)5(TeO3)2O5]. *J. Solid State Chem.*, **178**: 2922–2926, 2005. (see **page** 120)

[227] H. S. Ra, K. M. Ok, and P. S. Halasyamani. Combining second-order Jahn-Teller distorted cations to create highly efficient SHG materials: Synthesis, characterization, and NLO properties of BaTeM2O9 (M = Mo6+ or W6+). *J. Am. Chem. Soc.*, **125**: 7764–7765, 2003. (see **page** 122)

[228] Junjie Zhang, Zhonghan Zhang, Weiguo Zhang, Qingxin Zheng, Youxuan Sun, Chengqian Zhang, and Xutang Tao. Polymorphism of BaTeMo2O9: A New Polar Polymorph and the Phase Transformation. *Chem. Mater.*, **23**: 3752–3761, 2011. (see **page** 122)

[229] Jian Lin, Kariem Diefenbach, Justin N. Cross, Jean-Marie Babo, and Thomas E. Albrecht-Schmitt. Thermochromism, the Alexandrite Effect, and Dynamic Jahn-Teller Distortions in Ho2Cu(TeO3)(2)(SO4)(2). *Inorg. Chem.*, **52**: 13278–13281, 2013. (see **page** 122)

[230] Yue-Ling Shen, Hai-Long Jiang, Jian Xu, Jiang-Gao Mao, and Kok Wai Cheah. Luminescent Lanthanide Selenites and Tellurites Decorated by MoO4 Tetrahedra or MoO6 Octahedra: Nd2MoSe2O10, Gd2MoSe3O12, La2MoTe3O12, and Nd2MoTe3O12. *Inorg. Chem.*, **44**: 9314–9321, 2005. DOI: `10.1021/ic051376m` (see **page** 122)

[231] Peter C. Burns, Rodney C. Ewing, and Frank C. Hawthorne. The crystal chemistry of hexavalent uranium: polyhedron geometries, bond-valence parameters, and polymerization of polyhedra. *Can. Mineral.*, **35**: 1551–1570, 1997. (see **page** 122)

[232] Joanna Goodey, Kang Min Ok, Jake Broussard, Cristina Hofmann, Francisco V. Escobedo, and P. Shiv Halasyamani. Syntheses, structures, and second-harmonic generating properties in new quaternary tellurites: A2TeW3O12 (A=K, Rb, or Cs). *J. Solid State Chem.*, **175**: 3–12, 2003. DOI: `http://dx.doi.org/10.1016/S0022-4596(03)00079-3` (see **page** 125)

[233] Sau Doan Nguyen and P. Shiv Halasyamani. Synthesis, Structure, and Characterization of New Li+-d(0)-Lone-Pair-Oxides: Noncentrosymmetric Polar Li-6(Mo2O5)(3)(SeO3)(6) and Centrosymmetric Li-2(MO3)(TeO3) (M = Mo6+ or W6+). *Inorg. Chem.*, **51**: 9529–9538, 2012. (see **page** 125)

[234] Su-Yun Zhang and Jiang-Gao Mao. Syntheses, Crystal Structures, Magnetic and Luminescent Properties of two Classes of Molybdenum(VI) Rich Quaternary Lanthanide Selenites. *Inorg. Chem.*, **50**: 4934–4943, 2011. DOI: `10.1021/ic200149y` (see **page** 125)

[235] A. P. Tyutyunnik, V. N. Krasilłikov, V. G. Zubkov, L. A. Perelyaeva, and I. V. Baklanova. Synthesis, structure, and properties of V2O3(XO4)2 (X = S, Se). *Russ. J. Inorg. Chem.*, **55**: 501–507, 2010. DOI: `10.1134/S0036023610040042` (see **page** 125)

[236] Rdiger Kniep, Holger Engelhardt, and Cornelia Hauf. A First Approach to Borophosphate Structural Chemistry. *Chem. Mater.*, **10**: 2930–2934, 1998. DOI: `10.1021/cm980263g` (see **pages** 125, 129)

[237] Bastian Ewald, Ya-Xi Huang, and Rdiger Kniep. Structural Chemistry of Borophosphates, Metalloborophosphates, and Related Compounds. *Z. Anorg. Allg. Chem.*, **633**: 1517–1540, 2007. DOI: `10.1002/zaac.200700232` (see **pages** 125, 129)

[238] C. C. Torardi, C. Page, L. H. Brixner, G. Blasse, and G. J. Dirksen. Structure and luminescence of some CsLnW2O8 compounds. *J. Solid State Chem.*, **69**: 171–178, 1987. DOI: `http://dx.doi.org/10.1016/0022-4596(87)90023-5` (see **page** 127)

[239] E. Gallucci, C. Goutaudier, M. Th Cohen-Adad, B. F. Mentzen, and T. Hansen. A neutron diffraction study of non-stoichiometric ł-KYW2O8. *J. Alloys Compd.*, **306**: 227–234, 2000. DOI: `http://dx.doi.org/10.1016/S0925-8388(00)00764-7` (see **page** 127)

[240] M. Huyghe, M. R. Lee, M. Quarton, and F. Robert. Structure cristalline de K2Th(MoO4)3. *Acta Crystallogr., Sect. C: Cryst. Struct. Commun.*, **47**: 244–246, 1991. (see **pages** 128, 149, 151)

[241] Amanda J. Albrecht, Ginger E. Sigmon, Laura Moore-Shay, Rebecca Wei, Colleen Dawes, Jennifer Szymanowski, and Peter C. Burns. The crystal chemistry of four thorium sulfates. *J. Solid State Chem.*, **184**: 1591–1597, 2011. (see **page** 128)

[242] Matthias Weil. Two Modifications of (TeO)(HAsO4) and its Dehydration Product (Te3O3)(AsO4)2 - Three more Examples of Tellurium(IV) with a Fivefold Oxygen Coordination. *Z. Anorg. Allg. Chem.*, **640**: 128–135, 2014. (see **page** 128)

[243] T. L. Cremers, P. G. Eller, and R. A. Penneman. Orthorhombic thorium(IV) molybdate, Th(MoO4)2. *Acta Crystallogr., Sect. C: Cryst. Struct. Commun.*, **39**: 1165–1167, 1983. (see **pages** 128, 149, 151)

[244] J. C. J. Bart, G. Petrini, and N. Giordano. The Binary Oxide System Te-O. *Z. Anorg. Allg. Chem.*, **412**: 258–270, 1975. DOI: `10.1002/zaac.19754120310` (see **page** 131)

[245] G. Petrini and J. C. J. Bart. *Z. Anorg. Allg. Chem.*, **474**: 229–232, 1981. (see **page** 131)

[246] A. P. Mirgorodsky, T. Merle-Mjean, P. Thomas, J. C. Champarnaud-Mesjard, and B. Frit. Dynamics and crystal chemistry of tellurites: 1. Raman spectra of thallium tellurites: Tl2TeO3, Tl2Te2O5 and Tl2Te3O7. *J. Phys. Chem. Solids*, **63**: 545–554, 2002. (see **page** 132)

[247] Vidyavathy and K. Vidyasagar. Low-Temperature Syntheses and Characterization of Novel Layered Tellurites, A2Mo3TeO12 (A = NH4, Cs), and ero-Dimensional Tellurites, A4Mo6Te2O24·6H2O (A = Rb, K). *Inorg. Chem.*, **37**: 4764–4774, 1998. DOI: `10.1021/ic980102e` (see **page** 132)

[248] Fabien Burdet, Jacques Pcaut, and Marinella Mazzanti. Isolation of a Tetrameric Cationation Complex of Pentavalent Uranyl. *J. Am. Chem. Soc.*, **128**: 16512–16513, 2006. DOI: `10.1021/ja067445t` (see **page** 135)

[249] Bin Xiao, Thorsten M. Gesing, Lars Robben, Dirk Bosbach, and Evgeny V. Alekseev. Dinuclear Face-Sharing Bi-octahedral Tungsten(VI) Core and Unusual Thermal Behavior in Complex Th Tungstates. *Chem. Eur. J.*, **21**: 7629–7629, 2015. (see **page** 135)

[250] Bin Xiao, Martina Klinkenberg, Dirk Bosbach, Evgeny V. Suleimanov, and Evgeny V. Alekseev. Effects of Te(IV) Oxo-Anion Incorporation into Thorium Molybdates and Tungstates. *Inorg. Chem.*, **54**: 5981–5990, 2015. DOI: `10.1021/acs.inorgchem.5b00789` (see **page** 135)

[251] Tyler A. Sullens, Rebecca A. Jensen, Tatiana Y. Shvareva, and Thomas E. Albrecht-Schmitt. Cationation Interactions between Uranyl Cations in a Polar Open-Framework Uranyl Periodate. *J. Am. Chem. Soc.*, **126**: 2676–2677, 2004. DOI: `10.1021/ja031695h` (see **pages** 135, 136)

[252] Matthew R. MacDonald, Megan E. Fieser, Jefferson E. Bates, Joseph W. Ziller, Filipp Furche, and William J. Evans. Identification of the +2 Oxidation State for Uranium in a Crystalline Molecular Complex, [K(2.2.2-Cryptand)][(C5H4SiMe3)3U]. *J. Am. Chem. Soc.*, **135**: 13310–13313, 2013. DOI: `10.1021/ja406791t` (see **page** 135)

[253] C. S. Chen, S. F. Lee, and K. H. Lii. K(UO)Si2O6: A pentavalent-uranium silicate. *J. Am. Chem. Soc.*, **127**: 12208–12209, 2005. (see **page** 135)

[254] Christopher R. Graves and Jaqueline L. Kiplinger. Pentavalent uranium chemistry-synthetic pursuit of a rare oxidation state. *Chem. Commun.*, 3831–3853, 2009. (see **page** 135)

[255] Louise Natrajan, Fabien Burdet, Jacques Pcaut, and Marinella Mazzanti. Synthesis and Structure of a Stable Pentavalent-Uranyl Coordination Polymer. *J. Am. Chem. Soc.*, **128**: 7152–7153, 2006. DOI: `10.1021/ja0609809` (see **page** 135)

[256] Lucile Chatelain, Victor Mougel, Jacques Pecaut, and Marinella Mazzanti. Magnetic communication and reactivity of a stable homometallic cation-cation trimer of pentavalent uranyl. *Chem. Sci.*, **3**: 1075–1079, 2012. (see **page** 135)

[257] William J Evans, Stosh A Kozimor, and Joseph W Ziller. Molecular octa-uranium rings with alternating nitride and azide bridges. *Science*, **309**: 1835–1838, 2005. (see **page** 136)

[258] Polly L Arnold, Dipti Patel, Claire Wilson, and Jason B Love. Reduction and selective oxo group silylation of the uranyl dication. *Nature*, **451**: 315–317, 2008. (see **page** 136)

[259] Cheng-Shiuan Lee, Chia-Hui Lin, Sue-Lein Wang, and Kwang-Hwa Lii. [(Na7UO2)-O-IV((UO)-O-V)(2)((UO2)-O-V/VI)(2)Si4O16]: A Mixed-Valence Uranium Silicate. *Angew. Chem. Int. Ed.*, **49**: 4254–4256, 2010. (see **page** 136)

[260] V. N. Serezhkin, G. V. Sidorenko, D. V. Pushkin, and L. B. Serezhkina. Cation-cation interactions between uranyl(VI) ions. *Radiochemistry*, **56**: 115–133, 2014. DOI: `10.1134/S1066362214020015` (see **pages** 136, 142)

[261] Victor Mougel, Lucile Chatelain, Jacques Pcaut, Roberto Caciuffo, Eric Colineau, Jean-Christophe Griveau, and Marinella Mazzanti. Uranium and manganese assembled in a wheel-shaped nanoscale single-molecule magnet with high spin-reversal barrier. *Nature Chemistry*, **4**: 1011–1017, 2012. (see **page** 136)

[262] Chia-Hui Lin, Chih-Shan Chen, A. A. Shiryaev, Ya V. Zubavichus, and Kwang-Hwa Lii. K3(U3O6)(Si2O7) and Rb3(U3O6)(Ge2O7): A Pentavalent-Uranium Silicate and Germanate. *Inorg. Chem.*, **47**: 4445–4447, 2008. DOI: `10.1021/ic800300v` (see **page** 136)

[263] Victor Mougel, Pawel Horeglad, Grgory Nocton, Jacques Pcaut, and Marinella Mazzanti. Cation-Cation Complexes of Pentavalent Uranyl: From Disproportionation Intermediates to Stable Clusters. *Chem. Eur. J.*, **16**: 14365–14377, 2010. (see **page** 136)

[264] Shuao Wang, Evgeny V. Alekseev, Jared T. Stritzinger, Guokui Liu, Wulf Depmeier, and Thomas E. Albrecht-Schmitt. Structure-Property Relationships in Lithium, Silver, and Cesium Uranyl Borates. *Chem. Mater.*, **22**: 5983–5991, 2010. (see **page** 136)

[265] Shuao Wang, Juan Diwu, Evgeny V. Alekseev, Laurent J. Jouffret, Wulf Depmeier, and Thomas E. Albrecht-Schmitt. Cation-Cation Interactions between Neptunyl(VI) Units. *Inorg. Chem.*, **51**: 7016–7018, 2012. DOI: `10.1021/ic3009305` (see **page** 136)

[266] Karrie-Ann Kubatko and Peter C. Burns. Cationation Interactions in Sr5(UO2)20(UO6)2O16(OH)6(H2O)6 and Cs(UO2)9U3O16(OH)5. *Inorg. Chem.*, **45**: 10277–10281, 2006. DOI: `10.1021/ic0609453` (see **pages** 136, 139)

[267] Yaping Li, Christopher L Cahill, and Peter C Burns. Synthesis, structural characterization, and topological rearrangement of a novel open framework UO material:(NH4) 3 (H2O) 2 [(UO2) 10O10 (OH)][(UO4)(H2O) 2]. *Chem. Mater.*, **13**: 4026–4031, 2001. (see **page** 136)

[268] Evgeny V. Alekseev, Sergey V. Krivovichev, Wulf Depmeier, Oleg I. Siidra, Karsten Knorr, Evgeny V. Suleimanov, and Evgeny V. Chuprunov. Na2Li8[(UO2)(11)O-12(WO5)(2)]: Three different uranyl-ion coordination geometries and cation-cation interactions. *Angew. Chem. Int. Ed.*, **45**: 7233–7235, 2006. (see **page** 138)

[269] Evgeny V. Alekseev, Sergey V. Krivovichev, Wulf Depmeier, Thomas Malcherek, Evgeny V. Suleimanovl, and Evgeny V. Chuprunov. The crystal structure of Li-4[(UO2)(2)W2O10)] and crystal chemistry of Li uranyl tungstates. *Z. Kristallogr.*, **222**: 391–395, 2007. (see **page** 138)

[270] Andrey N. Seliverstov, Evgeny V. Suleimanov, Evgeny V. Chuprunov, Nikolay V. Somov, Elena M. Zhuchkova, Maxim I. Lelet, Konstantin B. Rozov, Wulf Depmeier, Sergey V. Krivovichev, and Evgeny V. Alekseev. Polytypism and oxo-tungstate polyhedra polymerization in novel complex uranyl tungstates. *Dalton Trans.*, **41**: 8512–8514, 2012. (see **pages** 141, 145)

[271] E. V. Alekseev, E. V. Suleimanov, M. O. Marychev, E. V. Chuprunov, and G. K. Fukin. Crystal structure of uranyl tungstate Cs2U2WO10. *J. Struct. Chem.*, **47**: 881–886, 2006. (see **pages** 141, 145)

[272] P. Shiv Halasyamani, Robin J. Francis, Susan M. Walker, and Dermot O'Hare. New Layered Uranium(VI) Molybdates: Syntheses and Structures of (NH3(CH2)3NH3)(H3O)2(UO2)3(MoO4)5, C(NH2)3(UO2)(OH)(MoO4), (C4H12N2)(UO2)(MoO4)2, and (C5H14N2) (UO2)(MoO4)2 H2O. *Inorg. Chem.*, **38**: 271–279, 1998. DOI: `10.1021/ic980836r` (see **page** 143)

[273] Ray L. Frost, Jakub Plil, Ji ejka, Ji Sejkora, Eloise C. Keeffe, and Silmarilly Bahfenne. Raman spectroscopic study of the uranyl mineral pseudojohannite Cu6.5[(UO2)4O4(SO4)2]2(OH)5·25H2O. *J. Raman Spectrosc.*, **40**: 1816–1821, 2009. (see **page** 143)

[274] Valrie Vallet, Ulf Wahlgren, and Ingmar Grenthe. Probing the Nature of Chemical Bonding in Uranyl(VI) Complexes with Quantum Chemical Methods. *J. Phys. Chem. A*, **116**: 12373–12380, 2012. DOI: `10.1021/jp3091123` (see **page** 144)

[275] V. I. Tsaryuk and V. F. Zolin. Vibration and vibronic spectra of lanthanide compounds with different types of coordination polyhedra of tungsten and molybdenum. *Spectrochim. Acta Mol. Biomol*, **57**: 355–359, 2001. (see **page** 144)

[276] Ping Yu, Shuao Wang, Evgeny V. Alekseev, Wulf Depmeier, David T. Hobbs, Thomas E. Albrecht-Schmitt, Brian L. Phillips, and William H. Casey. Technetium-99 MAS NMR Spectroscopy of a Cationic Framework Material that Traps TcO4- Ions. *Angew. Chem. Int. Ed.*, **49**: 5975–5977, 2010. (see **page** 147)

[277] Shuao Wang, Ping Yu, Bryant A. Purse, Matthew J. Orta, Juan Diwu, William H. Casey, Brian L. Phillips, Evgeny V. Alekseev, Wulf Depmeier, David T. Hobbs, and Thomas E. Albrecht-Schmitt. Selectivity, Kinetics, and Efficiency of Reversible Anion Exchange with TcO4- in a Supertetrahedral Cationic Framework. *Adv. Funct. Mater.*, **22**: 2241–2250, 2012. (see **page** 147)

[278] Shuao Wang, Evgeny V. Alekseev, Jie Ling, Guokui Liu, Wulf Depmeier, and Thomas E. Albrecht-Schmitt. Polarity and Chirality in Uranyl Borates: Insights into Understanding the Vitrification of Nuclear Waste and the Development of Nonlinear Optical Materials. *Chem. Mater.*, **22**: 2155–2163, 2010. (see **page** 147)

[279] M. Huyghe, M. R. Lee, S. Jaulmes, and M. Quarton. Structure de K8Th(MoO4)6. *Acta Crystallogr., Sect. C: Cryst. Struct. Commun.*, **49**: 950–954, 1993. (see **page** 149)

[280] Adam J. Bridgeman and Germn Cavigliasso. Bonding in [W4O16]8 isopolyanions. *Polyhedron*, **21**: 2201–2206, 2002. (see **page** 149)

[281] Junwei Zhao, Dongying Shi, Lijuan Chen, Pengtao Ma, Jingping Wang, and Jingyang Niu. Two 1-D multi-nickel substituted arsenotungstate aggregates. *CrystEngComm*, **13**: 3462–3469, 2011. (see **page** 149)

[282] Bryan M Gatehouse and Peter Leverett. Crystal structures of silver dimolybdate, Ag 2 Mo 2 O 7, and silver ditungstate, Ag 2 W 2 O 7. *Dalton Trans.*, 1316–1320, 1976. (see **page** 150)

[283] E. M. Larson, P. G. Eller, T. L. Cremers, R. A. Penneman, and C. C. Herrick. Structure of trigonal thorium molybdate. *Acta Crystallogr., Sect. C: Cryst. Struct. Commun.*, **45**: 1669–1672, 1989. (see **page** 151)

[284] R. D. Shannon. Revised effective ionic radii and systematic studies of interatomic distances in halides and chalcogenides. *Acta Cryst. A*, **32**: 751–767, 1976. (see **page** 151)

[285] R. F. Klevtsova, S. F. Solodovnikov, Y. L. Tushinova, B. G. Bazarov, L. A. Glinskaya, and Zh G. Bazarova. A new type of mixed framework in the crystal structure of binary molybdate Nd2Zr3(MoO4)9. *J. Struct. Chem.*, **41**: 280–284, 2000. DOI: `10.1007/BF02741593` (see **page** 152)

[286] B. G. Bazarov, V. G. Grossman, R. F. Klevtsova, A. G. Anshits, T. A. Vereshchagina, L. A. Glinskaya, Yu L. Tushinova, K. N. Fedorov, and Zh G. Bazarova. Crystal structure of binary molybdate Pr2Hf3(MoO4)9. *J. Struct. Chem.*, **50**: 566–569, 2009. DOI: `10.1007/s10947-009-0086-z` (see **page** 152)

[287] Rodney C Ewing and LuMin Wang. Phosphates as nuclear waste forms. *Reviews in mineralogy and geochemistry*, **48**: 673–699, 2002. (see **page** 152)

[288] Tatiana A. Vereshchagina, Elena V. Fomenko, Nataly G. Vasilieva, Leonid A. Solovyov, Sergei N. Vereshchagin, Zhibzema G. Bazarova, and Alexander G. Anshits. A novel layered zirconium molybdate as a precursor to a ceramic zirconomolybdate host for lanthanide bearing radioactive waste. *J. Mater. Chem.*, **21**: 12001–12007, 2011. (see **page** 152)

[289] J. Hanuza, M. MaŁczka, J. Lorenc, A. A. Kaminskii, L. Bohaty, and P. Becker. Polarised IR and Raman spectra of non-centrosymmetric Na3Li(MoO4)2· 6H2O crystal–a new Raman laser material. *J. Raman Spectrosc.*, **41**: 424–430, 2010. (see **page** 153)

[290] Franklin D. Hardcastle and Israel E. Wachs. Determination of molybdenum-oxygen bond distances and bond orders by Raman spectroscopy. *J. Raman Spectrosc.*, **21**: 683–691, 1990. (see **page** 153)

[291] V. O. Sokolov, V. G. Plotnichenko, V. V. Koltashev, and I. A. Grishin. On the structure of molybdateellurite glasses. *J. Non-Cryst. Solids*, **355**: 239–251, 2009. DOI: `http://dx.doi.org/10.1016/j.jnoncrysol.2008.11.017` (see **page** 153)

[292] G. A. Nazri and C. Julien. Far-infrared and Raman studies of orthorhombic MoO3 single crystal. *Solid State Ionics*, **5356, Part 1**: 376–382, 1992. DOI: `http://dx.doi.org/10.1016/0167-2738(92)90403-C` (see **page** 153)

[293] L. Seguin, M. Figlarz, R. Cavagnat, and J. C. Lassgues. Infrared and Raman spectra of MoO3 molybdenum trioxides and MoO3 · xH2O molybdenum trioxide hydrates. *Spectrochim. Acta, Part A*, **51**: 1323–1344, 1995. DOI: `http://dx.doi.org/10.1016/0584-8539(94)00247-9` (see **page** 153)

[294] N. D. Dahale, Meera Keskar, and K. D. Singh Mudher. Structural and thermal studies on Na2Th(MoO4)3, Na2Pu(MoO4)3, Na4Th(MoO4)4 and Na4Pu(MoO4)4. *J. Alloys Compd.*, **415**: 244–250, 2006. (see **page** 154)

Acknowledgement

First and foremost I would like to thank to my advisor, Dr. Evgeny V. Alekseev. Thank you for everything you have done for me in regards to my research, my education, and my work. Actually, my scientific journey as an inorganic chemist did not start in the chemistry realm. I was a physicist during my master research at the Chinese Academy of Science (CAS), and obtained the degree in Condensed Matter Physics. During that time, my research was more focused on the physical explanation of experimental behavior. It is you, Evgeny, my good mentor and also helpful friend throughout the course of my PhD career, who firstly brings me to the wonderful world of inorganic actinide chemistry, selflessly lends me your expertise and guidance, and kindly gives me useful advices and suggestions. Whenever I get into a trouble, no matter regarding working, studying or researching, you always spare no effort to help me, with careness and patience, and give me endless courage and strength. Your passion and enthusiasm toward the knowledge of actinide chemistry inspire me to work till harder. It has been an honor to work alongside with you in exploring the wonders of science. I sincerely hope for close collaborations with you all of my scientific life.

I would like to express my gratitude to Prof. Dr. Dirk Bosbach for giving me a chance to carry out my PhD work in IEK-6. You gave me great help in my research and insightful suggestion for this dissertation.

I also wish to thank all our group members. Philip, together, we have found lots of exciting results under the extreme synthesis condition. I cannot thank you enough for all of the kind help you have done for me over the past two years. Na Yu, Yucheng Hao and Eike Lange, you have been my best friends throughout the course of my Ph.D career. I am very grateful to the help and suggestions you have given me during my scientific researches.

I thank Prof. Thorsten M. Gesing and Dr. Lars Robben for making the temperature-dependent PXRD experiment and analysing the phase transition behaviors of my samples.

I especially thank Dr. Kowalski for the help of theoretical explanation of my research materials, and I would also like to thank all the other people in IEK-6 who have provided help over last three years.

Finally, I owe my deepest gratitude to my parents and my wife Yu Pan for their love, support and

understanding.

Personal data

Name: Bin Xiao
Gender: Male
Born: 15.05.1986
Nationality: Chinese

Currently studying as the PhD student at the *Institute of Energy and Climate Research (IEK-6), Forschungszentrum, Jülich, Germany.*

Adress: IEK-6, Wilhelm-Johnen-Strasse, D-52428 Jülich, Germany
Contact e-mail: b.xiao@fz-juelich.de
Phone: +49 2461 61 61 09
Fax: +49 2461 61 24 50

Education

2012.10—2015.12	PhD student in the field of **material science** at Forchungszentrum Juelich and RWTH Aachen University
2009.09—2012.07	Studying for the Master degree in Fujian Institute of Research on the Structure of Matter, Chinese Academy of Sciences (CAS), **Condensed Matter Physics**, Fuzhou China.
2005.09—2009.07	Bachelor of **Physics** in Southwest University, Chongqing China.

Research experience

Sep.2012-current

♦ PhD thesis of "The Crystal Chemistry of Thorium and Uranium Compounds with Oxo-anions from Group VI of Periodical Table (S, Se, Te, Cr, Mo and W)" at Institute für Kristallographie RWTH Aachen University and Forchungszentrum Juelich.

Sep.2009-Oct.2012

♦ Assisting Prof. Wang, Guofu with a national program (National Natural Science Foundation of China, No.61008060) entitled "Tunable laser properties of Cr^{3+}-doped $AMgB(MO_4)_3$(A=Na, K, Rb, Cs; B=Al, Sc, In; M=Mo, W) crystal, a new candidate for broadband laser applications."

Sep.2008-Sep.2009

♦ Participated in an undergraduate technology funded project entitled "Research on the electronic structure and magnetism of the Heusler alloy."

Skills

Experimental skills: X-ray crystallography, Polarized microscope, Spectroscopic methods (Raman, IR and UV-VIS-IR), NMR, TEM, SEM, MRI, Thermodynamic analysis, Methods of analytical chemistry, Methods of physical chemistry.

Computer skills: Matlab, Java and C/C^{++}.

Publications

[1] **Xiao, B.**; Schlenz, H.; Dellen, J.; Bosbach, D.; Suleimanov, E. V. & Alekseev, E. V.
"From 2D Layers to 3D Frameworks: Expanding the Structural Diversity of Uranyl Compounds by Cation-Cation Interactions"., **Crystal Growth & Design,** 15, 3775-3784 (DOI: 10.1021/acs.cgd.5b00427)

[2] **Xiao, B.**; Kinkenberg, M; Bosbach, D.; Suleimanov, E. V. & Alekseev, E. V.
"The Effects of Te(IV) Oxo-anion Incorporation into Thorium Molybdates and Tungstates"., **Inorg. Chem.**, 2015, 54, 5981-5990 (DOI: 10.1021/acs.inorgchem.5b00789)

[3] **Xiao, B.**; Dellen, J.; Schlenz, H.; Bosbach, D.; Suleimanov, E. V. & Alekseev, E. V.
"Dinuclear Face-Sharing Bioctahedral Tungsten(VI) Core and Unusual Thermal Behavior in Complex Th Tungstates"., **Chem. Eur. J.**, 2015, 21, 7746-7754 (**Cover Profile**) (DOI:10.1002/chem.201500900)

[4] **Xiao, B.**; Gesing, T.M. Bosbach, D.; Robben L. & Alekseev, E. V.
"Chemical and Structural Evolution in the Th-SeO_3^{2-}/SeO_4^{2-} system: from simple selenites to cluster based selenate compounds"., **Inorg. Chem.**, 2015, 54, 3022-3030 (DOI: 10.1021/acs.inorgchem.5b00133)

[5] **Xiao, B.**; Dellen, J.; Schlenz, H.; Bosbach, D.; Suleimanov, E. V. & Alekseev, E. V.
"Dinuclear Face-Sharing Bioctahedral Tungsten(VI) Core and Unusual Thermal Behavior in Complex Th Tungstates"., **Chem. Eur. J.**, 2015, 21, 7746-7754 (DOI:10.1002/chem.201500500)

[6] **Xiao, B.**; Dellen, J.; Schlenz, H.; Bosbach, D.; Suleimanov, E. V. & Alekseev, E. V.
"Unexpected Structural Complexity in Cesium Thorium Molybdates"., **Crystal Growth & Design**, 2014, 14, 2677-2684 (DOI: 10.1021/cg500418e)

[7] **Xiao, B**.; Gesing, T. M.; Kegler, P.; Modolo, G.; Bosbach, D.; Schlenz, H.; Suleimanov, E. V. & Alekseev, E. V.
"High-Temperature Phase Transitions, Spectroscopic Properties, and Dimensionality Reduction in Rubidium Thorium Molybdate Family". **Inorg. Chem.,** 2014, 53, 3088-3098 (Doi: 10.1021/ic403003f)

[8] **Xiao, B**.; Huang, Y.; Zhang, L.; Lin, Z; Wang, G.
"Growth, structure and spectroscopic characterization of Nd^{3+}- doped $KBaGd(WO_4)_3$ crystal with a disordered structure". **PLoS One** 7(7): e40229. (DOI: 10.1371/journal.pone.0040229)

[9] **Xiao, B**.; Lin, Z;, Huang, Y.; Zhang, L.; Wang, G.
"Growth, thermal and spectral properties of Er^{3+} doped and Er^{3+}/Yb^{3+} co-doped $Li_3Ba_2La_3(WO_4)_8$ crystals". **PLoS One** 7(7): e40631. (DOI: 10.1371/journal.pone.0040631)

[10] **Xiao, B**. Huang, Y.; Zhang, L.; Lin, Z; Wang, G.
"Growth, structure and spectral properties of Cr^{3+}-doped $LiMgAl(MoO_4)_3$ crystal with disordered structure". **RSC Adv**. 2012 (2): 5271-5276 (DOI: 10.1039/C2RA00050D)

[11] **Xiao, B**.; Zhang, L.; Lin, Z;, Huang, Y.; Wang, G.
"Growth and spectral properties of Nd^{3+}:$Li_3Ba_2La_3(WO_4)_8$ crystal". **Optoelectron. Adv. Mater.-Rapid Commun**, 2012 (6): 404-410.